The Location of Impurities in Polar Ice

Thesis

The Location of Impurities in Polar Ice

by
Piers Robert Fitzgerald Barnes

A thesis submitted for the degree of Doctor of Philosophy to the Open University in September 2002

Sponsoring establishment:
British Antarctic Survey
Cambridge
UK

Collaborating establishment:
University of Bristol,
UK

AUTHOR NO: T6218933
DATE OF SUBMISSION: 6 SEPTEMBER 2002
DATE OF AWARD 5 DECEMBER 2002

SE12
(August 2001)

THE OPEN UNIVERSITY

RESEARCH SCHOOL

Research Degrees in Sponsoring Establishments

Library Authorisation

Please return this form to the Research School, The Open University, Walton Hall, Milton Keynes, MK7 6AA with the two bound copies of the thesis to be deposited with the University Library. All candidates should complete parts one and two of the form. Part three only applies to PhD candidates.

Part One: Candidate Details

T6218133

Name: PIERS ROBERT FITZGERALD BARNES PI: DR. ERIC WOLFF

Degree: Ph.D. Sponsoring Establishment: BRITISH ANTARCTIC SURVEY

Thesis title: THE LOCATION OF IMPURITIES IN POLAR ICE

Part Two: Open University Library Authorisation

I confirm that I am willing for my thesis to be made available to readers by the Open University Library, and that it may be photocopied, subject to the discretion of the Librarian.

Signed: Eric Wolff pp PIERS BARNES Date: 11/11/02
(Piers is now in Antarctica for 3 months, but has authorised me to sign for him)

Part Three: British Library Authorisation [PhD candidates only]

If you want a copy of your PhD thesis to be available on loan to the British Library Thesis Service as and when it is requested, you must sign a British Library Doctoral Thesis Agreement Form. Please return it to the Research School with this form. The British Library will publicise the details of your thesis and may request a copy on loan from the University Library. Information on the presentation of the thesis is given in the Agreement Form.

Please note the British Library have requested that theses should be printed on one side only to enable them to produce a clear microfilm. The Open University Library sends the fully bound copy of theses to the British Library.

The University has agreed that your participation in the British Library Thesis Service should be voluntary. Please tick either (a) or (b) to indicate your intentions.

☑ I am willing for the Open University to loan the British Library a copy of my thesis.
A signed Agreement Form is attached

☐ I do not wish the Open University to loan the British Library a copy of my thesis.

Signed: Eric Wolff pp Piers Barnes Date: 11/11/02

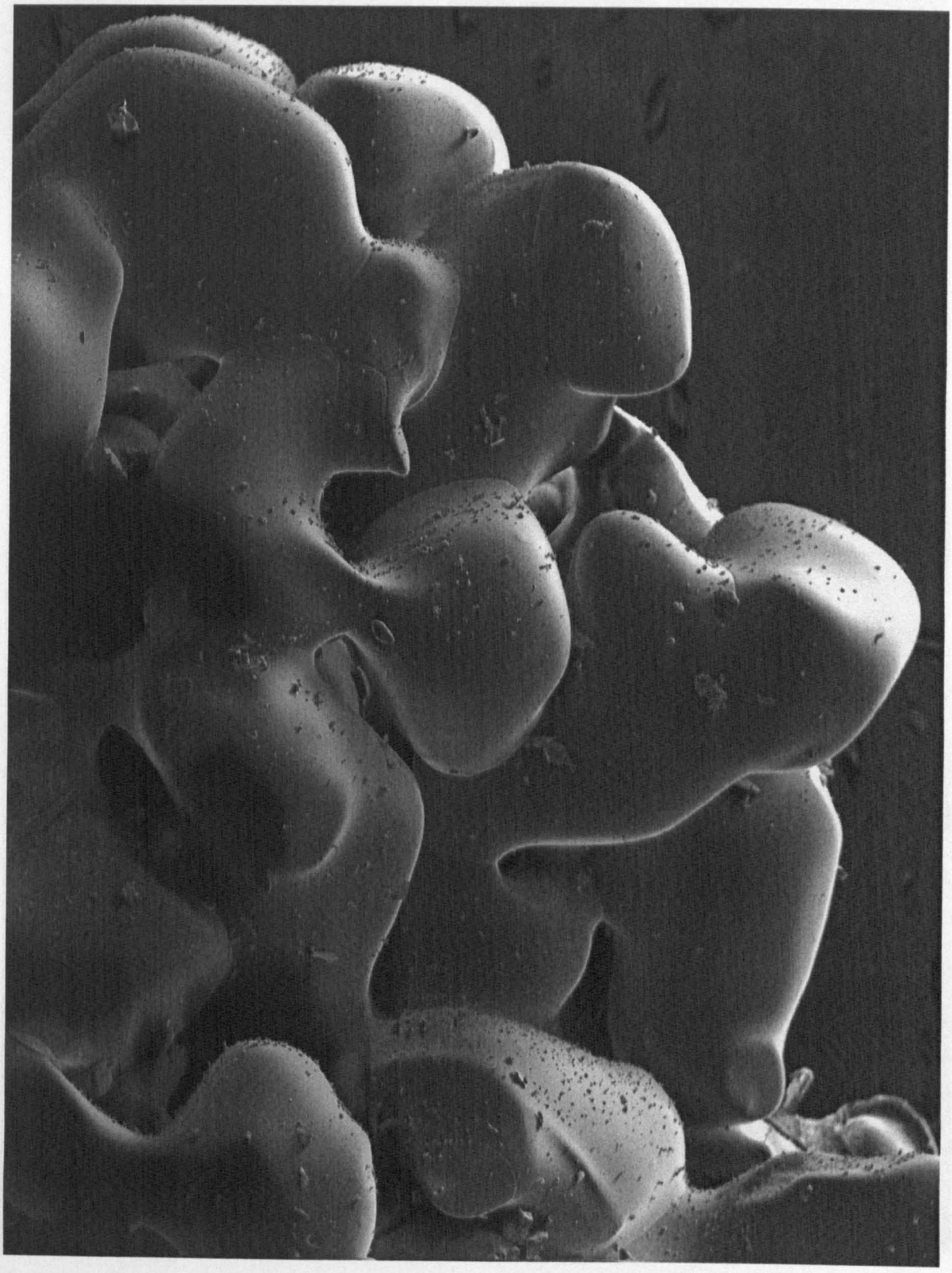

A scanning electron micrograph of surface snow grains from Dome C, coated with frost particles

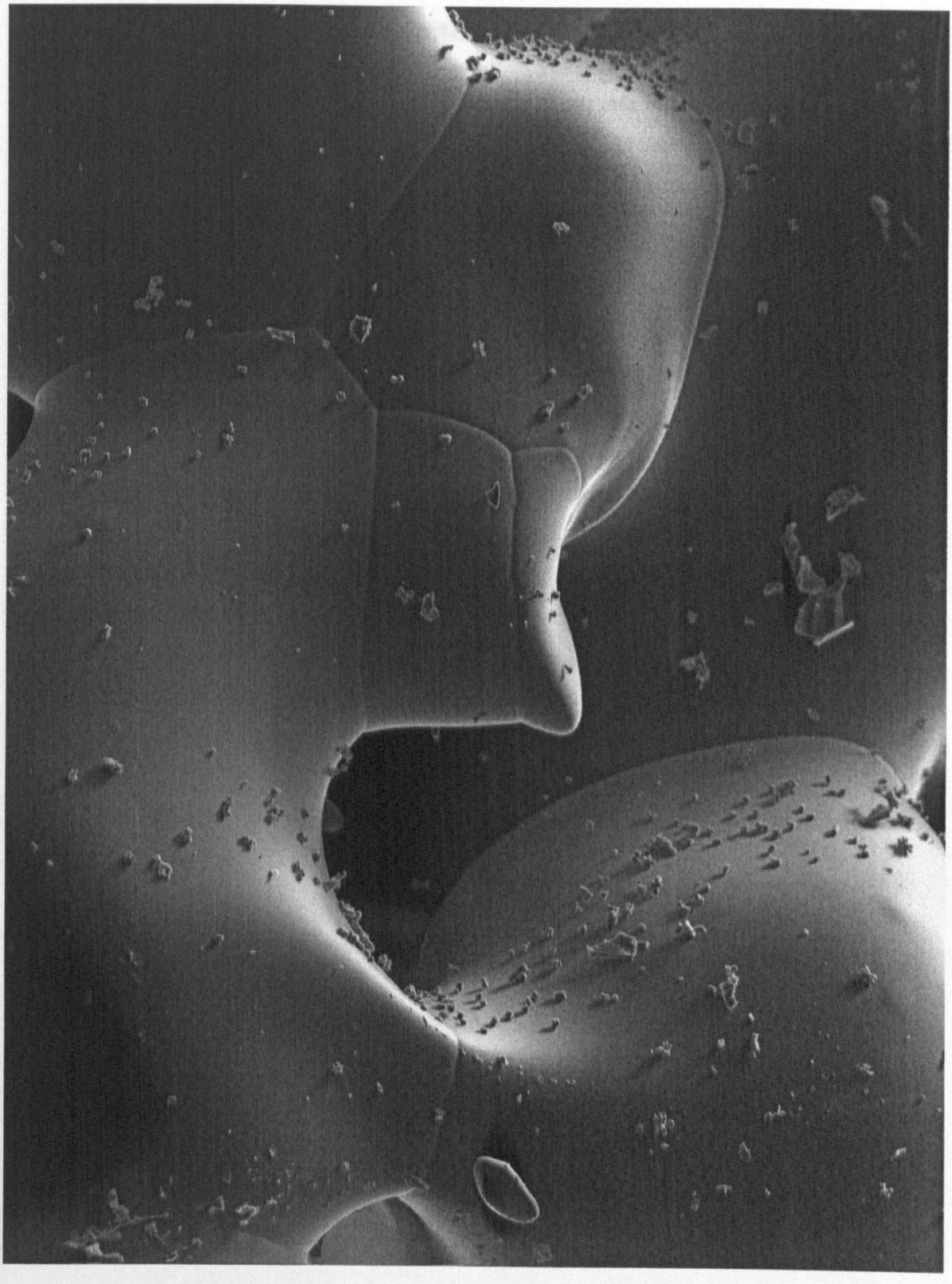

Grooves separating snow grains

Declaration

The work contained in this thesis is entirely that of the author, except where otherwise acknowledged, and has not been used in support of any other academic award. Some of the content has been published and copies of these articles can be found at the back of the thesis.

Acknowledgements

I sincerely thank Dr Eric Wolff for allowing me to undertake this study and for encouraging me throughout. His help, comments and suggestions really kept the threads of the project progressing. My other supervisor Dr Heidy Mader has also been very supportive and has provided many valuable insights for which I am most grateful.

Dr Rob Mulvaney's experience and knowledge of the subject assisted me significantly. Ken Robinson was of great help in matters concerning the microscope and encouraged me despite the seemingly dull subject matter. Dr Andrew Wood was also always on hand to provide answers to questions of maths and computing (as well as many other topics). Much of this work was reliant on data painstakingly collected by others: Dr Regine Röthlisberger, Dr Emiliano Castellano and Prof Roberto Udisti, all of whom I thank for allowing their use and for their comments on results.

I am also grateful to the many friends and colleagues at BAS who participated in numerous excellent teatime discussions, some of which were relevant to this work. I would like to express my gratitude to BAS and the EPICA project for their financial support.

Further thanks go: to Siân without whom my studies might have been completed a little earlier, but with inferior weekends; and to my parents who have ensured my route to this thesis was a smooth one.

Finally I am indebted to Prince Henry Battenburg (1851) whose colourful and tasty snack countered hunger both at the computer and on the river.

Contents

Figures and Tables

CHAPTER I Introduction

CHAPTER II Technique for examining polar ice using the scanning electron microscope

CHAPTER III Observations of polar ice morphology using the scanning electron microscope

CHAPTER IV The effects of density on electrical conductivity chemically laden of polar ice

CHAPTER V The evolution of peak shapes in the Dome C, Antarctica, ice core

CHAPTER VI Distribution of soluble impurities in polar ice

CHAPTER VII Summary and conclusion

APPENDIX **Enlarged micrographs**

Symbols, Constants and Abbreviations

A	Mean grain area of cross section (m^2)
A_0	Initial mean grain area of cross section (m^2)
a	Accumulation rate (either kg m^{-2} yr^{-1} or m yr^{-1})
B	Simplification symbol
B	Background
BAS	British Antarctic Survey
BP	Before present
b	Curve fitting constant
C	Constant of integration
c	Bulk ice concentration (μM = 1 $\times 10^{-6}$ moles L^{-1})
$c(t)$	Bulk ice concentration as a function of time (μM)
$c(z)$	Bulk ice concentration as a function of un-thinned ice equivalent depth (μM)
$C(\omega)$	Capacitance as a function of angular frequency (F = S s = A^2 s^4 kg^{-1} m^{-2})
c'	Rescaled bulk ice concentration (μM)
$c'(z)$	Rescaled bulk ice concentration as a function of un-thinned ice equivalent depth (μM)
c_0	Background concentration if no fluctuation of $c(z)$ (μM)
c_f	Mole fraction ($c_f = 18 \times 10^{-3} \times c$)
c_i	Concentration of impurity dissolved in the ice lattice (M)
c_v	Concentration of impurity situated in veins (M or moles m^{-3})
$\overline{c}$	Mean bulk concentration for the whole profile under observation (μM)
$\overline{c}_z$	Mean bulk concentration within an interval Δz starting at a depth z (μM)
D_{eff}	Effective diffusivity (m^2 yr^{-1})
DEP	Dielectric profile
EC	Etching channel
ECM	Electrical conductivity measurement
EPICA	European Project for Ice Coring in Antarctica
e	Charge of an electron (1.6 $\times 10^{-19}$ C)
e_L	Charge on a Bjerrum L defect (-0.37e)
F	Fraction of lattice sites remaining after grain growth
F_{GB}	Fraction of particles at grain boundary
F_{MS}	Ratio of the regression mean square to the residual mean square
FWHM	Full width half maximum
GB	Grain boundary
GBF	Grain boundary filament
GBS	Grain boundary spot
GRIP	Greenland Ice Core Project
$G(\omega)$	Conductance as a function of angular frequency (S = Ω^{-1} = A^2 s^3 kg^{-1} m^{-2})
g	Curve fitting constant
H	Amplitude of signal oscillation (μM)
H_0	Initial amplitude of signal oscillation (μM)
$h(z)$	Magnitude of fluctuations in concentration (peak height) at depth z (μM)
$\overline{h}$	Mean peak height for the entire profile (μM)
i	The imaginary number ($\sqrt{-1}$)
j	A subscript representing either 'air' or 'ice'
K	Grain growth rate (m^2 yr^{-1})
k	Wave number of mean peak (radians m^{-1})
k_{eq}	Equilibrium distribution coefficient
l	Diffusion length (m)
L	Mean cluster length (m)
L_f	The latent heat of freezing of water (306 MJ m^{-3})
$m(z)$	Mean absolute gradient of a peaks at depth z (μM m^{-1})
m_0	Initial mean absolute gradient of peaks (μM m^{-1})

$\overline{m}$	Mean absolute peak gradient for the entire profile (μM m^{-1})
$\overline{m}_z$	The mean absolute peak gradient within an interval Δz starting at depth z (μM m^{-1})
M_i	Intrinsic grain boundary mobility (m s^{-1} Pa^{-1} = s^{-1} N^{-1} m^{-1})
MS_{reg}	Regression mean square
MS_{res}	Residual mean square
N	Number of sites in the lattice
N_0	Initial number of lattice sites
N_A	Avagadro's number (6.02×10^{23})
N_{bulk}	Number density of particles in the grain bulk, not at boundaries (m^{-3})
N_{GB}	Number density of particles in the grain boundary region (m^{-3})
N_{tot}	Abundance of dust, number of particles per unit volume (m^{-3})
P	Fraction of filled lattice sites
$\overline{P}$	Expectation value for the faction of filled lattice sites after the removal of ΔF
P_0	Initial fraction of filled lattice sites
P_{bulk}	Number of particles counted in bulk
P_c	Critical fraction of filled lattice sites at which percolation occurs
P_{GB}	Number of particles counted within 6μm of grain boundary
p	Empirically derived exponent for conductivity coefficient curve
r	Correlation coefficient
R	Universal gas constant (8.314 J K^{-1} mol^{-1})
R_N	Ratio of the number densities of particles located at grain boundaries to bulk
RSD	Residual standard deviation
r_v	Radius of vein curvature (m)
SE	Standard error
SES	Surface etching spot
τ	Empirically derived exponent for percolation relation
t	Time (yr)
T_0	Melting point of pure ice (0°C or 273.16 K)
TJ	Triple junction
TJS	Triple junction spot
u_z	Velocity of un-thinned ice equivalent advection due to accumulation (m yr^{-1})
V_{bulk}	Volume of grain bulk searched (m^3)
V_{GB}	Volume of in grain boundary region searched (m^3)
V_{tot}	Total volume etched from sample surface (m^3)
f	Volume fraction of liquid in the ice
$\dot{\varepsilon}_z(t)$	Vertical strain rate at time t (yr^{-1})
$w(z)$	Mean peak width at depth z (m)
$\overline{w}$	Mean peak width for the entire profile (m)
$Y(\omega)$	Admittance as a function of angular frequency (S = Ω^{-1} = A^2 s^3 kg^{-1} m^{-2})
y	Specific complex admittance (complex admittivity S m^{-1})
Z	Lattice co-ordination number
z	Un-thinned ice equivalent depth (m)
z'	Un-thinned ice equivalent depth from the centre of a peak in the advecting ice frame of reference (m)
z_{total}	Total un-thinned ice equivalent depth of section under examination (m)
z_{firn}	Depth in the firn/ice (strained) (m)
α	Geometric factor describing vein area of cross section
α_{ib}	Impurity-boundary interaction parameter (Pa s m^{-1} = s N m)
$\beta(v)$	Conductivity coefficient calculated from regression coefficient as a function of volume fraction (S m^{-1} M^{-1})
β_{H2SO4}	Conductivity coefficient for sulphuric acid in solid ice (S m^{-1} M^{-1})
$\beta_{H2SO4}(v)$	Conductivity coefficient for sulphuric acid as a function of volume fraction (S m^{-1} M^{-1})
β_{HCl}	Conductivity coefficient for hydrochloric acid in solid ice (S m^{-1} M^{-1})
β_{Na}	Conductivity coefficient for sodium salts in solid ice (S m^{-1} M^{-1})
γ_{ii}	Ice-ice interface (grain boundary) free energy (J m^{-2})

γ_{il}	Ice-liquid interface free energy (J m^{-2})
γ_{iv}	Ice-vapour interface free energy (J m^{-2})
$\Delta c(z)$	Difference between successive concentration measurements (μM)
ΔF	Small fraction of sites removed from the lattice
ΔL	Change in cluster length (m)
ΔN	Number of sites removed from the lattice
Δz	Un-thinned ice equivalent depth section (m)
ε_0	Permittivity of free space (8.854×10^{-12} F m^{-1})
ε_{air}	Dielectric constant for air
ε_{ice}	Dielectric constant for ice
θ	Depression of freezing point below the melting point of ice (°C or K)
λ	Vein density (m m^{-3})
λ_0	Initial vein density (m m^{-3})
μ_L	Mobility of a Bjerrum L defect ($1.5 - 2.4 \times 10^{-8}$ m^2 V^{-1} s^{-1})
ρ	Density of firn (kg m^{-3})
ρ_i	Density of ice (917 kg m^{-3})
$\rho_{predicted}$	Density predicted by curve fitting (kg m^{-3})
σ	Vein area of cross section (m^2)
$\sigma'(\omega)$	Real part of the complex conductivity (S m^{-1})
$\sigma_{\infty Böt}(v)$	High frequency conductivity as a function of volume fraction, calculated from Böttcher's equation (S m^{-1})
$\sigma_{\infty Cl}$	Component of high frequency conductivity resulting from chloride ions (Sm^{-1})
$\sigma_{\infty int}(v)$	High frequency conductivity as a function of volume fraction, calculated from regression intercept (S m^{-1})
$\sigma_{\infty Loo}(v)$	High frequency conductivity as a function of volume fraction, calculated from Looyenga's equation (S m^{-1}).
$\sigma_{\infty pure}$	Pure component of high frequency conductivity (S m^{-1})
$\sigma_{\infty pure}(v)$	Pure ice component of high frequency conductivity as a function of volume fraction (S m^{-1})
σ_∞	High frequency conductivity (S m^{-1})
$\sigma_\infty(v)$	High frequency conductivity as a function of volume fraction (S m^{-1})
$\sigma_{DC\,air}$	Direct current conductivity of air (S m^{-1})
σ_{DC}	Direct current conductivity (S m^{-1})
v	Volume fraction of ice in firn
$v(t)$	Volume fraction of ice in firn as a function of time
v_c	Critical volume fraction at which percolation occurs
ω	Angular frequency (radians s^{-1})

CHAPTER I

Introduction

How are atmospherically derived impurities distributed in the cold polycrystalline ice of the polar ice caps? The answer is of considerable importance to the study of ice cores used to determine climate records. The distribution also influences the mechanical properties of ice sheets and is of general relevance to the physical properties of ice and polycrystalline materials. This thesis attempts to determine the micro-structural arrangement of impurity. In addition it considers the implications of the distribution for electrical conduction mechanisms and the possibility of post-depositional processes in the ice sheet. To achieve this, polar ice specimens are examined using low temperature scanning electron microscopy, and detailed electrical and chemical ice core records are analysed.

I.1. Ice sheets

The Earth's cold polar regions host great ice sheets covering the continental landmasses. The most notable are the East and West Antarctic Ice Sheets in the Southern Hemisphere, and the Greenland Ice Sheet in the Northern Hemisphere (figure I.1). Together they lock up approximately three quarters of the world's fresh water. They originate entirely from precipitation. Super-cooled

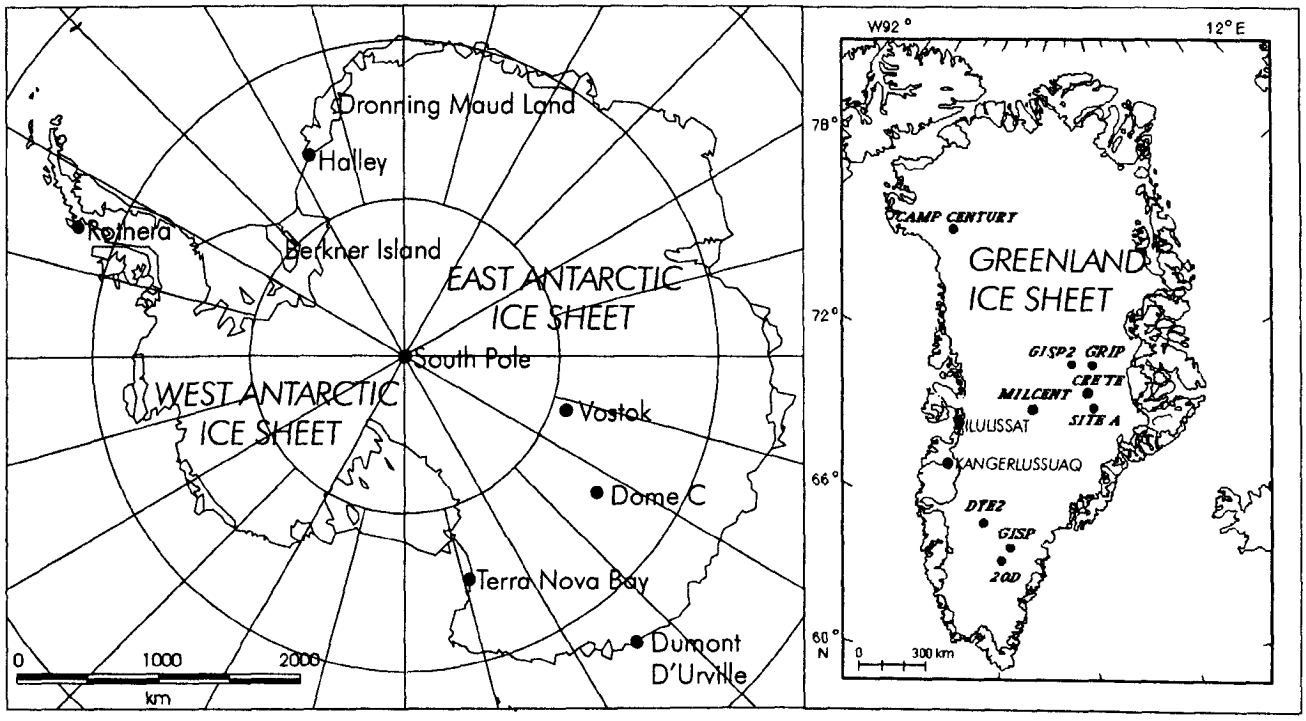

Figure I.1. The Antarctic and Greenland ice sheets.

water vapour in clouds over these regions condenses onto microscopic particles suspended in the air to form ice crystals that eventually fall as snowflakes scavenging more dust and aerosol on their journey to the surface.

Contained in the snow is information about the atmosphere at the time it fell. The prevailing sub-zero temperatures ensure that rather than melting, each layer is buried by further precipitation. Lower layers of snow are compressed by the weight of precipitation above them, and slowly transform, via a porous structure known as firn, to solid polycrystalline ice. During this process, air contained within the open pore spaces of the firn is eventually pinched into bubbles, trapping yet more information about the composition of the atmosphere. The layers of snow are deposited sequentially in time and rise up to three or four kilometres above ground level. Once an ice sheet reaches a steady state the influx of ice to the surface is balanced by loss of ice as mass flows out to the margins, under the influence of gravity, where it may melt or calve into icebergs. Deep in the sheet layers are progressively thinned by the flow (figure I.2). At the base of the ice sheet the ice can be more than a million years old, hence an enormous amount of information about the Earth's past climate and the ice sheets themselves is stored in the layers. This information if extracted can be used to test climate models, which may predict the future climate. Knowledge of the past's climate also enables us to put the currently observed global climate change into a longer-term context.

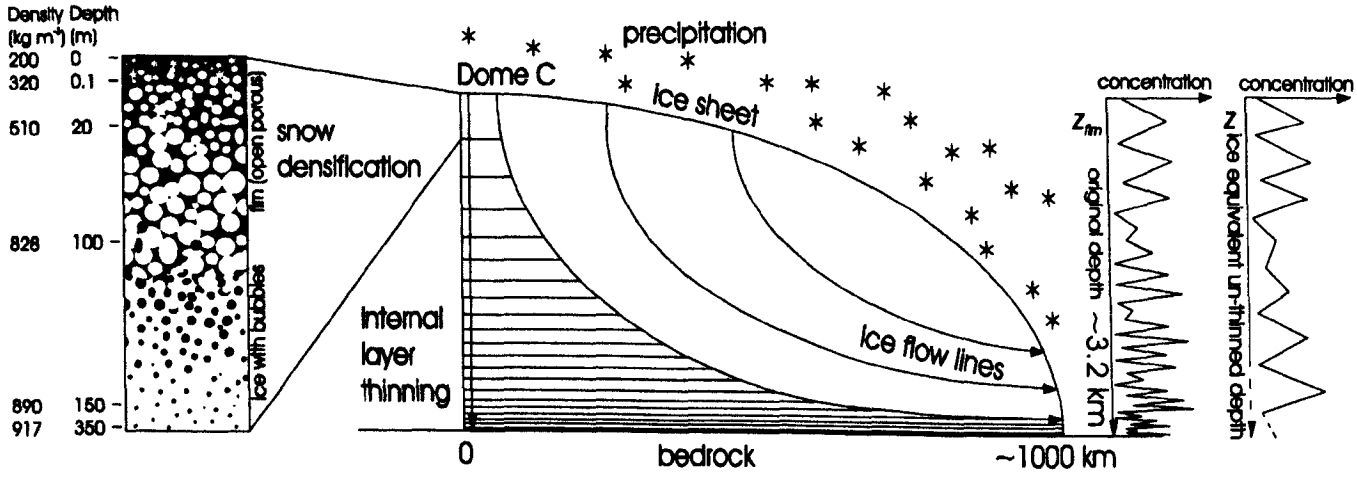

Figure I.2. Schematic of the cross section of an ice sheet. Densification of the firn occurs near the surface and the ice is thinned by vertical strain as the sheet diverges towards its edges. The impurity concentration profile is compressed by the thinning; this is shown in the schematic concentration profile on the left, whilst an un-thinned ice equivalent depth concentration profile is shown on the right.

I.2. Ice Cores

I.2.1. Drilling

An ice core drilled into the sheet provides a continuous sequence of ice aged from the present to the age at the base of the core. Most of the recently drilled deep cores have been extracted using an electromechanical drill that removes the core in sections 2 – 3 m in length (figure I.3). The drill is lowered on a wire cable and its teeth rotate to cut an annulus of ice around

a core, about 10 cm in diameter, which slides into the centre of the drill barrel. Chippings cut from around the core are carried away along the outside of the barrel and stored in the upper part of the drill. Once the drill barrel is full the section of core is broken out of the borehole and the drill winched to the surface ready for the section to be removed and the process repeated. To prevent the borehole collapsing from the pressure of the surrounding ice it must be filled with a low viscosity drilling fluid that closely matches the density of ice.

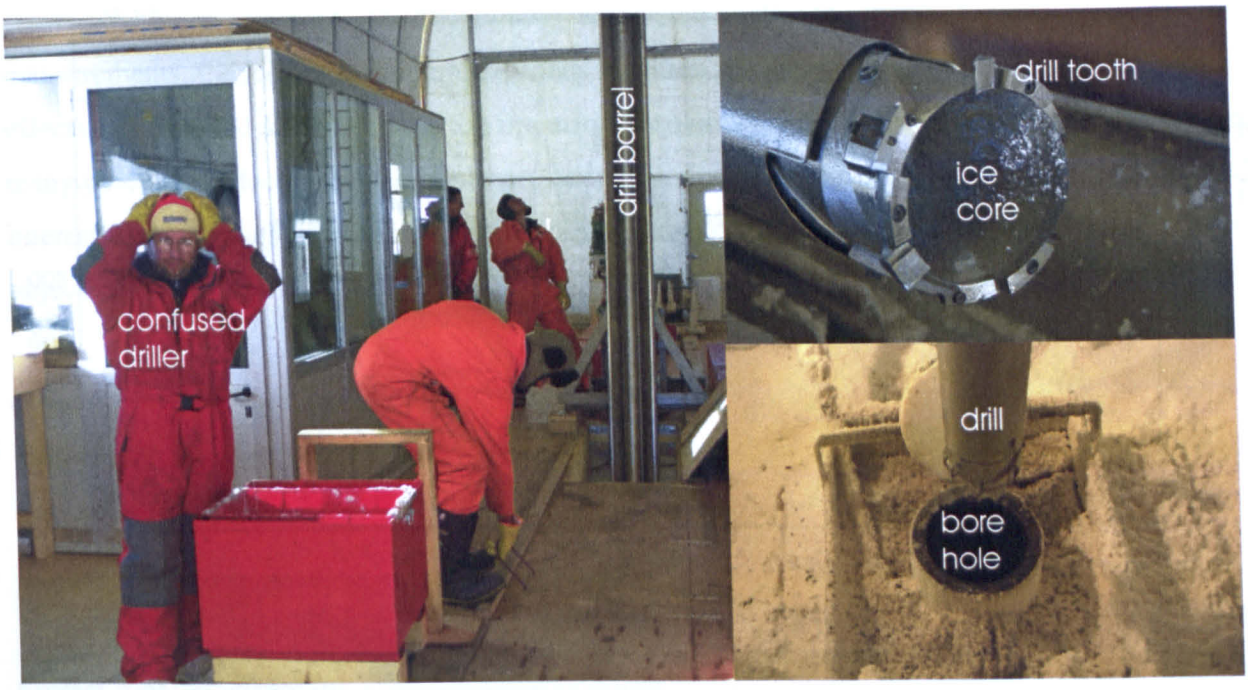

Figure I.3. Ice core drilling at Dome C.

I.2.2. Core measurements

By measuring the composition of the extracted ice and the quantities of impurities trapped in it, proxies for the state of the atmosphere in the past can be amassed to give a record of the past climate. A more detailed review of the measurements made and their applications is given by Wolff [2001]. Some of the variables analysed include: stable isotopes of hydrogen and oxygen used as proxies for temperature [e.g. *Johnsen et al.*, 2001]; dust content used to determine prevailing wind patterns and provenance [e.g. *Grousset et al.*, 1992]; and trapped bubbles revealing greenhouse gas composition [e.g. *Jouzel et al.*, 1993; *Petit et al.*, 1999] (figure I.4). Even the physical properties of the ice, such as crystal fabric orientation, grain size and clathrate hydrate content of the ice have been linked to paleo-climate [*Pauer et al.*, 1999; *Thorsteinsson et al.*, 1997]. The chemical composition of impurities in an ice core can be linked to a wide range of past climatic activity, from wind strength and storminess to volcanism e.g. [*Legrand and Mayewski*, 1997; *Petit et al.*, 1981]. Measuring the electrical conductivity of an ice core can be used as a rapid non-invasive method to determine its chemical composition particularly when a combination of both direct current and alternating conductivity is used [*Hammer*, 1980; *Moore et al.*, 1989]. These measurements can also be linked to radio echo sounding measurements of internal reflectors in the ice [*Miners et al.*, 2002], useful for determining accumulation rates across wide areas of ice sheets.

The records are dated by a number of methods ranging from counting layers of the cyclic annual fluctuation of a variable, where possible, to calculating the mean accumulation rate from known volcanic or radioactive horizons in the ice. In deeper ice where this is not possible the ice is dated by flow modelling of the ice sheet and by matching profiles to other long-term environmental data sets. All this information can be compiled to build a picture of both the past atmosphere and climate as well as previous states of the ice sheet.

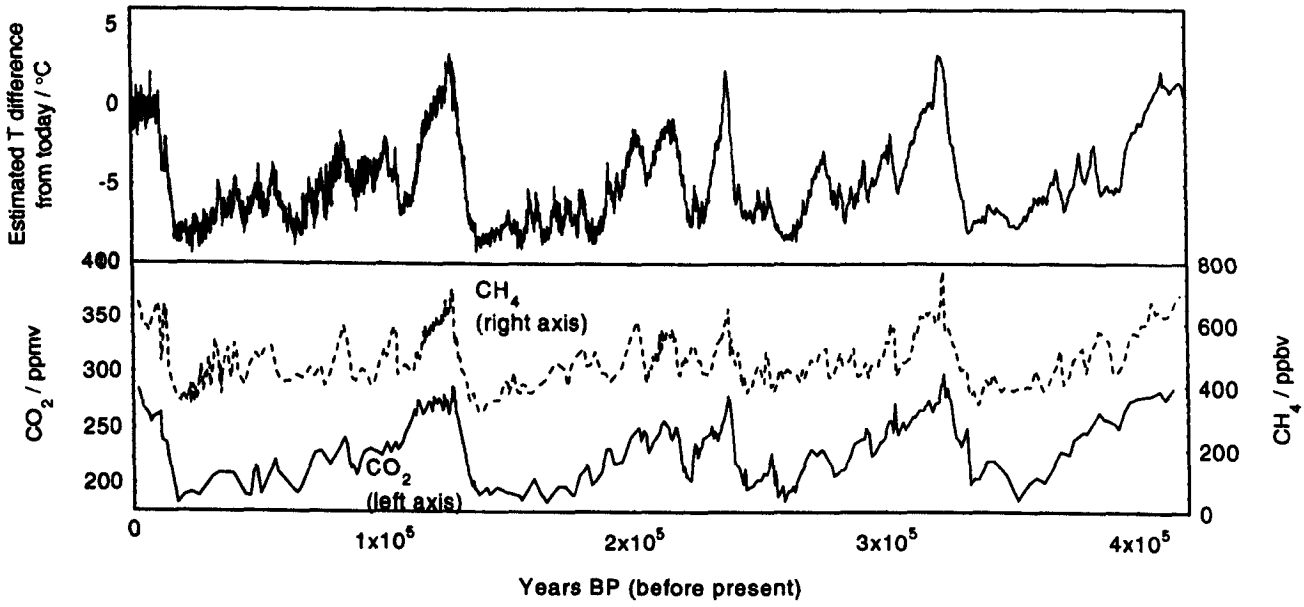

Figure I.4. The temperature and carbon dioxide profile from the Vostok ice core [*Petit et al.*, 1999].

I.3. Motivation for this study

Uncertainties remain in the interpretation of many of the records that require detailed understanding of processes occurring in the ice sheet. For example there is an offset between the age of the gas trapped in bubbles and the age of the ice surrounding it, which must be modelled by the diffusion of gasses through the firn [*Trudinger et al.*, 1997]. The concentration of CO_2 in bubbles can also be greater than the original atmospheric concentration at which it was trapped. This is thought to be due to the post-depositional production of CO_2 by the reaction of either precipitated organics with oxidants or dust particles with acid [*Anklin et al.*, 1995; *Tschumi and Stauffer*, 2000]. The extent of this process is dependent on the quantity of reagents that can physically contact each other, a process determined by the microstructure.

There are other sources of uncertainty and post depositional change in ice cores. Intra-annual variation in the deposition of an seasonally cyclic signal requires many years of accumulation to be sampled to give a representative description of a sub annual measurement [*McConnell et al.*, 1997]. Diffusion of oxygen and deuterium isotopes is known to damp fine scale temperature information in ice cores [e.g. *Cuffey and Steig*, 1998; *Johnsen et al.*, 2001], the proposed mechanisms for this are dependent on the ice microstructure [*Nye*, 1998]. The

calibrations of electrical measurements to chemical composition of cores are intrinsically dependent on the distribution of impurities [*Wolff et al.*, 1997]. Post-depositional migration of some soluble impurities has also been observed, sometimes with mechanisms apparently more complex than just simple diffusion [e.g. *Kreutz et al.*, 1998; *Pasteur and Mulvaney*, 2000]. It is even proposed that whole chemical signal in the ice could be displaced near the base of deep ice sheets by factors linked to the ice microstructure [*Rempel et al.*, 2001a].

With an element of uncertainty associated with so many fundamental ice core measurements, the ice microstructure demands attention to constrain the extent of post depositional effects. A detailed knowledge of the impurity distribution will enable a better understanding of many processes effecting ice core interpretation described above as well as being of more general interest to ice physics. Establishing the microstructure in relation to these processes is the primary objective of this thesis.

I.4. Ice as a material

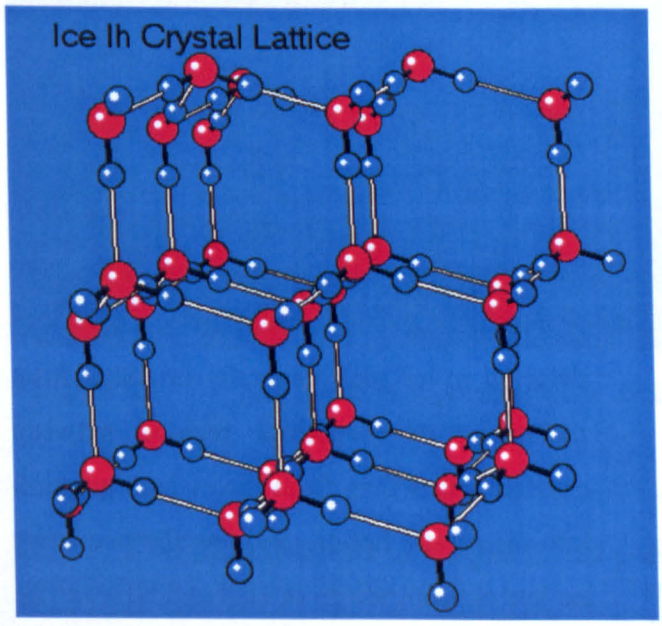

Figure I.5. Crystalline structure of the ice Ih lattice.

This section introduces the material ice and some of its basic properties as a brief background to the subject areas covered. The subject is reviewed in detail in the book by Hobbs, *Ice Physics* [1974] and more recently in Petrenko and Whitworth's book, *The Physics of Ice* [1999].

Ice, composed of water molecules (H_2O), has about 13 different crystalline arrangements, more than any other known material [*Petrenko and Whitworth*, 1999]. Most of these phases can only exist at temperature and pressure conditions far beyond the limits of those occurring within earth's environment. Here we are concerned with the most common and naturally occuring phase, ice Ih. The oxygen atoms are arranged in a hexagonal close packed arrangement where each oxygen is surrounded by four others in tetrahedra with atomic spacing of about 2.8 Å (figure I.5). The hydrogen atoms in ice are arranged according to the Bernal-Fowler rules: 1) two protons are close (about 0.98 Å) to each oxygen atom, much like in a free water molecule; 2) each H_2O molecule is oriented so that the two protons point toward two adjacent oxygen atoms; 3) there is only one proton between two adjacent oxygen atoms; 4) under ordinary conditions any of the large

number of possible configurations is equally probable. One of the ice's more important and unusual properties is its density (ρ_i = 917 kg m^{-3}), which is less than that of liquid water . This is a consequence of the open structure of the lattice caused by the geometry of the hydrogen bonds, which have a binding energy of 0.306 eV per bond (59 kJ per mole of H_2O).

Imperfections in the structure of the ice lattice are known as defects. The most relevant defects to this work are protonic defects and incorporated impurity atoms, although sub-grain boundaries where the crystal lattice is not quite aligned can also be considered as a form of defect. Protonic defects are present in the ice in pure crystals and their concentrations are temperature dependent; however they are also produced in greater quantities when impurity atoms are introduced to the lattice. They fall into two categories, ionisation defects and Bjerrum defects and form when ice rules 1) or 3) are broken. The arrangement of protons for each type of defect can be seen in figure I.6 where a proton is either missing from or added to an oxygen atom or a lattice bond contains two or no protons. The presence of these defects explains the intrinsic electrical conductivity of ice well [*Jaccard*, 1964; *Petrenko*, 1993], and an example of such conduction is shown in figure I.7.

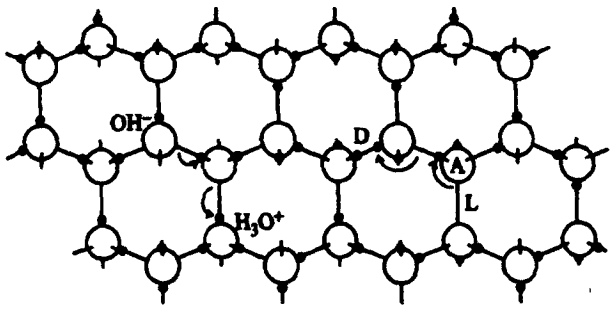

Figure I.6. Ionic (OH^- and H_3O^+) and Bjerrum (L and D) defects [*Petrenko and Whitworth*, 1999].

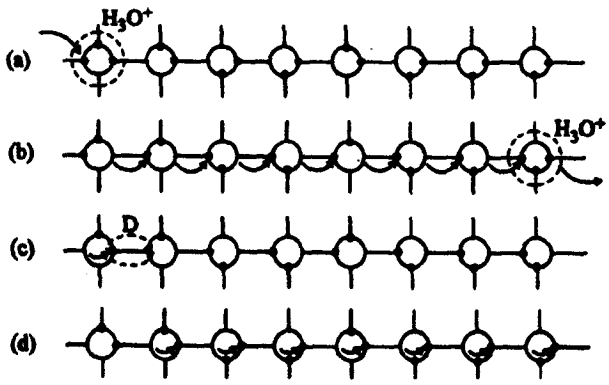

Figure I.7. The propagation of an H_3O^+ ion followed by a D-defect along a straightened out chain of water molecules [*Petrenko and Whitworth*, 1999].

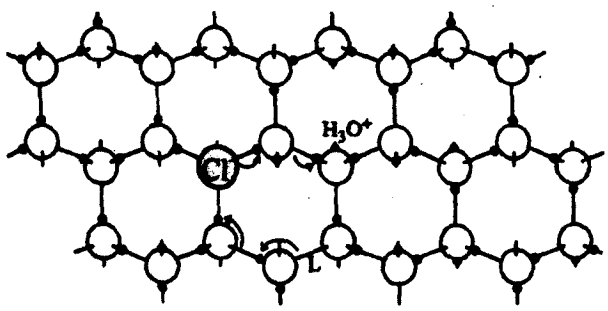

Figure I.8. The incorporation of HCl into the lattice to release an H_3O^+ ion and an L-defect [adapted from *Petrenko and Whitworth*, 1999].

Many substances are highly soluble in water. However the vast majority of them are virtually insoluble in ice. Most impurities detected in ice melt generally originate from inclusions or interstitial regions between crystals rather than from direct incorporation into the crystal lattice. In naturally occurring ice low concentrations of HCl and NH_3 can be incorporated into the crystal lattice with the additional creation of point defects (e.g. figure I.8). Other atmospheric impurities under some circumstances can be included interstitially within the lattice.

Under high pressure gas trapped in bubbles within the ice can transform to a clathrate hydrate crystal, where the Ih lattice alters to form regular cages of water

molecules surrounding enclosed gas molecules. Ice sheets at depths >~1000 m are the only place where air hydrates naturally occur.

Glacial ice is a polycrystalline material, in which crystals or grains are packed together in an initially random manner (figure I.9). Over time metamorphosis of the ice fabric by recrystallisation increases the average grain size by a process that reduces the total area of grain boundary in the glacier. The shear forces and overburden pressure present in ice sheets causes grains to deform and realign themselves, with the basal plane in the direction of strain [*Thorsteinsson et al.*, 1997].

The electrical conductivity of polycrystalline ice is strongly influenced by the presence of impurities. The abundance of grain boundaries are thought to provide alternative conduction mechanisms for the bulk substance [*Wolff et al.*, 1997], in addition to those described for solid ice.

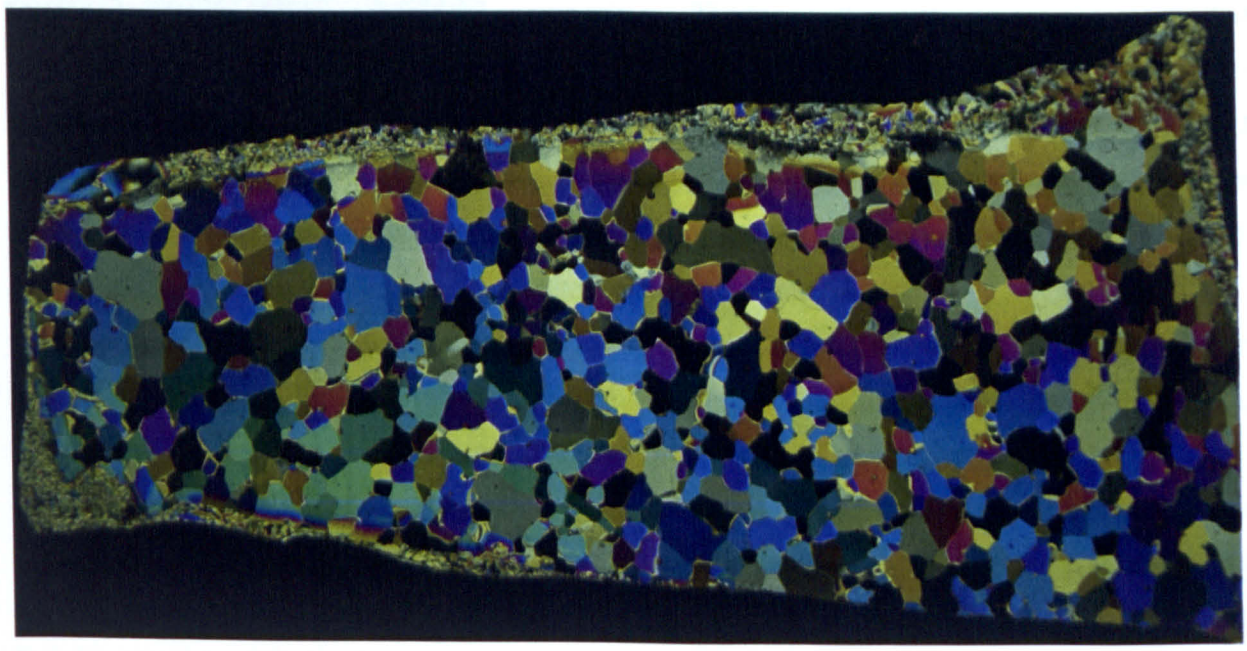

Figure I.9. A thin section of polycrystalline ice from Dome C viewed between crossed polarisers.

I.5. The distribution of impurity in polar ice

I.5.1. Present understanding of impurity distribution

Light microscopy was used with success to examine the microstructure of polycrystalline ice near the melting point [*Mader*, 1992a], and is widely used to observe many of the physical properties of polar ice. However it is inadequate for fully characterising impurity arrangement.

Prior to starting this work only a few direct studies on impurity location had been published. Mulvaney *et al.* [1988; *Wolff et al.*, 1988] used the scanning electron microscope (SEM) and x-ray analysis to show that sulphuric acid occurred at triple junctions in ice from Dolleman Island, Antarctica. This finding supported the theory of electrical conduction through veins [*Wolff and Paren*, 1984]. Fukazawa *et al.* [1998] found acidic SO_4^{2-}, NO_3^- and HSO_4^- as

liquids at triple junctions using Raman spectroscopy in ice from both Nansen and South Yamoto, Antarctica. These studies have in part stimulated this work to more thoroughly establish the impurity arrangement.

Recent studies of poly-crystalline ice using the scanning electron microscope (SEM) have also shown impurities *in situ*, both at the boundaries between ice grains and in the bulk of the crystals [*Cullen and Baker*, 2000; *Baker and Cullen*, 2002].

The conclusions from these different studies do not present a fully coherent description of either the arrangement of impurities or the factors that determine it. Mulvaney suggested that the majority of acid present in the ice might be located at triple junctions. Fukazawa's results indicated a lower proportion at triple junctions at one site whilst both Cullen and Baker concluded that a far greater proportion of impurity present was located at two-grain boundaries and as inclusions in the bulk.

I.5.2 Aims of the study

- To characterise the morphology and features observed in polar ice using the SEM.
- To establish the micro-structural arrangement of the dominant impurities in cold glacial ice.
- To investigate the relationship between electrical conductivity and impurity distribution.
- To investigate the effect of impurity distribution on some the post-depositional processes occurring in the ice sheet.

I.5.3. Material and Techniques used in this work

The majority of this work examines ice from the Dome C core, Antarctica (74°39'S, 124°10'E, 3240m elevation and -53.5°C mean annual temperature), (figure I.1). It is being drilled (1996 – present) as part of the European Project for Ice Coring in Antarctica (EPICA). This consortium of laboratories from ten European nations is drilling two ice cores to bedrock in Antarctica. The first at Dome C, aims to produce a high resolution record covering 750 kyr, the oldest polar ice core to date. Samples from other sites are also studied for comparison and variety: a 120 m Dronning Maud Land core drilled in 1998 (77°S, 10°W, 2200 m elevation and -38 °C mean annual temperature); surface snow collected in 1999 from the clean area near Halley Base situated on the Brunt Ice Shelf (75°35'S,26°30'W, 32 m elevation and -19.3 °C mean annual temperature), and the GRIP (Greenland ice coring project) deep ice core from Greenland drilled in 1990 (72°34'N, 37°37'W, 3232 m elevation and -32 °C mean annual temperature).

The thesis is centred around the study of the above ice using the scanning electron microscope (chapters II, III and VI). The SEM (figure I.10) allows the cross-sectional surface structure of ice samples to be examined with greater resolution and depth of field than is achieved with the conventional light microscope [*Wergin et al.*, 1998]. It works by scanning a focused beam

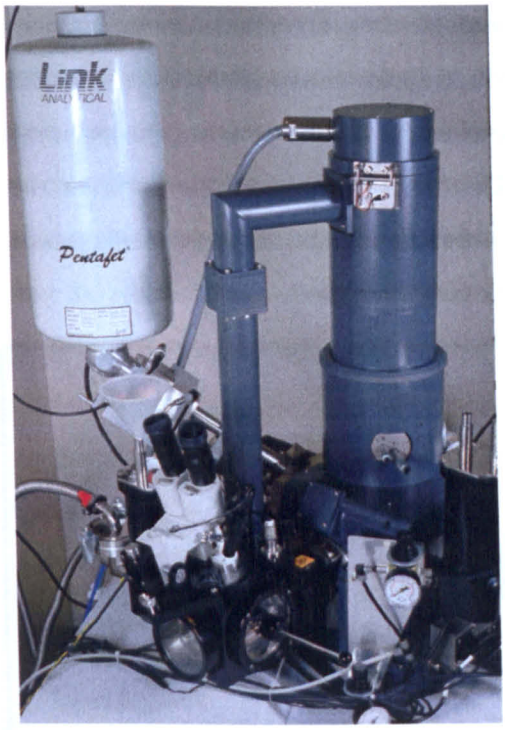

Figure I.10. The BAS scanning electron microscope.

of electrons across the surface of the specimen (see Echlin [1992] for a detailed description). The number of secondary electrons emitted from each point the beam passes is detected and builds up an image of the surface corresponding to variations in the topography and elemental composition. The SEM also has the advantage that it allows the composition of impurities to be determined by means of x-ray micro-analysis. This is where x-rays, emitted from the target elements by excitation from the incident electron beam, are detected to give an emission spectrum characteristic of the target composition. The low bulk concentrations present in most polar specimens mean that if the distribution is homogeneous throughout the bulk then *in situ* impurities exist below current detection limits. However if the impurity is in a concentrated form, for example a dust particle or an impurity at a triple junction or grain boundary, then it can be possible to detect using x-ray analysis.

Electrical conductivity data from the Dome C ice core are also used (particularly in chapter IV). The data were collected using a method developed at BAS known as dielectric profiling (DEP) and at Dome C is the first measurement made on the retrieved core. This non-invasive technique involves a series of opposing curved electrodes, positioned along the length of a section of core at a spacing of 2 cm. The capacitance and conductance of the enclosed ice are measured. A range of frequencies typically up to 300 kHz may be measured, allowing the value of the high frequency conductivity to be extrapolated [*Moore et al.*, 1989]. The stratified conductivity data gathered by these methods have been valuable for understanding radar surveys of ice [*Hammer*, 1980], and has also been related to the chemical content of the ice [*Moore et al.*, 1992].

I had originally intended to collect the DEP data used in this study myself. However an incident in which the drill became stuck in the bore hole during the 1998-1999 season meant drilling was delayed and a new core was drilled starting in 1999-2000. The data I collected from this new core (EDC1999, figure I.11) are not used in this thesis but rather the previously collected DEP record from the old core (EDC1996). A comparison of the EDC1996 and EDC 1999 DEP profiles shows very good agreement (figure I.12).

Figure I.11. A core is logged before placing it in the DEP.

The chemical data were collected by others using ion chromatography and continuous flow analysis [*Röthlisberger et al.*, 2000; *Udisti et al.*, 2000]. Ion chromatography involves passing the core melt over charged resin surfaces that differentiate between the speeds of the differing ionic species, allowing their concentrations to be determined. Continuous flow analysis involves the analysis of a continuous stream of melt from the base of a core mixed with various reagents, using optical detectors.

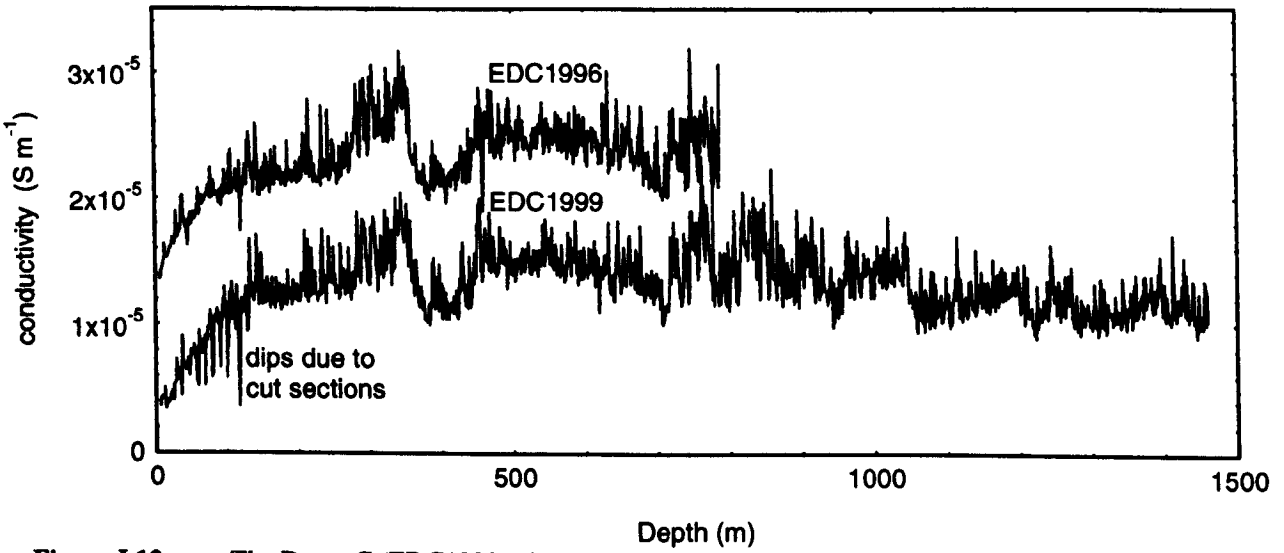

Figure I.12. The Dome C (EDC1999) electrical conductivity (DEP) record, smoothed to 1 m averages, compared with the old record (EDC1996) offset by 1 x 10 $^{-5}$ S m^{-1}.

I.6. Scope of the thesis

Chapter II describes the technique developed in this work to observe ice specimens using the SEM. In the following chapter III, the general features found in polar ice using the SEM are described such as grain structure, bubbles, clathrate hydrates and dust particles. It is the first time many of these features have been observed using the SEM. The next chapter, IV, considers the problem of impurity distribution from a different angle. The relationship between the electrical conductivity of the Dome C ice and its impurity content is explored in detail, and the variation of this relationship with ice core density is observed. This enables inferences to be drawn about the conductivity mechanisms at work and hence the arrangement of conducting impurity in the core. Chapter V looks at the fine scale shape of the chemical profile of the Dome C ice core, and how the characteristics of the profile have changed with age and depth. These observations help constrain the integrity of the ice core record, and are explained by models that are dependent on impurity arrangement. Chapter VI returns to the SEM to examine in detail the distribution of soluble impurity derived from atmospheric aerosols. The arrangement between grain and within crystals in snow, firn and ice helps answer questions raised in the previous chapters. The final chapter VII summarises the main findings and implications of the thesis.

INTRODUCTION

The majority of the material in chapters II – VI forms the basis of separately published/submitted articles (copies at back of volume). The content and ideas in these papers is predominantly my own, however a considerable quantity of both the chemical and electrical data were collected by the co-authors. To acknowledge input from them and to minimise superfluous editing, the pronoun 'we' is used throughout. Chapters II – VI are relatively self-contained, and may be read independently, consequently there is a degree of redundancy in the basic information presented from chapter to chapter.

CHAPTER I

CHAPTER II

Technique for the examination of polar ice using the scanning electron microscope

The microstructure and location of impurities in polar ice is of great relevance to ice core studies. We describe a reliable method to examine ice in the scanning electron microscope (SEM). Specimens were cut in a cold room and could have their surfaces altered by sublimation either before (pre-etching) or after (etching) introduction to the cryo-chamber of the SEM. Pre-etching was used to smooth surfaces and collect impurity, whilst etching stripped away layers from the specimen surface, aiding the location of particles and impurities *in situ*. It also allowed embedded structures to be revealed. X-ray analysis was used to determine the composition of localised impurities, which in some cases had been concentrated on the surface by etching. Examining uncoated surfaces was found to be advantageous and did not detract from qualitative x-ray analysis. Uncoated imaging was performed at low accelerating voltages and probe currents to avoid problems of surface charging.

II.1. Introduction

Measurements on ice cores are prolific and are used to reconstruct the climate of the past [*Wolff*, 2001]. They often involve the determination of the composition of the ice to find the atmospheric fallout deposited with the snow [*Legrand and Mayewski*, 1997]. Ice from the polar ice sheets of Greenland and the Antarctic is of particular interest for these studies. The permanently low temperatures of these regions mean that there is virtually no melt so that impurities remain generally fixed in the layers in which they were originally deposited. Polar ice is a polycrystalline structure which is formed from the compaction and growth of individual grains initially formed from snowflakes. Atmospheric fallout such as dust particles, salt aerosol or acid from volcanoes is trapped in or between the ice grains. However relatively little is known about where and how these impurities are distributed within the polycrystalline structure. Knowledge of the location of impurities allows questions of post-depositional chemical change to be tackled as well as issues relating to the growth of grains and the physical and electrical properties of ice. This will in turn help the interpretation of ice core records and our understanding of the conditions that formed the ice we find today.

The scanning electron microscope (SEM) allows the cross-sectional surface structure of ice samples to be examined with much greater resolution and depth of field than the conventional light

microscope [*Wergin et al.*, 1998]. The SEM also has the advantage that it allows the composition of impurities to be determined by means of x-ray microanalysis. The SEM has been used in studies on laboratory ice [*Cross*, 1969; *Schulson and Baker*, 1989], as well as studies on frozen aqueous solutions [*Dubochet et al.*, 1982] and their x-ray analysis [*Reid et al.*, 1992]. A study has also been made on fractured surfaces of temperate glacier ice [*Rango et al.*, 2000]. Early SEM work on polar ice by Mulvaney *et al.* [1988] and Wolff *et al.* [1988] found sulphuric acid at the intersection between three grains (triple junction), and more recently Cullen and Baker [2000] found soluble impurities located at both grain boundaries and triple junctions. These studies have confirmed that a significant proportion of the soluble impurities exists between grains, although similar questions remain about the distribution of dust in polar ice.

There are various technical difficulties associated with the preparation of ice samples for observation in the SEM. Early studies kept the ice frozen by evaporative cooling under the vacuum conditions [*Cross*, 1969]. However to examine a sample without significant sublimation under the vacuum required in the sample chamber (~10^{-6} torr) it must be held at a low temperature (< -130 °C). These temperatures are achieved using a liquid nitrogen cooled stage, a technique favoured in the studies referred to in the above paragraph (figure II.1). The low temperature means that the sample surface is very susceptible to the condensation of stray moisture in the local environment of the sample. Other problems are associated with the preparation of samples, and include the brittle structure of ice, which hinders easy cutting of the samples, as well as the relatively non-conducting nature of the solid, which can cause charge build up on the surface during scanning hence distorting the image.

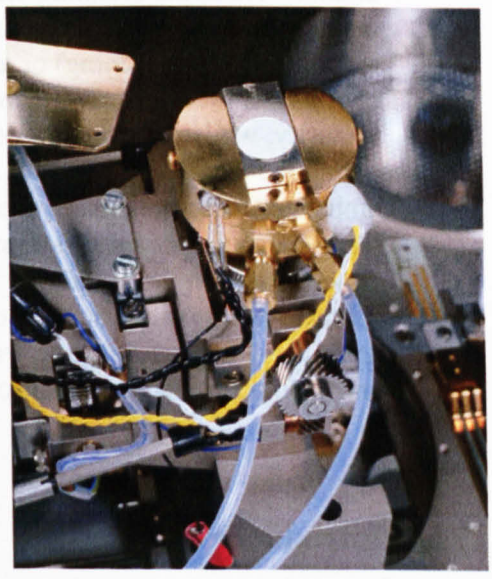

Figure II.1. The SEM cryo-stage. Cooled nitrogen gas circulated in the stage maintains a low temperature.

Although meteorologically formed ice, originating from snow, is significantly different from most other forms of ice found naturally or grown in the laboratory, the general techniques for its preparation remain the same. This chapter describes a reliable method for preparing and examining polar ice using an SEM, based upon that used by Mulvaney *et al.* [1988] and Wolff *et al.* [1988], with further refinements. A variety of preparation techniques allowed different surface qualities to be achieved. Methods for minimizing redistribution of impurities after cutting are considered, an area hitherto neglected. A technique of sublimation from the ice surface is described which can be used to quantitatively search a given volume of a sample. Methods for establishing the shape of structures embedded within the ice are also considered. Impurities were located and analysed using x-ray microanalysis.

II.2. Sample preparation

The basic instrument used in this study was a Leica S360 SEM (figure I.10), with the addition of a four quadrant solid state back-scattered electron detector and an Oxford Instruments CT1500 cold stage. Two x-ray analysis systems were used: an Oxford Instruments INCA system with an ATW Germanium energy dispersive detector and an Oxford Instruments Microspec 400 wavelength dispersive detector. An Oxford Instruments cryo-transfer device was used to introduce samples to the SEM cryo-chamber.

Specimens of approximately 5 mm in diameter were cut from the core using a cleaned hacksaw and scalpel. The specimens should be less than 5 mm thick. Cylindrical brass stubs of diameter 10 mm and height 8 mm were used to mount the ice. The relatively high stubs (as compared to conventional cryo-mounting stubs of height 5 mm) help to retain a brass cap used later to protect the sample from condensation. An ambient temperature circa -20 °C was found to be suitable for cutting and preparation, as will be discussed later.

Specimens were handled in the isolated environment of a cold room using cleaned forceps whilst wearing latex gloves to prevent condensation reaching the surfaces. Samples were stuck down to the roughened end of a stub using Leit-C conducting carbon cement. Six hours drying time was required depending on the consistency of the cement, the temperature and the ventilation.

To avoid carbon originating from the Leit-C contaminating the specimens (useful if searching for biological matter), samples could alternatively be attached using pure water applied with a pipette to the interface between the ice and the stub. Clean powdered ice or snow was applied around the base of the samples before the addition of the water (J. Kipfstuhl, personal communication). This ensured that the water was at freezing point when it contacted the sample surface, and minimized the disruption to the structure by melting and refreezing which could otherwise cause the movement of impurities in the specimen.

A flat surface was achieved using a sledge microtome with the knife angled at 25° (figure II.2); a rotary and a glass knife microtome were also tried and gave satisfactory, although slightly rougher, surfaces. A hardened steel knife was found to give fewer cutting artefacts than a tungsten carbide tipped blade, figure II.3a and II.3b. Planing was carried out at

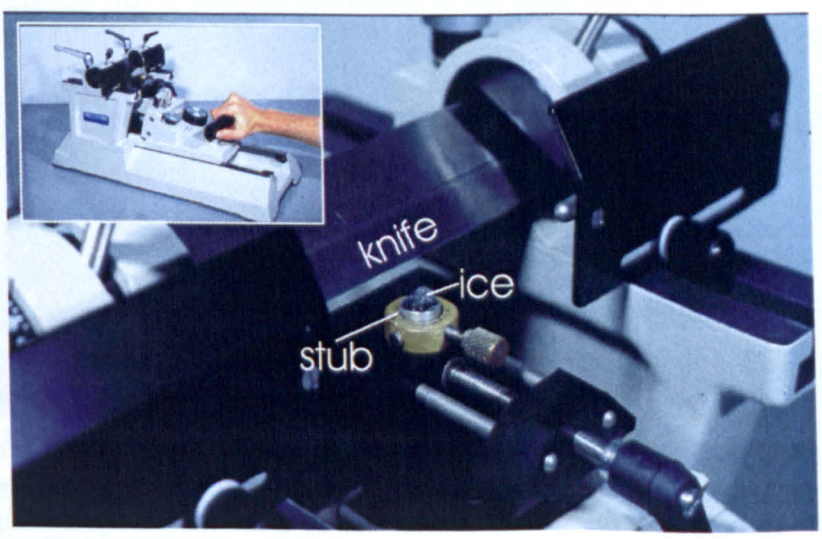

Figure II.2. A Bright sledge microtome with a hardened steel knife was used to cut surfaces on ice samples mounted on small cylindrical stubs.

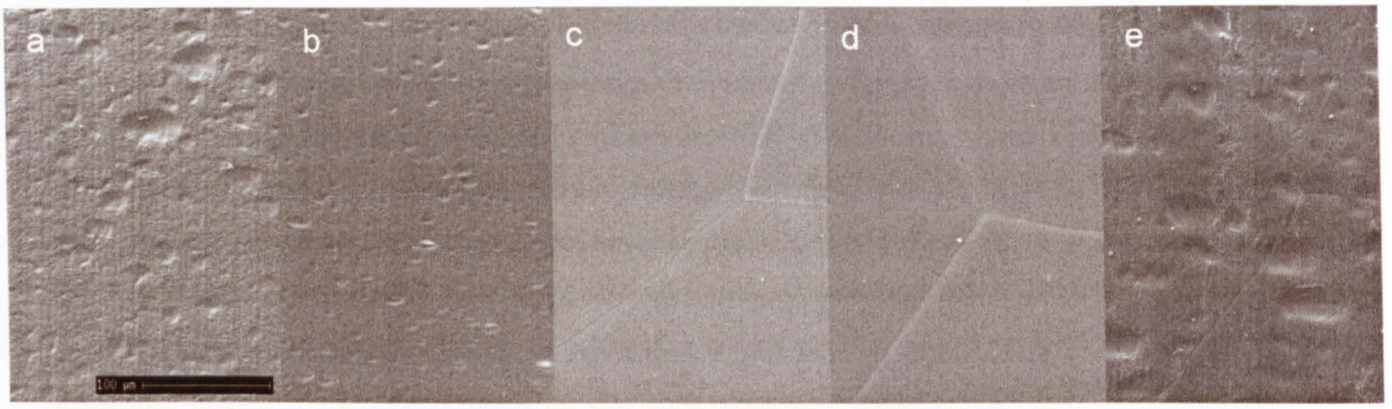

Figure II.3. Different planed surfaces from Antarctic ice; images orientated with cutting direction down the page; all surfaces are at the same magnification, scale bar 100 μm. **(a)** Surface cut at -20 °C using a tungsten carbide blade (see appendix). **(b)** Surface cut at -20 °C using a hardened steel edge, the surface has less cutting fracture marks than can be seen in (a) (see appendix). **(c)** Surface cut as (b) but specimen pre-etched for four hours at -20 °C before introduction to SEM, almost all the irregularity is lost from the surface by this time (see appendix). **(d)** Surface cut as (b) but pre-etched for 16 hours at -20 °C, little improvement in the surface can be seen when compared to (c). **(e)** Specimen cut above -10 °C, melt and re-freeze marks can be seen on the surface.

the ambient temperature in the cold room to prevent condensation forming on the newly prepared surface. The depth of initial cuts was up to 40 μm; greater than that risked dislodging the sample. Once the required surface area had been exposed, cutting depth was reduced down to one micron per section, for the final few sections, leaving the surface relatively free of cutting marks.

The technique is similar to cryo-planning techniques used for the preparation of biological samples reviewed by *Nijsse and Van Aelst* [1999]. In some cases cutting debris was removed from the surface using aerosol propellant, held far enough from the sample to avoid propellant condensing on the surface (figure II.4a).

Samples left to stand in the cold room in a sealed container underwent a surface smoothing process that we will call pre-etching. This is thought to be due to a combination of evaporation and re-condensation of water molecules on the surface of the ice, and movement of a pre-melted quasi-liquid layer [*Dash et al.*, 1995; *Petrenko and Whitworth*, 1999] to reduce the free energy of the surface. There is a noticeable change in the smoothness in a matter of hours. At cold room

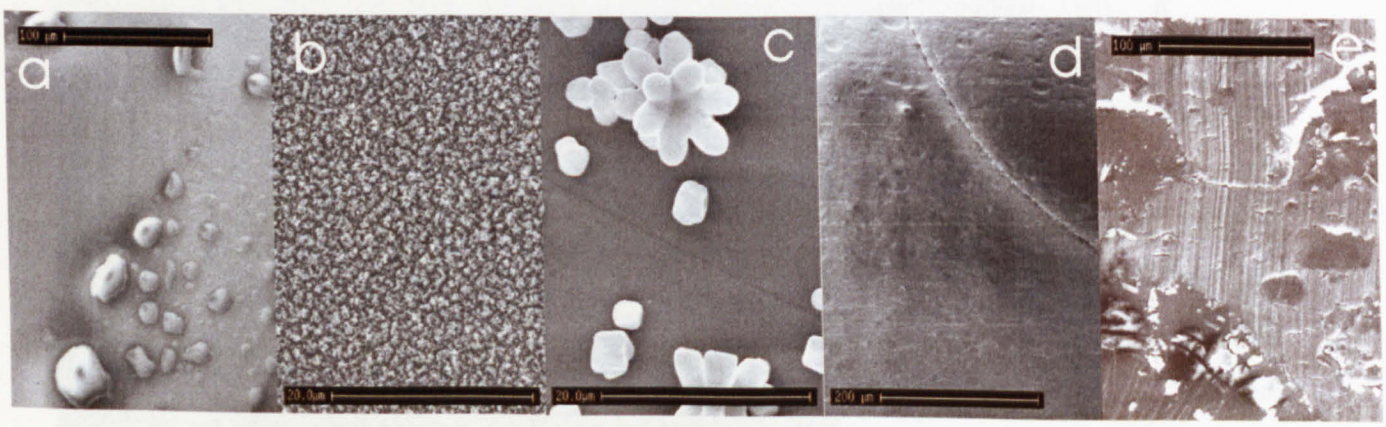

Figure II.4. Surface contamination. **(a)** Aerosol propellant frozen to the surface during cleaning, scale bar 100 μm. **(b)** Micron scale condensation formed on the surface during direct transfer to the SEM cryo-chamber without the use of a brass cap to protect the specimen, scale bar 20 μm. **(c)** Ice crystals deposited on the specimen surface by slushing nitrogen, scale bar 20 μm. **(d)** Scratches left on surface by 'cryo brush' used to remove frost. **(e)** An example of a surface cut inside the SEM cryo-chamber at a temperature of -160 °C. The cutting fracture marks are much larger than those seen in figure II.3, there is also a lot more cutting debris on the surface, scale bar 100 μm.

temperatures the thickness of the liquid layer (~3 Å [*Dash et al.*, 1995]) is significantly increased in the proximity of soluble impurities. This could allow the dispersion of impurity across the surface from regions of high concentration such as grain boundaries and triple junctions, to equilibrate the layer thickness. This diffusive process could obliterate surface features originally present after planing. Pre-etching should therefore be treated with caution. It removes cutting artefacts and enhances grain and sub-grain boundaries by making groovessince preferential sublimation and pre-melting occurs at these low energy sites (compare the surface in figure II.3b with figure II.3c, both show a surface on which grain boundaries and a triple junction are present).

A cutting temperature/pre-etching time survey was carried out between -10 and -30 °C with pre-etching times of up to 3 days, to determine the relative quality of surfaces prepared. No significant advantage in surface smoothness beyond a period of 4 hours was found, see figure II.3c and 3d. Temperature did not have a large impact on surface quality although at temperatures higher than -10 °C there is a risk of pressure melting on the surface of the sample during the cut, leaving refrozen streaks running across the surface (figure II.3e). A higher proportion of samples are dislodged during cutting at higher temperatures, whilst at lower temperatures (-30 °C) it takes longer for the carbon glue to dry. We concluded that cutting was best performed at -20 °C and a pre-etching time of 4 hours was adequate if a smoother surface was required. Pre-etching for longer durations (several days) collects impurity at triple junctions for some specimens (this is discussed further in chapter VI).

Either immediately after cutting or after pre-etching, specimens were covered by a brass cap to prevent contamination and condensation. The brass cap (figure II.5), which was engineered to fit snugly over the stub and cleaned with acetone, was found to be the best of a variety of methods for reducing condensation (figure II.4b) forming on the specimen surface. This eliminated the need to sublimate frost from the surface by etching, which was required in other studies [e.g. *Adams et al.*, 2001]. Specimens were then immediately cooled by immersion in liquid nitrogen (-198 °C) before being introduced to the SEM. This avoided the surface sublimation and consequent impurity redistribution that occurs on exposing a comparatively warm surface (~ -20 °C) to a

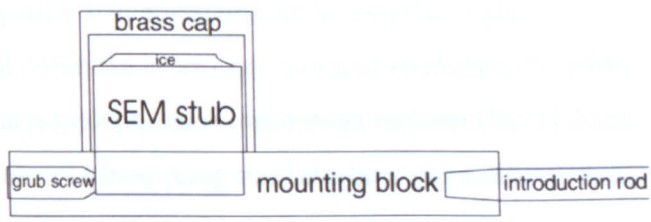

Figure II.5. The arrangement of the specimen before loading into the cryo-chamber of the SEM. The ice is attached to the brass stub fixed into the mounting block, and the stub is covered by the brass cap.

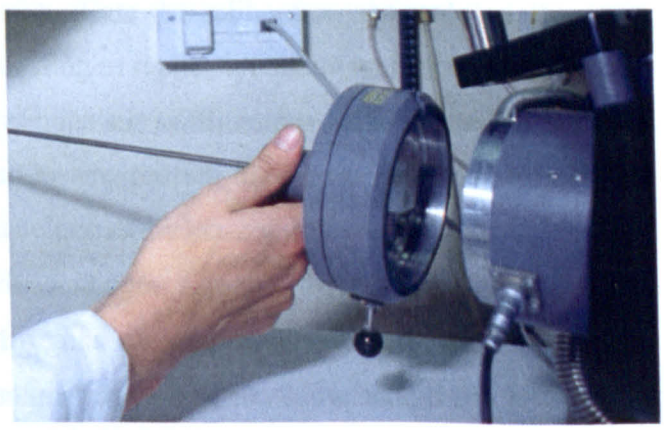

Figure II.6. Specimen introduction using the vacuum transfer device.

vacuum that was a feature of studies by Cullen and Baker [2001]. If samples are not cooled before introduction it is difficult to interpret the original distribution of impurities in the ice. The cap was tipped off the sample once in the air lock of the cryo-chamber of the SEM (figure II.6). Suspended ice particles from the liquid nitrogen were sometimes left deposited on the specimen surfaces (figure II.4c). A 'cryo-brush' inside the evacuated cryo chamber (P. Echlin personal communication) was tested as a means of removing such debris, however brushing was found to scratch the ice surface, figure II.4d.

To reduce the risk of external contamination, whilst preventing post-cutting movement of impurity, some specimens were cut in the cryo-chamber of the microscope. Since the ice was at a much lower temperature (approximately -160 °C) than the cutting conditions previously described, it was considerably more brittle. For this reason, care was required to ensure that large chunks of ice were not broken off the sample or that the sample was not knocked off the stub completely. The disadvantage of this technique is that the surface quality is inferior to surfaces cut externally, being rougher with more shallow fractures and cutting debris left on the surface, see figure II.4e, making it of less value for locating impurities.

II.3. Coating and x-ray analysis

Some samples were sputter-coated with gold. However as will be discussed later, it was often advantageous to leave specimens uncoated for the purpose of detecting impurities. Mulvaney *et al.* [1988] used an aluminium coating [*Reid et al.*, 1993]. This was found to be more suitable for quantitative x-ray analysis than gold, partly because the gold Mα peak obscures the location of the sulphur Kα peak. However an aluminium coating masks the aluminium content of dust particles. Other coating alternatives such as carbon, beryllium and chromium are discussed by Echlin [1992], although all have the disadvantage of using evaporative coating which require high temperatures in close proximity to the specimen surface, risking damage. Metal coatings can also produce a larger interaction volume as well as causing absorption effects at different energies from fluorescing x-rays.

There was often some drift of the sample relative to the electron beam, caused by thermal contraction and expansion of the sample stage. It was therefore often beneficial to keep repositioning the beam during x-ray collection.

Two methods of x-ray detection were available: energy dispersive and wavelength dispersive. The latter method, despite giving a higher resolution and peak to background ratio, required much higher probe currents to get similar count rates to the energy dispersive detection. Since high probe currents led to surface charging, and longer collection times allowed greater thermal drift, energy dispersive detection was preferred as it requires less time to detect an

impurity.

Since the quantities of impurities in polar ice are low (approximately 10^{-6} of the total volume) the signal strengths were low. As expected, gold coatings were found to mask some of the x-ray peaks that we are interested in (particularly sulphur), as well as contributing significantly to the x-ray background spectrum [*Echlin*, 1992]. Figure II.7 shows an example of spectra collected at 10 kV from a typical dust particle, found on the surface of a Greenland specimen, before and after gold coating. Consequently spectra were generally collected from uncoated specimens, allowing greater versatility with etching as will be described.

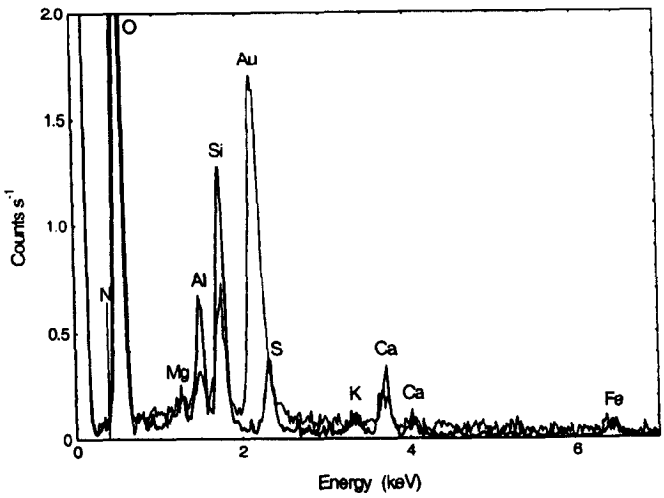

Figure II.7. Thick line: an example of a spectra emitted from a dust particle found on an uncoated surface. The three main peaks of interest are Si, Al and Mg peaks between 1 and 2 keV. Thin line: the same dust particle analysed after gold sputter coating, the peaks are smaller relative to the background level, the sulphur peak is obscured by the presence of the gold, and the iron peak is no longer easily discernable. The position of the nitrogen Kα peak is marked, due to the close proximity of the oxygen peak it is not possible to positively identify the presence of nitrogen.

II.4. X-ray analysis calibration

It is difficult to adequately calibrate x-ray measurements where an impurity of size less than the excitation volume is surrounded by a medium of different conductivity. To calibrate x-ray analysis measurements Reid et al. [1992] froze aqueous standards into nuclepore filters (track etched polycarbonate membranes containing cylindrical holes) to simulate impurity filled veins in ice. Constraining the acid in the filter holes prevented significant partitioning of the impurity phase during freezing. They found a linear relationship between elemental concentration and the x-ray count rate stimulated by the incident electron beam. Here the calibration was repeated, this time using sulphuric acid solutions without a surface coating to replicate conditions in this study. Acids of 0.5, 1.0 and 4.9 molar (the eutectic concentration) were used, frozen into 0.4 μm pores in the polycarbonate membrane. The absence of a conductive coating allowed a large variation in the detected x-ray count rates; however an approximately linear relationship was still seen between the integrated elemental count rate for sulphur and the acid concentration (figure II.8a). The presence of a small carbon peak in the collected spectra indicated the x-ray excitation volume extended beyond the circumference of the holes. The count rates were very variable for the same acids frozen into larger pore sizes (2 and 8 μm) suggesting that impurity segregation was occurring in the frozen mixture.

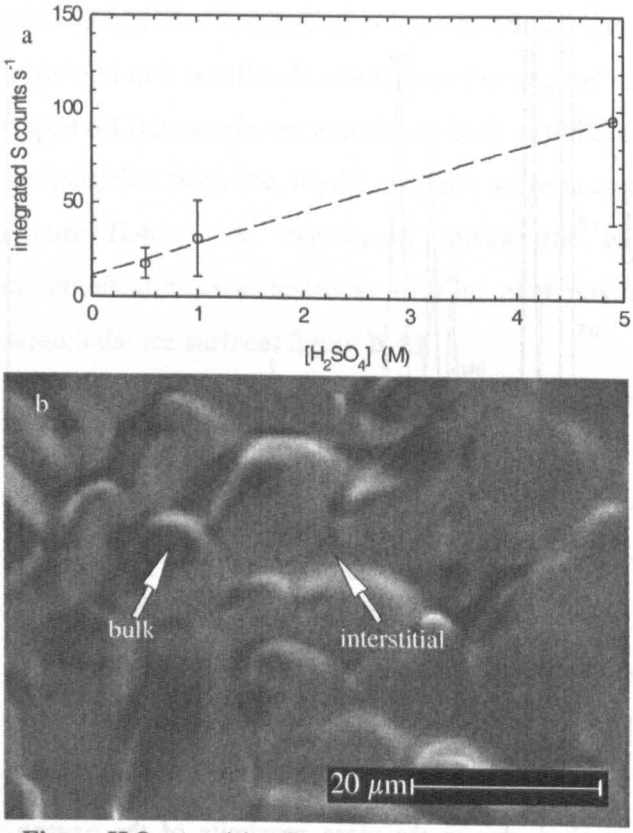

Figure II.8. **(a)** The relationship between integrated count rate collected by x-ray analysis and concentration of sulphuric acid frozen into 0.4 μm holes. **(b)** Cut surface of frozen 0.5 M sulphuric acid. Partitioning can be clearly seen between the bulk ice and the interstitial acidic components.

We make a crude estimate of the minimum quantity of sulphate detectable on an ice surface under the conditions in this study. The shape and volume of interaction of electrons within ice is not well established, particularly in the presence of impurities. Echlin [1992] reviewed various studies on the subject. The most pertinent is the work by Oates and Potts [1985] measuring the penetration depths of incident electrons in ice. They detected sulphur from below an ice layer 3 μm thick when stimulated with electrons accelerated by 15 kV. However 90 % of x-ray emission should occur within the top 2 μm. On this basis the volume of acid stimulated in a hole of diameter 0.4 μm is approximately 0.25 μm^3; if the acid is at 0.5 M then the signal emitted originates from 1.3 × 10^{-16} moles of sulphur. In this study a signal around 5 times less than this was no longer distinguishable from a background spectrum. Given a linear relationship between count rate and impurity concentration this indicates that the minimum detectable quantity of sulphur is 2 – 3 × 10^{-17} moles. We estimate the minimum detectable quantities for Na, Mg and Cl to be factors of 2.6, 1.0 and 1.5 greater than the value for sulphur respectively [*Reid et al.*, 1992].

It is generally presumed that the frozen solution formed between rapidly cooled ice grains is at the eutectic composition regardless of the bulk ice concentration. This is expected for liquid components of the polar specimens in this study on freezing in liquid nitrogen. To test whether this is the case, sulphuric acid droplets of varying concentration were rapidly frozen on a copper block cooled by immersion in liquid nitrogen (-196 °C). Flat surfaces were microtomed for the 0.5 and 1M droplets, but the 4.9 M droplet (the eutectic concentration) was left as a droplet since it would be liquid at the cutting temperature of -20 °C. Figure II.8b shows an example of a cut surface of a frozen 0.5 M H_2SO_4 droplet; no sulphur is detectable from the surfaces of the ice grains, but it is clearly present in the interstitial regions surrounding the small rapidly formed grains. If the interstitial solution is at the eutectic composition in all cases we expect similar count rates from each droplet. The net sulphur peak count rate integrals of the measured spectra were 53 ± 39, 102 ± 75 and 36 ± 9 counts s^{-1} for the 0.5, 1.0 and 4.9 M specimens respectively. A minimum of five spectra were used for each measurement and the standard deviations are shown. The large variance

in signal strength does not allow reliable comparison between the signals and is likely to be mainly due to the effects of charging in the microscope and the geometry of the 4.9 M droplet. The results however do not rule out a uniform interstitial concentration.

II.5. Etching techniques

Un-coated specimens mounted within the SEM could be etched, by heating the sample to sublimate ice from the surface. Etching was used to sublimate ice from the surface whilst leaving impurities to coagulate on the surface as hydrated salts. It was also used to evaporate any small scale cutting debris, and produce etching channels at the location of grain boundaries that could not previously be easily identified. Etching was best performed on un-coated samples, and subsequently the specimen could be coated if desired. Etching samples already coated caused the coating to rupture and crack as the ice sublimed underneath.

The formation of a conductive vapour over the sample during sublimation neutralised surface charging effects. Consequently un-coated specimens could be observed reasonably well during etching. The etching rate at -80 °C from an ice surface under vacuum was measured to be 6.2 ± 0.4 μm min^{-1} by timing the complete evaporation of a piece of ice of measured thickness. This is close to the theoretical evaporation rate of about 5 μm min^{-1} [*Davy and Branton*, 1970]. The sublimation rate was controlled by raising the cryo-stage temperature to -80, -70 or -60 °C achieving etching rates on a flat surface of 6, 20 or 60 μm min^{-1} [*Davy and Branton*, 1970].

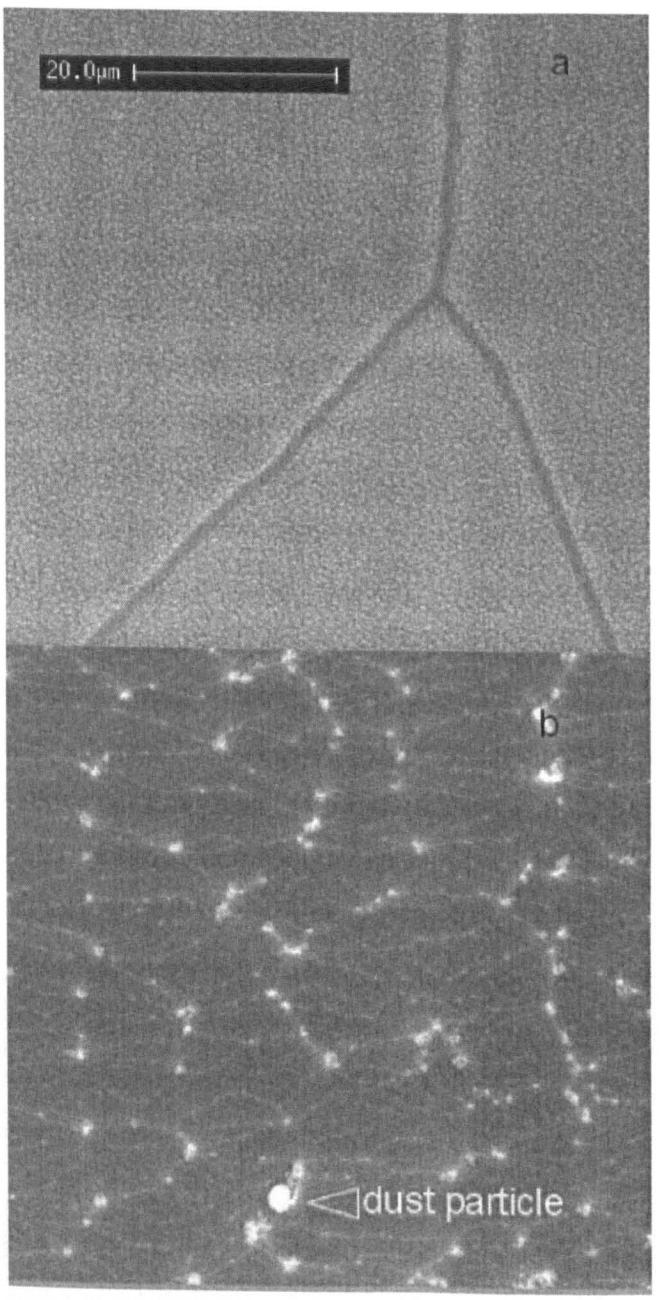

Figure II.9. A dust particle revealed by etching at - 80 °C. The scale bar is 20 μm and the sample is uncoated. **(a)** Shows the surface after 2 minutes of sublimation, the ice grain boundaries are still clearly visible at this stage. **(b)** The same section after 15 minutes of sublimation, a dust particle (marked) is revealed embedded in the ice. The original location of the grain boundaries has almost been lost by this stage as the etching facets grow. The other bright spots on the surface are charged peaks formed by etching. Distinguishing between these and impurities can be difficult.

Prolonged etching was used in some cases to strip away layers from the surface of the sample. This was useful when searching for the location of dust. Since the rate at which ice is lost from the surface is known, the volume searched can easily be calculated by simply measuring the etching time and exposed ice area. The method relies on the assumption that the impurities are not evaporated by this treatment. There is a possibility that the more volatile impurities (e.g. HCl) may be lost from the surface during etching at high temperatures. Figure II.9 shows an example of a dust particle being revealed by sublimation. A similar technique has been used by Cullen and Baker [2000] to concentrate impurities at grain boundaries. They estimated the thickness of ice sublimed from a boundary from the width of the impression left by the boundary channel. For etching at -80 °C we found that an estimate of this sort significantly (by up to a factor of 10) underestimates the depth of ice that has been sublimed from the surface.

By holding the field of view constant, a series of images could be recorded showing the surface evolving with time as the sample evaporates. Figure II.10 shows an example of such a time series, where the impression of a plate-like inclusion (probably hexagonal) is revealed. The specimen was taken from the Greenland ice core project at a depth of 1980 m, a depth at which no bubbles and only clathrate hydrates are expected in the ice. The inclusion is likely to be the site of a hydrate from which the gaseous component has evaporated, although it is also possible that the structure had formed during post-drilling ice core relaxation [*Pauer et al.*, 1999]. These structures have previously only been viewed using light microscopy, and here we see only its impression since the air hydrate complex is unstable and decomposes under vacuum. The time series of images superimposed on one another to build up an idea of the appearance of the 'footprint' of the embedded structure, using extended image focusing (EFI, S. I. S. Analysis Auto package). This

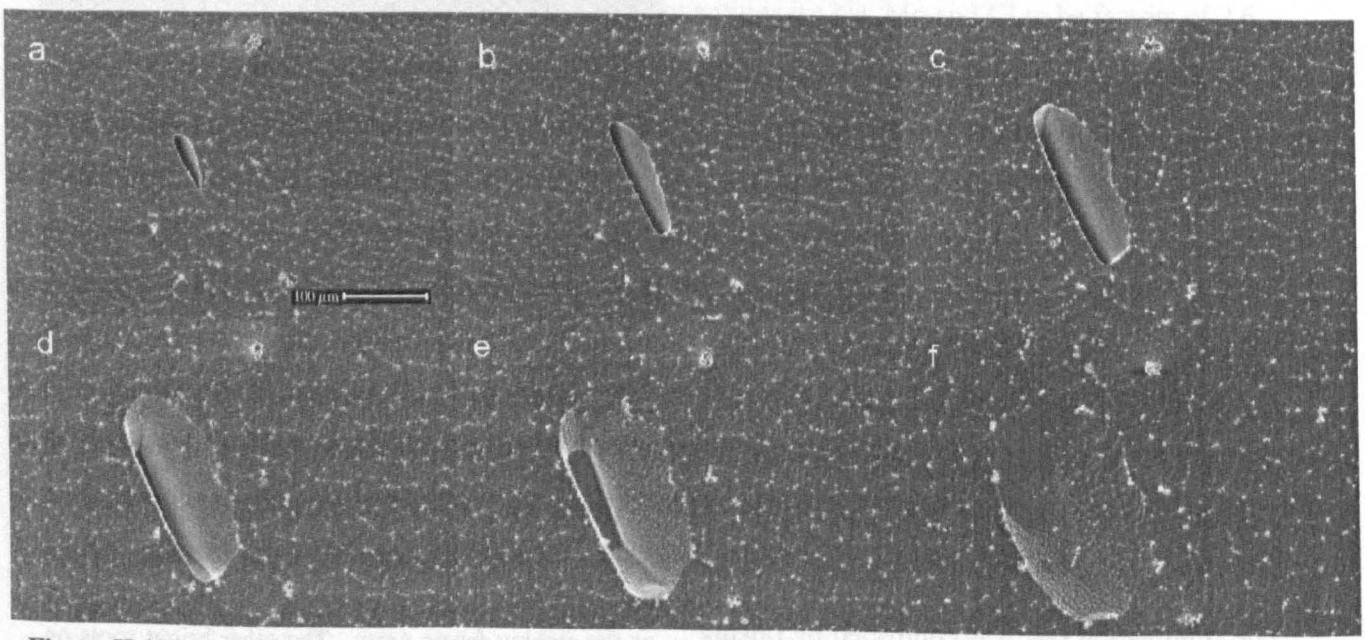

Figure II.10. Time series of a surface being etched or sublimed at -80 °C, with a sublimation rate of approximately 6 microns per minute. A clathrate hydrate 'hole' [*Pauer et al.*,1999] is revealed as the surface sublimes. The scale bar is 100 µm, and the specimen is uncoated. From left to right and from top to bottom, the images were recorded 1, 9, 17, 27, 39 and 61 minutes after the first appearance of the hole. Note the increase in distance between the etching peaks.

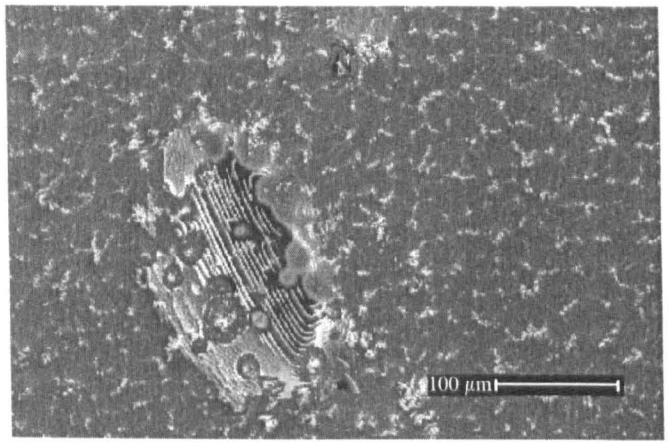

Figure II.11. Extended image focusing. This image is a combination of the areas of greatest contrast from over twenty images, some of which are shown in figure II.9, of a surface being etched at a constant rate to reveal a clathrate 'hole'. The image gives an impression of the footprint of the structure in the ice.

technique is normally applied when imaging an object which has a large depth of field: several images are recorded of the same field of view, but are focused at different depths on the object; an image is obtained with a greater depth of field. Here the EFI image gave an outline of the projection of the structure onto the surface during etching and the structure could be interpreted as having a hexagonal shape, figure II.11.

The drawback of using etching is that the surface becomes progressively rougher as the facets between etching peaks become larger, making the identification of dust more difficult. During sublimation coagulated impurities may often be found on the specimen surface at 'facet peaks'. The origin of these particles can be difficult to pinpoint since they are frequently highly mobile and can jump around the surface due to charging effects. Cullen and Baker [2000] have suggested that impurities located at peaks originate from the bulk of the ice crystal. The amount of movement of impurities on the surface during etching is currently not clearly quantified, and establishing this would certainly benefit impurity location studies.

II.6. Interpreting etching

Understanding the features of an etched surface is important when ascertaining the origin of observed impurity. Figure II.12 shows the trough of an air bubble embedded in the surface of ice cut from a depth of 140 m in the Dome C core. The surface was pre-etched for one day after cutting at -20 °C to achieve a smooth surface and clear grain boundary grooves. Once the specimen was introduced into the SEM the surface was etched for 10 minutes at -70 °C, sublimating approximately 200 μm from the specimen surface. During etching clear channels develop on the surface at the original position of the grain boundary grooves, with a channel width about one fifth the depth of sublimed ice. However grain boundary grooves visible in the bubble cavity – a site where less sublimation has occurred due to curvature – do not match the location of the surface etching channels at the top and bottom of the image. In fact no indication could be detected on the surface of the intersection of the grain boundary with the surface at the positions expected from the bubble. Only where the grain boundary is congruent with the smoother base of the etching channel, can the intersection of the grain boundary be observed during etching (this is

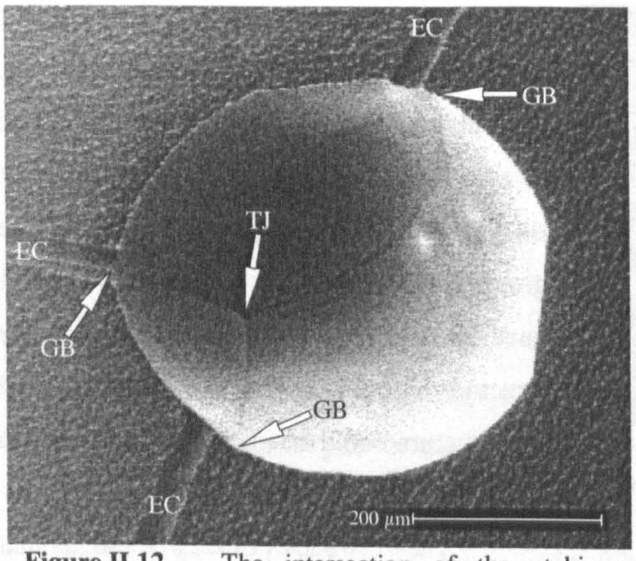

Figure II.12. The intersection of the etching surface with the grain boundary (GB) grooves on the bubble cavity surface, marked by arrows. The ice taken from 140 m at Dome C had been cut and pre-etched for a day at –20 °C before being etched for 10 minutes at -70 °C in the SEM. Note the mismatch between the grain boundary location (GB) and the etch channels (EC) on the cut surface; there is no sign of the grain boundary on the surface when the two do not match.

seen in the left hand grain boundary of figure II.12). In this case a ridge or filament is forming, probably due to the coagulation of hydrated impurity salts concentrated at the boundary.

There is a close correspondence between the duration of pre-etching (and hence the depth of the grain boundary grooves developed on the surface) and the depth and clarity of etching channels developed during etching in the SEM. Other studies assumed that grooves observed on an etched surface are caused by preferential sublimation at the grain boundary [*Cullen and Baker*, 2001], similar to the formation of grooves caused by sublimation under quasi-equilibrium conditions (pre-etching). Figure II.12 indicates that under dynamic sublimation conditions (i.e. etching as opposed to pre-etching) this is not the case; rather etching accentuates grooves already present on the surface at the start of etching but does not follow the grain boundary. Consequently grain boundaries and triple junctions on an etched surface will only be distinguishable by surface fabric differences, unless they coincide with etching channels. During etching any impurity at a grain boundary perpendicular to the surface will coagulate as a filament on the retreating surface. However impurity at a grain boundary or vein that is not parallel with the direction of etching will be spread across the retreating surface, ending up as coagulated surface spots. Some data in previous studies using etching should be re-evaluated in light of this.

II.7. Imaging techniques

Images of coated specimens were obtained at a working distance of 8-9 mm with an accelerating voltage of 15kV and probe current of 200 pA. Similar imaging conditions can be used on un-coated samples during etching without a significantly detrimental charge build up. If the sample is examined un-coated under normal cold conditions (-160 °C) surface charging will occur. To minimize this effect, the probe current was reduced (50 - 100 pA) and the accelerating voltage reduced to 2 - 3 kV. The lower probe power allows the dissipation of sufficient charge for reasonable images to be obtained. However reducing the accelerating voltage has the disadvantage

of only producing lower energy x-rays for micro analysis. A short working distance is also used for imaging. The use of higher accelerating voltages and probe currents with a fixed beam can rapidly 'burn' holes into the ice surface, or increase the sublimation rate of a localized scanned surface, caused by a local temperature rise. Maintaining samples at temperatures between -120 and -130 °C also reduced the effects of surface charging to an acceptable level, and was useful when collecting x-ray spectra. These temperatures allow enough sublimation for excess charging on the surface to be masked by the ionised vapour, whilst not significantly altering the surface topography (sublimation rate < 10 nm min^{-1} [*Davy and Branton*, 1970]).

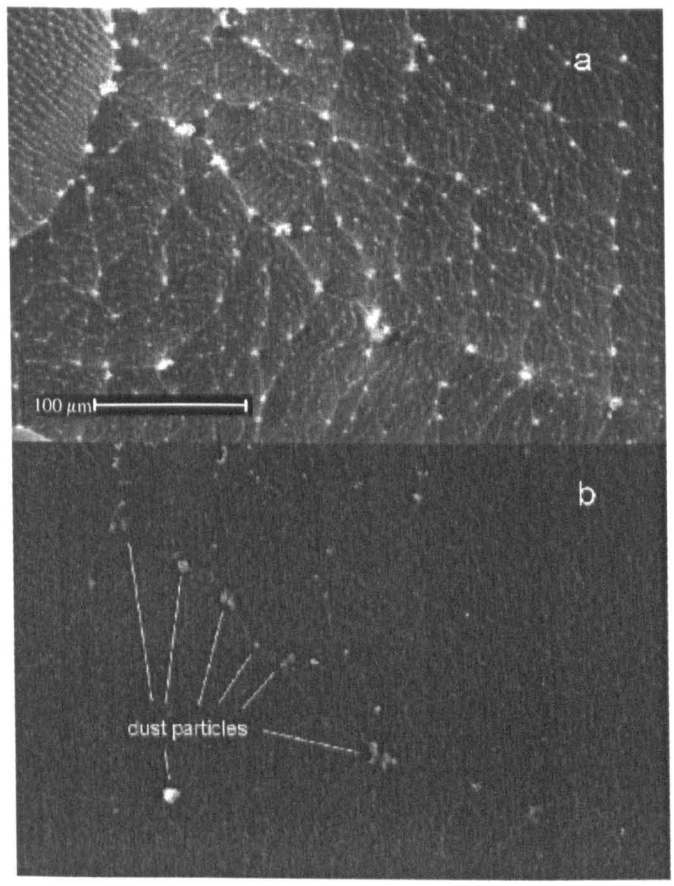

Figure II.13. **(a)** Normal secondary electron image of an etched surface, the majority of the bright spots are due to charging, however some are dust particles. **(b)** The same surface imaged using backscattered electron detection, the bright spots due to charging seen in (a) are no longer observed, leaving spots only where dust and coagulated salts are located. The scale bar is 100 μm.

Two forms of imaging are available. Secondary electron imaging collects low energy electrons emitted by stimulation from the incident electron beam near the sample surface by applying a small positive bias to the detector. The electrons can be pulled round surface topography, and is the principal imaging mode give electron micrographs their three dimensional appearance. Incident electrons that are bounced directly back from the specimen surface (usually with at least 80 % of their original energy) can be detected using a detector positioned above the specimen with a small negative bias which filters out secondary electrons. Backscattered electron emission increases with increasing atomic number .

As previously described, charged peaks sometimes containing detectable coagulated impurity appeared on a surface after etching (figure II.9b). Using secondary electron imaging, it was sometimes difficult to differentiate between the charged peaks on the surface and dust particles or impuruity. Backscattered electron imaging can be useful for distinguishing between the two. Reasonably noise free images of dust particles were obtained using this technique. The dust is composed of heavier elements producing a greater backscattered electron yield than ice, backscattered images showed fewer charging effects than respective secondary electron images. Figure II.13 shows secondary and backscattered images of the same surface where the dust particles are more clearly discernible in the latter. However because it takes longer to acquire a

noise free backscattered image than a secondary electron image, it is generally quicker to search a surface using a secondary electron image that can be used to quickly locate potential particles for subsequent verification by x-ray analysis.

II.8. Conclusion

We have reported a method for the preparation and examination of polar ice samples. It is important that during the preparation steps are taken to insure that redistribution of impurity in the specimen is kept to a minimum. Here we achieved this by immersion in liquid nitrogen immediately after cutting. However still better would be to cut surfaces under liquid nitrogen, if the problems of the brittle structure could be overcome so that a flat horizontal surfaces free from cutting debris could be obtained. Examining samples without coating was advantageous although required a low accelerating voltage and probe current to minimise charging and beam penetration or temperatures high enough to allow limited sublimation. Surface etching and pre-etching are useful tools for concentrating impurities, but the features produced by them must be interpreted with caution. Currently x-ray analysis can qualitatively indicate the composition of micron-sized particles embedded in the ice and of soluble impurities concentrated at grain boundaries. However quantitative measurements have a high uncertainty, in part due to uncertainties caused by surface charging. A method which could accurately measure the concentration of soluble impurity on a sample surface would be of great interest to the ice core community. The next chapter (III) considers the general features observed in polar ice using the SEM.

CHAPTER III

Observation of polar ice morphology using the scanning electron microscope

Samples taken from the Dome C ice core, Antarctica, and the GRIP ice core, Greenland are examined using the scanning electron microscope (SEM) to determine their microstructure. For both cores, samples are taken from two differing climatic periods: the Holocene and the last glacial period. Many of the usual features in similar samples under the light microscope are seen, including: bubbles, grain boundaries and clathrate hydrates. Features not resolvable using the light microscope are also found. Dust particles are found *in situ*. 85 % of those observed contained silicon, which was generally associated with aluminium and magnesium. The relative proportions of dust particles located at grain boundaries and in the bulk of the ice grain are estimated. At Dome C a higher proportion than expected from a random distribution of particles was found located at grain boundaries, although in Greenland this was not found to be the case for most samples. Direct evidence is also presented indicating the role of dust particles and microscopical inclusions in impeding or 'pinning' grain boundary migration. Soluble impurities are also detected at some triple junctions and grain boundaries.

III.1. Introduction

The analysis of ice cores provides a window on the past, and measurement of the composition of cores provides proxies for many climatic variables. The presence of impurities is established on a bulk scale by various analytical techniques generally involving the ice being melted, with a corresponding loss of structural information. To help our interpretation of ice core records and our understanding of the conditions that formed the ice as we find it today, knowledge of the microstructure becomes useful.

Polar ice sheets are composed of a polycrystalline structure that does not experience the warm summer melt which is characteristic of glaciers in temperate regions. It is formed by a combination of processes during the diagenesis of snow through firn into solid ice that includes the formation of bubbles as pores between grains are closed off [*Paterson*, 1994]. The surface free energy of the grain boundaries in the system is reduced by the transformation of small complex grain structures to larger, close packed structures, by the migration of grain boundaries to reduce their curvature. As well as temperature determining boundary mobility, the concentration of both soluble and insoluble impurity in the core also influences grain growth by impeding the migration

of grain boundaries [*Alley et al.*, 1986a]. Knowledge of impurity location will help to describe the extent to which grain growth rate and other mechanical deformation properties are influenced by impurity content. This distribution is also of great relevance to chemical transformations that may occur after deposition in the ice sheet, for example, processes that might produce CO_2 in ice [*Tschumi and Stauffer*, 2000], since it dictates the ability and likelihood of different chemical species to come into contact with each other. The mechanisms for the electrical conductivity of polar ice are also dependent on impurity location [*Wolff et al.*, 1997].

This chapter shows and describes the general features seen in scanning electron microscope images of polar ice. It concerns the general microstructure of ice from deep ice cores in both Greenland and the Antarctic, at depths corresponding to both the Holocene and last glacial periods. The chapter is presented in the form of observations of the typical features such as: grain boundaries, bubbles and clathrate hydrates. A study of dust particles *in situ* (which cannot be resolved using the light microscope) is made to try to establish the relative proportions at grain boundaries. Images indicating the influence of dust particles on grain growth are also included. Finally some examples of specimens with soluble impurities at both grain boundaries and triple junctions are considered.

III.2. Method

III.2.1. The samples

Greenland samples were taken from the GRIP ice core (72°34'N, 37°37'W, elevation 3232 m and mean annual temperature -32 °C) from depths of 1312.30 - 1312.85 m which was drilled in 1990, with an age of 7915 years BP (the Holocene) and 1979.45 - 1980.00 m, drilled in 1991, aged 23,200 years BP (the last glacial period) [*Johnsen et al.*, 1997]. Visible bands are present in the core from both depths, particularly in the glacial period where the bands are associated with increased abundances of micro-particles [*Alley et al.*, 1997]. Samples were cut from both the clear and cloudy sections of the glacial ice for comparison. The Antarctic samples were taken from the Dome C core (74°39'S, 124°10'E, elevation:3240 m and mean annual temperature -53 °C) from the depths of 269.50 - 270.05 m and 500.50 - 501.05 m, drilled in 1999, which correspond to ages of approximately 8,420 and 20,200 years before present in the Holocene and last glacial periods [*Schwander et al.*, 2001]. Some images presented are also of samples from a Dronning Maud Land core (77°S, 10°W, elevation 2200 m and mean annual temperature -38 °C) from 115 m, drilled in 1998, corresponding to an age of approximately 1200 years. All specimens were stored at -20°C before examination.

III.2.2. Technique

The specimens were prepared by the general method described in Chapter II. The temperature of the cold stage was generally kept at around -150 °C for imaging, but was raised to etch surfaces. Many images presented in this chapter show specimens that have had their surface etched for 1 minute at -80 °C: this was found to remove a layer 6 μm thick from the surface. The removal of this layer serves to sublimate ice-cutting debris from the surface and to effectively increase the volume of ice searched when looking for dust particles. Etching probably does not evaporate impurities on the surface (chapter II) but rather can serve to concentrate them [*Cullen and Baker*, 2000]. It is likely that etching allows impurities some mobility although not by the mechanisms suggested for pre-etching (chapter II) because of the lower temperatures. For this reason the technique should be used with caution when considering the origin of an impurity.

Some surfaces presented have a gold sputter coating to improve the image quality by allowing higher probe currents and accelerating voltages with fewer charging effects on the surface than on an uncoated sample. X-ray analysis was used to qualitatively determine the elemental composition of the features observed, normally with the beam accelerated to around 10 kV, and focussed on a specific spot on the specimen.

III.3. Observations

III.3.1. Grain boundaries and triple junction

Figure III.1a shows grain boundaries intersecting at triple junctions that are free from detectable impurity. The smooth surface has been achieved by pre-etching. As well as the clearly defined grain boundaries, two fine lines, indicated by arrows, can be discerned below the triple junction on the left side of the image, one of which intersects the boundary at a slight bend. We interpret these finer lines as indicating the presence of sub-grain boundaries referred to by Thorsteinsson *et al.* [1997]; these may be linked to a gradual reorientation of the crystal along its basal plane. Grains of different orientations can be seen in figure III.1b, a specimen from the GRIP core, 1980 m, which has been etched for more than 21 minutes at -80 °C. This corresponds to sublimation of approximately 125 μm of ice from the original cut surface. Under these conditions the pattern of peaks and facets left on the surface as ice sublimes varies depending on the orientation of the lattice. Thus the different surface texture indicates different fabric. The impressions left by the grain boundaries can be clearly seen and are about 20 μm wide.

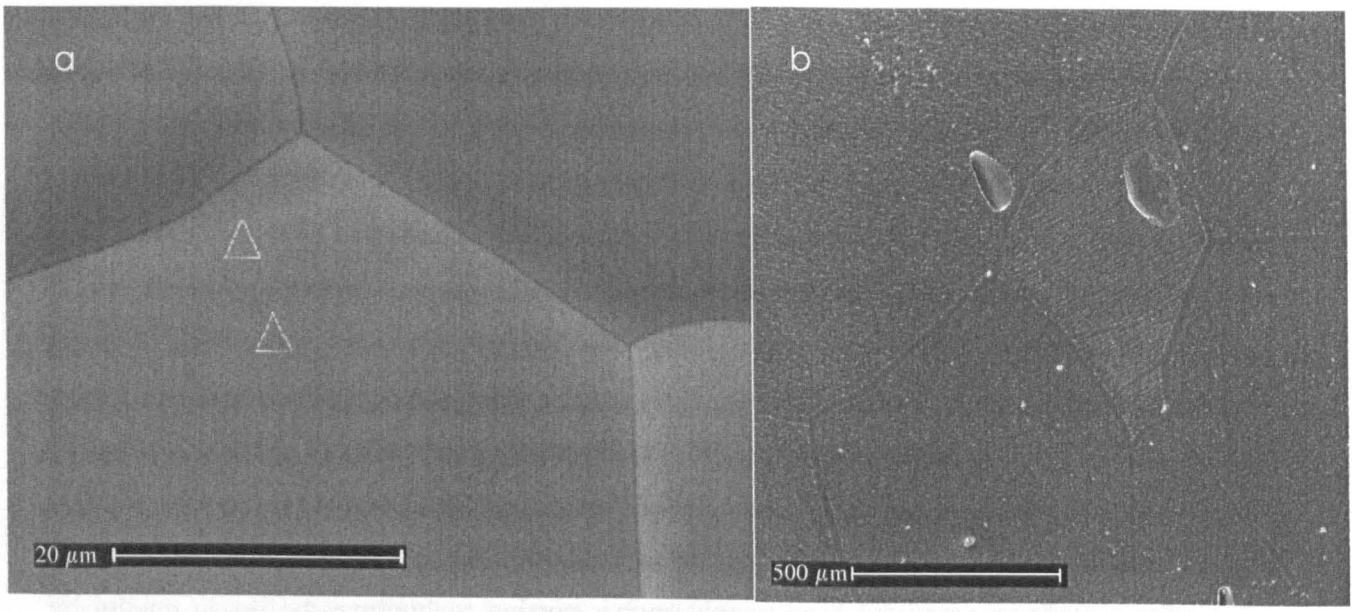

Figure III.1. **(a)** Grain boundaries and triple junctions from Dronning Maud Land core (115 m), pre-etched for 1 day, scale bar: 20 μm. Note the faint lines below the grain boundary on the left of the image indicated by arrows, which are interpreted as sub-grain boundaries (see appendix). **(b)** An etched surface (21 minutes at -80 °C) from the GRIP core (1980 m) with surface texture differing between grains. The holes on surface are impressions left by clathrate hydrates, scale bar: 500 μm.

III.3.2. Bubbles

Bubbles are expected in all ice above a depth of around 1500 m. From depths of around 400 - 500 m and below at Dome C and 1000 m and below for GRIP the occurrence of bubbles falls and air hydrate crystals appear and become more abundant with increasing depth [*Shoji*, 2000]. Number densities and volume fractions of bubbles have been linked to climatic parameters [*Lipenkov*, 2000]. The SEM is of limited use for such studies because of the small sample sizes examined. However we note from our observations that the majority of bubbles are situated at grain boundaries as opposed to existing internally within a crystal. Table III.1 gives the numbers and location of bubbles observed in Dome C specimens where 56 % of the bubbles observed intersected grain boundaries at a depth of 270 m whilst at 500 m all bubbles observed lay at grain boundaries. This difference may be linked to the difference in grain size at the two depths and the mobility of bubbles during boundary migration. Figure III.2a shows a bubble from relatively shallow ice (115 m in the Dronning Maud Land core). The particles on the surface are shavings of the carbon glue that was used to stick the specimen down. Visible on the surface, which has been etched, are grain boundaries, many of which intersect at the bubble.

When deep ice is brought to the surface during drilling there is a large reduction in the overburden pressure on the core. It is thought that this reduction in pressure allows gases dissolved in the ice to form micro-bubbles, possibly nucleating on dust particles, as the ice relaxes [*Alley et al.*, 1997; *Shoji*, 2000]. In this study micron sized bubbles were observed, often occurring at grain boundaries in the deep samples examined. Figure III.2b shows typical micro bubbles seen at a grain boundary during etching at -80 °C; they have a diameter of around 1 μm and the sample is from the Greenland glacial period. It is likely that these bubbles have formed during storage, and

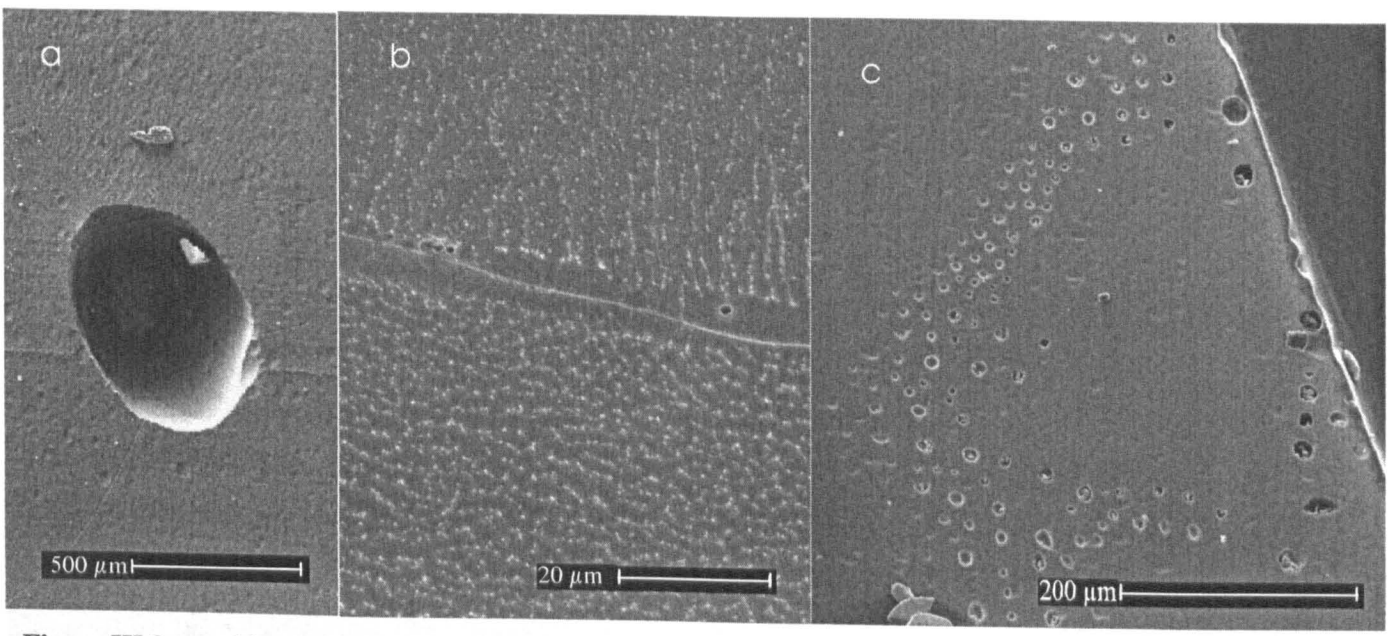

Figure III.2. **(a)** An air bubble from the Dronning Maud Land core (115 m), situated at the intersection of several grain boundaries, scale bar: 500 μm (see appendix). **(b)** Micro-bubbles of approximately 1 μm diameter observed whilst etching a specimen from GRIP (1980 m), scale bar: 20 μm. There is also a filament running along this boundary although no impurities were detectable. **(c)** A 'rash' of bubbles near the edge of the core of a Dronning Maud Land specimen (115), scale bar: 200 μm.

their presence at the grain boundaries implies a diffusion of dissolved gas through the lattice to the high density of low energy sites that defines the grain boundary. Figure III.2c shows a 'rash' of bubbles found on a sample at the outside edge of the Dronning Maud Land core (115 m). It is possible that they are an artefact of the drilling process, with nucleation of the bubbles caused by high stresses placed on the surrounding ice by the cutting blade of the drill.

III.3.3. Clathrate Hydrates

As already mentioned, at depths below 1000 m in the GRIP core, the formation of air hydrate crystals is expected in the ice, and such crystals can been observed using light microscopy [*Shoji*, 2000]. Since clathrate hydrates are unstable at atmospheric pressure and cold room temperatures, they can be expected to decompose soon after exposure by cutting. If they are not decomposed before introduction to the SEM, the presence of a vacuum (approximately 10^{-9} bar) will ensure their decomposition within minutes unless the temperature is below about -220 °C [*Kuhs et al.*, 2000]. Since no bubbles exist in the ice below depths of 1500 m, any bubble-like structures observed on surfaces of samples from below this depth are either holes left by the

Table III.1. Air bubbles and clathrate hydrates: proportions at grain boundaries (GB).

	Period	depth m	age kyrs	no. of samples	surface area $\times 10^{-6}$ m^2	no. of bubbles or globular hydrates	% at GB	no. of plate-like hydrates or inclusions	% at GB
Dome C	Holocene	269.50 - 270.05	8.4	6	59	9	55	1	100
	Glacial	500.50 - 501.05	20.2	5	43	7	100	0	-
GRIP	Holocene	1312.30 - 1312.85	7.9	11	135	34	65	35	3
	Glacial	1979.45 - 1980.00	23.2	13	144	137	93	154	4

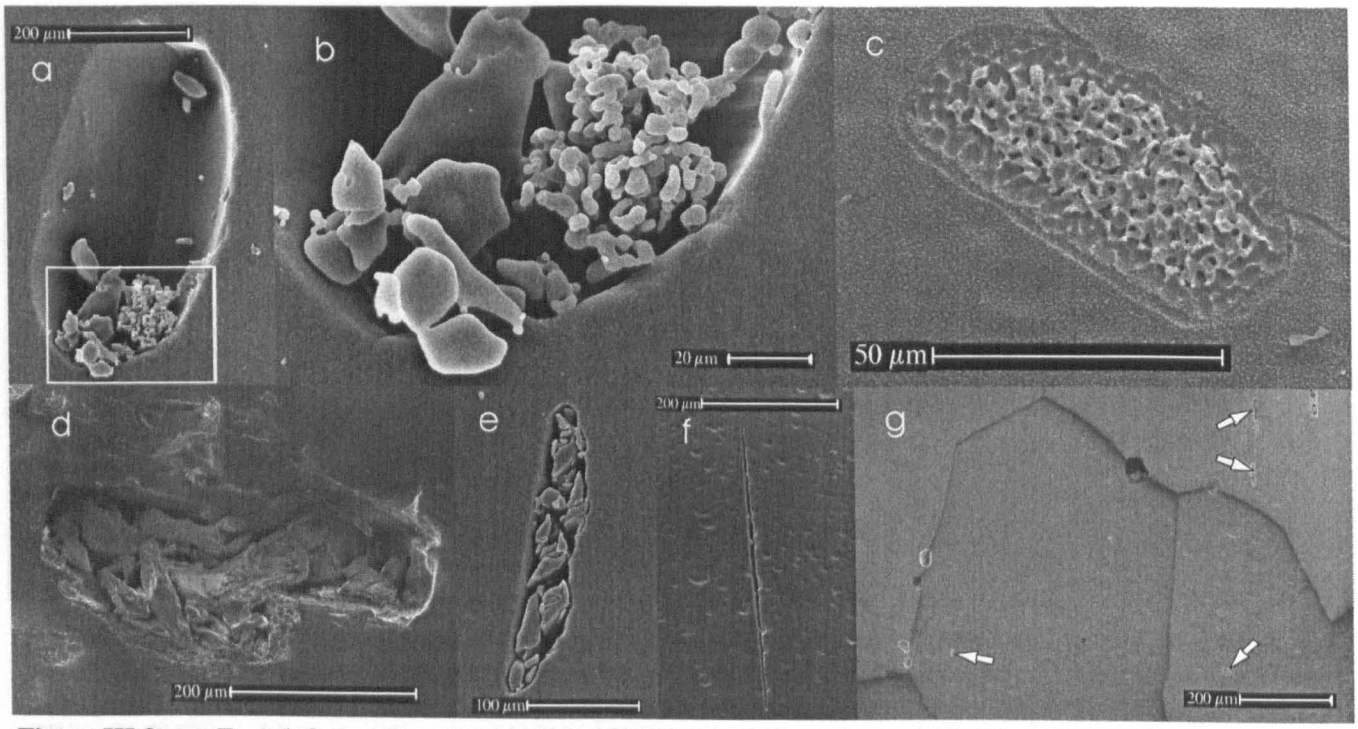

Figure III.3. From left to right and top to bottom. **(a)** Hole in the surface of GRIP (1980 m) specimen, containing clathrate hydrate remains, scale bar: 100 µm. **(b)** Inset of (a), scale bar: 20 µm. **(c)** Globular clathrate hydrate remains (GRIP 1312 m), scale bar: 50 µm. **(d)** Globular clathrate hydrate remains (GRIP 1980 m). **(e), (f)** Plate like clathrate hydrate remains, scale bars: 100 and 200 µm respectively. **(g)** Surface (GRIP, 1980 m) showing globular clathrate structures at grain boundaries and plate like structures (examples marked with arrows) in the bulk of grains. The grain boundaries can be seen clearly due to charging effects on the surface, scale bar: 200 µm (see appendix).

decomposition of clathrate hydrates, or bubbles formed from clathrate hydrate decomposition during core relaxation (possibly with the inclusion of dissolved gasses). There were two main types of structure noted in the GRIP samples: globular structures and plate like structures. The globular structures often looked similar to a bubble impression, but normally also contained ice debris suggesting the remains of an air hydrate crystal which had already partially decomposed before examination and from which the gaseous component had evaporated (figures III.3a and b). The other globular structures had a more solid appearance, with a 'pocked' or broken surface suggesting the remains of a solid hydrate crystal which had subsequently decomposed, possibly through a thin layer of ice at the surface, figures III.3c and d. The globular structures were typically 100 - 300 µm in diameter, with 'pocked' specimens (figure III.3c) tending to be a little smaller. The plate like structures were seen as thin holes in the surface, typically about 200 µm long, often filled with what appeared to be the decomposed remains of the ice component of the crystal (figures III.3e and f). Etching the surface (as described in chapter II) revealed that many of these holes had a hexagonal-plate structure, which was confirmed by examination using the light microscope. No elongated (several millimetres long) air hydrate crystals as described by Shoji *et al.* [*Shoji*, 2000] were noted in the GRIP specimens.

Table III.1 summarises the numbers and relative location of hydrate structures noted for the GRIP specimens. 94 % of the globular structures observed in the GRIP samples from 1980 m were located on grain boundaries, whilst only 4 % of the plate-like structures were associated with boundaries. The surface shown in figure III.3g is typical of this distribution. The proportion of

both types of structures at boundaries with respect to the total number of structures observed was 46 %; a value close to the ratio observed by Uchida *et al.* [*Uchida et al.*, 1993] in the Vostok core at a similar depth. In the shallower specimens from the GRIP core (1312 m) the ratio of globular structures including both clathrate hydrate remains and bubbles lying at grain boundaries was lower at 65 %. This could imply that a significant proportion of the structures observed were secondary clathrates that have fragmented [*Kipfstuhl et al.*, 2001] since primary clathrates are initially formed from bubbles, which are generally located on grain boundaries.

III.3.4. Dust

Dust particles were located on the surfaces of samples from both Antarctica and Greenland. Etching was used to strip away a surface layer and remove most of the cutting debris. X-ray analysis was required to distinguish between any ice debris left on the surface and genuine dust particles. It was not possible to positively identify particles of a diameter less than 0.5 μm using x-ray analysis, so some imaged particles could not be confirmed as dust. Figure III.4a is an example of a particle found in the bulk of a grain from a GRIP specimen from the glacial period. X-ray analysis indicated that it contained: magnesium, aluminium, silicon, chlorine, potassium, calcium and iron. Silicon usually in conjunction with magnesium and aluminium was found in 85 % of particles from both Greenland and the Antarctic, and indicates that the majority of particles are unlikely to be highly water soluble. These dust particles may have a pre-melted liquid layer surrounding them allowing them some mobility in the ice [*Rempel et al.*, 2001b]. Figure III.4b shows a dust particle located at a grain boundary (since the position of the grain boundary could change relative to the position of a dust particle on the surface during etching, any particle within 6 μm of a boundary after 1 minute of etching at -80 °C was considered to be located on it). The particle contained Ca, Al, Mg, Si and K and the boundary appears to have a filament running down its centre. No impurities could be detected in this filament, however its existence suggests that soluble impurities may be present but in quantities below the x-ray analysis detection limit. In this case the soluble impurity would be available to react with the dust particle at the grain boundary. Figure III.4c shows another example of a group of particles found on a boundary with an enlargement of one of the particles inset.

A survey of dust particles of diameter greater than 0.5 μm was made on both the Greenland and Antarctic samples to estimate the relative proportions of particles situated at boundaries and in the bulk of the grains. The search for particles was conducted by etching a layer of 6 μm from the surface of the sample and examining all grain boundaries visible on a surface then also searching a number of randomly chosen fields for particles. The results of the survey are summarised in table 2. The distribution of the dust particles on the surface was found to be extremely inhomogeneous. Particles in the bulk were normally found in small clusters, and this was also the case to a lesser extent on grain boundaries. The number of specimens examined in the survey was low, which

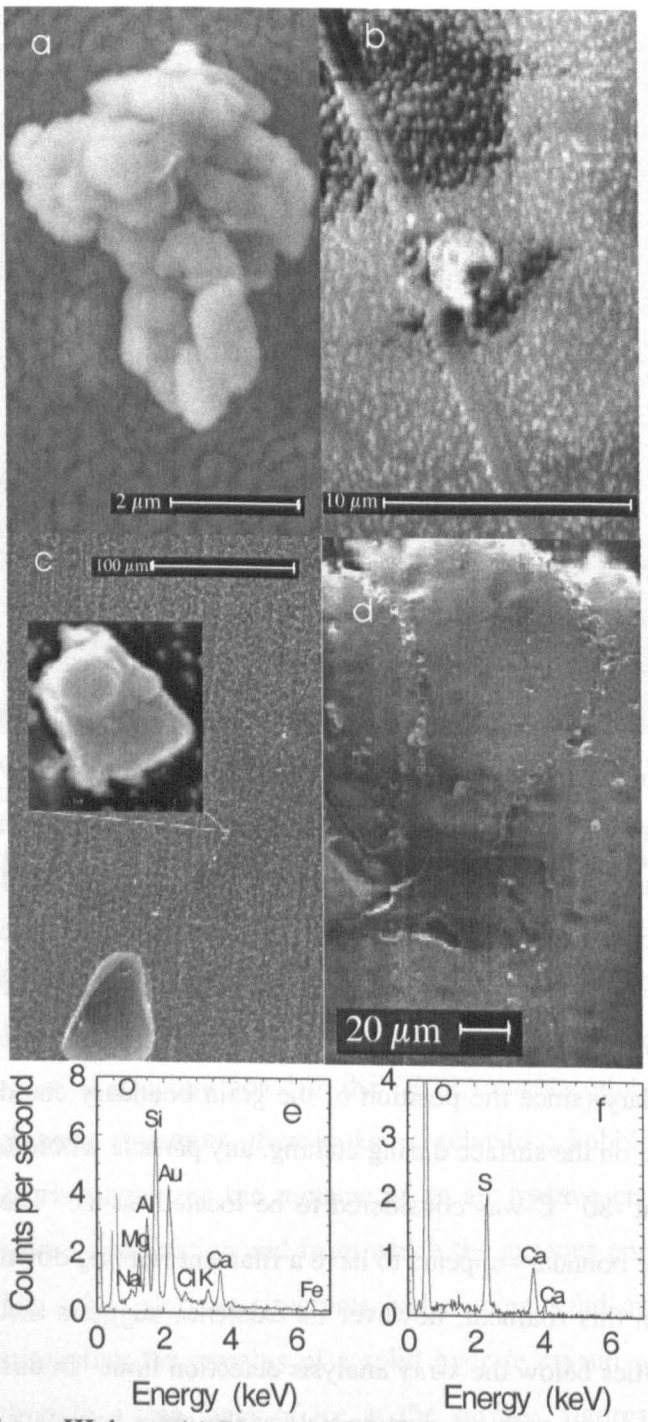

Figure III.4. **(a)** Dust particle (GRIP, 1980 m) found in the bulk of a grain on the surface, scale bar: 2 μm. **(b)** Particle at grain boundary (GRIP, 1980 m). The boundary has been etched for 1 minute at -80 °C and has a filament containing no detectable impurities at its centre. **(c)** Overview of particles at a grain boundary (GRIP, 1980 m); the inset image shows an enlargement of one of the particles (see appendix). **(d)** Section of surface from specimen from GRIP 1980 m, (precise depth: 1979.74 m, the centre of a cloudy band and calcium peak) which has also been etched for one minute removing approximately 6 μm from the surface. The bright specks on both the grain boundaries and the bulk of the grains correspond to dust particles, the majority containing silicon. There are also tracks of bubbles corresponding with the grain boundaries, scale bar: 20 μm. The variation in the brightness of the surface is a result of surface charging effects. **(e)** X-ray spectrum for particle shown in (a). **(f)** X-ray spectrum for particle shown in (c).

meant that the discovery of one cluster of particles on an otherwise empty surface could lead to a much higher estimate of the number density of particles in the bulk than was likely to be present in the specimen.

Expected abundances of dust, N_{tot}, for each sample location were found from Petit *et al.* [1981] for Dome C and were estimated using dust mass information from Steffensen *et al.* [1997] for the GRIP core with a modal mass particle diameter of 1 μm (table III.2). The Dome C data are generalised for each climatic period and do not correspond to a single depth in the core. The data are for particles of a diameter of greater than 0.8 μm, we expect the number density for particles larger than 0.5 μm to be at least twice as great. The values of N_{bulk} are higher for both the Holocene and the last glacial period than the predicted values of N_{tot} at both sites. This is in part due to the measurement of different particle diameters for the expected and observed distributions mentioned above; it can also be attributed to localised variations in number densities and the small sample size increasing the impacts of particle clusters on the statistics. The value for the glacial period (6.4×10^{12} m^{-3}), is heavily skewed towards the number density found in the cloudy bands (6.7×10^{12} m^{-3}) because the volume of ice searched in the cloudy bands was almost 10 times greater than the clear sections. As expected N_{bulk} is substantially higher in the glacial ice from both cores than from the Holocene, and still higher in the cloudy bands of the GRIP core.

The ratio of the number densities of particles in the grain boundary region to the number density in the bulk of the ice, R_N, indicates the relative proportion of particles at the grain boundaries. A value of R_N close to unity indicates that the number of particles found at the boundary is no higher than expected for a random distribution of particles in the ice. $R_N > 1$ implies either that some grain boundaries have been pinned by the presence of dust particles which have been situated on the boundary since deposition or that migrating boundaries have, on encountering a dust particles, dragged some of the dust with them.

The values of R_N in the Dome C samples are 48 and 14, and although these values should be treated with caution due to the low sample number of dust particles observed in the specimens, they indicate that more dust particles are situated on grain boundaries than would be expected in a random distribution. The fraction of dust particles at the grain boundaries, F_{GB}, is estimated at 0.4 in the Holocene and 0.2 in the glacial samples. For the Greenland samples the numbers look quite different, with values of $R_N < 1$ for both the Holocene and glacial clear samples. This indicates the high uncertainties in the observed values, particularly in N_{bulk}. These results combined with a more reliable result from the cloudy bands, where a greater volume was searched and $R_N = 1$, suggests a random distribution of dust particles with no preference for grain boundaries. This however is in contrast with some observed evidence that was discounted from table III.2. Figure III.4d shows the

Table III.2. Dust particle survey, particle diameter greater than 0.5 μm.

	Period	depth m	age kyrs	no. of samples	mean grain size $\times 10^{-6}$ m^2	P_{bulk}	P_{GB}	V_{bulk} $\times 10^{-11}$ m^3	V_{GB} $\times 10^{-11}$ m^3	N_{tot} $\times 10^9$ m^{-3}	N_{bulk} $\times 10^9$ m^{-3}	N_{GB} $\times 10^9$ m^{-3}	R_N	F_{GB}
Dome C	Holocene	269.50 - 270.05	8.4	6	1.6	1	11	4.3	1.0	7*	23	1100	48	0.44
	Glacial	500.50 - 501.05	20.2	4	0.9	1	7	1.6	0.8	20*	62	870	14	0.24
GRIP	Holocene	1312.30 - 1312.85	7.9	9	1.2	4	1	0.48	2.3	30†	830	43	0.05	0.001
	Glacial	1979.45 - 1980.00	23.2	8	0.5	107	123	1.7	2.3	400†	6400	5400	0.85	0.023
		clear sections		3	0.7	5	5	0.16	0.6		3100	860	0.28	0.007
		cloudy bands		5	0.3	102	118	1.5	1.7		6700	7000	1.0	0.028
Total				26	0.9	113	142	8.1	6.2		-	-	-	-

P_{bulk} total number of particles counted in search fields

P_{GB} total number of particles counted within 6 μm of a grain boundary

V_{bulk} bulk volume searched

V_{GB} grain boundary region, volume searched

V_{tot} total volume etched on surface of sample

N_{bulk} number density of particles within the grain bulk = P_{bulk} / V_{bulk}

N_{GB} number density of particles within the grain boundary region = P_{GB} / V_{GB}

R_N ratio of number densities = N_{GB} / N_{bulk}

F_{GB} fraction of particles at grain boundaries in the sample = $P_{GB} / (P_{GB} + N_{bulk} V_{tot})$

N_{tot} number density found / estimated from the literature

* from Petit and others (1981) for particles of diameter greater than 0.8 μm

† from Steffensen and others (1997) using dust mass fraction and a modal mass diameter of 1 μm.

surface from a specimen from the GRIP glacial period that was taken from one of the cloudy bands in the core. This specimen contained numerous dust particles at both grain boundaries and in the bulk of the grains. The majority of the particles contained silicon, magnesium and aluminium. The particles were too numerous to include in the survey; however examination of the image revealed that the majority of the visible dust lay at grain boundaries. It is also interesting to note the small grain sizes of this specimen. The mean grain area was 1.2×10^{-7} m^2 compared to 7×10^{-7} m^2 on samples from a similar depth but not from cloudy bands that contained fewer dust particles. The small grain size implies grain boundary pinning, probably due to the dust particles, has prevented the growth of the grains. This is further discussed in the following section. From the evidence presented it remains unclear whether a higher proportion of dust lies at grain boundaries in the GRIP core, and further investigation is required to definitively answer this.

III.3.5. Grain boundary pinning

Particles have been observed located at 'bends' in grain boundaries, directly indicating the role that they may play in inhibiting grain boundary migration. Figure III.5a shows an example of particles found on a bend which appears as if the boundary has been held back by the particles' presence. Figure III.5b shows a bubble that similarly appears to be inhibiting boundary migration. In some cases kinks in boundaries are observed which do not have any obvious cause (figure III.5c), however since the image is a two-dimensional section, it is quite possible that there may have been some structure pinning the boundary that has not been intersected by the surface. Figure III.5d shows a kink in a boundary from a GRIP Holocene sample that coincides with a cluster of micro bubbles. If micro-bubble formation has been nucleated by dust particles in this case, the bubbles in this image may indicate the presence of dust particles pinning the boundary immediately above or below the surface of the sample. Alley *et al.* [1986b] stated that for clear ice, the concentration of micro-particles was not high enough to cause significant reduction in grain growth rates if the particles are immobile, and the same was the case for bubbles where they could move rapidly by diffusion of ice through the vapour phase. For cloudy bands where there is a high concentration of dust particles it was found that it is possible for a grain boundary to be effectively pinned in place by the dust. At GRIP the values of R_N suggest that the grain boundaries are able to break free from most dust encountered. However the values of R_N for the Dome C samples indicate that at this site either some boundaries are being pinned by grain boundaries or some particles may be 'caught' by grain boundaries during their migration. This discrepancy may be linked to the temperature difference of the two sites altering the mobility of the grain boundaries, and a difference in the size distributions and hence drag of the particles. Work by Weiss *et al.* [2002] indicates that variations in grain size in the Dome C core can be explained by pinning by immobile micro-particles if a significant proportion are located at grain boundaries. In the case of a particle being trapped by a grain boundary and normal boundary migration continuing, then the force

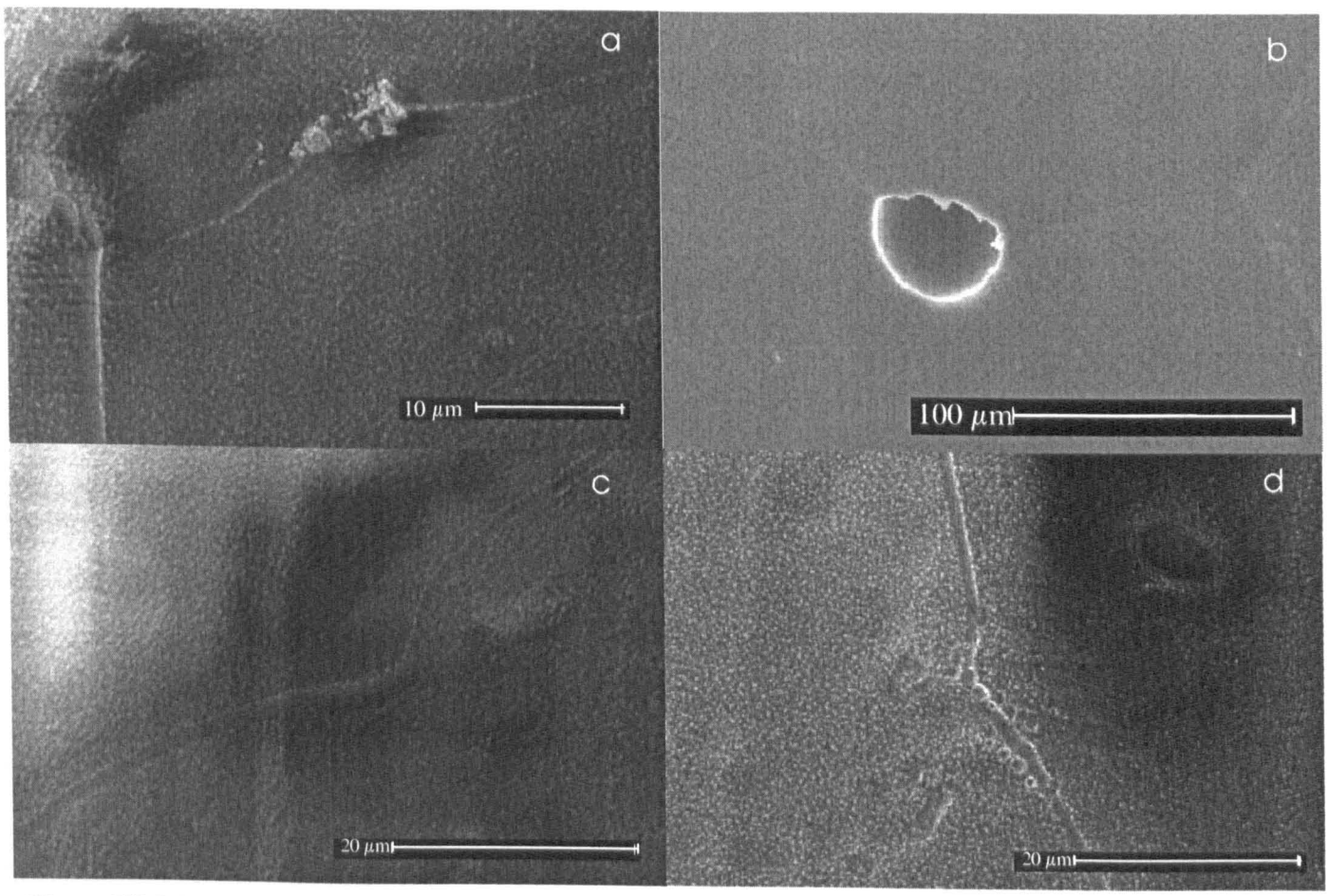

Figure III.5. Grain boundary pinning. **(a)** Dust particles at a kink in a grain boundary (Dome C, 501 m), scale bar:10 μm. **(b)** A bubble apparently involved in pinning a grain boundary (Dronning Maud Land, 115 m), scale bar: 100 μm (see appendix). **(c)** Kink in grain boundary without obvious reason (Dome C, 501 m), scale bar: 20 μm. **(d)** Micro bubbles located at a kink in a grain boundary (GRIP 1312 m), scale bar: 20 μm.

driving boundary migration is less than the force required to separate the particle from the boundary and implies the particle has a degree of mobility. This could be possible if the particle were surrounded by a pre-melted layer [*Rempel et al.*, 2001b].

III.3.6. Soluble impurities

For completeness in showing the features seen in the SEM, a few examples of soluble impurity are shown here; this is studied in detail in chapter VI. Soluble impurities were located on some specimen surfaces cut without pre-etching. The grain boundaries and triple junction shown in figure III.6a were found to contain both sodium and chlorine using x-ray analysis (figure III.6e) and are from the Dronning Maud Land core at 115 m. The grain boundaries, which have not been etched, have a thickness of 1 - 2 μm and are darker than the surrounding ice. This was typical of the majority of grain boundaries on this specimen although was not observed in other samples from the same depth and site. The presence of salts at grain boundaries is not unexpected in samples where the summer temperature is above the NaCl eutectic point (-23 °C). The image adds to the body of evidence suggesting that salts can exist as liquids outside the ice grains, although in this case they are not specifically confined to the triple junctions. Figure III.6b shows an example of trace quantities of sodium and chlorine detected at a triple junction in a Dome C glacial sample.

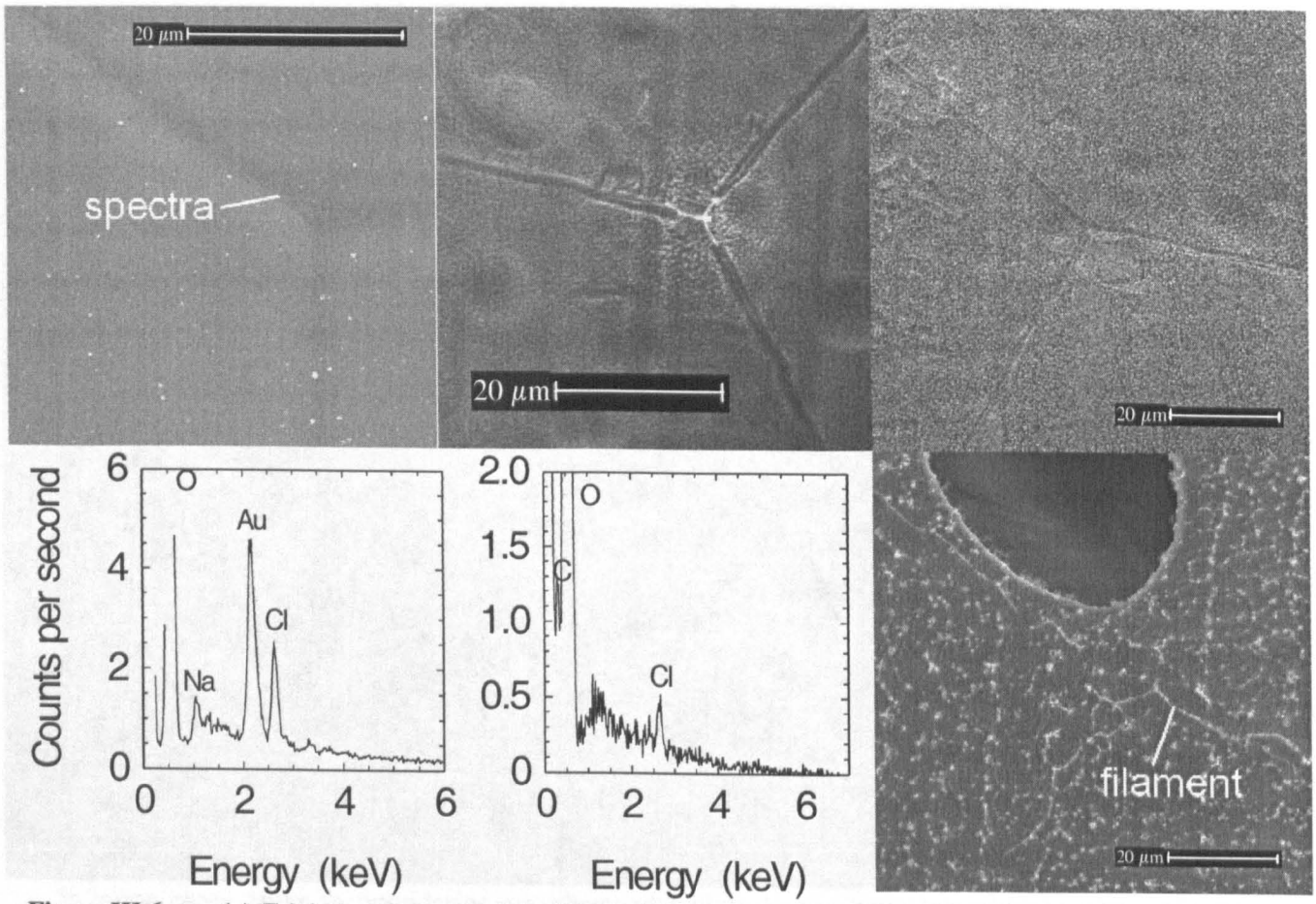

Figure III.6. **(a)** Triple junction and grain boundaries (Dronning Maud Land, 115 m) containing sodium and chlorine, scale bar: 20 μm. **(b)** Triple junction (Dome C, 501 m) found to contain traces of sodium and chlorine, scale bar: 50 μm. **(c)** Grain boundaries (GRIP 1312 m) with filaments in which no impurities could be detected, before etching, scale bar: 20 μm. **(d)** Grain boundary pictured in (c) after 6 minutes of etching at -80 °C (approximately 36 μm of ice removed); traces of chlorine were detected in the filament, which is indicated on the image. The dark circular structure is a bubble revealed during the etching. **(e)** X-ray spectrum from grain boundary shown in (a), containing sodium and chlorine. **(f)** X-ray spectrum from filament in (d) contains chlorine, carbon is also present, but could be contamination from the glue.

This was not found to be typical of triple junctions from this depth, most of which contained no detectable impurity, however it does suggest that at least some of the sodium chloride in the core could be residing in veins at triple junctions. It is also likely that a significant proportion of the salts will be incorporated into the ice lattice by this depth, and further observation is required to quantitatively estimate this distribution.

By pre-etching and etching samples from the GRIP core Cullen and Baker [2000] found sodium chloride concentrated into filaments at grain boundaries. In this study similar filaments were also noted in both the Greenland and Antarctic samples after brief periods of etching (1 - 3 mins at -80 °C) although no impurities were detectable by x-ray analysis. Further etching of these boundaries concentrated the contents to detectable levels: figures III.6c and d show such a filament before and after etching from the GRIP core at a depth of 1312 m (the top edge of a bubble has been revealed during the etching). Low levels of chlorine were detected in the filament (figure III.6f), which could indicate the presence of hydrochloric acid or sodium chloride in the case where the sodium is still not detectable. Traces of carbon were also found but are likely to be linked to

the carbon glue used to attach the sample. Isolated examples of soluble impurities have been observed in this chapter, and surface etching has proved to be a useful tool for detecting it despite questions of impurity mobility

III.4. Conclusion

Many interesting surface features can be observed at high resolution in the SEM, giving insights into physical processes. Some of these features have not been directly observed previously such as: soluble impurity at a grain boundary on an un-etched surface, resolvable micro-bubbles linked to cloudy bands, dust *in situ.* and grain boundary pinning. Whilst others have not previously been imaged with the SEM such as sub grain boundaries and clathrate hydrate remains. However the greatest potential of SEM is to simultaneously image and analyse small areas to assess the localisation of impurities. Further investigation in Chapter VI focuses on the distribution soluble impurities at grain boundaries and triple junctions. In the following chapter (IV) however we consider the subject from a different angle. The electrical response of the Dome C ice core to soluble impurities and variation in density has implications for the conduction mechanisms at work, which are dependent on impurity distribution.

CHAPTER III

CHAPTER IV

The effect of density on electrical conductivity of chemically laden polar ice

Electrical conductivity measurements made using the dielectric profiling technique (DEP) are compared to chemical data from the top 350 m of the Dome C ice core in Antarctica. The chemical data are used to calculate the concentration of the major acidic impurities in the core: sulphuric acid and hydrochloric acid. The conductivity coefficients in solid ice for sulphuric acid (β_{H2SO4}) and hydrochloric acid (β_{HCl}) are found to be 4.9 and 4.5 S m^{-1} M^{-1}. These are consistent with previously found values for the acid conductivity coefficient at different sites and suggest that the same conductivity mechanisms are important in all polar ice. A method of rolling regression analysis is used to find the variation of the pure ice conductivity ($\sigma_{\infty pure}$) and the conductivity coefficient of sulphuric acid, β_{H2SO4}, with depth. $\sigma_{\infty pure}$ and β_{H2SO4} are then assessed against changes in core density and hence volume fraction of ice, v. Looyenga's model for dielectric mixtures applied to conduction in firn broadly predicts the variation observed in $\sigma_{\infty pure}$ but does not fit well for ice above 110 m. A previous application of the theory of percolation in random lattices is used to model the conductivity coefficient in firn. β_{H2SO4} is linked to v by the power law: $\beta_{H2SO4}(v) \propto \beta_{H2SO4}(1)\,(v - v_c)^{\tau}$; where v_c is a threshold volume fraction below which no conduction can take place and is related to the geometry of the conducting lattice being modelled. The value of the exponent τ is also dependent on the structure of the lattice and is here found to be $\tau = 2.5$, which is slightly lower than the previously obtained value of $\tau = 2.7$ for a structure where each grain has between 14 and 16 nearest neighbours. This model is consistent with the concept of conduction, via liquid H_2SO_4, taking place at two grain boundaries for firn. The model does not however preclude conduction taking place via acid situated at three grain boundaries or in an interconnected vein network at densities above 640 kg m^{-3}.

IV.1. Introduction

Electrical conductivity of polar ice cores has been measured many times, and data gathered in this manner are of use in paleoclimatic studies. Direct current through the ice may be measured using the electrical conductivity measurement (ECM) method, where two electrodes are dragged across a freshly cut surface of the ice core, and the current flowing between them is measured [*Hammer*, 1980]. Alternating current conductivity may be measured using the Dielectric Profiling

(DEP) method. This non-invasive technique involves a series of opposing curved electrodes, positioned along the length of the core section, and measurement of the capacitance and conductance of the ice between them. A range of frequencies typically up to 300 kHz may be measured, allowing the value of the high frequency conductivity (σ_∞) to be extrapolated [*Moore et al.*, 1989]. The stratified conductivity data gathered by these methods have been valuable for understanding radar surveys of ice [*Hammer*, 1980; *Miners et al.*, 2002], and it can also be related to the chemical content of the measured ice core [*Moore et al.*, 1992]. It is now established that the total conductivity measured is a combination of the conductivity of pure ice in addition to the effects of any chemical impurities trapped within the ice [*Moore et al.*, 1992].

The dry densification of snow to ice in polar regions has also been well studied [*Herron and Langway*, 1980; *Kameda et al.*, 1994]. Many mechanisms are involved in the process which is dependent on both temperature and accumulation rate. The densification process has implications for the measured conductivity of the bulk ice. As the air trapped in the ice is compressed the measured permittivity and conductivity of the bulk changes with the volume fraction of ice. Several models have been suggested to describe the effect of the inclusion of bubbles of one dielectric substance into another on the conductivity and permittivity of the whole mixture. The dielectric properties of heterogeneous systems were reviewed by Beek [1967]; models best suited to describing bubbly ice over a full range of densities were those proposed by Looyenga and Böttcher [*Glen and Paren*, 1975]. The model proposed by Looyenga was first used by Glen and Paren to describe the change in conductivity of the pure component of polar ice with depth as the density changed. Reynolds [1985] made further observations linking firn density to the high frequency conductivity of polar ice, although the chemical content of the samples was only considered qualitatively. No one has yet studied the effect of densification on the conductivity of ice with a varying chemical composition.

This chapter considers the chemical and electrical DEP data gathered from the Dome C core (74°39'S, 124°10'E, elevation: 3240m and mean annual temperature: -53.5°C), drilled during 1998 and 1999, by the European Project for Ice Coring in Antarctica (EPICA). Calculated sulphuric acid and hydrochloric acid records for the top 350 m metres of the core are presented and used, with the sodium record, to find the electrical response of the DEP to those species in solid ice. The conductivity coefficients are compared with previous calibrations from a variety of polar sites. The variation of the conductivity with density will be examined and compared with empirical and theoretical models. The conductivity coefficient of sulphuric acid as a function of volume fraction is also presented and compared with the predictions of various models for conduction.

IV.2. Methods

IV.2.1. Data

The conductivity data from the core were gathered using the DEP technique with a resolution of 2 cm at 100 kHz, and temperature corrected to -15°C [*Wolff et al.*, 1999]. Wolff et al. [1999] found that the 100 kHz conductivity value is within 1-2 % of the high frequency conductivity value of ice, σ_∞, and is here used as an approximation to σ_∞. The chloride and sulphate data were gathered by means of a rapid ion chromatography method used in the field; the

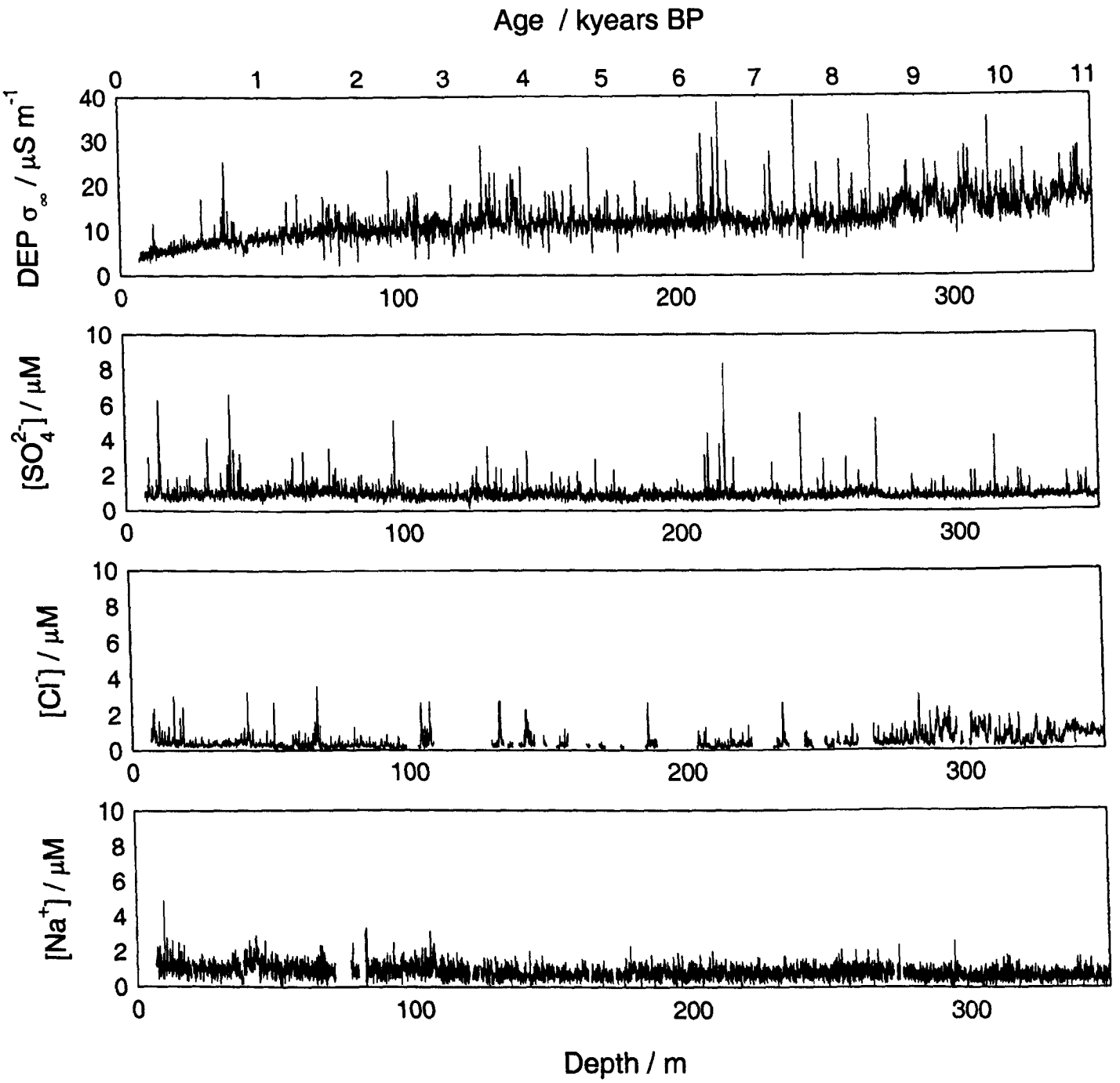

Figure IV.1. The raw data from the Dome C ice core used for the investigation. **(a)** The high frequency conductivity, σ_∞, measured using the DEP technique at 100 kHz (within 2 % of σ_∞) and corrected to -15°C. **(b)** and **(c)**, the sulphate and chloride concentrations of the core measured using ion chromatography, sample resolution between 7 and 3 cm; and **(d)** the sodium concentration measured using a spectrophotometric method plotted at 2 cm mean values.

sample resolution was increased from ~ 7 to 3 cm of ice with depth [*Udisti et al.*, 2000]. The sodium data were collected from continuous flow analysis [*Röthlisberger et al.*, 2000]. The density measurements were made along the length of a 120 m satellite core in close proximity to the main bore hole by weighing samples of a known volume, and the standard error of these measurements is estimated at 2%.

For the purposes of this chapter, the top 350 m of core were studied, a section originating from the Holocene period. The age of the ice at 350 m is 11,000 years [*Schwander et al.*, 2001]. Dome C is situated on the East Antarctic plateau, a site that is around 1000 km from the coast. The large distance of the site from the sea, and from any vegetation, means that both sea salt and ammonium have low concentrations in the ice relative to coastal sites. It is known that using the DEP method, the conductivity responds to both acid and non-acidic components in ice [*Moore et al.*, 1992]. Due to the low concentrations of sea salts (figure IV.1) and ammonium [*Röthlisberger et al.*, 2000] the conductivity at Dome C is dominated by the presence of atmospherically derived acids in the ice. This should allow the comparison between conductivity and the acid without significant interference from non-acidic components. It is also in this top section of the core that the most significant changes in density occur.

Figure IV.1 shows the raw data used for the investigation; gaps exist in the sodium and chloride data. On preliminary inspection there is clearly a close relationship between the sulphate and conductivity levels. The majority of significant peaks from both series occur at the same depths. There is also a noticeable correspondence between chloride peaks and some of the high conductivity levels below 100 m and particularly in the section of core below 270 m. The other obvious feature is the increase of the background level of the conductivity with depth, whilst the background sulphate level remains approximately constant. The correlation between sodium levels and conductivity is less clear. Udisti et al. [2000] discuss the chemical and electrical signatures of the core in more detail. The electrical and sodium data were linearly interpolated to the depth of the sulphate and chloride points which were of a lower spatial resolution.

IV.2.2. Calculating the acidic components

Acidity itself (H^+) has not been directly measured on the Dome C ice core. Additionally, there is some evidence that the DEP response to acidity has some dependence on the specific anions present, possibly because the acid may be partly un-dissociated [*Moore and Fujita*, 1993; *Wolff and Paren*, 1984]. As a result, we need to calculate acidity, accounting for each acid separately. The following method for determining the acidic concentrations is outlined by Legrand and Delmas [1988]. The method does not take into account every chemical species present in the core, but uses only the most significant of those which have been measured. Any errors in the calculated values are carried over into the subsequent statistical analysis. Elements or compounds enclosed by square brackets in the equations below denote the concentration in the meltwater in

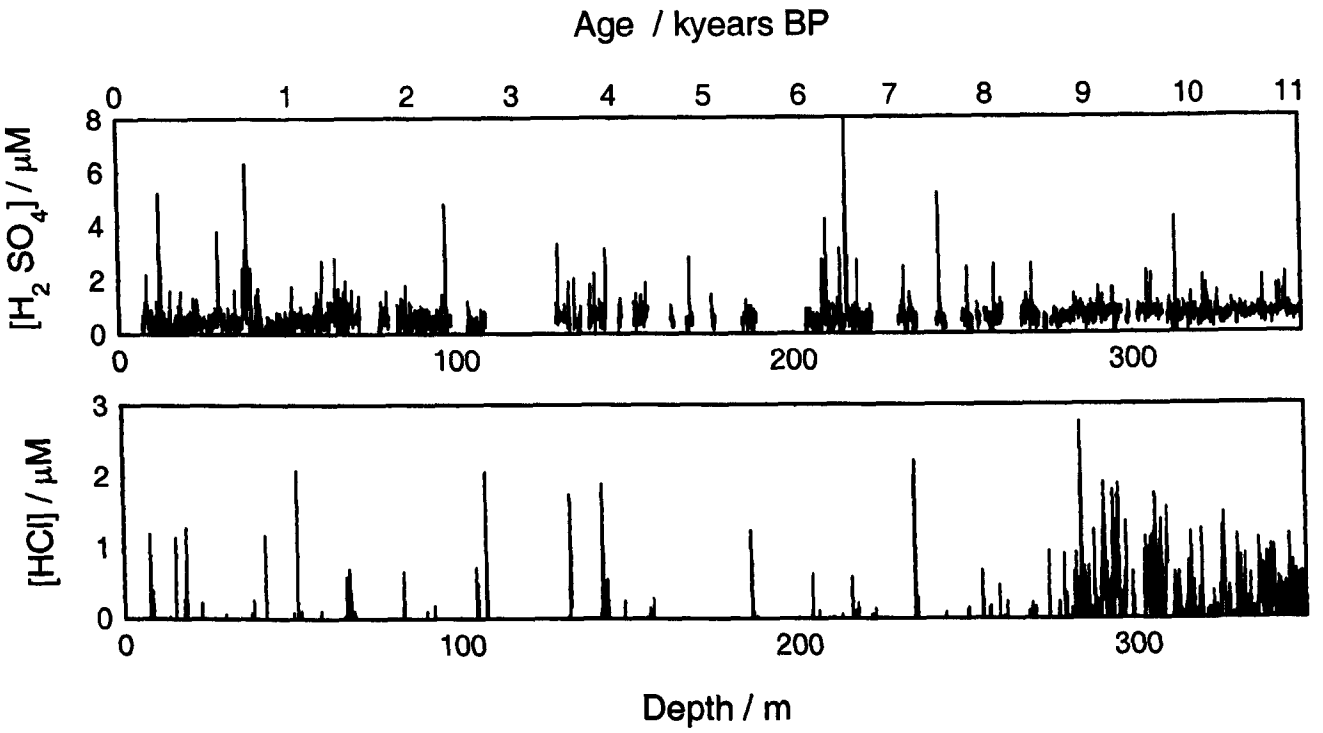

Figure IV.2. The calculated concentrations of (**a**) sulphuric acid and (**b**) hydrochloric acid, found using (IV.4) and (IV.2).

μM. Chloride and sulphate ions derived from sea salts are considered to be in fixed ratios to the quantity of sodium ions in the core. This is because the only significant source of sodium in this section of the Dome C core is from sea salt, which has a known ionic composition. The chloride, which is not accounted for by sea salt, is known as excess chloride, $xsCl^-$, and is calculated as follows using standard mean ocean water ratios:

$$[xsCl^-] = [Cl^-] - 1.165[Na^+] \qquad \text{(IV.1)}$$

$xsCl^-$ can have either positive or negative values; if the value is positive then the concentration of chloride not accounted for by sea salt may be assumed to be of an acidic form. If the value of $xsCl^-$ is negative, all chloride present in that sample must be considered salty, and the concentration of hydrochloric acid must be taken as zero:

$$[HCl] = \begin{cases} [xsCl^-] & [xsCl^-] > 0 \\ 0 & [xsCl^-] \leq 0 \end{cases} \qquad \text{(IV.2)}$$

A similar argument is used to find the find the excess sulphate, $xsSO_4^{2-}$, although this value is seldom negative because of the relatively high concentration of sulphuric acid compared to sea salt in the core.

$$[xsSO_4^{2-}] = [SO_4^{2-}] - 0.12[Na^+] \qquad \text{(IV.3)}$$

If the value of $xsCl^-$ is negative then there is a positive excess of Na^+ ions. This is a result of the reaction $2NaCl + H_2SO_4 \rightleftharpoons 2HCl + Na_2SO_4$, in the case where the Na_2SO_4, but not the HCl, is present in the ice core, possibly due to loss of HCl either during or after deposition. The negative $xsCl^-$ is balanced by positive $xsSO_4^{2-}$, and therefore the acidic sulphate is calculated by adding the (negative) $xsCl^-$ to the xs SO_4^{2-}:

$$[H_2SO_4] = \begin{cases} [xsSO_4^{2-}] & [xsCl^-] \geq 0 \\ [xsSO_4^{2-}] + \frac{1}{2}[xsCl^-] & [xsCl^-] < 0 \\ 0 & [xsSO_4^{2-}] + \frac{1}{2}[xsCl^-] < 0 \end{cases} \quad \text{(IV.4)}$$

Nitrate will also play a role in neutralising negative excesses of chloride and sulphate. However since the concentration of nitrate in this section of core is low, $[NO_3^-]_{mean} = 0.23$ μM, and the data are less complete than for the other variables its effects here are ignored. Note that H_2SO_4 is calculated in μM, and would contain two acid ions if fully dissociated while HCl has only one.

The calculated values of HCl and H_2SO_4 can be seen in figure IV.2, for the sections where data are available. The background trend of H_2SO_4 is approximately constant and the mean is $[H_2SO_4]_{mean} = 0.63$ μM compared to that of the total sulphate $[SO_4^{2-}]_{mean} = 0.97$ μM. The background level of HCl is generally zero for the top 270 m of the core, punctuated by sharp acidic peaks which correspond to volcanic eruptions. Beyond 270 m there is a marked increase in the concentration of HCl in the core. The concentration jumps by almost an order of magnitude from $[HCl]_{mean(0\text{-}270m)} = 0.03$ μM to $[HCl]_{mean(270\text{-}350m)} = 0.24$ μM. However the majority of the chloride in

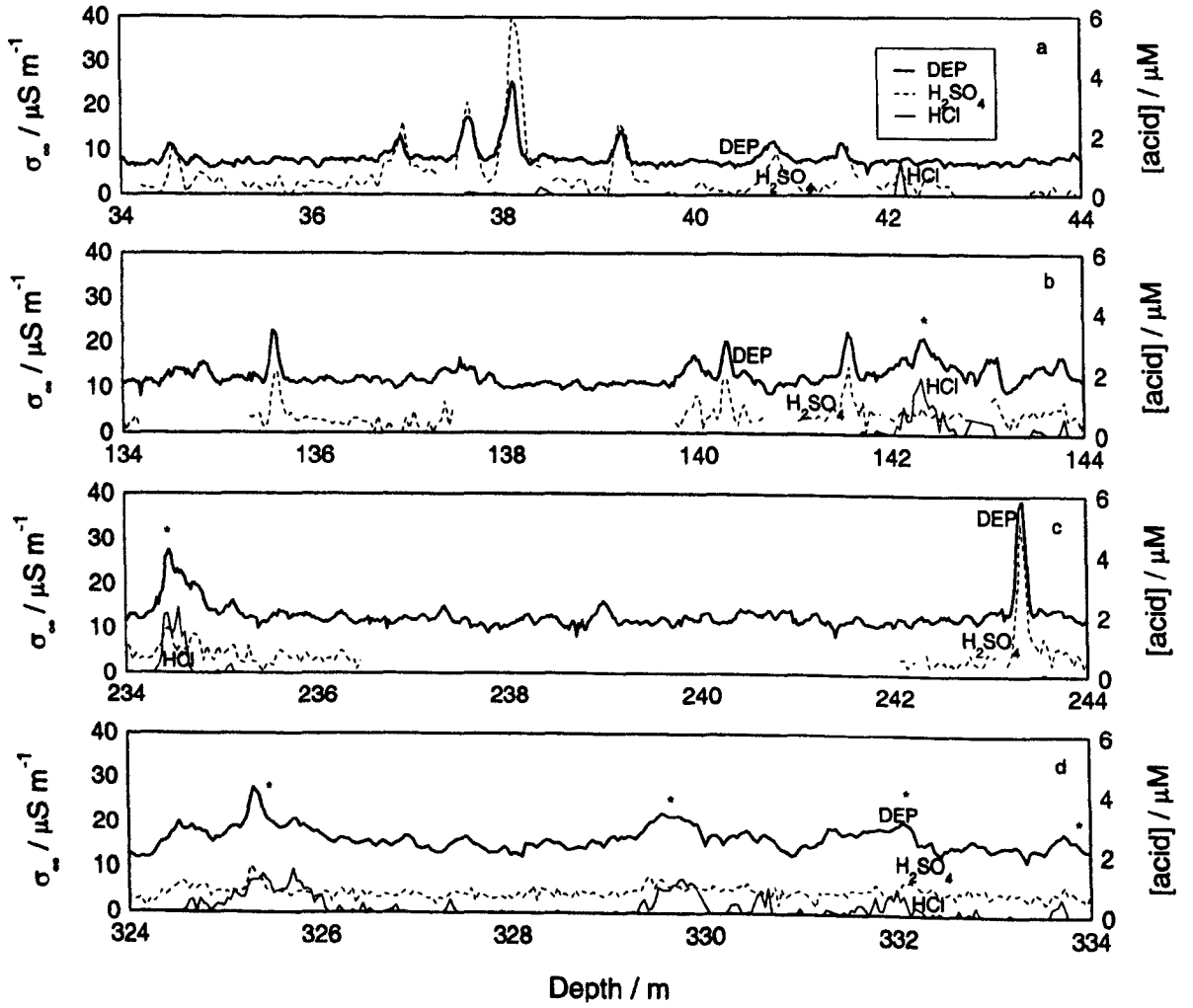

Figure IV.3. Detailed sections of σ_e with $[H_2SO_4]$ and [HCl] at depths **(a)** 34 - 44 m, **(b)** 134 -144 m, **(c)** 234 - 244 m and **(d)** 324 - 334 m. The blank sections indicate that data are missing from the profile. Correlation may be seen between the majority of the chemical and electrical peaks. DEP peaks marked with a * are examples of an electrical response to hydrochloric acid.

the core is still salty since $[Cl^-]_{mean(0\text{-}270m)} = 0.38$ μM and $[Cl^-]_{mean(270\text{-}350m)} = 0.79$ μM.

The connection between the conductivity and acidity can be seen more closely in figure IV.3 at a series of 10 m sections down the core. While most peaks in σ_∞ correspond to $[H_2SO_4]$, a few also respond to [HCl].

IV.2.3. Core density

The latter parts of this chapter are concerned with the impact of density on conductivity. The density profile and hence volume fraction of ice, v, were determined by fitting the density model proposed by Robin [1958] to density measurements (figure IV.4a). The model, used by Herron and Langway [1980], is based on the proportional change in air space being linearly related to the change in stress due to overlying snow, and is of the form:

$$\frac{d\rho}{\rho_i - \rho} \propto \rho \, dz_{firn} \qquad \text{(IV.5)}$$

There ρ is the density of the firn and ρ_{ice} is the density of solid ice (917 kg m^{-3}). This implies that there is a linear relationship between $\ln[\rho / (\rho_{ice} - \rho)]$ and depth, z_{firn}, so we can predict the density, $\rho_{predicted}$, using:

$$\rho_{predicted} = \frac{\rho_{ice}}{1 + e^{-(gz_{firn}+b)}} \qquad g = \begin{cases} g_1 \\ g_2 \end{cases} \text{ and } c = \begin{cases} b_1 & \text{above critical depth} \\ b_2 & \text{below critical depth} \end{cases} \qquad \text{(IV.6)}$$

where g and b are constants found by least squares fitting, see figure IV.4b. Three stages of densification were identified by Herron and Langway [1980]; initially a settling and packing of

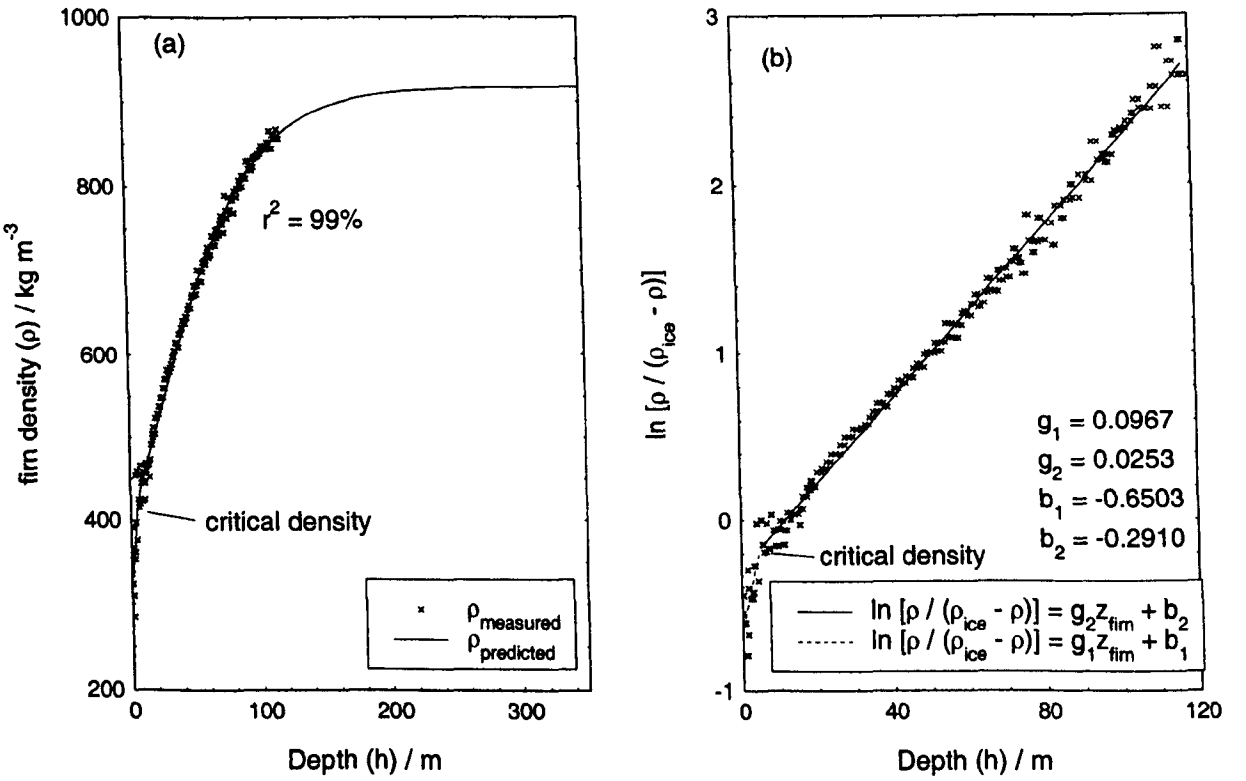

Figure IV.4. **(a)** Core density against depth for satellite core in close proximity to the main Dome C core. Points give measured density profile, solid line gives predicted density using (IV.6). **(b)** ln [ρ / (ρ_{ice} - ρ] against depth, solid lines fitted using least squares to give coefficients g_1, g_2, b_1 and b_2 used in (IV.6).

grains in the upper layers of snow leading to rapid densification down to a critical depth. Below this level the density increases more slowly leading to the closing off of interconnecting air ways and further densification continues with the compression of the air bubbles formed after close off. Figure IV.4b shows that the first two stages can clearly be identified with densification taking place at different rates. The critical depth occurs at 5 m in this core, which corresponds to a density of 421 kg m^{-3} and a volume fraction of 0.46. It is interesting to note that this critical density is considerably lower than the value proposed by Benson [1962] which was around 550 kg m^{-3} corresponding to a volume fraction of 0.6 which has been found to occur at many other polar sites and is agreement with laboratory packing experiments [*Anderson and Benson*, 1963; *Herron and Langway*, 1980]. We will not here attempt to explain this discrepancy. The pore close off depth at Dome C is at around 100 m and the second fitted line in figure IV.4b passes through the close off depth and continues to fit the data well. It is therefore considered that the values of m and c found from this line are adequate to describe the densification beyond the close off depth. The fit is good, $r^2 = 0.99$, between measured and predicted density and equation 6 has therefore been used to both interpolate and extrapolate values of density for a given depth. Knowing $\rho_{predicted}$, the fractional volume of ice to bulk volume, v, may easily be found from $v = \rho_{predicted} / \rho_{ice}$.

IV.3. The chemical electrical relationship in the deeper ice

IV.3.1. Conductivity mechanisms

The complex quantity of admittance, $Y(\omega)$, can be used to describe the polarisation or susceptibility of an ice lattice under the influence of an alternating electric field of angular frequency ω. Y(ω) may be written in terms of the conductance $G(\omega)$ of the ice and its capacitance $C(\omega)$ [*Petrenko and Whitworth*, 1999]:

$$Y(\omega) = G(\omega) + i\omega\, C(\omega) \qquad \text{(IV.7)}$$

$G(\omega)$ corresponds to the real part of the complex conductivity, $\sigma'(\omega)$. At high frequencies (microwave) the value of $\sigma'(\omega)$ reaches a plateau which is estimated by the DEP as σ_∞. $C(\omega)$ corresponds to the real part of the relative permittivity of ice.

Jaccard theory [1964] is often used to describe conduction mechanisms in an ice crystal. Conduction takes place by the movement of protons through the crystal lattice under the influence of the electric field; this is allowed by the existence of lattice defects. The concentration of the defects in the ice is dependent on temperature but may be greatly increased by the introduction of a dopant into the lattice, creating what are known as ionic and Bjerrum defects.

Without the use of specially adapted electrodes, conduction by the movement of defects quickly stops under a static electric field as the material becomes fully polarised. Direct current measurements such as the ECM technique only detect a current when traces of acid are present in

the core, and similar quantities of salts do not produce a response. The dc response to acid is now commonly thought to be because the majority of the acid is not incorporated into the lattice but is situated outside the ice grains conducting through the liquid phase [*Wolff et al.*, 1997]. The presence of an ECM signal across single crystals from the GRIP core [*Taylor et al.*, 1997] challenges this but can be explained by assuming the presence of an acidic liquid on the exposed surface of the grains. Alternating current measurements such as the DEP technique respond to the presence of both acids and salts. The response to salts can be explained if chloride ions are viewed as being incorporated directly into the ice lattice; their inclusion and the subsequent production of Bjerrum defects changes the dielectric constant of the ice matrix and hence its conductivity. If dc conduction takes place through acids in the liquid phase, it is likely that the contribution of acids to σ_∞ also occurs through the liquid phase [*Wolff et al.*, 1997]. In the latter parts of this chapter we therefore test the application of dc conduction models to the acidic component of σ_∞.

IV.3.2. Relationship between σ_∞ and chemistry

In this section we establish the relationship between the different chemical components of the deeper 'solid' ice and σ_∞, regardless of the conductivity mechanism. In addition to the pure ice component, $\sigma_{\infty pure}$, the concentration of chemical impurities contribute linearly to σ_∞:

$$\sigma_\infty = \sigma_{\infty\,pure} + \beta_{H2SO4}[H_2SO_4] + \beta_{HCl}[HCl] + \beta_{Na}[Na^+] \qquad \text{(IV.8)}$$

β refers to a conductivity coefficient or molar conductivity of a particular species indicated in subscript. The largest source of acid in the core is sulphuric acid (figure IV.2). Hydrochloric acid contributes more significantly at depths below 270 m than above. The density of the ice below 200 m is within 2% of the density of solid ice, $\nu \geq 0.98$ (figure IV.4). For the purposes of determining the relationship between the chemistry and conductivity for solid ice, the density of the core between 200 - 350 m to a first approximation will be considered to be that of solid ice ($\nu = 1$).

Linear least squares regressions were performed between σ_∞ and $[H_2SO_4]$, [HCl] and $[Na^+]$, over the sections 200 - 270 m and 270 - 350 m, containing 985 and 1839 sets of points respectively. There was some correlation between the chemical species: a negative correlation was noticed between the sodium and the other two species due to the role of sodium in calculating the acid values. The correlation coefficients were: $r([H_2SO_4],[HCl]) = 0.18$, $r([H_2SO_4],[Na^+]) = -0.35$ and $r([HCl],[Na^+]) = -0.29$. However for the purposes of the subsequent regression analysis, the three variables will be treated as independent. Table IV.1 summarises the different combinations of variables tested.

$[H_2SO_4]$ was clearly found to be the most significant predictor variable, giving r^2 statistics of 70.4 % for the region 200 - 270 m which contained low HCl levels, and 43.3 % for the section 270 - 350 m containing a higher proportion of HCl. Regressions where the predictor variables excluded $[H_2SO_4]$, gave very poor fits and were not significant. All the regression models shown in table IV.1 show high F_{MS} values (the ratio of regression to residual mean squares) well beyond

Table IV.1. Molar conductivities from regression analysis for solid ice[a].

Parameter	Depth: 200-270m Data points 985 Value	SE	Depth: 270-350m Data points 1839 Value	SE
Model 1: $\sigma_\infty = \sigma_{\infty pure} + \beta_{H2SO4}[H_2SO_4]$				
$\sigma_{\infty pure}$, μS m^{-1}	10.09	0.09	11.77	0.14
β_{H2SO4}	4.86	0.1	6.7	0.18
r^2, %	70.4		43.3	
RSD, μS m^{-1}	1.80		2.12	
$MS_{reg} / MS_{res} = F_{MS}$	2340		1403	
Model 2: $\sigma_\infty = \sigma_{\infty pure} + \beta_{H2SO4}[H_2SO_4] + \beta_{HCl}[HCl]$				
$\sigma_{\infty pure}$, μS m^{-1}	10.08	0.08	11.7	0.11
β_{H2SO4}	4.72	0.09	5.67	0.15
β_{HCl}	4.88	0.34	3.47	0.11
r^2, %	75.5		62.4	
RSD, μS m^{-1}	1.63		1.73	
$MS_{reg} / MS_{res} = F_{MS}$	1516		1523	
Model 3: $\sigma_\infty = \sigma_{\infty pure} + \beta_{H2SO4}[H_2SO_4] + \beta_{HCl}[HCl] + \beta_{Na}[Na^+]$				
$\sigma_{\infty pure}$, μS m^{-1}	8.7	0.17	9.14	0.17
β_{H2SO4}	4.88	0.09	6.28	0.14
β_{HCl}	5.17	0.33	4.06	0.11
β_{Na}	1.59	0.17	2.58	0.15
r^2, %	77.5		67.3	
RSD, μS m^{-1}	1.56		1.61	
$MS_{reg} / MS_{res} = F_{MS}$	1129		1261	

[a]Summary of linear regressions performed on Dome C sections 200-270 m and 270-350 m, data corrected to -15°C. β_{H2SO4} is the regression coefficient for sulphuric acid, β_{HCl} is the coefficient for hydrochloric acid, β_{Na} is the coefficient for sodium, SE is the standard error, RSD is the residual standard deviation of the regression and F_{MS} is the ratio of the regression mean square to the residual mean square.

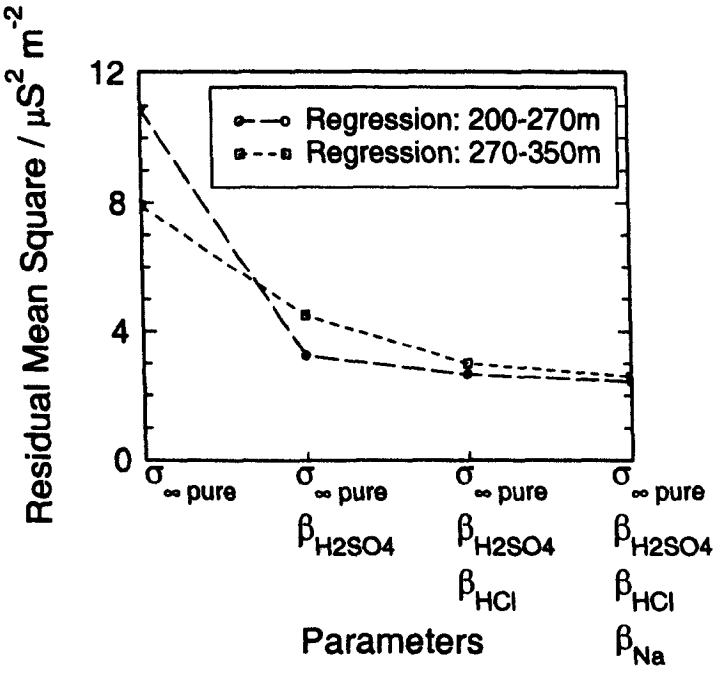

Figure IV.5. Residual mean square of regression against number of regression parameters. The Error tails off with increasing parameter number.

the 99% significance level of $F_{MS} \approx 4 - 6$, indicating statistical likelihood of the predictor variables influencing the response variable.

To assess the value of complicating the regression model of σ_∞ against H_2SO_4 by including the additional predictors of HCl and Na^+, it is useful to consider the residual mean square (MS_{res}) of the different models [*Draper and Smith*, 1998]. The residual mean square is the square of the residual standard deviation (RSD) which is the standard deviation of the difference between the actual value and that predicted by the model; the lower the value the better the model. Figure IV.5 shows the MS_{res} against the number of predictor variables or parameters used in the models. The first variable is known as a dummy variable, and corresponds to the mean value of the response variable in a model with only one parameter. We state arbitrarily that for an additional parameter to be worthwhile it must reduce the total MS_{res} by a minimum of 10%. It can be seen that for the section 200-270 m the use of two parameters is sufficient to reduce MS_{res} from 10.9 to 3.2 μS^2 m^{-2} (70%); the addition of a further two variables only reduces MS_{res} to 2.4 (a further 7.5% reduction), hence we quote model 1

from table IV.1 to describe this section of core:

$$\sigma_\infty = 10.1 + 4.9\,[H_2SO_4] \qquad \text{(IV.9)}$$

$r^2 = 70.4\%$ RSD = 1.80 μS m^{-1}

where σ_∞ is in μS m^{-1}. For the section 270-350 m, the MS_{res} is reduced from 7.9 to 3.0 $\mu S^2\ m^{-2}$ by changing from a one to a three parameter model (43% followed by 19% reductions in MS_{res}), while the addition of a fourth parameter (Na^+) only gives a slight improvement of MS_{res} to 2.6 $\mu S^2\ m^{-2}$ (a 5.3% reduction). Model 2 is chosen to describe the section:

$$\sigma_\infty = 11.7 + 5.7\,[H_2SO_4] + 3.5\,[HCl] \qquad \text{(IV.10)}$$

$r^2 = 62.4\%$ RSD = 1.73 μS m^{-1}

A regression covering both sections gave the following results including all three predictor variables:

$$\sigma_\infty = 9.8 + 5.4\,[H_2SO_4] + 5.1\,[HCl] + 1.5\,[Na^+] \qquad \text{(IV.11)}$$

$r^2 = 68.1\%$ RSD = 1.93 μS m^{-1}

IV.3.3. Comparison of coefficients with previous work

Coefficients have been determined previously for a number of sites both in Greenland (Greenland Ice Coring Project - GRIP and Site G) and Antarctica (Dolleman Island). Generally the acidity part of the relationship has been expressed in terms of a single $[H^+]$ concentration, which has been estimated in various ways, making it hard to make direct comparisons. However Table IV.2 shows a summary of conductivity coefficients previously obtained which may be compared with those found in Table IV.1. All values considered in the tables and in the subsequent discussion have been corrected to a temperature of -15 °C

IV.3.3.1. Pure ice conductivity. The pure ice components are generally slightly higher than the accepted value found by Camplin et. al. of $\sigma_{\infty pure}$ = 9 μS m^{-1} [1978]. In the case of models containing fewer variables than significant chemical species this can be explained by the constant term also including responses from variables not measured. For GRIP, Site G, and Dome C, where acidity dominates the chemical response, the pure ice values all lie around 10 - 12 μS m^{-1} with the exception of one shallow GRIP calibration which lies at 14.9 μS m^{-1} (table IV.2).

IV.3.3.2. Acidic conductivity coefficients. The coefficients for H_2SO_4 and HCl, β_{H2SO4} and β_{HCl}, are somewhat higher than those derived from a theoretical conductivity model [*Wolff and Paren*, 1984]; they could be consistent with the model if part of the conduction occurs along two grain boundaries in films as well as three grain boundary veins. This is because their model contains a geometric factor of 1/3 to describe conduction paths through liquid existing in randomly orientated veins, and this factor would increase towards 2/3 in the case where some of the liquid also exists in sheets at two grain boundaries. If all the liquid existed at two grain boundaries then the coefficients expected would be double those quoted in table IV.2: β_{H2SO4} = 7.96 S m^{-1} M^{-1} and β_{HCl} = 6.48 S m^{-1} M^{-1}, higher than the values measured here. The coefficients for

Table IV.2. Molar Conductivities, used in experimental DEP calibration[a].

	Depth (m)	Data Description	Model	Reference
Theoretical conductivity model		$\sigma_\infty = 1/3\, f\, \sigma_{solution} + \sigma_{other\ terms}$. f = volume fraction of solution. The factor of 1/3 describes liquid existing in veins	$\sigma_\infty = 3.98\ [H_2SO_4]$ + other terms $\sigma_\infty = 3.24\ [HCl]$ + other terms $\sigma_\infty = 3.52\ [HNO_3]$ + other terms	Wolff and Paren, 1984
Dolleman Island, Antarctica	26 – 71	number of samples ~ 800 Density corrected by Looyenga's equation (IV.13a) [salt] = 1.05 ($[Na^+]$ + $[Mg^{2+}]$) [acid] = $[Cl^-]$ + $[SO_4^{2-}]$* + $[NO_3^-]$ - [salt] $[SO_4^{2-}]$* measured in $\mu Eq\ l^{-1}$	$\sigma_\infty = 19 + 2.0$ [acid] + 0.49 [salt] Acid coefficient appears low since the majority of acid in core is H_2SO_4 and likely to be singly dissociated.	Moore *et al.*, 1989
		$[H^+*]$ calculated using only single proton dissociation of H_2SO_4 component [sea salt Cl^-] calculated from standard mean ocean water ratios	σ_∞ = const + 3.6 $[H^+*]$ + 0.55 [sea salt Cl^-] 0.55 [sea salt Cl^-] ~ 0.64 $[Na^+]$ ($[Cl^-]/[Na^+]$ in seawater = 1.165)	Moore and Fujita, 1993
Site G, Greenland	68.75 – 69.85 Laki eruption	number of samples ~ 44 $[H^+]$ calibrated using ECM, and tested against acid titration values	$\sigma_\infty = 10.7 + 2.6\ [H^+]$ or	Moore *et al.*, 1992
		$[H_2SO_4]$ calculated from $[H^+]$ (see above) considering only a single proton dissociation	$\sigma_\infty = 10.7 + 5.2\ [H_2SO_4]$	Moore and Fujita, 1993
GRIP, Greenland	1625 - 1660	NH_4 peaks	$\sigma_\infty = 1.0\ [NH_4^+]$ + other terms	Moore *et al.*, 1994
	250 - 270	$[H^+]$ calculated by ECM calibration	$\sigma_\infty = 14.9 + 3.74\ [H^+]$	
	770 - 790		$\sigma_\infty = 10.7 + 5.25\ [H^+]$	
	2370 - 2410		$\sigma_\infty = 11.8 + 4.51\ [H^+]$	
	2800 - 2840		$\sigma_\infty = 11.3 + 4.67\ [H^+]$	
Combination of Sites		GRIP records for $[H^+]$ and $[NH_4^+]$, Dolleman Island for $[Cl^-]$ and [*Camplin et al.*, 1978] for $\sigma_{\infty\ pure}$	$\sigma_\infty = 9 + 4\ [H^+] + 1\ [NH_4] + 0.55\ [Cl^-]$	Wolff *et al.*, 1995

[a]All values are temperature corrected to -15°C using the following activation energies, E_{H2SO4} = 0.29 eV, E_{HCl} = 0.25 eV, E_{HNO3} = 0.26 eV [*Wolff and Paren*, 1984], E_{acid} = 0.27 eV, E_{salt} = 0.19 eV, $E_{pure\ ice}$ = 0.5 eV [*Miners*, 1998]. Concentrations are in μM^{-1} unless otherwise stated and coefficients in $Sm^{-1}M^{-1}$.

H_2SO_4 are a little higher than those for HCl (except in the case of model 3, table IV.1, between 200 and 270 m where the coefficients are not significantly different), particularly in the deeper 270 - 350 m section containing higher HCl concentrations. The differences however are certainly not a factor of two, which is consistent with the idea of only one conducting proton being available from each H_2SO_4 molecule.

For the sites where calibrations have been attempted before, both Dolleman Island and Site G (Laki eruption) are cores in which sulphuric acid, particularly in the peaks, dominates the contribution to the conductivity. Therefore, the relevant coefficients for comparison are those of: β_{H2SO4} = 4 (Dolleman), 5.2 (Site G), 4.9 and 5.7 S m^{-1} M^{-1} for the two sections at Dome C. For

GRIP, nitric acid dominates the background, and sulphuric acid dominates the major peaks [*Moore et al.*, 1994]. The acidity used in the GRIP calibration was based on ECM data which had themselves been calibrated against a few chemical data, so that there is considerable uncertainty. Since the GRIP DEP acid calibrations are based on many data points not dominated by the volcanic peaks, they probably would correspond best to [HNO_3]. We have no estimate of an HNO_3 coefficient for Dome C, but the GRIP values between 3.74 and 5.25 S m^{-1} M^{-1} are anyway close to those we have derived for the other coefficients.

In summary, calibrations for four sites (coastal Antarctic, central Antarctic and central Greenland) for very different time periods all yield coefficients between about 4 and 5.5 S m^{-1} M^{-1} for acidity, with the differences probably at least in part accounted for by differences in the nature of the associated anion, and by errors in the acidity estimate or temperature correction. This suggests that the same conduction mechanisms are at work at these very widely separated sites.

IV.3.3.3. Salt conductivity coefficients. The salt coefficient for [Na^+] at Dome C is significantly higher than the coefficient found at Dolleman Island; the term 0.55 [sea salt Cl^-] corresponds to a value of 0.64 [Na^+] [*Moore and Fujita*, 1993]. This is more than a factor of two times smaller than the coefficient found for the 200 - 350 m section of the Dome C core (IV.11), 1.5 [Na^+] which equates to 1.3 [sea salt Cl^-]. Although the value of the coefficient is statistically significant, it has little impact on the prediction of conductivity, and cannot be considered well established because [Na^+] is anti-correlated to the other acidic species. It is also possible that the Na^+ ions measured in the core could be correlated to an unmeasured ionic species to which the DEP responds.

The incorporation of Cl^- ions from salts into the ice lattice are not thought to produce ionic defects since no DC conduction is observed in ECM records due to sea salt chloride [*Wolff et al.*, 1997]; they do however produce Bjerrum L-defects. For each Cl^- incorporated in the lattice, we would expect the formation of two L-defects where previously two hydrogen bonds would have been associated with the oxygen of a water molecule. The chloride conductivity attributed to these defects is then given by [*Jaccard*, 1964]:

$$\sigma_{\infty Cl} = n_L \mu_L |e_L| \qquad \text{(IV.12)}$$

where n_L is the concentration of L-defects, e_L is the charge on an L-defect and μ_L is its mobility. The charge e_L is given as e_L = -0.37e where $e = 1.6 \times 10^{-19}$ C and at -15°C μ_L is 1.5 - 2.4 × 10^{-8} m^2 V^{-1} s^{-1} [*Petrenko*, 1993]. By substituting the molar conductivity, β_{Cl}, for $\sigma_{\infty Cl}$ in equation 8, the actual number of L-defects per chloride ion can be found from β_{Cl} / (1000 N_A μ_L $|e_L|$), where N_A is Avogadro's number. At Dolleman Island where β_{Cl} = 0.55 S m^{-1} M^{-1} we find 0.6 - 1.0 L-defects per chloride ion present in the core. These values are lower than the 2 L-defects per ion expected, suggesting that a proportion of the Cl^- ions have not entered the lattice. The proportion of Cl^- ions incorporated in the lattice could be dependent on the age of the ice, the surface area of ice in contact with salt ions and the phase in which the ions exist.

The conductivity coefficient for sea salt chloride for Dome C is here found to be much higher than that at Dolleman. The value of $\beta_{Cl} = 1.3$ S m^{-1} M^{-1} using the arguments outlined above corresponds to a ratio of 1.5 - 2.4 L-defects per chloride ion, suggesting that sea salt chloride is almost completely incorporated into the lattice in the section measured. This would be more consistent with the conductivity mechanism for NH_4^+ ions in the GRIP core where by similar arguments the ratio of NH_4^+ ions to Bjerrum D-defects was found to be between 1.3 - 2.0 which was in agreement with Jaccard theory if the NH_4^+ ions were almost completely incorporated into the ice. There could be more chlorine in the lattice at Dome C than Dolleman island because the lower temperature and a longer equilibration time.

IV.4. Conductivity response to variation with density

In the following sections we address a situation where the density of the ice core no longer remains constant, and we use a model where the variation with v of the pure ice and impurity components of the conductivity $\sigma_\infty(v)$ are treated separately:

$$\sigma_\infty(v) = \sigma_{\infty\,pure}(v) + \beta_{H2SO4}(v)[H_2SO_4] \qquad \text{(IV.13)}$$

In this case we limit the model to a contribution from the most dominant impurity H_2SO_4. Mechanisms by which both the pure and chemical components vary are tested against the measured results.

IV.4.2. Pure ice conductivity models

The models describing the permittivity of a dielectric mixture proposed by Looyenga and Böttcher [*Beek*, 1967] consider one dielectric forming spherical inclusions in the other. They were applied to ice to predict the high frequency conductivity of chemically pure firn, $\sigma_{\infty\,pure}(v)$ [*Glen and Paren*, 1975]. Depending on whether we are considering high density ice or low density firn, the inclusions may either be viewed as bubbles of air in ice or spheres of ice in air. If ε is the relative permittivity of the mixture and ε_1 and ε_2 are the relative permittivities of the two components in the mixture, then Looyenga's model is written:

$$\varepsilon^{1/3} - \varepsilon_1^{1/3} = v(\varepsilon_2^{1/3} - \varepsilon_1^{1/3}) \qquad \text{(IV.14)}$$

and Böttcher's:

$$\frac{\varepsilon - \varepsilon_1}{3\varepsilon} = \frac{v(\varepsilon_2 - \varepsilon_1)}{\varepsilon_2 + 2\varepsilon} \qquad \text{(IV.15)}$$

where v is the volume fraction of ε_2. Since the equations are symmetrical between the two phases they are suitable for describing the permittivity from low density firn through to solid ice. ε_1 can be set to 1 since part of the mixture is air and $\varepsilon_2 = \varepsilon_{\infty\,pure}$ since the other part is ice where $\varepsilon_{\infty\,pure} = 3.17$. From Looyenga's equation (IV.14), the high frequency conductivity of the mixture, $\sigma_{\infty\,Loo}(v)$,

can then be found by taking the imaginary part of ε giving an approximation to $\sigma_{\infty\ pure}(\nu)$ [*Glen and Paren*, 1975]:

$$\sigma_{\infty\ pure}(\nu) \approx \sigma_{\infty\ Loo}(\nu) = \sigma_{\infty\ pure}(1)\ \nu(0.68 + 0.32\nu)^2 \qquad \text{(IV.16)}$$

$\sigma_{\infty\ pure}(\nu)$ can also be approximated from Böttcher's equation numerically making the same substitutions to give $\sigma_{\infty\ Böt}(\nu)$. Both $\sigma_{\infty\ Loo}(\nu)$ and $\sigma_{\infty\ Böt}(\nu)$ are plotted against depth in figure IV.6a, where ν has been determined from $\rho_{predicted}$, and $\sigma_{\infty\ pure}(1) = 9\ \mu S\ m^{-1}$ [*Camplin et al.*, 1978]. It can be seen that there is not a great deal to choose between the two models, and for the purposes of simplicity only Looyenga's model will be further considered in this chapter.

IV.4.3. Pure ice component of the conductivity

In order to find the contribution of pure ice to σ_∞, the variation due to chemical impurities had to be removed from the data. As discussed earlier, sulphuric acid was found to be by far the most electrically significant impurity in the top 270 m of the core. The pure ice component, $\sigma_{\infty\ pure}(\nu)$, was therefore predicted by the conductivity not due to sulphuric acid and was found by a method of rolling regression. This involved performing a, linear, least squares regression of σ_∞ on $[H_2SO_4^{2-}]$ for the data within 5 m of each point. There were an average of 192 data points per regression giving a line of best fit between $[H_2SO_4]$ and σ_∞. The intercept of this line with the conductivity axis, $\sigma_{\infty\ int}(\nu)$, gave the prediction of $\sigma_{\infty\ pure}(\nu)$. The gradient of the line, $\beta(\nu)$, gave an estimate of the molar conductivity coefficient, $\beta_{H2SO4}(\nu)$, since σ_∞ has been found to be linearly related to acid concentration [*Wolff et al.*, 1997]. The standard error on $\sigma_{\infty\ int}(\nu)$ and $\beta(\nu)$ was calculated for each point in the analysis. Rolling regressions were also performed using all three chemical parameters, $[H_2SO_4]$, [HCl] and $[Na^+]$, however the results showed such large scatter on the HCl and Na^+ coefficients that no conclusion could be drawn.

Figure IV.6a shows $\sigma_{\infty\ int}(\nu)$ against depth and may be compared with the curves $\sigma_{\infty\ Loo}(\nu)$ and $\sigma_{\infty\ Böt}(\nu)$; the form of which are broadly similar in shape although the modeled curves lie more than one standard error below the measured curve for the top 120m of core. The noisy form of this curve is due to local outliers causing a significant impact on the data relationship; the standard error of the intercept is shown by the dashed lines. There is a clear increase in the value of $\sigma_{\infty\ int}(\nu)$ with depth in the core which plateaus to $9.7 \pm 1.6\ \mu S\ m^{-1}$ in the region of 120-270 m. The expected value for pure ice of $\sigma_{\infty\ pure}(1) = 9\ \mu S\ m^{-1}$ [*Wolff et al.*, 1997], and the value predicted by Looyenga's equation, $\sigma_{\infty\ Loo}(0.99) = 8.8\ \mu S\ m^{-1}$ fall with the lower limits of $\sigma_{\infty\ int}(\nu)$ in this range. It is encouraging to note that the value of $\sigma_{\infty\ int}(\nu)$ does not significantly drop below the modeled values of $\sigma_{\infty\ Loo}(\nu)$ and $\sigma_{\infty\ Böt}(\nu)$ at any point along the core, since much of the discrepancy is likely to be from untested or unmeasured species which add a positive contribution to $\sigma_{\infty\ int}(\nu)$.

The residual of the deviation of $\sigma_{\infty\, int}(v)$ from $\sigma_{\infty\, Loo}(v)$ (ie residue = $\sigma_{\infty\, int}(v) - \sigma_{\infty\, Loo}(v)$) is examined in figure IV.6b. In the deeper part of the section, below 270 m the residue can be partially accounted for by the increased HCl levels. We can estimate the contribution of Na^+ to the residue in the solid part of the core using $\beta_{Na} = 1.5$ S m^{-1} M^{-1} (IV.11) since $[Na^+]_{mean\,(200\text{-}350m)} = 0.7 \pm 0.3$ μM which implies that 0.6 - 1.5 μS m^{-1} of $\sigma_{\infty\, int}(v)$ is caused by salt. In the top 110 m of the core $\sigma_{\infty\, int}(v)$ can be seen to be between 1 and 3.5 μS m^{-1} greater than that predicted by Looyenga, lying outside the error range. Given $[Na^+]_{mean\,(0\text{-}110m)} = 1.1 \pm 0.4$ μM, it is likely that sodium is contributing to $\sigma_{\infty\, int}(v)$ although it is difficult to assess its impact for the more porous ice, where the coefficient will be lower than for the solid ice. HCl does not appear responsible for the residue above 110 m so this remains unaccounted for. Since Looyenga's model under-predicts the conductivity of very low density firn near the surface, it must be surmised that: either there is a significant ionic species not identified in this section of core or that the models of Looyenga and Böttcher do not fully describe the pure component of conductivity in shallow ice.

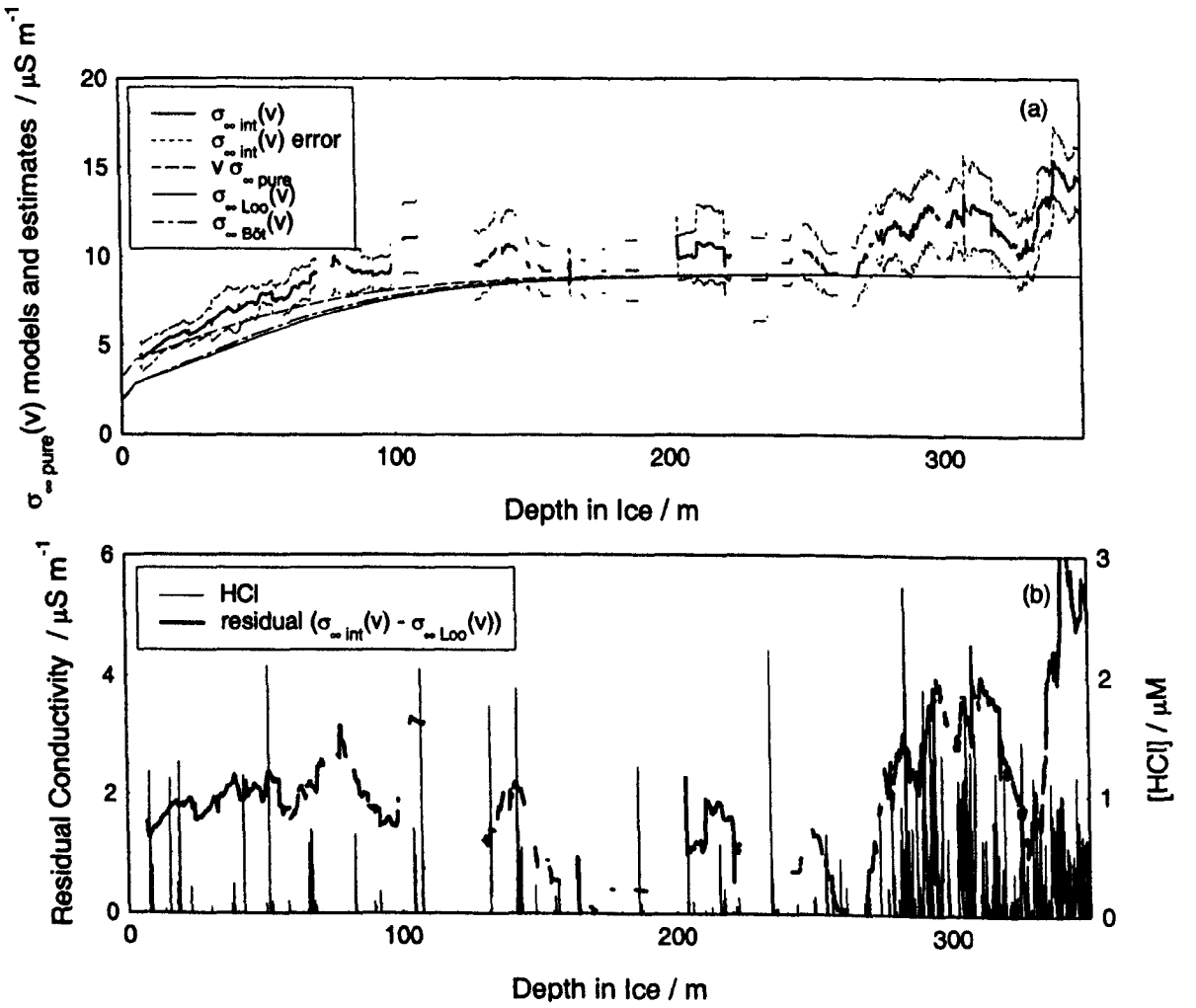

Figure IV.6. **(a)** Estimate of pure ice conductivity, $\sigma_{\infty\, int}(v)$, from rolling regression against depth given by the thick solid line, dotted lines indicate boundary of one residual standard deviation from $\sigma_{\infty\, int}(v)$. Thin solid line gives pure ice conductivity predicted by Looyenga, equation 11, and dot-dashed line gives pure ice conductivity predicted by Böttcher in equation 12. **(b)** Residue of $\sigma_{\infty\, int}(v) - \sigma_{\infty\, Loo}(v)$ against depth (thick line), compared with concentration of HCl in the core (thin line).

Also plotted in figure IV.6a is a curve of $\sigma_{\infty\ pure}(v) = v\ \sigma_{\infty pure}(1)$ where $\sigma_{\infty pure}(1) = 9\ \mu S\ m^{-1}$. This alternative model simply corrects the pure ice component of the conductivity to the volume fraction of ice being measured. Despite no physical basis to choose this as a mechanism for the variation of $\sigma_{\infty pure}(v)$, more of this curve falls within the region of one standard error of $\sigma_{\infty int}(v)$ than the above models, suggesting that other approaches may be better suited to describing the measured data.

IV.4.4. The variation of $\beta(v)$ with v

$\beta(v)$ is the measured conductivity coefficient relating σ_∞ to $[H_2SO_4]$. Figure IV.7a shows $\beta(v)$ against depth; it can be seen that there is even more scatter in these molar conductivities than for $\sigma_{\infty\ int}(v)$ shown in figure IV.6a. This is again predominantly due to the strong effect that high valued data points have on the regression in any 10 m section. The value of $\beta(v)$ may change by up to 2 S m^{-1} M^{-1} in the space of a few metres. Some of the scatter in the points may be related to the other chemistry known to affect conductivity not examined in this work and possibly to variations in ice grain size and fabric, which may alter localized conductivities.

Fluctuations aside there is a clear increasing trend in the value of $\beta(v)$ with depth, and therefore with v. Values of $\beta(v)$ below 270 m can be seen to rise significantly more than expected for the small change in volume fraction at these depths. This is explained by high HCl concentrations in this section of core causing an increase in the DEP signal which is seen in figure IV.7a as an apparent increase in $\beta(v)$. We proceed to examine the dependence of $\beta_{H2SO4}(v)$ on v.

IV.4.4.1. Linear model. During chemical analysis the $[H_2SO_4]$ is measured by volume of melt water, rather than the total volume of firn. The impact of this is that the DEP method is actually responding to an impurity concentration of v $[H_2SO_4]$. Hence one might expect due to this first effect a linear relationship between $\beta(v)$ and volume fraction. However $\beta(v)$ is plotted against volume fraction, v, and depth in figure IV.7 (curve 1), and it is clear that the data are not best described by a straight line but falls off faster than the linear model predicts as density reduces. This implies that another mechanism is better suited to describe the variation.

IV.4.4.2. Looyenga model of conduction. The relationship between high frequency conductivity, σ_∞, and acid concentration has been found to be linear [*Wolff et al.*, 1997]. For direct current conductivity, σ_{dc}, the relationship determined by current calibrations is not linear although this may be due to responses of varying strengths from different acid species in the ice. We can test Looyenga's model employed to describe either a dc or an ac mechanism for the high frequency chemical component of the conductivity, $\beta_{H2SO4}(v)$.

Each of the dielectric components, ε_{air} and ε_{ice}, can be represented by a specific complex admittance y_j of the form (c.f. IV.7):

$$y_j = \sigma_{j dc} + i\omega\varepsilon_0\varepsilon_j \qquad \text{(IV.17)}$$

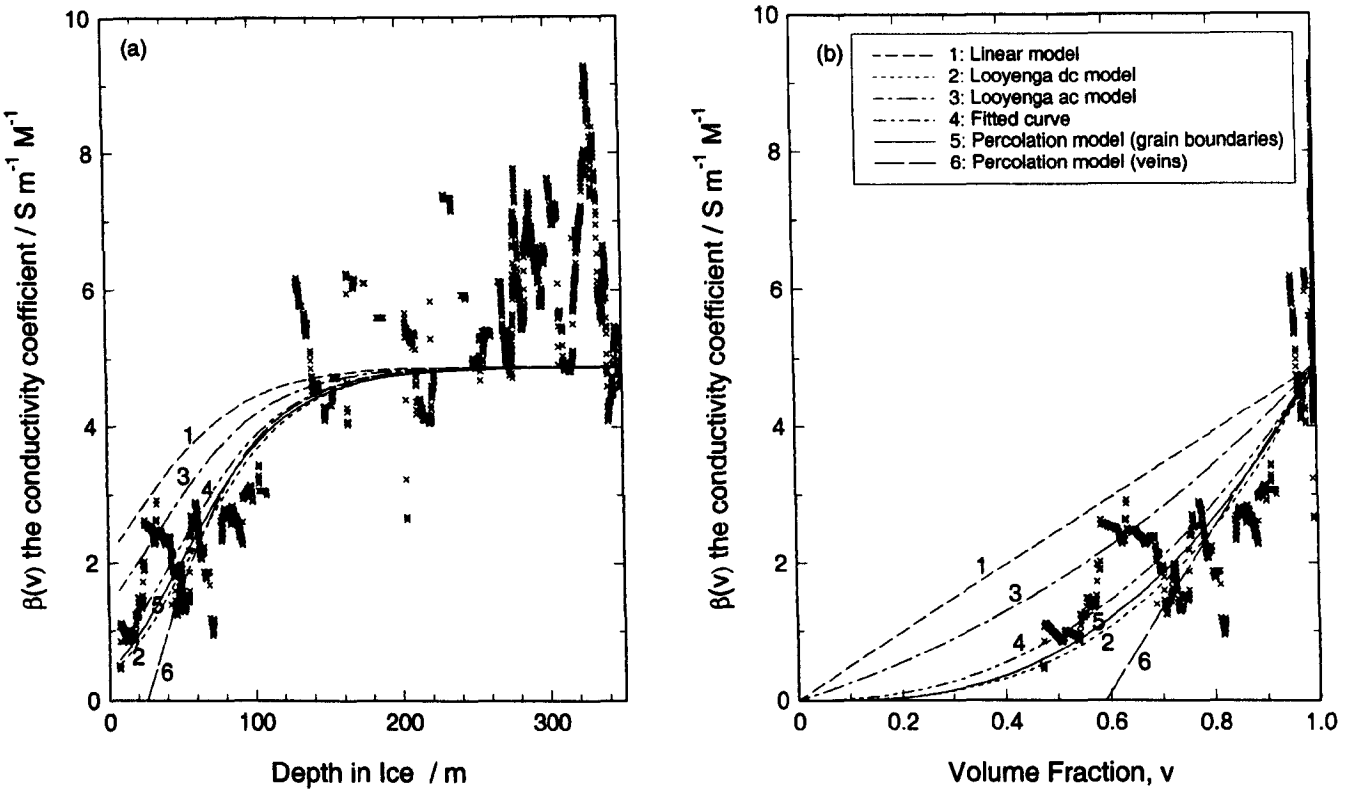

Figure IV.7. Points show **(a)** the estimate of the molar conductivity of H_2SO_4, $\beta(v)$, against depth. **(b)** $\beta(v)$ against volume fraction v. For all curves $\beta_{H2SO4}(1) = 4.9$ S m^{-1} M^{-1} Curve (1) gives $\beta_{H2SO4}(v)$ linearly related to volume fraction. (2) is the direct current component of conductivity from Looyenga's model, given by equation 18. (3) is the high frequency conductivity component of Looyenga's model, given by equation 20. (4) the non-linear fit, equation 19. (5) gives the percolation theory model for conduction in a firn lattice where z = 14 - 16. The fitted curve is given by equation 25. (6) gives the percolation theory model for conduction through interconnected veins at triple junctions where z = 4. The fitted curve is given by equation 26.

where ε_0 is the permittivity of free space, ε_j is the relative permittivity of either air or ice and ω is the angular frequency. The relevant form (j = *air* or j = *ice*) of this expression for y_j may be substituted into the corresponding relative permittivity terms in equation 14. In the case of a dc current in firn, $\omega = 0$, and the dc conductivity of air $\sigma_{dc\,air} = 0$ then [*Shabtie and Bentley*, 1994]:

$$\sigma_{dc}(v) = \sigma_{dc}(1)v^3 \qquad \text{(IV.18)}$$

Since the dc conductivity of pure ice is approximately zero, σ_{dc} refers to the net bulk conductivity of both the ice crystals and the acids incorporated in or around them. Fluctuations in $\sigma_{dc}(1)$ are dependent on acid concentration, and in the case of Dome C predominantly on $[H_2SO_4]$. This means that $\sigma_{dc}(v)$ is simply the conductivity due to the acid if the ice were solid, corrected for density. Hence if we apply the dc conduction model of equation 18 to the acidic component of σ_∞, then $\beta_{H2SO4}(v)$ (a measure of the dependence of σ_∞ on $[H_2SO_4]$) can be related to v:

$$\beta_{H2SO4}(v) = \beta_{H2SO4}(1)v^3 \qquad \text{(IV.19)}$$

The curve produced by this equation can be seen plotted with the measured data in figure IV.7 as curve 2 where $\beta_{H2SO4}(1) = 4.9$ S m^{-1} M^{-1} from equation 9.

Moore et al. [1989] used Looyenga's high frequency conductivity relation (IV.16) to correct conductivity data for density, regardless of the chemical composition of the ice, and beyond

this correction no statistically significant variation of the conductivity coefficient with v was found. This is likely to be linked to the higher concentrations of sea salts in the Dolleman core. The correction is given by:

$$\beta_{H2SO4}(v) = \beta_{H2SO4}(1)\, v(0.68 + 0.32v)^2 \qquad \text{(IV.20)}$$

and is plotted as curve 3 in figure IV.7 for comparison with the dc model (curve 2) where again $\beta_{H2SO4}(1) = 4.9$ S m^{-1} M^{-1}.

IV.4.4.3. Fitted model. In this section we fit a simple curve to $\beta(v)$ to model $\beta_{H2SO4}(v)$. The curve can be partly constrained because it is clear that when $v = 0$ then $\beta_{H2SO4}(0) = 0$ since conduction cannot take place in a situation where there is no ice and hence no acid; it is possible that $\beta(v)$ could still be zero when $v > 0$. A model of the form $\beta_{H2SO4}(v) = \beta_{H2SO4}(1)\, v^p$ is chosen because of its similarity to the Looyenga dc model, and is fitted to $\beta(v)$ using non linear regression analysis. Both $\beta_{H2SO4}(1)$, the solid ice molar conductivity, and p are empirically derived. The $\beta_{H2SO4}(1)$ coefficients found for 0 - 270 m and 0 - 350 m were 4.9 and 5.5 S m^{-1} M^{-1} and p = 2.4 and 2.7 respectively. The values of $\beta_{H2SO4}(1)$ compare well with the β_{H2SO4} coefficients found using linear regression for the sections 200 - 270 m and 200 - 350 m in equations 5 and 7, and the higher value for 0 - 350 m can be partially explained by the slight correlation (r = 0.18) between HCl and H_2SO_4 in the section 270 - 350 m, so we consider the value of 4.9 S m^{-1} M^{-1} as the more reliable of the two since it has less interference from HCl. These values also seem consistent with those quoted in previous work (table IV.2) and help to confirm that the value of $\beta_{H2SO4}(1)$ is largely independent of site location in polar ice. $\beta_{H2SO4}(v) = 4.9\, v^{2.4}$ is plotted as curve 4 in figure IV.7.

IV.4.4.4. Percolation model of conduction. Work by Shabtaie and Bentley [1994] considered the relationship between the direct current conduction in firn $\sigma_{dc}(v)$ and volume fraction v, using the theory of percolation in disordered systems. They took ice grains to be semi-regular truncated octahedrons with a co-ordination number (number of nearest neighbours) $Z = 14$ - 16. Each grain was considered as a site on a conducting lattice in solid ice, and firn was modeled by removing sites randomly in proportion to the volume of firn occupied by air (1 - v) which is an insulator. The conductivity of the lattice was then found according to the fraction of conducting sites present. For firn in a lattice of connected ice grains ($Z \sim 15$) the threshold volume fraction at which conduction no longer takes place was found to be, $v_c = 0.075$ (a hypothetical instance since the structure would collapse at this density). Using conductivity data gathered from Dome C by standard 4-electrode dc resistivity profiling, they derived the following equation from percolation theory which relates conductivity to volume fraction:

$$\frac{\sigma_{dc}(v)}{\sigma_{dc}(1)} = \left(\frac{v - v_c}{1 - v_c}\right)^{\tau} \qquad \text{(IV.21)}$$

where the exponent τ was found empirically to be $\tau = 2.7 \pm 0.15$ so:

$$\sigma_{dc}(\chi) = \sigma_{dc}(1)\, 1.23(\chi - 0.075)^{2.7} \qquad \text{(IV.22)}$$

The conductivity exponent, τ, was also found to be more generally related to the coordination number of sites in a lattice, Z:

$$\tau = 3\left[1 - e^{-0.4(\frac{Z}{2}-1)}\right] \qquad \text{(IV.23)}$$

Because of the likelihood that dc conduction in polar ice is predominantly due to the presence of liquid impurities held outside individual grains, Shabtaie and Bentley concluded that electrical transport must take place on the surface of ice crystals. This would allow conduction between a shell of impurity coating a grain and its 14 to 16 neighbours. As the density decreases the number of nearest neighbours is also reduced and hence the conductivity also decreases. This model seems reasonable for polar firn where the presence of air networks and bubbles could provide a structure where conduction can occur in a liquid film of impurities covering the grains.

If $\beta(v)$ is considered as being dependent on a dc mechanism of conduction through H_2SO_4 then equation 21 may be adapted to give a percolation model describing the variation of β_{H2SO4} with v because $\sigma_{dc}(v)$ is a function of $[H_2SO_4]$ which varies independently of v:

$$\frac{\beta_{H2SO4}(v)}{\beta_{H2SO4}(1)} = \left(\frac{v - v_c}{1 - v_c}\right)^{\tau} \qquad \text{(IV.24)}$$

A model of this form was fitted to the data in figure IV.7b for densities down to 270m, using v_c = 0.075 and $\beta_{H2SO4}(1) = 4.9$ S m^{-1} M^{-1}, the following relation was determined:

$$\beta_{H2SO4}(\chi) = \beta_{H2SO4}(1)\,1.21(\chi - 0.075)^{2.5} \qquad \text{(IV.25)}$$

$\tau = 2.5$ is just outside the confidence interval found by Shabtaie and Bentley, but seems close enough to confirm the form of the percolation model to describe DC conductivity in firn. The curve predicted by equation 25 can be seen plotted in figure IV.7 as curve 5.

IV.4.4.5. Conduction through liquid filled veins. A model for the electrical conduction in polar ice was proposed by Wolff and Paren [1984] that involved dc conduction through liquid veins of acid situated at triple junctions between grains. The majority of the sulphuric acid in solid ice may be assumed to exist in the liquid phase in a network of interconnected veins at the grain triple junctions since this is the most energetically favourable site for its location. Sulphate ions have been found to exist at the triple junctions between grains in polar ice, helping to verify this [*Mulvaney et al.*, 1988]. The acid will be held at close to its saturation concentration for the temperature of the surrounding ice (4.3 M at -53.5°C if no other impurities are present) and it is through this liquid phase that conduction is considered to happen, the DC conductivity of the pure solid ice grains being negligible.

Shabtaie and Bentley applied a similar network of conducting veins to their percolation theory for conduction in firn. The coordination number for sites connected by such a network of veins is Z = 4, since the point at which different triple junctions meet is a four grain boundary or node. For a lattice with a coordination number of 4, the critical volume fraction at which

conduction may no longer take place was found to be $v_c = 0.59$ for a square lattice and 0.435 for a tetrahedral lattice. Since for firn at the surface of the Dome C core $v = 0.34$, Shabtaie and Bentley [1994] concluded that the vein conduction model is clearly not applicable for firn at low densities because DC conduction is observed when $v < v_c$. Equation 23 with $Z = 4$ gives $\tau = 1$, and with $v_c = 0.59$ equation 24 gives:

$$\beta_{H2SO4}(v) = \beta_{H2SO4}(1)2.44(v - 0.59)^{1.0} \qquad \text{(IV.26)}$$

This is plotted as curve 6 in figure IV.7 where $\beta_{H2SO4}(1) = 4.9$ S m^{-1} M^{-1}, it does not describe the data for volume fractions less than about 0.7, at higher values of v the fit is comparable to equations 25 and 20. This suggests that significant conduction along three grain boundaries at densities greater than approximately 640 kg m^{-3} would be consistent with the data and with Shabtaie and Bentley's model, but that conduction at two grain boundaries would have to take over as density dropped below 640 kg m^{-3}.

IV.4.5. Predicting the conductivity

Several possible mechanisms for the chemical component of conduction in firn have now been proposed. In this section we summarise the models and discuss their suitability for predicting the conductivity. Figure IV.7 shows the resultant curves produced by the various models and fits. In all cases $\beta_{H2SO4}(1) = 4.9$ S m^{-1} M^{-1} to ease comparison. The models responsible for each curve may be summarized as follows: *Curve 1:* Linear fit of volume fraction against depth, this would be expected if the acidic component of conductivity was directly proportional to volume of ice measured by the electrodes of the DEP process. *Curve 2:* Direct current component of conductivity from Looyenga's model, given by equation 19. The model is suited to cases where liquid impurities, situated externally from the grains, are contributing to σ_∞ by a dc conduction mechanism. *Curve 3:* High frequency conductivity component of Looyenga's model, given by equation 20. This model is physically reasonable for situations where the chemical impurities are incorporated in to the ice lattice, hence directly changing the dielectric properties of the ice. *Curve 4:* Non-linear fit on the section of core not significantly influenced by HCl, $\beta_{H2SO4}(v) = 4.9\ v^{2.4}$. This curve does not relate to a physical model, but is plotted to show similarity to other models included. *Curve 5:* Percolation theory model for conduction in a firn lattice where $Z = 14$ - 16. The fitted curve is given by equation 25. This model is similar to curve 2, and simulates conduction, via liquid films over crystal surfaces to neighbouring grains, by a dc mechanism. *Curve 6:* Percolation theory model for conduction through interconnected veins at triple junctions where $Z = 4$. The curve is given by equation 26, a specific form of equation 24 where $\tau = 1$ and $v_c = 0.59$ which corresponds to conduction through a square lattice. The model describes the case where liquid impurities exist at three grain boundaries and contribute by a dc mechanism to σ_∞.

To assess the applicability of the above models figure IV.7 may be examined. Curve 1 gives the least good fit to the data, and may be discarded as a plausible model. Curve 3 also gives a

poor fit, suggesting that in this core the component of conductivity due to H_2SO_4 is not best described by a high frequency mechanism, and that acidic ions are not incorporated into the lattice. There is very little to choose between the curves 2, 4 and 5, and curve 6 is only applicable for $\nu > 0.7$. The relatively good fit of curves 2 and 5 helps reinforce the theory that bulk of the chemical component conduction is taking place in the liquid phase, since conduction is modeled by a dc mechanism. This conclusion is drawn with some reservation about the applicability of both the Looyenga dc model and the percolation model. At the limit where $\omega = 0$ the Looyenga model has not been proven to hold for conductivity and it may not be as suitable for describing processes that occur at grain boundaries as processes in the bulk. Percolation theory is better suited to modeling a dc process than an ac one since ac conduction is less reliant on the connectedness of pathways. Despite the similarity in the results of the two models the dc component of Looyenga's equation does not agree theoretically with percolation theory since the cubic exponent implies that Z is infinite in percolation theory (each grain being spherical) [*Shabtie and Bentley*, 1994].

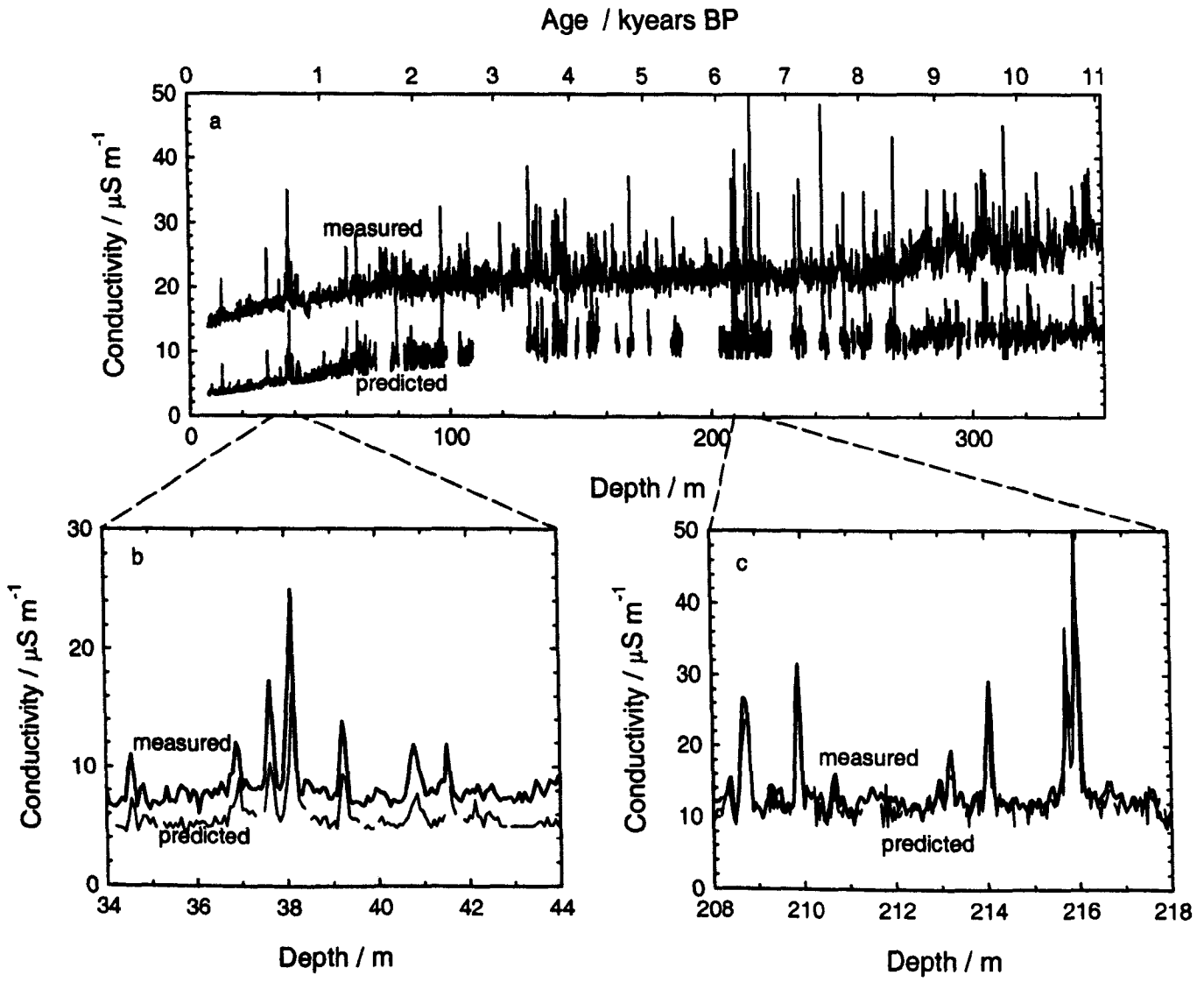

Figure IV.8. (a) Predicted σ_{ac} (IV.25, thin line) and measured σ_{ac} (thick line) against whole depth of core. The measured σ_{ac} is offset by 10 μS m^{-1}. (b) Close up of 34 - 44 m (no offset). (c) Close up of 208 - 218 m (no offset). Note the difference in the background levels of the two curves in (b) compared to (c).

It should now be possible to predict σ_∞ of the core at any given depth if the density and chemical composition are known. Looyenga's equation can be used to provide the pure ice component of the conductivity with the relation given in equation 16. The chemical component of the conductivity could be given by any of the relationships shown by curves 2, 4 and 5 and we will here use the percolation model shown by curve 5. Hence the DEP conductivity of the core may be predicted at -15°C if the concentration of sulphuric acid and volume fraction are known with depth:

$$\sigma_\infty(v) = \sigma_{\infty\,pure}(1)\,v(0.68 + 0.32v)^2 + \beta_{H2SO4}(1)\,1.21(v - 0.075)^{2.5}[H_2SO_4] \qquad \text{(IV.27)}$$

Here $\sigma_{\infty\,pure}(1) = 9$ μS m^{-1}, $\beta_{H2SO4}(1) = 4.9$ S m^{-1} M^{-1} and $\tau = 2.5$. This relation may be tested by comparing the predicted conductivity to the measured conductivity, figure IV.8. The proportion of actual variation accounted for by equation 24 is $r^2 = 75\%$. The predicted curve is consistently lower than the measured curve in the top 110 m of the core as is expected given the divergence of Looyengas model from $\sigma_{int}(v)$ in figure IV.6. Aside from the pure component of conductivity the values predicted will always differ in reality, due to the presence in the core of other ionic species not accounted for here.

It has not been possible here to test the relationship between density and the electrical response of other ionic species due to the dominance of sulphuric acid in the core. It is expected that similar results would occur for other acids that provide a direct current component to conductivity. For salts it seems more reasonable that the molar conductivity would respond in a manner consistent with a mechanism by which chloride ions are incorporated into the lattice, and so a density correction to the coefficient of the form given by (IV.20) would be more appropriate than other models presented.

IV.5. Conclusion

In agreement with previous work relating the conductivity of polar ice to its chemical composition, a clear correlation between the concentration of sulphuric acid and DEP conductivity has been confirmed for the top 350 m of the Dome C core. The value of the molar conductivity of H_2SO_4 in solid polar ice from this work falls between 4.8 and 6.7 S m^{-1} M^{-1} with a best estimate of its value being $\beta_{H2SO4}(1) = 4.9$ S m^{-1} M^{-1}. This assumes that a single value for $\beta_{H2SO4}(1)$ applies for solid ice, which may not be the case particularly given the scatter seen in figure IV.7. A separate correlation has also been established between hydrochloric acid concentration and conductivity; the value of the coefficient has been constrained to between 3.4 and 5.2 S m^{-1} M^{-1} with a the most likely value being around 4.5 Sm^{-1} M^{-1}; this appears compatible with previous results and current theory. The relationship found between salt (represented by sodium concentration) and conductivity was higher than expected and the values obtained cannot be considered well

established universally for polar ice given the limited number of sites tested for the salt dependence of conductivity. However the value (1.5 S m^{-1} M^{-1}) is consistent with the complete incorporation of the associated sea salt chloride into the ice lattice.

The change in the pure ice component of conductivity with density is broadly similar to that predicted by Looyenga's model applied to conduction in firn, but is higher than expected in the upper 110 m of the core. For solid ice the pure ice component of conductivity is found to be 9.8 ± 1.9 μS m^{-1}, which agrees with previously found values.

The conductivity coefficient of sulphuric acid has been seen to vary with firn density; the molar conductivity increases as the volume fraction of the firn increases. The relationship is however not linear and the models that best fit the data suggest that acidic conduction in the firn is contributing to the direct current component of the conductivity. The percolation theory of conductivity through a random network as applied by Shabtaie and Bentley [1994] may be used to represent the variation of the conductivity coefficient with volume fraction: $\beta_{H2SO4}(v) = \beta_{H2SO4}(1)\ [(v - v_c)/(1 - v_c)]^{\tau}$. The value of the exponent τ is dependent on the structure of the lattice and is here found to be $\tau = 2.5$, which is slightly lower than their previously obtained value of $\tau = 2.7$ for a structure where each grain has between 14 and 16 nearest corresponding to conduction in liquid films surrounding grains. Due to the large scatter of the data, it is impossible to say that this model is significantly better than the direct current component of Looyenga's model: $\beta(v) = \beta_{ice}\, v^3$ which also gives a reasonable fit to the data. If conduction is taking place in the liquid impurity phase then the applicability of this percolation model implies that the impurity exists on grain surfaces and two grain boundaries in firn of all densities.

The data also appear to be consistent with a model of conduction by liquid sulphuric acid situated in a network of interconnected veins. However conduction by this mechanism could only take place at densities greater than approximately 640 kg m^{-3} ($v > 0.7$). It seems plausible that there could be a gradual change in the conductivity mechanism from conduction at two grain boundaries in shallow firn to conduction at three grain boundaries in solid ice. This would correspond to a change in coordination number from $Z = 14$ -16 to $Z = 4$ as the density increased. Due to the nature of the uncertainty of methods used in this here, other approaches might be required to test this hypothesis. We return to this issue in chapter VI where direct evidence of impurity location using the SEM is assessed. To study the variation of other conductivity coefficients with depth in a similar manner to that used here would require analysis of data from sites dominated by other chemical species.

In the following chapter (V) we examine the same chemical data series for signs of diffusion. Mechanisms by which impurity could be transported are described which are strongly dependent on impurity distribution.

CHAPTER V

The evolution of chemical peak shapes in the Dome C, Antarctica, ice core

Interpretation of the chemical layers measured in ice cores requires knowledge of processes occurring after their deposition on the ice sheet. We present evidence for the diffusion of soluble ions in the top 350 m of the Dome C ice core, Antarctica, that helps explain the unexpectedly broad volcanic peaks observed at depth. A windowed-differencing operation applied to chemical time series indicates a damping of the signals over the past 11,000 years, independent from minor climatic variation, for sulphate and chloride, but not sodium. This implies a diffusive process is transporting both sulphate and chloride ions whilst the sodium ions remain fixed. We estimate the effective diffusivity in the core to be 4.7×10^{-8} m^2 yr^{-1} for sulphate and 2.0×10^{-7} m^2 yr^{-1} for chloride. These values are not high enough to significantly disrupt chemical interpretation in this section of core but could be significant for older ice. The temperature of this section of ice (-53 °C) implies that the predominantly acidic sulphate and chloride ions will exist in the liquid phase whilst the sodium may be solid. We propose and develop two new mechanisms that could explain the observed solute movement. One involves the diffusion of solute through a connected vein network driven by liquid concentration imbalances instigated by the process of grain growth. The other considers a system of discontinuous veins where grain growth increases connectivity between isolated vein clusters allowing the spread of solute. In both mechanisms the effective diffusivity is governed indirectly by grain growth rate; this may be a significant factor controlling effective diffusion in other cores.

V.1. Introduction

Climate records extending back as much as five hundred thousand years are collected from ice cores recovered from the polar ice sheets. Climate data are extracted from the ice by the precise measurement of its composition and structure. The profile of a measured variable (for example concentration of sulphate) with depth can be dated to give a time series that enables the construction of a climatic history. However the relationship between the measured concentration in the core and the state of the atmosphere at the time of deposition is complicated by many factors including: rate of snow accumulation, changes in the transport processes between the source and the core site, and post-depositional change. Signals from several ice core variables such as stable isotope ratios ($\delta^{18}O$ and δD), hydrogen peroxide (H_2O_2) and methane sulphonate (MSA) are known to be modified with age in the ice, either reducing the amplitude of variations, or modifying the

seasonality of signals (MSA) [*Cuffey and Steig*, 1998; *Johnsen et al.*, 2000; *Kreutz et al.*, 1998; *Pastuer and Mulvaney*, 1999]. This work examines signals from more stable soluble impurities, such as sulphate, chloride and sodium (which are commonly considered fixed in cold ice) for post-depositional change. We know that many chemical layers, even in the deep and old cores, can remain distinctly resolved [e.g. *Zielinski et al.*, 1997] implying that little movement has occurred. However it remains an unsubstantiated hypothesis to assume that the signal is locked in the original ice with which it was deposited. Recent work by Rempel et al. [2001a] suggests that the downward advection of the whole soluble impurity profile is theoretically possible under conditions where there is a significant temperature gradient in the ice. Additionally concentration profiles across volcanic layers (chemical peaks) often imply that these events lasted longer than their likely atmospheric duration, even after accounting for mixing of surface snow. This suggests the existence of some form of soluble impurity transport within the ice, causing peak broadening.

If post-depositional movement of chemical species occurs then it will be important to understand the migration process in order to interpret the ice core data correctly (particularly for deep, high resolution records). A thorough investigation of the mechanisms that might lead to movement is needed to determine the nature and extent of the possible effects. Until recently data of a high enough resolution at ages where it is possible to look for the peak broadening have been sparse. This chapter addresses the question of whether there is evidence for diffusion of sulphate, chloride and sodium in the Dome C ice core and if there is, what is the mechanism? There are two main parts: analysis of the core records for signs of peak broadening (section V.2), and the proposal of mechanisms that could allow the movement of chemical species in the ice (section V.3).

V.2. Diffusion evidence

In this section we examine chemical data from the recently drilled Dome C ice core, Antarctica. By looking at the profile in young and old ice we can test whether the mean characteristics of the signal are the same now as they were in the past. Changes that cannot be attributed to changes in climate or volcanic activity must be related to post-depositional processes in the ice. Time and depth dependent frequency analysis and a windowed-differencing operation are applied to the concentration profiles (rescaled to account for climatic variability) to search for peak broadening. We present evidence that limited but significant movement of solute occurs for sulphate and chloride ions, a large proportion of which we expect to exist in the liquid phase. Conversely no signal damping is noted for the sodium profile, which is in keeping with the species being either dissolved in the lattice or in a solid phase at grain boundaries or veins. Effective diffusion coefficients are estimated with the aid of a numerical model.

V.2.1. Data

We examine the records of sulphate, chloride and sodium in the upper 350 m of the Dome C core, drilled during 1998 and 1999, by the European Project for Ice Coring in Antarctica (EPICA). This section of the core, dating back to about 11,000 years before present, originates from the Holocene period [*Schwander et al.*, 2001] during which there has been only relatively minor climatic variation [*Ciais et al.*, 1994]. Dome C is situated on the East Antarctic plateau (74°39'S, 124°10'E, elevation: 3240m and mean annual temperature: -53.5°C), at a location around 1000 km from the coast, resulting in only a small fraction (composed chiefly of sodium chloride) of the total trapped impurities originating directly from the ocean. The remainder is predominantly composed of sulphuric acid from volcanic eruptions (spikes) and from marine biogenic activity (background) and hydrochloric acid from the interaction of acid and salt in the atmosphere and snowpack. We place particular emphasis on the sulphate record, as it is the dominant impurity at these depths; sulphate and chloride data are used as good proxies for sulphuric and hydrochloric acid (Chapter IV).

Sulphate and chloride were measured in the field using rapid ion chromatography where the sampling interval decreased from ~ 0.07 to 0.03 m corresponding to an approximately constant ice equivalent depth [*Udisti et al.*, 2000]. Sodium was also measured in the field using continuous flow analysis with an effective resolution around 0.02 m [*Röthlisberger et al.*, 2000]. The effects of wind driven mixing of snow layers on the surface combined with the mean annual accumulation rate at the site (28 kg m^{-2} yr^{-1}) prevent the resolution of annual layers in the core. Wind driven mixing will cause some smoothing and alteration of the profile but will have no significant impact on the mean characteristics of the profile over time scales greater than a year. In this work we consider only changes that have occurred after the initial deposition and settling of the snow at the surface. Throughout the chapter, sections of core where a significant proportion of the chemical data are missing from the profile are excluded from the analysis for that species. Density measurements were made along the length of a 120 m satellite core. The temperature in the bore hole changes only slightly from –54.2 °C near the surface (30 m) to –51.6 °C at 350 m (personal communication R. Mulvaney and E. Lefebvre).

The depth coordinates of the chemical data were corrected for densification and strain to give an un-thinned ice equivalent depth, z. The Herron and Langway model [1980] applied in chapter IV was used for densification and the one dimensional flow model applied by Schwander *et al.* [2001] was used to give the un-strained depth in the ice.

Variation in the accumulation rate (the standard deviation of the annual accumulation rate for this section of core is 8%) was not found significantly to influence the results of the subsequent analysis. Hence for simplicity when estimating the diffusion coefficient a constant accumulation rate was assumed, which was set at the long term rate for the period, a = 0.030 m yr^{-1}. The time

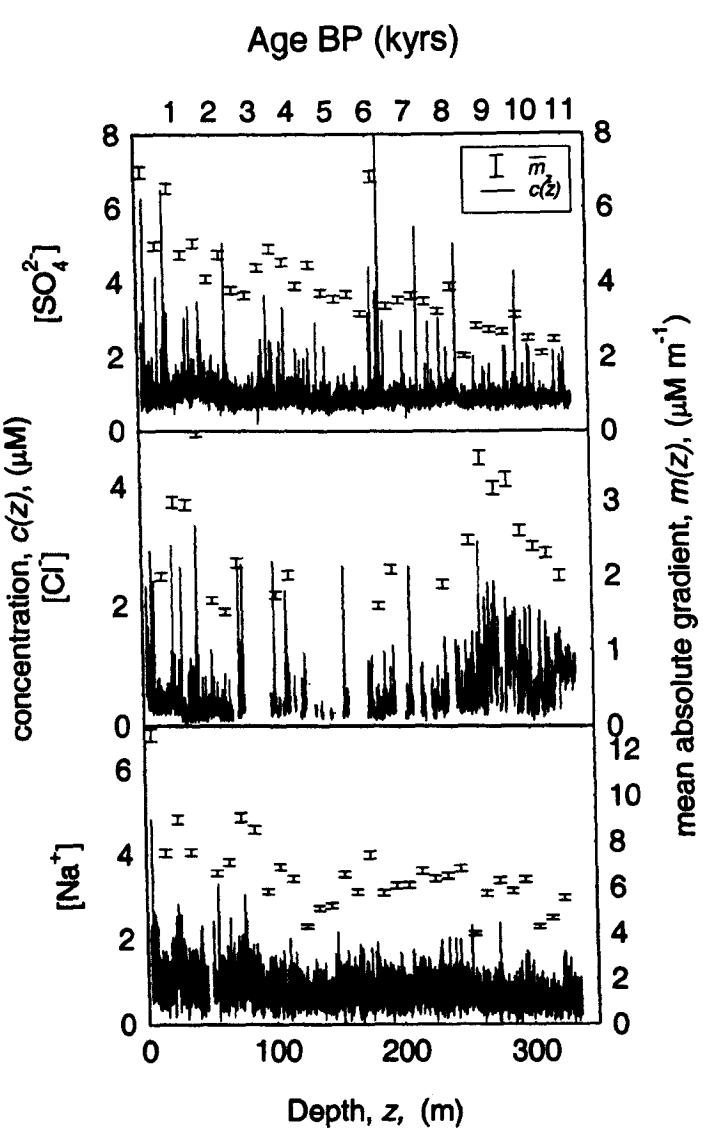

Figure V.1. Solid lines, concentration of chemical data, c, for SO_4^{2-}, Cl^- and Na^+ against un-thinned ice equivalent depth and time in the core, z. The profile spans a period of around 11,000 years. The vertical lines bounded by error bars show the mean absolute gradient, $\overline{m}_z$, of the profile, calculated within 10 m windows. Points are removed when more than 65% of expected data are missing from a 10 m section. Errors bars give the statistical uncertainty on $\overline{m}_z$, calculated using an estimated error of 2% on chemical measurements.

series profile of concentration, c, against time, t, can then be given by: $c(t) = c(z / a)$. The uncertainty on the age of the core is ± 200 yr by an age of 10 kyr [*Schwander et al.*, 2001].

Figure V.1 shows the chemical profiles used for the investigation, plotted against both un-thinned ice equivalent depth and time. The background sulphate concentration remains approximately constant, however the background concentration of chloride fluctuates and the concentration of sodium declines with increasing depth. Figure V.2 shows examples of two pairs of sulphate peaks from the $c(t)$ profile of a similar integrated area (total flux contained in the peak) that we might expect to have been deposited over similar time scales if they are of volcanic origin, first in shallow ice and then deeper in the core. The durations of the older peaks have considerably longer full-width-half-maximum (FWHM) values than the younger ones. This effect, although typical, is not seen for every peak observed in the deeper ice, occasional peaks having durations similar to the upper core. A generalised method is required to quantify this observed peak damping.

V.2.2. Method

V.2.2.1. Profile analysis. Post-depositional movement of chemical species in an ice core will be indicated by changes in the mean characteristics of the profile with depth that cannot be attributed to climatic trends. No strong periodicities were observed in the profiles (figure V.3.).

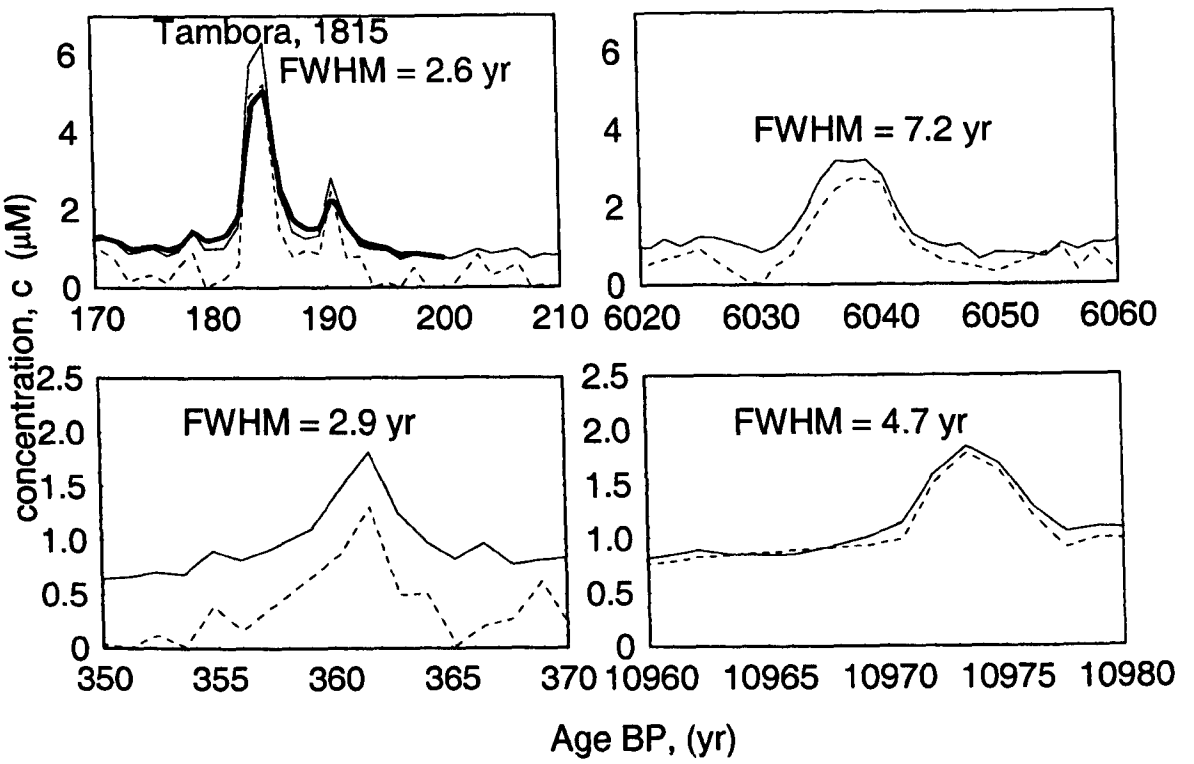

Figure V.2. Example of sulphate profile (solid line) and sulphuric acid profile (dashed line, chapter IV) across volcanic horizons in ice of different ages. The bold line in the upper left hand plot shows the predicted sulphate profile of the Tambora peak after 11,000 years of grain growth using the connected grain growth model. Full width half maximum (FWHM) values are indicated and measured from the lowest point of each sulphate peak.

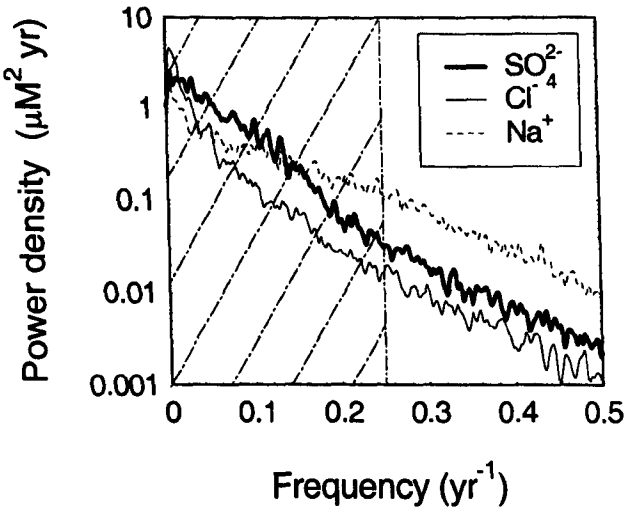

Figure V.3. Power spectra from impurity concentration profiles *c(t)* for sulphate, chloride and sodium from the top 350 m of the Dome C core. Calculated from mean values of spectra from 10.24 m (338 yr) sections to reduce spectral variance [*Krauss et al.*, 1994]; missing data points have been ignored. The sloping trends are indicative of a coloured noise [*Percival and Walden*, 1993], with no strong periodicity obvious. The section free from hatching represents the frequency band used for measuring the spectral power at intervals down the core.

Time dependent frequency analysis indicated a reduction in high frequency spectral power with increasing age for all three species (figure V.4).

The profiles were also examined for a variable we could relate more directly to diffusive processes of the random signal, where the mechanism for diffusion is unknown. The gradients of individual peaks are of little interest because the circumstances by which each peak was deposited will be unique in each case. However the mean absolute peak gradient, $\overline{m}_z$, within a section of ice Δz tends to become representative of the 'sharpness' of chemical peaks or fluctuations for ice of an age corresponding to its depth z:

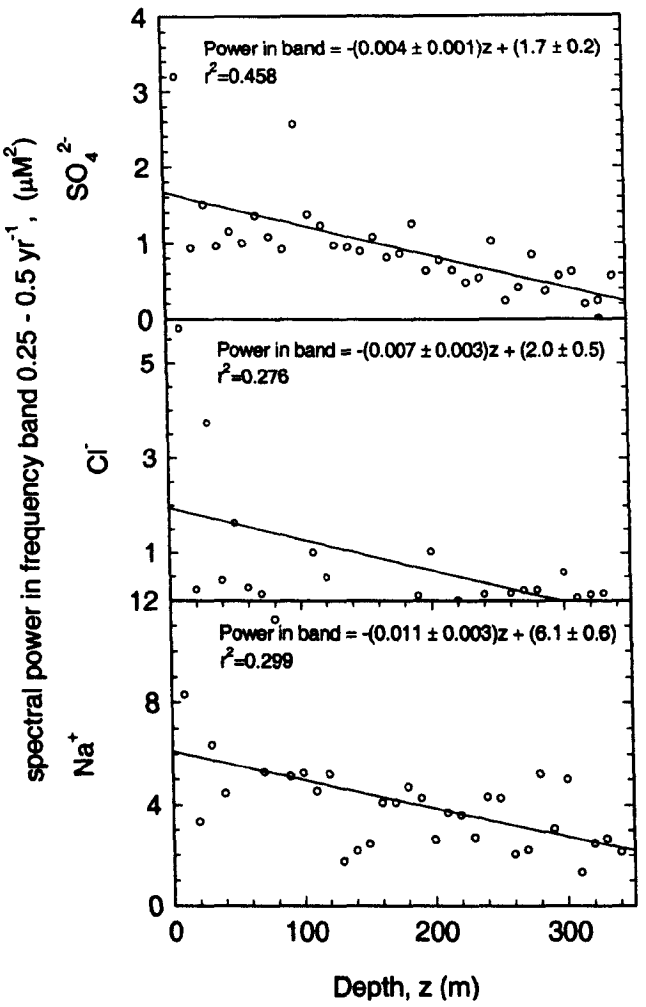

Figure V.4. Spectral power contained within the frequency band corresponding to 2 to 4 years (λ = 0.06 – 0.12 m), calculated within 10 m sections of the core, for the sulphate, chloride and sodium concentration profiles (over-sampled at 0.33 yr intervals). A significant decreasing trend is noted for the power in the frequency band for all three chemical species.

$$\overline{m}_z = \frac{1}{\Delta z}\sum_{z}^{z+\Delta z}\left|\delta c(z)\right|, \qquad (V.1)$$

where $\delta c(z)$ is the difference between successive points of $c(z)$. Hence strong fluctuations in the concentration profile correspond to a high value of $\overline{m}_z$, and if a diffusive process is occurring in the ice then we expect a reduction in the value of $\overline{m}_z$ with age as the size of fluctuations decrease. Equation (V.1) can be viewed as performing a windowed differencing operation on the concentration profile. Figure V.1 also shows $\overline{m}_z$, calculated using 10 m windows, plotted against depth for sulphate, chloride and sodium. The magnitude $\overline{m}_z$ varies broadly with the size of fluctuations in the profiles $c(t)$; for sulphate, and sodium a significant downward trend in $\overline{m}_z$ with depth and age is evident, whilst chloride shows a small decline in the peak gradients then a rise and decline corresponding to the increase in concentration between z = 250 - 336 m. This increased chloride concentration was observed by Udisti *et al.* [2000], and it is considered to be linked to a higher accumulation rate during the period.

V.2.2.2.Amplitude rescaling. Neither frequency analysis nor the mean absolute gradient can confidently distinguish between signal damping caused by climatic variation and damping due to post-depositional diffusion. For example the decreasing sodium trend (figure V.1) is coupled with a decline in the strength of signal oscillations (and $\overline{m}_z$), which we could interpret as resulting from diffusion. However it appears more likely that the effect is simply due to weaker climate signals reaching the core in the past. A further operation must be performed on the profiles, to attenuate the impact of climatic variation during the period under study.

The profiles were broken into peaks where the boundaries of the peaks were defined by local minima in concentration. The area under each peak was calculated, with its base set at the concentration level of the local minimum. 10 m sections of the core were examined; the total 'area' contained within chemical peaks (μM m) for each section is plotted against the mean

concentration for the section, $\bar{c}_z$, in figure V.5. All three plots suggest that there is an approximately linear relationship between the mean concentration and signal fluctuation. This implies that ice with higher mean concentration also has higher variability. The chloride and sodium curves pass close to the origin; however extrapolating the curve for sulphate indicates that if the fluctuations in the profile drop to zero there would still be a residual concentration of c_0 = 0.54 μM. This seems physically plausible if background sulphate is attributed to biogenic production from the ocean with relatively low variability whilst larger superimposed fluctuations are predominantly volcanic. Since impurity is conserved in the ice, the mean concentration of a section can be used to infer information about the variability of the signal at the time of deposition if we assume that these linear relationships hold for the mean characteristics of the signal. On this basis the concentration measurements were rescaled by effectively normalising the data to its local background concentration, to produce a more consistent signal for analysis, where the original climatic information is no longer important. This operation cannot completely eliminate the impact of variation in volcanic frequency, but should aid comparisons between different sections of the core.

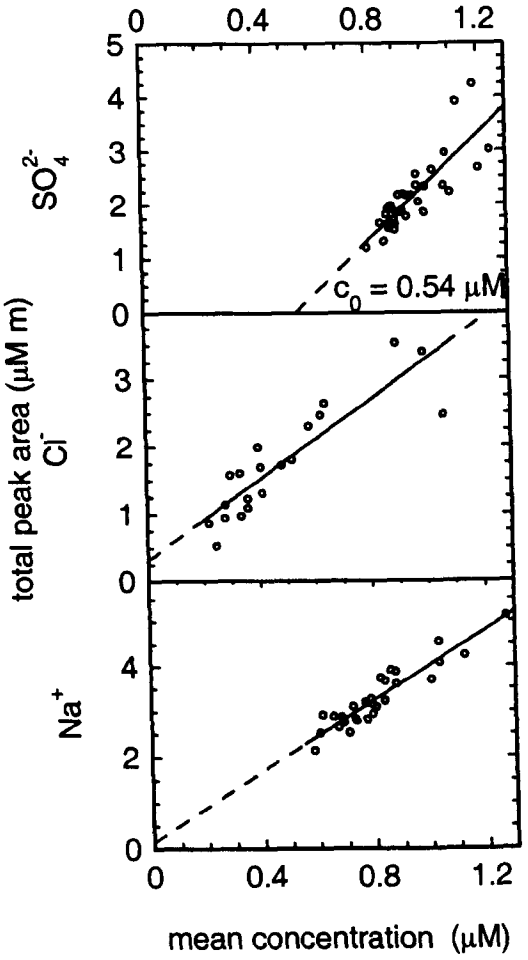

Figure V.5. Integrated area contained within chemical peaks plotted against the mean concentration of the section of core containing the peaks. Measurements made from 10 m sections down the length of the core. The intercepts, c_0, of the fitted lines with the mean concentration axes for SO_4^{2-}, Cl^- and Na^+ are 0.54 ± 0.04, -0.09 ± 0.06 and -0.05 ± 0.05 μM respectively.

The chloride and sodium profiles are rescaled to give $c'(z)$:

$$c'(z) = \left(\frac{c(z)}{\bar{c}_z}\right)\bar{c}, \tag{V.2}$$

and the rescaled sulphate profile is given by:

$$c'(z) = \left(\frac{c(z) - c_0}{\bar{c}_z - c_0}\right)\left(\bar{c} - c_0\right) + c_0, \tag{V.3}$$

where $\bar{c}$ is the mean concentration for the complete profile and $\bar{c}_z$ is the mean concentration in a Δz long section of core at depth z. As well as scaling fluctuations in the concentration to the local background level, trends are removed from the profile at time scales greater than $\Delta z\, a^{-1}$ (where a is

the accumulation rate). The correction does not influence the measurement of the diffusive component of the signal because $\bar{c}_z$ is independent of any diffusive processes. The mean absolute gradient for the corrected concentration profile, $\overline{m}_z'$, was found substituting $c'(z)$ from (V.2) or (V.3) into (V.1).

V.2.2.3.Effective diffusion. Diffusion can be modelled using a one-dimensional model since the chemical content of the ice can be assumed to be horizontally isotropic. The downward velocity of the signal in solid un-strained ice is assumed constant for the period under consideration, and can be taken from the accumulation rate to give $u_z = 0.030$ m yr^{-1} since $z = u_z t$, where t is the time since the deposition of the ice. We consider the peak's frame of reference, where z' represents the vertical distance from the centre of the peak at $z' = 0$. The diffusion of the bulk concentration is described by:

$$\frac{\partial c'}{\partial t} = v(t) D_{eff} \frac{\partial^2 c'}{\partial z'^2}; \qquad \text{(V.6)}$$

D_{eff} represents the effective diffusion coefficient for the chemical species through the solid ice. The variation in the volume fraction of ice in the firn, $v(t)$, is also included to account for densification. However the value actually represents a time-averaged effective diffusivity that includes the effects of strain on the ice.

When solving a relation of the form given by (V.6) describing the diffusion of stable isotopes in a core, Johnsen *et al.* [2000] relate a diffusion length, l, to the $D_{eff}(t)$:

$$\frac{dl^2}{dt} - 2 \cdot \dot{\varepsilon}_z(t) \cdot l^2 = 2 \cdot D_{eff}(t). \qquad \text{(V.7)}$$

Since in this case we are considering the un-thinned ice equivalence depth profile, the vertical strain rate, $\dot{\varepsilon}_z(t) = 0$. They then expressed the solution of (V.7) for a harmonic cycle of wave number k to give the amplitude of a signal oscillation, H:

$$H = H_0 e^{\left(-\frac{1}{2}k^2 \cdot l^2\right)}, \qquad \text{(V.8)}$$

where H_0 is the initial amplitude. Here peaks are taken to be triangular in shape, an adequate approximation given the sampling frequency. The wave number can be related the mean peak width as $k \sim 2\pi/\overline{w}$, where the mean peak width (vertical span in ice) for the whole profile (z_{total}) calculated from:

$$\overline{w} = \frac{4}{\overline{m} \cdot z_{total}} \sum_{0}^{z_{total}} \left| c'(z) - \bar{c} \right| \delta z, \qquad \text{(V.4)}$$

δz is the distance between consecutive $c'(z)$ measurements. Mean height of fluctuations (peak height) at a detph z is related to the mean peak width and absolute gradient by:

$$h(z) = \tfrac{1}{2} w(z) \cdot m(z). \qquad \text{(V.5)}$$

By ignoring the effects of densification we can assume that D_{eff} is constant in time. We approximate $H \sim h(z)$ and relate the wave number to the mean peak width as $k \sim 2\pi/\overline{w}$ in (V.8); solving (V.7) then using (V.5) and (V.8), the effective diffusion coefficient is given by:

$$D_{eff} = -\frac{1}{k^2 t} \cdot \log\left(\frac{m(z)}{m_0}\right), \qquad (V.9)$$

where m_0 is the initial mean absolute peak gradient.

V.2.3. Results

The rescaled profiles of $c'(z)$ with a re-scaling window depth of Δz = 10 m (330 yr) are plotted in figure V.6 for all three impurities. The variation of $\overline{m}_z'$ with time and depth is also plotted in figure V.6. The sulphate and chloride profiles show a significant downward trend in the value of $\overline{m}_z'$ with age, whilst sodium does not. Given that the bulk of the effects of climatic variability are removed at least on a timescale > 330 yr, the decline in $\overline{m}_z'$ indicates that, in the top 350 m of the Dome C core, SO_4^{2-} and Cl^- ions exhibit some mobility since peaks either become broader or are damped with depth whilst Na^+ ions appear to remain fixed. This is the quantitative expression of the visual observation of peak broadening exemplified in figure V.2. Mean peak characteristics for the profiles are presented in table V.1.

Curves of $m(z)$ were then numerically fitted using (V.9) to the observed data for $\overline{m}_z'$ in figure V.6 to give the values of D_{eff} for SO_4^{2-} and Cl^- of 3.9 × 10^{-8} and 20 × 10^{-8} m^2 yr^{-1} respectively (1 × 10^{-15} and 6 × 10^{-15} m^2 s^{-1}) and for m_0 of 4.7 and 3.4 μM m^{-1}, see table V.1. These values were checked against results from a numerical model of diffusion containing the $v(t)$ term where (V.6) was discretised to construct a finite difference model, using a forward-time, centred-space scheme where:

$$c_j^{n+1} = c_j^n + \frac{\chi(n) D_{eff}(n) \Delta t}{\Delta z'^2}\left(c_{j-1}^n - 2c_j^n + c_{j+1}^n\right) \qquad (V.6a)$$

Δt and $\Delta z'$ represent the time step and position step lengths respectively; n represents the time step number and j the spatial position co-ordinate. The initial peaks were determined using $\overline{w}$ and m_0

Table V.1. Mean rescaled peak characteristics and effective diffusion coefficients; observed and modelled.

	SO_4^{2-}	Cl^-	Na^+
$\overline{h}$ (μM)	0.36	0.42	0.48
$\overline{m}$ (μM m^{-1})	3.82	2.83	7.28
$\overline{w}$ (m)	0.19	0.29	0.13
Peak Area (μM m)	0.034	0.063	0.032
Fitted m_0 (μM m^{-1})	4.7 ± 0.3	3.4 ± 0.4	6.1 ± 0.3
Fitted D_{eff} (m^2 yr^{-1})	(3.9 ± 0.8) × 10^{-8}	(20 ± 6) × 10^{-8}	(-0.1 ± 0.4) × 10^{-8}
Diffuse D_{eff} (m^2 yr^{-1})	2.4 × 10^{-8}	15 × 10^{-8}	-
Connected D_{eff} (m^2 yr^{-1})	(7 – 5) × 10^{-8}	-	-
Un-connected D_{eff} (m^2 yr^{-1})	3 × 10^{-8}	-	-

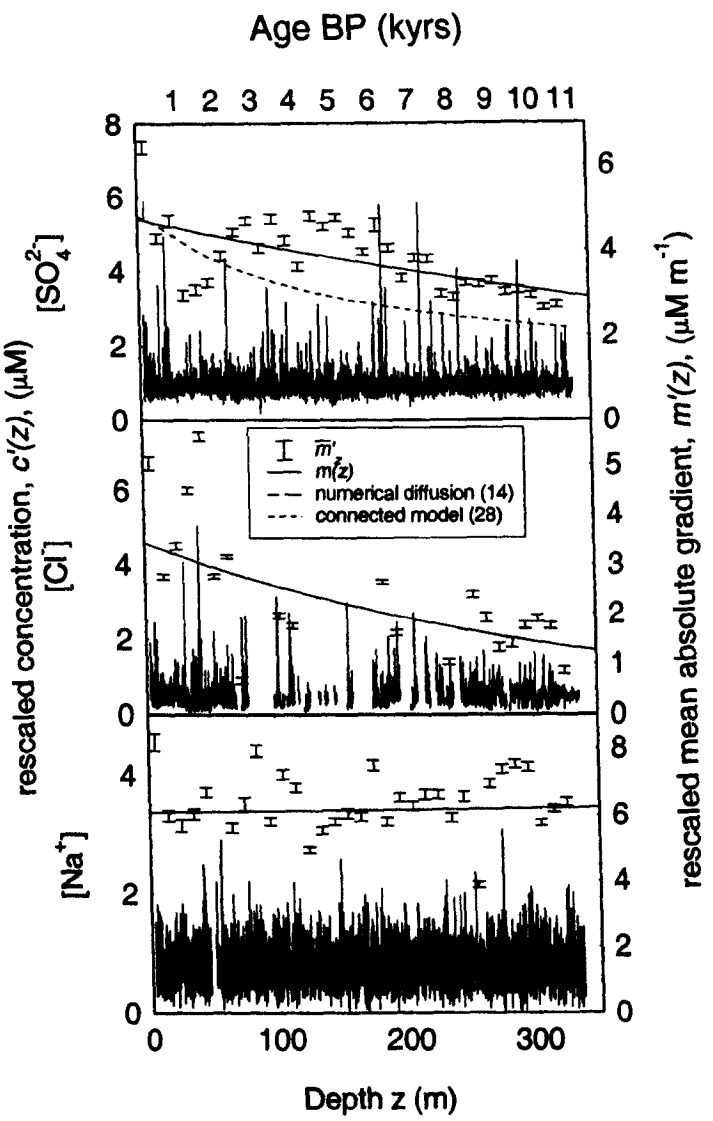

Figure V.6. Solid line, the rescaled concentration of chemical data, c', against un-thinned ice equivalent depth, z. The vertical lines bounded by error bars show the rescaled mean absolute gradient, $\overline{m}'_z$, of the profile, calculated within 10 m windows. Points are removed when more than 65% of expected data are missing from a 10 m section. Errors bars give the statistical uncertainty on $\overline{m}'_z$, calculated using an error of 2% on chemical measurements. Solid curve – fitted using (V.9), where $m(z) = m_0 \exp[-D_{eff} (2\pi/\lambda)^2 z/a]$. Dashed curve ($SO_4^{2-}$ and Cl^-) – fitted from the numerical diffusion model (V.13). Dotted curve (SO_4^{2-}) – output from the connected vein diffusion model driven by grain growth (V.27).

(table V.1). The diffusion coefficients found to fit $\overline{m}'_z$ best are close to those determined using (V.9); they can be seen in table V.1 and the model outputs are plotted in figure V.6. The model was not significantly sensitive to changes in initial peak shape.

V.2.4. Discussion

Although here we only consider the top 350 m, where climate and layer thickness change little, it seems as if the process continues with depth. Sulphate data are not yet available for the last interglacial period (around 1650 m, 130 kyr); however dielectric profiling (DEP) data have been collected; DEP peaks are normally congruent with sulphate peaks [*Udisti et al.*, 2000]. When comparing signals from very different depths care must be taken since temporal resolution is lost due to layer thinning. However DEP peaks at 1650 m are typically around 0.30 m width, which would represent over 20 years, while peaks in previous interglacials are even broader and much more attenuated in amplitude (E. Wolff, personal communication, 2002).

Observation of aerosol loading in the stratosphere shows decay rates for eruptions of significantly varying magnitude are broadly similar; the full width half maximum (FWHM) atmospheric loading is about 2 years [*Rosen et al.*, 1994]. Typically the signal lasts about three years above the background level; this has been confirmed for volcanic events over the past 700 years by study of the high accumulation (700 kg m^{-2} yr^{-1}) ice core at Law Dome, Antarctica

[*Palmer et al.*, 2001]. This can be compared with the example peak widths in figure V.2 where broader signals are seen in deeper ice.

It is not clear whether volcanic activity throughout the Holocene has continued at a constant rate. This is often implicitly assumed and has been found to be the case for the last 1000 years [*Roscoe*, 2001]. However Cole-Dai *et al.* [*Cole-Dai et al.*, 2000] have inferred an increase in volcanism over the past 4000 years by examining large sulphate peaks from an East Antarctic core (Plateau Remote). Increased explosive volcanism compared to the present was also noted in the northern hemisphere at the transition from the last ice age up to 6000 years before present [*Zielinski et al.*, 1997]. A change in volcanic activity will obviously influence the variability of the signal, and the fluxes of acid reaching the site. It is clear on comparison with figure V.1 that the rescaled sulphate profile (figure V.6) is partially influenced by volcanic activity because the two main sources of sulphate (biogenic background and volcanic) vary independently. Consequently diffusion estimations for sulphate made using the original data in figure V.1 could be more appropriate but do not significantly chage our conclusions.

Layer thinning will increase the spatial concentration gradient across chemical peaks as the signal is compressed; by the bottom of this section (z = 336 m) a layer is 88% of its original ice equivalent thickness. This could allow more rapid diffusion than we measure on un-thinned ice equivalent depth scale where the peaks at lower depths are 'stretched' back to their un-thinned shape.

To establish unequivocally whether the diffusion apparent here is a real phenomenon in this section of core, analysis of a similar chemical signal from an ice core with a differing accumulation rate is required. As long as the content of the profiles from the differing cores is dominated by the same climatic signal then direct comparison of chemical peak shapes would yield the effective diffusivity.

V.3. Diffusion mechanisms

This section discusses the possible arrangements of the impurities in ice, and develops two mechanisms by which impurities could be transported. One considers liquid transported through veins under the action of grain growth, and the other considers liquid confined to disconnected clusters. We concentrate on the example of sulphuric acid. The phases and distribution of impurity, which will determine the pathways available for transport, are considered initially.

V.3.1. Impurity phase and distribution

V.3.1.1.Vapour phase. Vapour transport might be expected in the upper layers of ice through the pore space between the crystals, in particular if the surfaces of the crystals were coated

with the impurity. Below the pore close-off depth (z ~ 71 m) vapour diffusion would be exclusively confined to the insides of bubbles and hence negligible. However the partial vapour pressure of sulphuric acid is extremely low at -53.5 ° C [*Gmitro and Vermeulen*, 1964], such that the ratio of acid molecules in the vapour phase to the liquid phase is $< 10^{-14}$ in firn where $v = 0.5$ and $c = 1$ μM. If the diffusivity of sulphuric acid vapour in air is ~ 10^3 m^2 yr^{-1} (approximated from the diffusivity of water vapour in air) then the effective diffusivity of sulphuric acid in ice through the vapour phase is negligible ($< 10^{-11}$ m^2 yr^{-1}). Examination of $\overline{m}_z'$ in figure V.6 indicates that peak broadening continues at a similar rate after the pore close off depth, further confirming that vapour diffusion of sulphuric acid is not a dominant mechanism.

Hydrochloric acid is considerably more volatile than sulphuric acid, and this may in part explain its greater diffusivity. Significant quantities of HCl are thought to be lost through the vapour phase from top few metres of the firn at Dome C [*Traversi et al.*, 2000]. It seems plausible that transport is occurring in the upper part of the core ($z < 71$ m) however there is too much scatter for certainty (figure V.6).

V.3.1.2.Solid phase. Observation of concentrated liquid sulphuric acid at triple junctions in cold polar ice with relatively low bulk concentrations ($c = 7.5$ μM) e.g.[*Mulvaney et al.*, 1988] allows an estimation of its solubility limit in the ice. The bulk concentration, c, is related to the volume fraction of liquid in the ice, f, by:

$$f = \frac{c - c_i}{c_v - c_i} \tag{V.10}$$

where c_i is the concentration of solute dissolved in the lattice, and the concentration of liquid in the veins, c_v, is determined to a first order by temperature of the ice (c_v ~ 4.3 M at Dome C). Solute will diffuse from the veins into the lattice until it is saturated or $f = 0$ (with an estimated diffusion length of $l = 0.2$ mm and if sulphate diffusivity is of the same magnitude as the self diffusion of water, D_{H2O} ~ 10^{-10} m^2 yr^{-1} this could occur within about 400 years at Dome C). Therefore at equilibrium a lattice solubility limit $< 10^{-5}$ M is indicated when $f > 0$ contradicting a recent study finding a solubility limit of 112 μM in laboratory ice [*Trickett et al.*, 2000].

A similar argument holds if the concentration in the lattice is determined not by absolute solubility but by the ratio of solute concentration in ice to concentration in liquid, described as the equilibrium distribution coefficient:

$$k_{eq} = c_i / c_v \,. \tag{V.11}$$

The volume fraction in the veins is then:

$$f = \frac{c - k_{eq}\, c_v}{c_v - k_{eq}\, c_v} \tag{V.12}$$

Values of k_{eq} often quoted at ~10^{-4} [*Alley et al.*, 1986a; *Dash et al.*, 1995] would preclude liquid being present in veins at bulk concentrations $c < 430$ μM, which is contrary to observation of liquid

filled veins implying $k_{eq} < 2 \times 10^{-6}$. We therefore conclude that it is unlikely that a significant concentration of SO_4^{2-} is in the lattice.

Even if substantial quantities of sulphate ions were dissolved in the lattice, they could not diffuse fast enough to explain the observed movement. D_{eff} is ~ 10^{-8} m^2 yr^{-1} (section V.2.3.) compared to the self diffusivity in ice $D_{H2O} = 2.7 \times 10^{-10}$ m^2 yr^{-1} at -53.5 ° C [*Ramseier*, 1967] which we use as an upper bound for the diffusivity of sulphate ions in the lattice. The diffusivity of interstitial defects which might contain sulphate ions is even lower: 8×10^{-12} m^2 yr^{-1} at –53.5 °C [*Petrenko and Whitworth*, 1999].

The thermo-dynamics of hydrochloric acid in ice were considered by Thibert and Dominé [1997], who found that solid ice is slightly soluble to hydrochloric acid (k_{eq} ~ 3.5 10^{-4} at –53 °C) and that its diffusivity through a single crystal is about 3×10^{-9} m^2 yr^{-1}. Although a significant proportion of the hydrochloric acid could reside within the lattice direct diffusion through the solid would be too slow to explain the observed diffusion (~ 2×10^{-7} m^2 yr^{-1}).

V.3.1.3 Liquid phase. The eutectic point of sulphuric acid is at –73 °C [*Gable et al.*, 1950], so it is possible for the acid to exist as an aqueous solution within the ice at Dome C. The diffusion coefficient of sulphate ions in water at –53 °C is estimated to be $D = 7 \times 10^{-2}$ m^2 yr^{-1} [*Weast*, 1977-1978], significantly greater than D_{eff}. Consequently a mechanism where impurity moves within the liquid phase seems the best candidate for describing the observed peak broadening. We must first consider how liquid can be arranged in the ice.

V.3.1.4.Liquid distribution. The liquidus relation defines to a first order the concentration of liquid acid in the ice with varying temperature. This is plotted as far as the eutectic point at which the whole mixture freezes, in figure V.7 [*Gable et al.*, 1950; *Weast*, 1977-1978]. The temperature of the Dome C bore hole in the upper 350 m is –53.5 °C, so the concentration of liquid sulphate in the veins will be c_v ~ 4.3 M regardless of c. It is the volume fraction of liquid in ice that varies with bulk concentration. If the impurities were not mixed, H_2SO_4 and HCl (if it is not dissolved in the lattice or the lattice is saturated) should be in the liquid form while NaCl should be solid since it is below its eutectic temperature of –21 °C. Although low temperature phase compositions for mixtures of these impurities are not known the absence of diffusion noted in figure V.6 strengthens the hypothesis that sodium is 'locked' in the solid phase

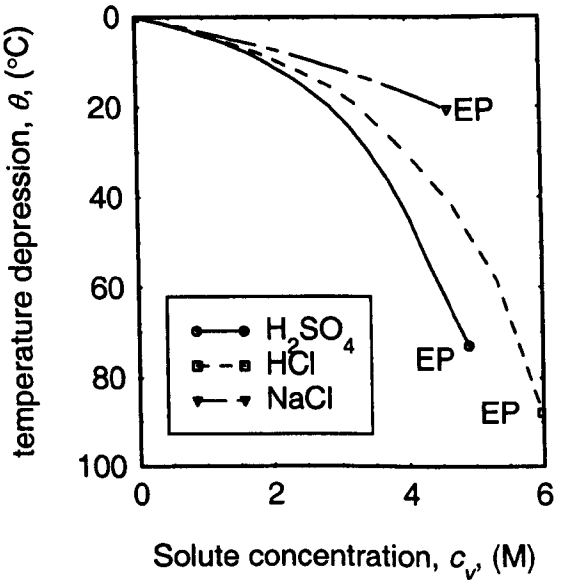

Figure V.7. The liquidus relations for sulphuric acid, hydrochloric acid and sodium chloride solution, the eutectic points are marked: EP, [*Pickering*, 1893; *Weast*, 1977-1978]. To a first order the surrounding temperature determines the concentration of the impurity solution trapped in the ice.

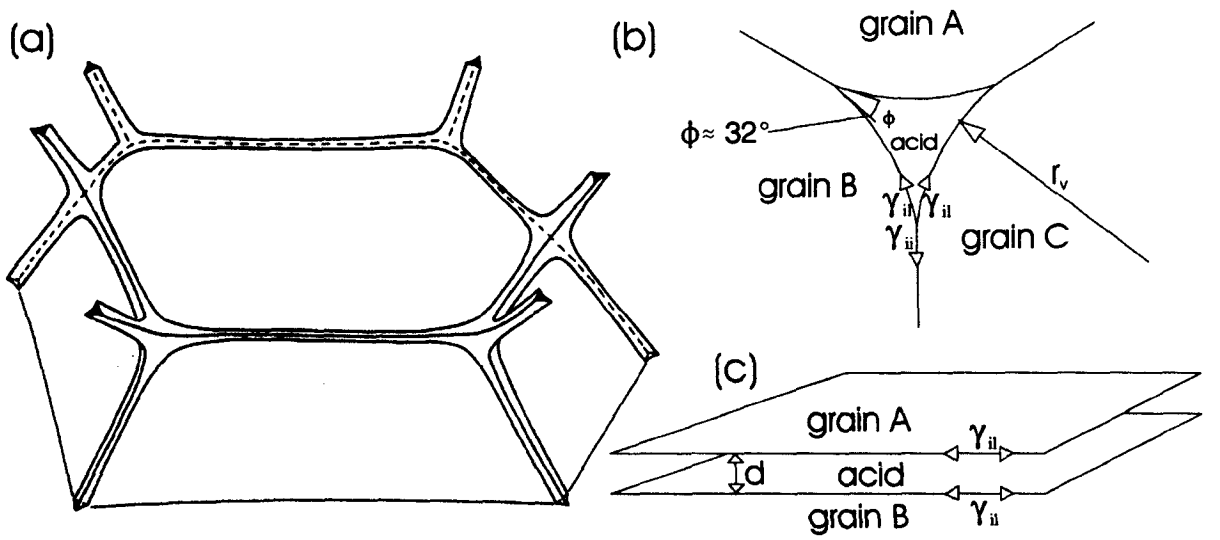

Figure V.8. **(a)** The connected vein system where dihedral angles $\phi < 60$ °, not to scale, and **(b)** a cross-section of a vein, also not to scale (from Nye [1989]). **(c)** The arrangement of acid at a grain boundary, not to scale. The surface free energies for the ice-ice and ice-liquid interfaces are indicated by the arrows γ_{ii} and γ_{il},. The radius of vein curvature is indicated by r_v and the thickness of the grain boundary by d.

Studies have shown sulphuric acid to exist in veins at the triple junctions between grains of polar ice in some samples [*Fukazawa et al.*, 1998; *Mulvaney et al.*, 1988]. Theoretical studies by Nye [1991a] and laboratory studies by Mader [1992b] have addressed the implications raised by the existence of liquid in veins in polar ice (figure V.8). A more recent study by Rempel *et al.* [2001a] showed that the temperature gradient of an ice sheet causes a liquid concentration difference in a network of connected veins that could allow the migration of the chemical profile like a moving wave. Other recent work by Cullen and Baker [2000] and evidence presented in chapters III and VI suggests that some impurities are also located in films at grain boundaries. It is also likely that some impurity forms a liquid layer coating the inside of bubbles. The occurrence of liquid at grain boundaries will be dependent on the relative free energies of the ice-ice interface, γ_{ii}, and the ice-liquid interface, γ_{il} (~34 mJ m^{-2}), which are not well established for the bore hole temperature. It is also not established whether liquid in veins or grain boundaries is connected throughout the ice sheet; this will be related to relative interfacial energies and the lattice solubility.

V.3.1.5.Vein structure. Pressure, solute concentration and curvature [*Woodruff*, 1973] components contribute to the total temperature depression of the freezing point in a vein, θ; at 0 °C it is given by Mader [1992b] as:

$$\theta = \frac{T_0}{L_f}\left(\frac{1}{\rho_i} - \frac{1}{\rho_l}\right)p + \frac{RT_0}{L_f}c_v + \frac{\gamma_{il}T_0}{L_f}\frac{1}{r_v} \qquad \text{(V.13)}$$

where T_0 is the melting point of pure ice (273.16 K), L_f is the latent heat of freezing (306 MJ m^{-3}), ρ_i and ρ_l, are the densities of ice and water respectively, R is the universal gas constant (8.314 J K^{-1} mol^{-1}), c_v is the concentration of solute in the veins (mols m^{-3}). Note that r_v (the radius of curvature of the vein faces) is related to the area of cross section of the vein, σ, by a geometric factor α such

that $\sigma = \alpha r_v^2$. The value of α is determined by the dihedral angle of the veins; a generally accepted mean value for polar ice is $\alpha = 0.0725$ [*Nye*, 1991a].

In this study we can neglect the effects of overburden pressure melting which is insignificant over depths scales corresponding to typical signal periods ($dT/dP = 0.0074$ °C/bar; so the freezing point is depressed a further 3×10^{-4} °C over a depth of 0.5 m in ice). The ideal solution term (second term on the right hand side of (V.13)) is unsuitable for the temperatures observed at Dome C since it diverges from the observed liquidus relation. We use a linear interpolation of the liquidus relation for sulphuric acid (figure V.7) at the temperature of interest (approximately -53 °C), so that the temperature depression is given by:

$$\theta = \frac{c_v - 2715}{29.4} + \frac{\gamma_{il} T_0}{L_f} \frac{1}{r_v}. \qquad \text{(V.14)}$$

The concentration in a vein, c_v, is related to the radius of curvature and the bulk concentration, c, by:

$$c_v = \frac{c}{\lambda \alpha r_v^2} \qquad \text{(V.15)}$$

where λ is the vein density, i.e. the length of vein per unit volume of ice (m^{-2}). Since θ is defined by the temperature of the surrounding ice, and is constant for the top 350 m of the core, we can find the concentration of the liquid in the veins if λ and c are known at a particular depth. By substituting r_v from (V.15) into (V.14), and solving we get:

$$c_v = \left[\tfrac{1}{2}\left(\sqrt{B^2 + 4(29.4\theta + 2715)} - B\right)\right]^2$$

where (V.16)

$$B = \frac{29.4 \gamma_{il} T_0}{L_f} \sqrt{\frac{c}{\alpha \lambda}}.$$

For the case of liquid at grain boundaries rather than just at triple junctions, the curvature term (third term on right hand side) in (V.13) can be substituted by a term that describes the depression of the freezing point as the thickness of the liquid layer, d, decreases. This is due to the action of electrostatic forces such as Van der Waals between the interfaces [*Dash et al.*, 1995]. It follows that since in this case $\gamma_{ii} \geq 2\,\gamma_{il}$, as the film thickness increases, the surface energy of the whole boundary decreases from $\gamma_{ii} \rightarrow 2\,\gamma_{il}$, which requires an increase in the solute concentration for the film to remain liquid. The subsequent model results in section V.3.4.1 are therefore qualitatively applicable to liquid at grain boundaries as well as liquid in veins.

It is also likely that some solute may be located in liquid layers on the inside of air bubbles and possibly also coating dust particles. The implications of this possibility will not be explored in this work.

V.3.2. Transport mechanisms

The presence of liquid in an ice sheet does not in itself imply an obvious mechanism for the movement of solute. There is no significant temperature gradient in this part of the core so concentration of solute in the vein network is constant to the first order. Two distinct possibilities arise; one is that the acid located in veins or at grain boundaries forms a network of connected pathways throughout the ice through which solute could move. The other is that the liquid filled veins or grain boundaries are not fully connected, and are scattered throughout the ice sheet in pinched off clusters of varying size. We propose a mechanism for each case to account for the observed peak broadening. The driving force for both models is normal grain growth, without which very little change would be expected in the chemical profile. Both consider liquid to be located at veins, although they are qualitatively applicable for liquid at grain boundaries, which is a more plausible distribution in the shallow firn (chapter IV).

If the impurities are located in a connected network of veins or grain boundaries, then grain growth can induce variation in liquid concentration. Presuming solute concentration inhibits grain boundary movement then this first mechanism (section V.3.3) can describe the observed diffusion remarkably well. For the case where grain growth is not inhibited by soluble impurity a second mechanism is also proposed where we infer that the liquid impurity may not be fully connected in most parts of the ice sheet. This mechanism (section V.3.4) allows solute movement in regions of high concentration, but only limited movement in sections of low concentration. As grain growth continues the likelihood of solute movement increases throughout the ice; a rough estimate of the mechanism's effective diffusivity is also close to the observed diffusion.

Study of the detailed microstructure of ice will help to determine the most likely of the mechanisms. There may be other plausible mechanisms for diffusion not considered here, perhaps involving a limited lattice solubility, where the veins act as pathways for diffusion into and out of grains in different concentration regions. However it is hard to envisage how impurity in veins could exist detectably under such circumstances.

V.3.3. Connected model

A connected network of veins implies that, if the temperature is constant, the concentration of liquid in all the veins should be close to equilibrium. Variation in the bulk concentration, c, can then only be accounted for by variation in the volume fraction of liquid f. If we take the simplest case where ice is insoluble to sulphuric acid so that $c_i = 0$ then $f = c / c_v$ (see (V.10)). A chemical peak in $c(z)$ can then either be accounted for by an increase in the vein cross section, σ, with a corresponding increase in r_v, or there must be an increase in the vein density, λ (vein length per unit volume), with a corresponding decrease in the crystal size (figure V.9). Variation in f by differing vein diameters is unstable since differences in r_v imply the existence of concentration gradients, (V.15) and (V.16), leading to the loss of bulk variation within decades. If the impurity is connected

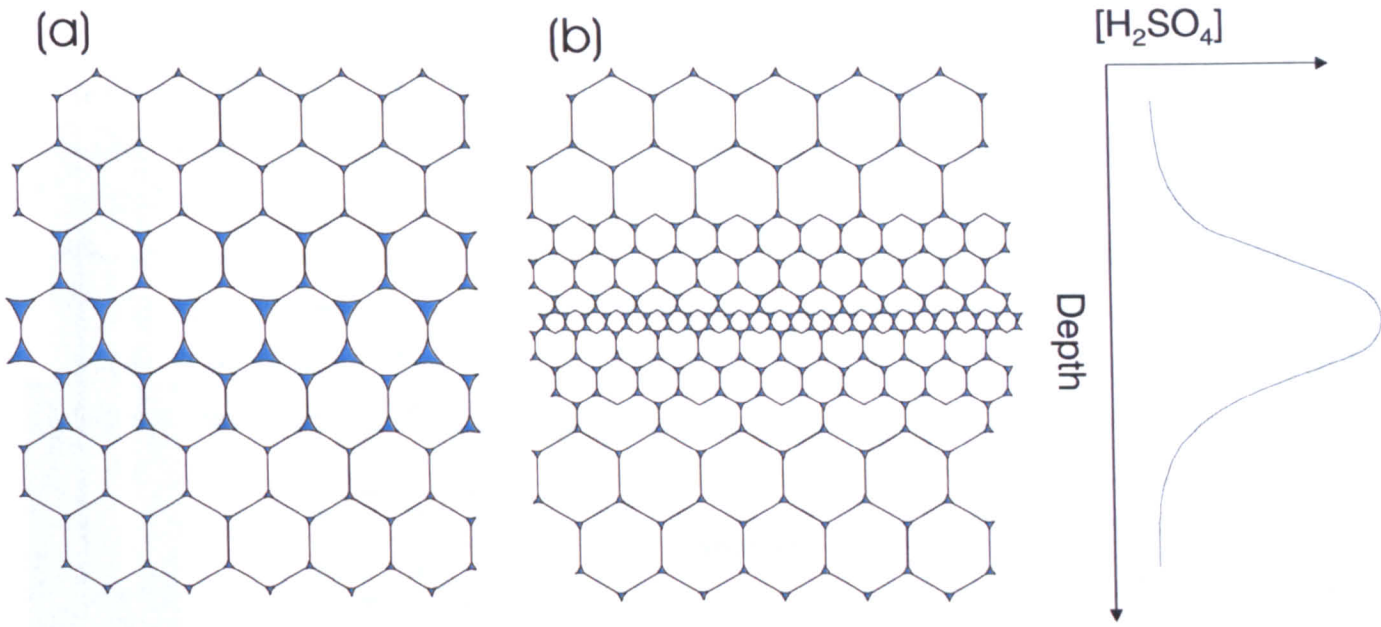

Figure V.9. Schematic cross-section of the possible arrangements of liquid filled veins (at the vertices of grain boundaries) across an acidic peak in a connected system. A schematic of the concentration profile is shown on the right hand side. (**a**) The vein radius of curvature, r_v, and area of cross-section, σ, increase to accommodate the higher bulk concentration, or (**b**) the increased volume of liquid is distributed in a higher vein density, λ, where all veins have a similar r_v, but the grain size is correspondingly smaller.

in the liquid phase there must be a variation in crystal size and λ to accommodate fluctuations in c. At equilibrium under such a situation there is no concentration gradient to move solute, and thus we would expect the chemical signal to remain fixed. Evidence exists to suggest that grain size is anti-correlated with impurity content, and could affect grain growth rates causing variation in grain size [*Alley et al.*, 1986b]. In addition recent work on laboratory ice indicates sulphate ions impede grain growth rate a temperature of -20 °C (Azuma, Takeda and Inoue, *ICE*, 2002 issue 2). However work by Weiss [2002] on the Dome C core showed that soluble impurities are much less significant in influencing grain growth rate than previously thought, variation being primarily correlated to dust content.

This first model proceeds by assuming that at an early stage during the deposition process the presence of sulphuric acid inhibits grain growth such that λ correlates with c. The mean grain area, A, increases linearly with time [*Gow*, 1969]:

$$A = A_0 + Kt \tag{V.17}$$

where A_0 is the initial size of the grains and t is the time since deposition ($A_0 = 0.8$ mm^2 at Dome C [*Duval and Lorius*, 1980]). We estimate the dependence of the grain growth rate, K, on impurity content using the relation described by Alley [1986a] where:

$$\frac{1}{K} = \frac{81}{32 \cdot \gamma_{ii}} \left(M_i^{-1} + \alpha_{ib} \cdot c_f \right), \tag{V.18}$$

M_i is the intrinsic mobility of a grain boundary and is dependent on temperature, and α_{ib} is the impurity-boundary interaction parameter, and $c_f = 18 \times 10^{-3} \times c$, is the atomic fraction of impurity in the ice (where c is the concentration in M). At Dome C, $M_i = 7.2 \times 10^{-16}$ (m s^{-1})/(N m^{-2}), and α_{ib} = 7.5×10^{22} (N m^{-2})/(m s^{-1}) for chloride ions [*Alley et al.*, 1986a]; we here use this value as an

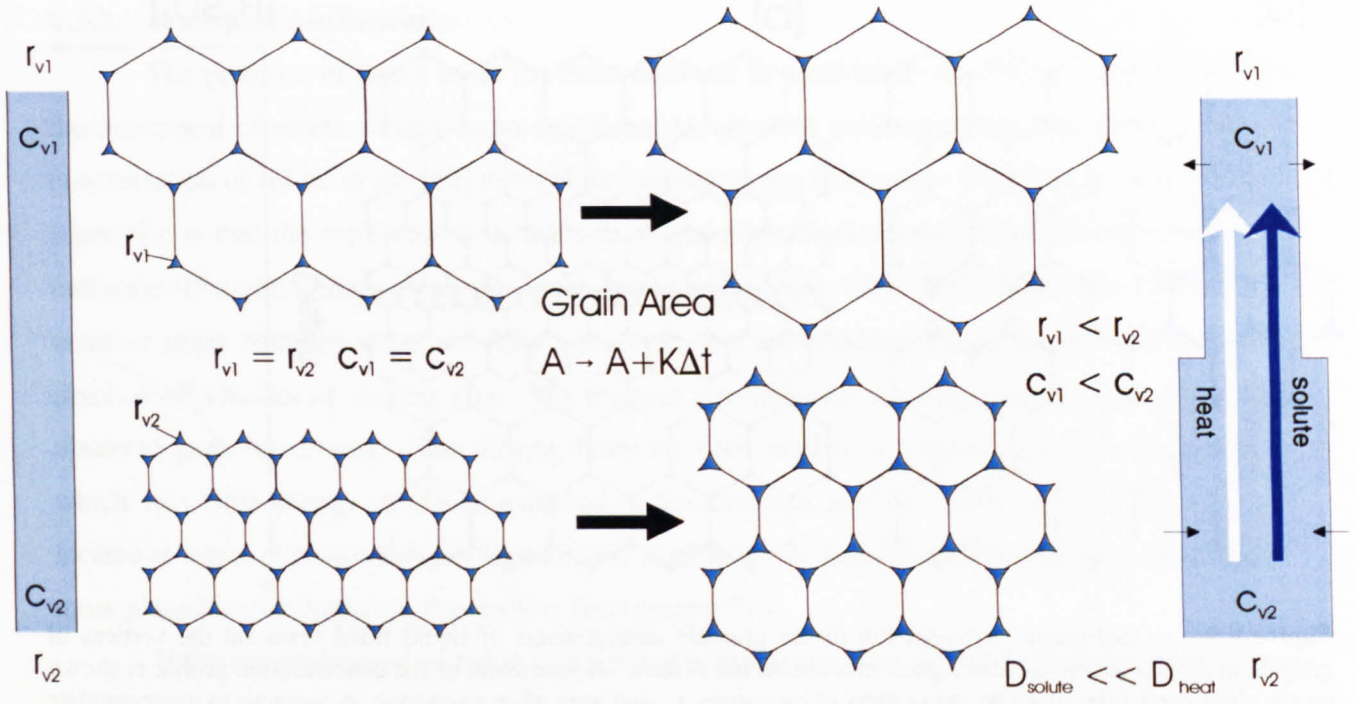

Figure V.10. Impact of grain growth on vein size in the connected grain growth model, schematic cross-section. Two sections of ice with vein radius r_{v1} and r_{v2}, and vein concentration c_{v1} and c_{v2} that initially have veins of equal radius but differing grain size undergo constant grain growth. The resulting imbalance of vein radius causes the diffusion of solute and heat along the veins, where diffusivities are denoted by D.

estimate of the impact of sulphate ions on boundary drag. As the grains grow the mean vein density is reduced; following Nye [1991a] we set $\lambda \approx 3 / A$, so that using (V.17) vein density changes according to:

$$\lambda \approx 3\left(\frac{3}{\lambda_0} + Kt\right)^{-1} \tag{V.19}$$

where λ_0 is the initial vein density, and the proportional rate of change of the vein density is:

$$\frac{1}{\lambda}\frac{\partial \lambda}{\partial t} = -K\left(\frac{3}{\lambda_0} + Kt\right)^{-1} \tag{V.20}$$

Note that vein density will decrease more rapidly in a region with a higher value of λ_0 (i.e. smaller grains) than a region starting with a lower vein density despite inhibition of growth rate by impurity. Applying (V.15) and (V.16) after grain growth has occurred shows that any differences in $(1/\lambda)\partial\lambda/\partial t$ cause perturbations in σ and r_v with corresponding perturbations in the vein concentration c_v; this is shown schematically in figure V.10. Slight variation in c_v will allow diffusion through veins towards equilibrium, however during continued grain growth equilibrium cannot be reached because vein densities in sections of different concentration alter at different rates causing further perturbations in c_v. Under conditions where the impurity-boundary interaction parameter, α_{ib}, is small enough (as is the case when using the parameter for Cl^-) the net result is a movement of solute away from regions of high bulk concentration in chemical peaks. The following numerical model demonstrates the effect.

Initial conditions are determined using the initial bulk concentrations for peaks as used in the numerical diffusion model in section V.2.3. All variation in c is assumed to be correlated to λ so that initially r_v and c_v are constant and are determined using (V.15) and (V.16). The time step used was $\Delta t = 25$ yr, the local depth increment was $\Delta z' = 0.01$ m, $\gamma_{ii} = 34 \times 10^{-3}$ J m^{-2} [*Nye*, 1991a], K is calculated using (V.18). The mean value of $A_0 = 0.8 \times 10^{-6}$ m^2 gives a mean $\lambda_0 = 3.75 \times 10^6$ m^{-2}. For each time step the new values of λ are calculated across the peaks, this gives rise to new values of c_v which are recalculated from (V.16). A diffusion step is then run to find the new distribution of c; the following was discretised:

$$\frac{\partial c}{\partial t} = \frac{v}{3} D \frac{\partial}{\partial z}\left(\frac{c}{c_v}\frac{\partial c_v}{\partial z}\right), \tag{V.21}$$

and given by:

$$c_j^{n+1} = c_j^n + \frac{1}{2}\frac{vD}{3}\left[\left(\frac{c_j^n}{c_{v\,j}^{\,n}} + \frac{c_{j-1}^n}{c_{v\,j-1}^{\,n}}\right)\left(c_{v\,j-1}^{\,n} - c_{v\,j}^{\,n}\right) - \left(\frac{c_{j+1}^n}{c_{v\,j+1}^{\,n}} + \frac{c_j^n}{c_{v\,j}^{\,n}}\right)\left(c_{v\,j}^{\,n} - c_{v\,j+1}^{\,n}\right)\right]\frac{\Delta t}{\Delta z'^2} \tag{V.21a}$$

where the factor of 1/3 takes into account the proportion of veins orientated vertically. D is the diffusivity of sulphate ions in water at –53 °C ($D = 7 \times 10^{-2}$ m^2 yr^{-1} [*Weast*, 1977-1978]). The gradient, m, of a typical peak (with an initial gradient of m_0, table V.1) diffused in the model can be seen in figure V.6 (from the change in c seen in figure V.11) and it corresponds reasonably well to the observed change in $\overline{m}_z'$. This gives us confidence that if the veins in ice are connected it is

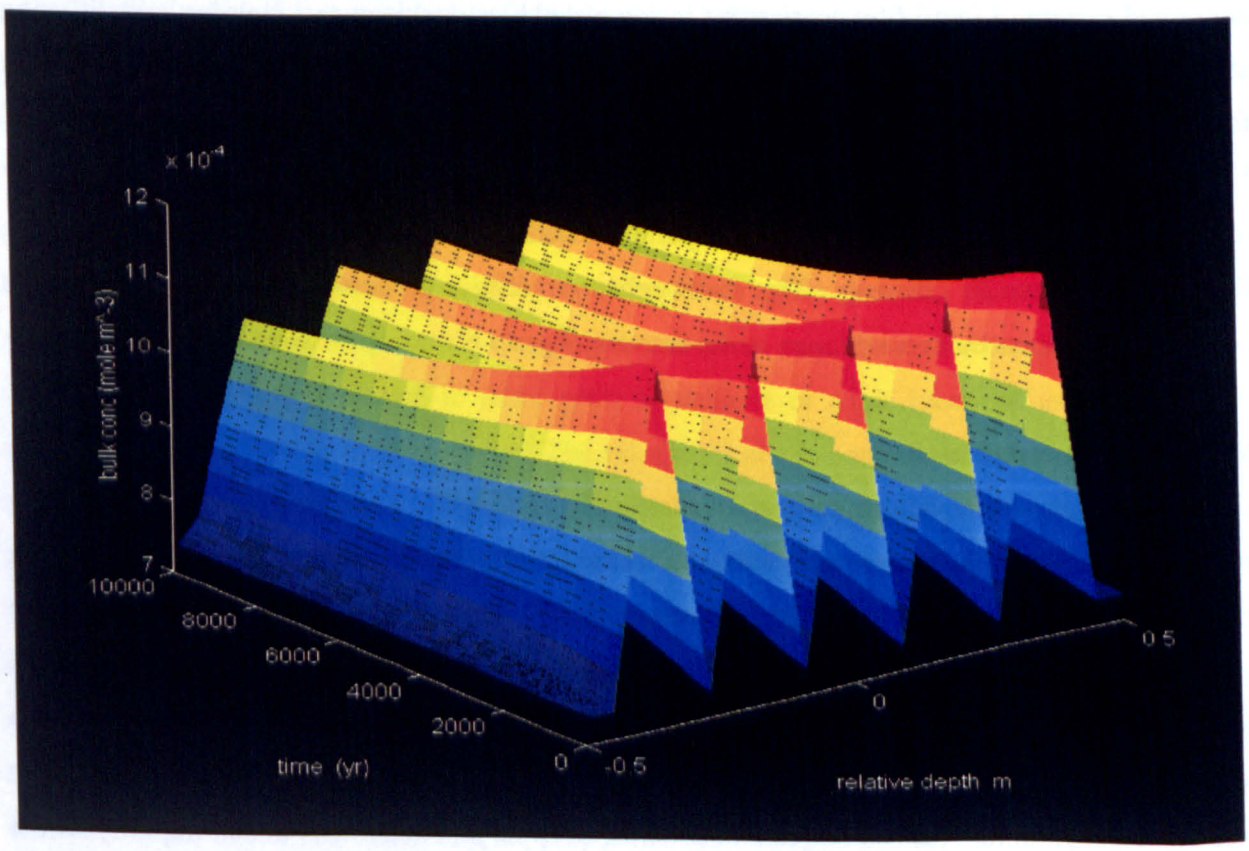

Figure V.11. The evolution in time of regularly spaced bulk concentration (c) sulphuric acid peaks with time under the influence of normal grain growth. Note the reduction in peak amplitude.

possible for grain growth to instigate solute movement along veins at a rate comparable to that observed at Dome C. Diffusion by this mechanism yields an effective diffusion coefficient, D_{eff} = (5 – 7) × 10^{-8} m^2 yr^{-1} from the methods outlined in section V.2.3. This value is remarkably close to the observed diffusion, given the number of estimations included in the model. The model is sensitive to variation in the growth inhibition parameter, α_{ib}. If α_{ib} is doubled, D_{eff} changes by a factor of 0.6 and if α_{ib} is halved D_{eff} increases by a factor of 1.5. Variation in the initial conditions of grain size (and hence λ) also has a significant impact on the model output. If no variation in grain size is assumed initially, then the corresponding large variation in r_v causes a very rapid diffusion in the first 1000 years corresponding to D_{eff} ~ 6 × 10^{-7} m^2 yr^{-1}. After this much of the initial variation in bulk concentration is lost and D_{eff} soon drops to around 10^{-8} m^2 yr^{-1}.

Using this mechanism we can predict the future shape of a peak in the upper layers of the firn. The upper left hand plot in figure V.2 shows the current shape of the sulphate signal from the Tambora eruption at Dome C and its profile in 11000 years time if the normal grain growth continued with solute movement occurring by the above mechanism. The initial conditions assume variation in grain size across the peak.

The model cannot be considered realistic for veins in the upper part of the firn; at these depths an interconnected vein network will not exist at least until the volume fraction of ice in the firn is v = 0.435 – 0.59 [*Shabtaie and Bentley*, 1994]; connection can be expected between grain boundaries however, although the role of ice-air interfaces is not fully understood. Tortuosity is not included in the model and could reduce effective diffusion rates particularly in a less well connected system. Liquid film coating the inside of bubbles could act as a sink for acid diffusing in from the adjacent veins, possibly slowing peak broadening by more than just the correction factor v. It is interesting to speculate on the impact of the mechanism proposed by Rempel *et al.* [2001a] when applied to the strong annual temperature variation on impurities in the upper layers of firn. One might expect the solute to be 'pumped' both upward and downward cyclically by the fluctuating temperature gradients. This could enhance diffusive processes in the top section of the core as the solute encounters variation in the amount of grain boundary or vein for its location.

V.3.4. Disconnected model

There is some evidence to suggest that liquid confined to veins or grain boundaries may not be fully connected (many triple junctions and grain boundaries observed under the scanning electron microscope appear to be free from impurity). Weiss *et al.* [2002] did not note large variation in grain size across volcanic peaks and this suggests that if there is liquid it may not be connected vertically in the core since without variation in crystal size a connected vein or grain boundary network would be an unstable configuration for bulk chemical variation to persist (section V.3.3.). In this case some grain boundaries of triple junctions will contain impurity whilst others will remain impurity free.

The theory of percolation in random lattices can be used to describe the connectedness of a system [*Stauffer and Aharony*, 1992]. When a critical fraction (P_c) of sites in the system or lattice are occupied they form a continuous connected pathway through the lattice that is then said to percolate. The change from disconnected to connected or percolating occurs abruptly with only a small change in the site occupation probability, P. Polycrystalline ice can be considered as a lattice of grain boundaries surrounding ice crystals or the triple junctions connecting them. Shabtaie and Bentley [1994] applied this idea to model ice grain boundaries or triple junctions as a lattice of connected conductors where conducting pathways were broken by the removal of sites due to air bubbles.

Consider lattice points formed by either grain boundaries or triple junctions that are empty if they do not contain impurity. If adjacent sites are filled, they are said to be connected, and form part of a cluster. The process of normal grain growth removes sites from the lattice. We hypothesise that in the case of filled veins or grain boundaries (modelled as occupied sites in a lattice), the dimensions of connected clusters increase during grain growth. This is modelled by the removal of sites from the lattice with a corresponding movement of impurity from removed sites to neighbouring ones. This effect could explain the observed peak broadening in a poorly connected network.

To demonstrate the concept, a two-dimensional square lattice is used (this has a co-ordination number of 4 similar to a vein network). Sites are randomly filled according to an occupation probability P; a higher density of occupied sites (initially containing an arbitrary concentration value of 1 as opposed to 0) represents a higher concentration of impurity in the ice. A chemical peak is described by varying P with depth, see the thick solid curve in figure V.12, the thin curve represents the normalised sum of all the points in that row of the lattice. Any adjacent filled points are connected together in a cluster. The content of the cluster (sum of its points) will adopt the mean value of all its points to simulate the equilibration in vein size referred to in section V.3.3. Removing sites from the lattice then represents grain growth. If an occupied site is removed, its contents jump randomly to a neighbouring site regardless of whether it is filled, this represents liquid being relocated to other grain boundaries or triple junctions as the grain they surrounded is 'swallowed up' by others. The relocation of the contents of filled sites may cause some clusters to re-equilibrate as they receive the contents of previously unconnected sites. By this process, regions of high concentration are spread, mimicking the broadening of chemical peaks. The evolution of a 2D lattice can be seen in figure V.12, where bright squares in the lattice represent filled sites, although the brightness of the square not its size, represents the site concentration. To assess this mechanism applied to a network of veins or grain boundaries (sites) in an ice sheet where the individual sites may either contain impurity or no impurity (filled or unfilled) we must first determine how the proportion of filled sites will vary with grain growth.

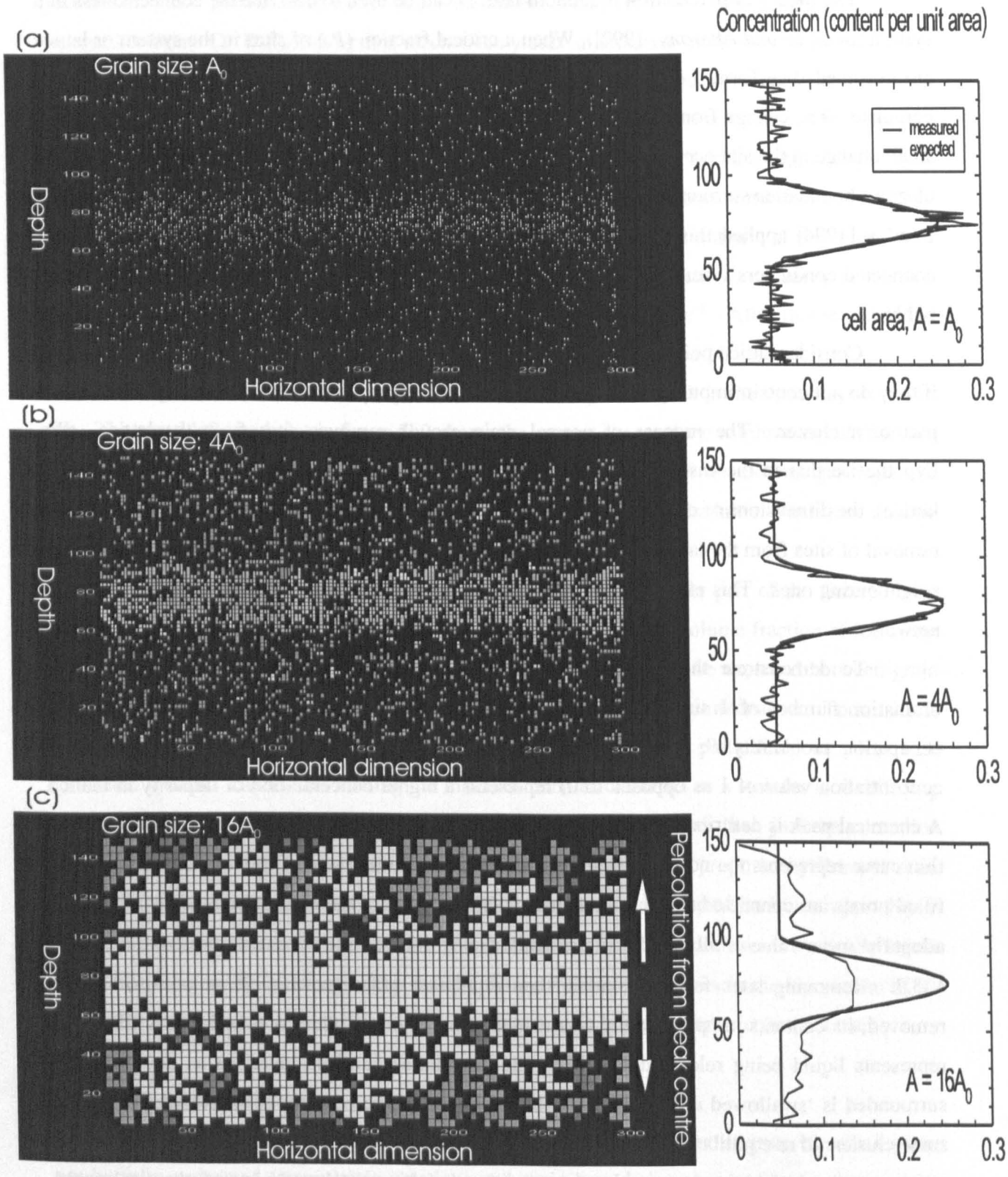

Figure V.12. Peak broadening by percolation in a two-dimensional lattice during grain growth of a disconnected system. The blocks on the left hand side represent a two dimensional lattice of sites in which a bright square indicates a filled site. The vertical axis represents the vertical spatial dimension and the horizontal axis represents a horizontal spatial direction. The occupation probability of a site is given by P, which varies across the peak (bold line). The normalised summation of the contents of each horizontal row in the lattice models the impurity concentration at that depth (fine line). **(a)** The initial distribution of filled sites in the lattice simulates a chemical layer in ice. The initial grain size corresponding to a site is A_0. Two grain-growth steps increase the grain size of the lattice from A_0 to $4A_0$ **(b)** and $16A_0$ **(c)** with the resulting movement of site contents through connected clusters to cause a peak broadening.

content of the lattice is conserved the total number of lattice sites is not; so removing a filled site from the lattice does not remove its contents, which must move to an adjacent site. A small fraction, ΔF, of the total number of sites in the lattice is then removed (representing grain growth). For any site that is randomly removed from the lattice there are the following possibilities: (a) the removed site was empty, (b) the removed site was filled and its contents jump to a neighbouring empty site and (c) the removed site was filled and its contents jump to a neighbouring filled site. The probability of each of these events is given by:

$$(1-P) \tag{V.22a}$$

$$P\left(1-\frac{P-\Delta F}{1-\Delta F}\right) \tag{V.22b}$$

$$P\left(\frac{P-\Delta F}{1-\Delta F}\right). \tag{V.22c}$$

We are initially only concerned with whether a site is filled or unfilled, regardless of its total amount of content. The summation of the probability of each event multiplied by the fraction of sites that will be filled if the event occurs gives the expectation value of a site being filled after a growth step:

$$\overline{P} = (1-P)\left(\frac{P}{1-\Delta F}\right) + P\left(1-\frac{P-\Delta F}{1-\Delta F}\right)\left(\frac{P}{1-\Delta F}\right) + P\left(\frac{P-\Delta F}{1-\Delta F}\right)\left(\frac{P-\Delta F}{1-\Delta F}\right). \tag{V.23}$$

The removal of the fraction Δf sites gives a difference in the occupation probability:

$$\Delta P = \overline{P} - P$$

$$\Delta P = \frac{P\Delta F(1-P)}{(1-\Delta F)^2}. \tag{V.24}$$

N is the total number of sites in the lattice and $-\Delta N$ is the change in the number of sites such that $\Delta F = -\Delta N / N$, thus:

$$\frac{\Delta P}{\Delta N} = -\frac{P(1-P)}{N}\left(1+\frac{\Delta N}{N}\right)^{-2}. \tag{V.25}$$

Considering the ice sheet as a continuum we find:

$$\lim \Delta N \to 0 \quad \frac{dP}{dN} = -\frac{P(1-P)}{N}. \tag{V.26}$$

This can be rearranged and integrated to give:

$$\log P - \log(1-P) = \log C - \log N,$$

$$\frac{P}{1-P} = \frac{C}{N}, \tag{V.27}$$

where C is a constant of integration. Given that initially $P = P_0$ and $N = N_0$ and $F = N/N_0$ is the fraction of sites remaining after grain growth, then:

$$P = \left[1 + F\left(\frac{1 - P_0}{P_0}\right)\right]^{-1} . \qquad (V.28)$$

Using the grain size, A, we approximate the site density (the number of possible sites per unit volume) as $N \approx 3 / A^{3/2}$, so F may be found using (V.17):

$$F = \left(\frac{A_0}{A}\right)^{\frac{3}{2}} . \qquad (V.29)$$

If the distribution of filled sites remains close to random - a reasonable assumption if sites were removed randomly from the lattice - an estimation of the mean cluster length can be found using a standard percolation theory relation. The mean length of a cluster, L, (scaled by the lattice point dimensions, $A^{1/2}$) is approximated by [*Stauffer and Aharony*, 1992]:

$$L = \frac{A^{1/2}}{\left(P_c - P\right)^{\upsilon}} , \qquad (V.30)$$

where P_c is the critical site occupation probability and υ is an argument related to the geometry of the lattice. If impurities are located at grain boundaries then $\upsilon = 0.5$ and $P_c = 0.08$, if they are located in veins then $\upsilon = 1.35$ and $P_c = 0.435 - 0.59$ [*Shabtie and Bentley*, 1994]. In either case L increases rapidly as P increases towards P_c. This tells us that when P_c is reached in any particular section a connected cluster will be formed in which impurity concentration can equilibrate. Thus as grain growth occurs we expect P_c to be reached in the centre of a peak earlier than at its edges since the occupation probability is highest where the concentration is highest. In this manner impurity will spread away from the centre of the peak as the percolation probability is reached during grain growth, and cluster lengths increase around the peak. The movement of solute is limited by its ability to move from peaks where P has exceeded P_c to the surrounding background where $P < P_c$; it is apparent that cluster lengths in the background ice will dictate diffusive effects.

We now obtain an estimate for the effective diffusivity of the system. Given a background concentration in the upper core of 0.7 μM we can estimate the initial occupation probability, P_0, for the veins if the initial area of cross section of a vein is $\alpha r_v^2 = 1$ μm^2 and the mean grain size is $A \sim 1$ mm^2. We calculate P_0 by finding the length of filled vein using (V.15) and the total length of vein from $\lambda_{total} = 3/A$:

$$P_0 = \frac{\lambda_{filled}}{\lambda_{total}} \qquad (V.31)$$

With the above values $P_0 = 0.054$. The change in the mean cluster length during grain growth is then approximated by substituting (V.17), (V.28) and (V.29) into (V.30) using a constant rate of grain growth $K = 4 \times 10^{-4}$ mm^2 yr^{-1} [*Gow*, 1969] (figure V.13). Figure V.13 shows that there is a change in the cluster length, ΔL of around 18 mm over a period of 10000 years, giving an approximate D_{eff} (where $D_{eff} \sim \Delta L^2 / t$) of 3×10^{-8} m^2 yr^{-1}, close to the observed value for sulphate. This value is dependent on the value of P_0, which is here determined by the choice of crystal size

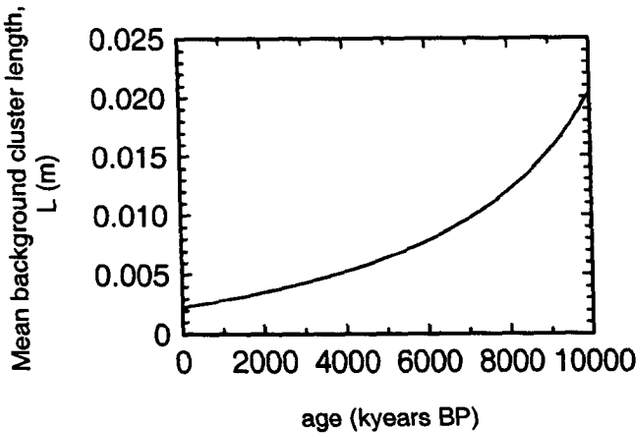

Figure V.13. The mean length of clusters of connected veins or grain boundaries in ice of background concentration against time, calculated from the discontinuous grain growth model.

and vein area. Note that diffusion within peaks for this method will be considerably higher than at its edges due to the variation in P (and consequently connectedness) across the peak. This implies much less solute movement will be observed in regions of low concentration than in regions of high concentration.

V.4. Conclusion

The chemical profiles at Dome C show evidence for post-depositional movement of sulphate and chloride ions but not sodium in the ice sheet. The observed diffusion rates indicate minimal loss in signal resolution and detail after 11000 years. Only events of a comparable magnitude to the background fluctuations in the sulphate and chloride signals are no longer detectable. There is however a reduction in the amplitude of the signal, as solute is transported to the surrounding ice, and this corresponds to some broadening. Caution is needed before drawing conclusions about factors where the relative concentrations and durations of peaks are important, particularly at low accumulation rate sites. For example the values of D_{eff} should be used to estimate the extent of the signal damping before assessing volcanism and eruption rates. The total volcanic flux (the integral of the peak concentration in terms of ice equivalent depth, kg km^{-2}) remains a reasonably robust measure of the magnitude of a signal for clearly defined volcanic peaks in this section of core. However total volcanic flux is likely to be underestimated in cases where the peak boundaries run into neighboring background peaks at the lower end of the section and for even older peaks in the ice.

Diffusion of either sulphate or chloride solely through the ice lattice is too slow to explain our observation, although vapour diffusion of HCl may explain peak broadening in the porous part of the core. Diffusion through the liquid phase seems the most plausible possibility; however, in ice of a uniform temperature, variation in the bulk concentration is matched by variation in liquid volume not concentration, so a liquid concentration gradient is absent.

We have developed two mechanisms for liquid solute movement. Both the proposed mechanisms rely on the process of grain growth to move solute. The similarity of the D_{eff} values from each model suggests that the growth rate is the variable controlling the observed effective

diffusivity in the core. If this link proves to be robust, grain growth rate could be a useful tool for assessing post-depositional change in cores at other sites.

Understanding the transport mechanisms that could be at work allows us to assess the extent of signal loss at depths greater than those observed here. In ice from the last glacial period we expect a lower proportion of the impurity at Dome C to be in the liquid phase, partly due to the neutralisation of acids by dust particles, a substantial proportion of which are found at grain boundaries (chapter III). This, compounded with a halt in grain growth due to the pinning of boundaries by the particles, would lead to a reduction in impurity mobility in these sections.

In previous interglacial ice grain growth does not continue indefinitely; maximum grain size is reached either by pinning or other factors, such as polygonisation caused by sheer stress and overburden pressure. We may expect to see residual structural detail remaining in the profile at substantially reduced amplitude in ice that is hundreds of thousands of years old. With the mechanisms proposed by this chapter, a halt to grain growth would also halt the movement of solute within veins or grain boundaries. If the net grain size began to reduce again then it is conceivable that chemical peaks could become sharper again if veins are connected. However when layer thinning continues even though grain size remains constant the result is that soluble impurity in a peak does not experience the vertical strain of the ice surrounding it. This 'stretches' the duration of the peak in the time domain as the ice is thinned, so the diffusion length comes to represent an increasing age increment. Analysis of high resolution records from greater depth should throw further light on the processes described here.

At very great depths near the bottom of the ice sheet, warmer temperatures will increase grain growth and there will be extreme layer thinning. The effects noted above will have a much greater impact on the fine scale detail of the ice core record which will be obliterated, leaving only longer term climatic trends. The higher temperatures deeper in the core could also lead to the mobilisation of previously fixed solutes such as sodium chloride.

The following chapter returns to scanning electron microscope observations as a means to establish the actual distribution of impurities.

CHAPTER VI

Distribution of Soluble Impurities in Cold Glacial Ice

A detailed study of polar snow and ice using the Scanning Electron Microscope (SEM) and x-ray analysis revealed the micro-structural distribution of soluble impurities. Sublimation under vacuum (etching) concentrated impurity from both the bulk and grain boundaries onto the specimen surfaces in detectable quantities. Sublimation in the cold room before examination (pre-etching) allowed observable quantities of impurity to accumulate at triple junctions. A heterogeneous distribution of impurities was observed. Chloride was frequently found dissolved in the lattice, but not usually at triple junctions. Other impurities, particularly sodium chloride, were detected at grain boundaries and bubble surfaces. Sulphate was often found at triple junctions in specimens containing a high bulk concentration of the acid, frequently in conjunction with other cations. This implies veins were only filled with significant amounts of impurity when the surrounding grain boundaries were saturated with at least a monolayer close to the eutectic concentration. The results reconcile differences between previous SEM studies, and are consistent with recent electrical conduction observations. The disconnected arrangement of impurity filled grain boundaries and veins limits opportunities for post-depositional solute movement.

VI.1. Introduction

The arrangement of natural impurities in polar ice plays an important role in determining many of its physical properties, and is particularly relevant to the study of past climates using ice cores. The distribution has implications for: the possibility of post-depositional movement of chemical species [*Rempel et al.*, 2001a], the likelihood of chemical interactions between different components trapped in the ice [*Tschumi and Stauffer*, 2000], and the mechanisms for electrical conduction in chemically doped ice [*Wolff et al.*, 1997]. A thorough understanding of the spatial arrangement of impurities should allow better interpretation of the ice core measurements used to unravel the climate history. The great age of deep polar ice (many thousands of years old) also allows the distribution of impurities to be studied under conditions close to equilibrium, a luxury unavailable when examining laboratory grown ice.

Virtually all precipitation nucleates on dust or aerosol particles. Of the snow flakes examined by Kumai from the South Pole 60 % had dust nuclei whilst 20 % had nucleated on aerosols, with the remainder unidentifiable or unobserved [*Kumai*, 1976]. However the majority of particulate impurity was attached to or embedded in snowflakes, but not as the nucleus. As fine

structured snowflakes sinter in the snow pack the majority of mass is transported via the vapour phase with less significant transport by diffusion of mass across the surface [*Colbeck*, 1998]. Solid particulate impurity e.g. dust or salt aerosol below the eutectic temperature, will either pin two-grain boundaries or be engulfed within the bulk of grains, presuming no pre-melting around the particles which could allow their expulsion from the advancing freezing front [*Rempel et al.*, 2001b]. Aqueous impurities will be continuously rejected by the advancing lattice (at least at concentrations above the solubility limit) and hence remain in a liquid like state at the ice-air surface [*Wolff and Paren*, 1984]. Following densification the most thermodynamically preferable location for aqueous soluble impurity is considered to be at triple junctions between grains at temperatures close to 0 °C [*Harrison and Raymond*, 1976; *Nye and Frank*, 1973]. This arrangement can explain the electrical conductivity of polycrystalline ice [*Wolff and Paren*, 1984]. At lower temperatures the most thermodynamically stable state is not well established.

Several recent studies of poly-crystalline ice using the scanning electron microscope (SEM) have shown impurities *in situ*, both at the boundaries between ice grains and in the bulk of the crystals (chapter III), [*Baker and Cullen*, 2002; *Cullen and Baker*, 2000]. Prior to these only a couple of direct studies on impurity location had been published. Mulvaney *et al.* [1988; *Wolff et al.*, 1988] used the SEM and x-ray analysis to show sulphur inferred to be sulphuric acid at triple junctions in ice from Dolleman Island, Antarctica. Fukazawa *et al.* [1998] found acidic SO_4^{2-}, NO_3^- and HSO_4^- as liquids at triple junctions using Raman spectroscopy in ice from both Nansen and South Yamoto, Antarctica. The conclusions from these different studies do not present a fully coherent description of either the arrangement of impurities or the factors that determine it. Mulvaney suggested that the majority of acid present in the ice might be located at triple junctions. Fukazawa's results indicated a lower proportion at triple junctions at one site whilst both Cullen and Baker concluded that a far greater proportion of impurity present was located at two-grain boundaries and as inclusions in the bulk.

This chapter provides further detailed experimental information to help resolve the issue. It describes the analysis of ice taken form four different sites, but concentrates on ice sampled from the Dome C ice core, Antarctica. Low temperature scanning electron microscopy and x-ray analysis are used to search the micro-structure for impurities. A description of the technique employed is provided including variations to the previously published method, and an attempt to quantify x-ray analysis measurements. The results indicate that impurities are present in a wide range of locations including grain surfaces, grain boundaries, triple junctions and dissolved in the lattice. We infer the preferred arrangement of the main impurity species within the ice both interstitially and within the lattice.

VI.2. Method

Specimens were taken from the following sites: the Dome C core, Antarctica, drilled in 1999 (74°39'S, 124°10'E, 3240m elevation and -53.5°C mean annual temperature), a Dronning Maud Land core drilled in 1998 (77°S, 10°W, 2200 m elevation and -38 °C mean annual temperature), surface snow collected in 1999 from the clean area near Halley Base situated on the Brunt Ice Shelf (75°35'S,26°30'W, 32 m elevation and -19.3 °C mean annual temperature), and the GRIP ice core from Greenland drilled in 1990 (72°34'N, 37°37'W, 3232 m elevation and -32 °C mean annual temperature). All specimens were stored in a cold room at -20 °C before examination. Table VI.1 lists the sites, depths, ages and chemical compositions of sulphate, chloride and sodium ions measured in the melt water [*Röthlisberger et al.*, 2000; *Udisti et al.*, 2000]. All samples were from relatively acidic ice of Holocene age except for the Dome C samples at 501 m, and GRIP samples at 1980 m in which much of the acid has been neutralised. The four different sites were used to provide ice of varying composition for the study rather than for the purpose of making climatic comparisons between the sites.

The samples were prepared and examined using the technique outlined in Chapter II with minor modifications. A beam power of 15 kV and 500 pA was used for all microanalysis in this study and maintaining samples at temperatures between -120 and -130 °C reduced the effects of surface charging to an acceptable level. Etching was used to sublimate ice from the surface whilst leaving impurities to coagulate on the surface as hydrated salts as described in chapter II. The sublimation rate was controlled by raising the temperature of the sample stage to -80, -70 or -60 °C achieving etching rates on a flat surface of 6, 20 or 60 μm min^{-1} [*Davy and Branton*, 1970]. Pre-etching was used to concentrate impurity at triple junctions.

VI.3. Results

This section presents evidence gathered using the SEM, from the examination of more than 100 samples collected from the four sites at a wide range of depths. The images show some of the clearer examples pertaining to soluble impurities in the ice. Most impurity species could be found in a range of different locations, and considerable variation was found even between specimens from an identical depth. General observations concerning specimens from each location are summarised in table VI.1.

VI.3.1. Snow and firn

Figure VI.1 shows images of surface snow through to firn at the pore close off depth. The complex faceted structures observed in snow crystals [*Rango et al.*, 1996] and diamond dust [*Kumai*, 1976], rapidly sinter and densify to the observed smooth surfaced structures.

Table VI.1. Summary of experimental observations[a].

Specimen location and depth	Dominant soluble impurities in melt and age	Impurity location			
		Grain cavity surface (uncut)	Grain boundary	Triple junction	Bulk and dislocations
Dome C surface snow	$[SO_4^{2-}]$ ~ 0.7μM $[Na^+]$ ~ 1 μM $[Cl^-]$ ~ 3 μM < 3 yr	Na and Cl in exceptional cases (fig. VI.3a)	Filament ridges often observed after etching, no detectable impurity (fig. VI.4b)	Only after etching were filaments seen linked at triple junctions in some cases	Cl detectable in surface etch spots after heavy etching
Dome C firn low density, 23.30 m	$[SO_4^{2-}]$ ~1.8 μM $[Na^+]$ ~ 1.0 μM $[Cl^-]$ ~ 0.3 μM ~ 390 yr	Not observed	Filament ridges observed on some etched surfaces	Only after etching were filaments seen linked at triple junctions in some cases	Si, S and Cl detected in mobile particles revealed by heavy etching
Dome C firn, medium density, 51.90 m	$[SO_4^{2-}]$ ~1.2 μM $[Na^+]$ ~ 1.2 μM $[Cl^-]$ ~ 0.3 μM 1.1 kyr	Filament observed on un-etched cavity surface with Mg and S.	Etching concentrated filaments at cut surface interfaces. Cl and trace S detected	Some triple junctions joined by filaments after etching	Etching revealed many coagulated spots close to grain boundary filaments containing Cl and trace Na. Other background spots contained trace Cl.
Dome C firn high density, 95.8m	$[SO_4^{2-}]$ ~1.2 μM $[Na^+]$ ~ 1.2 μM $[Cl^-]$ ~ 0.2 μM 2.3 kyr	Not observed	Most boundaries did not reveal filaments when etched	Not observed even after etching	Surface etch spots containing S and Cl revealed on etching
Dome C small sulphate peak, 140.05 m	$[SO_4^{2-}]$ ~1.6 μM $[Na^+]$ ~ 1.1 μM $[Cl^-]$ ~ 0.4 μM 3.7 kyr	Not observed	Many boundaries did not reveal filaments when etched	Low levels of S and Na detected directly in triple junctions after pre-etching	Cl detected in surface etching spots
Dome C medium sulphate peak, 218.95 m	$[SO_4^{2-}]$ ~2.9 μM $[Na^+]$ ~ 0.7 μM $[Cl^-]$ ~ 0.4 μM 6.6 ky	Not observed	Filaments seen at some grain boundaries after etching	S, Na and at many triple junctions after pre-etching (fig. VI.5f)	Cl alone as well as Na and Cl detected in surface etching spots (fig. VI.6a)
Dome C large sulphate peak, 243.30 m	$[SO_4^{2-}]$ ~5.2 μM $[Na^+]$ ~ 0.8 μM $[Cl^-]$ ~ 0.2 μM 7.5 kyr	Cl and S spots observed on the rims of bubbles during etching	Distinct etching filaments produced in some cases, containing a variety of species including Na, Cl, S, K and Ca (fig. VI.4e)	Triple junctions containing S (fig. VI.5d) and others containing a mixture: Na, S and K and Ca (fig. VI.5e) detected after surface pre-etching	Surface etching spots containing Cl and occasionally Na revealed (fig. VI.4e)
Dome C background to sulphate peak, 243.50 m	$[SO_4^{2-}]$ ~1.3 μM $[Na^+]$ ~ 1.0 μM $[Cl^-]$ ~ 0.3 μM 7.5 kyr	Filament and spots coagulated on rim of bubbles during etching containing Na and Cl (fig. VI.3b)	Distinct etching filaments containing Na and Cl (fig. VI.3b)	No impurity detected even after long pre-etch periods	Etching revealed inclusions of Na and Cl, also possible dislocations containing Na and Cl, surface etch spots had a similar composition (fig. VI.6b)
Dome C 269.5-270.05 m	$[SO_4^{2-}]$ ~1.0 μM $[Na^+]$ ~ 0.8 μM $[Cl^-]$ ~ 0.4 μM 8.4 kyr	Not observed	Filament ridges not generally observed after minor etching	Not observed	Cl, S and Na detected in surface etching spots
Dome C 500.5-501.05 m	$[SO_4^{2-}]$ ~2.7 μM $[Na^+]$ ~ 4 μM $[Cl^-]$ ~ 4 μM 20.2 kyr	Not observed	Filament ridges occasionally apparent during etching	Incidence of Na and Cl noted at TJ after brief etching with no pre-etching (fig. VI.5c)	Na and Cl inclusions noted during etching
Halley surface snow	$[SO_4^{2-}]$ ~0.9 μM $[Na^+]$ ~ 18 μM $[Cl^-]$ ~ 21 μM < 3 yr	Not observed	Filaments observed at grain boundaries after etching (fig. 4a), detectable S and Na noted at one (fig. 4d)	Etching filaments joined at triple junctions	Impurity not detected in surface etching spots
Dronning Maud Land 115 m	$[SO_4^{2-}]$ ~ 1.4μM $[Na^+]$ ~ 1.0 μM $[Cl^-]$ ~ 1.4 μM 1.2 kyr	Not observed	Na and Cl clearly detected in a thick layer at pre-etched grain boundaries in one specimen, grain boundary filament ridges also noted (fig. VI.5c)	Pre-etched triple junctions noted containing Na, Mg, Al, S, Cl, K and Ca, possible dust particle in vein	Etching experiments not performed
GRIP, 1312.30-1312.85 m	$[SO_4^{2-}]$ ~ 0.3μM $[Na^+]$ ~ 0.3 μM $[Cl^-]$ ~ 0.3 μM 7.9 kyr	Not observed	Filament ridges observed sometimes during etching, detectable Cl noted in one case	Not observed, other than joining etched ridges	Cl and Mg detected in some surface etching spots, as well as inclusions
GRIP, 1979.45-1980.00 m	$[SO_4^{2-}]$ ~ 2.8μM $[Na^+]$ ~ 3 μM $[Cl^-]$ ~ 3.5 μM 23.2 kyr	Not observed	Majority of grain boundaries clear of filament ridges	Not observed	Inclusions containing multiple impurity species revealed by etching

[a]The absence of observations of an impurity from a particular location and site does not preclude the possibility that it was present but not detected. Images showing examples of the features are indicated where applicable.

Grain boundary grooves and triple junctions are apparent between the grain surfaces and at the necks between crystals. The dihedral contact angle was measured at grain boundaries between sintering snow crystals in instances where the bond between grains was perpendicular to the angle of observation, and the specimen had not been etched. Measurements of grain boundaries at 13 bonds from 3 different specimens (two from Halley one from Dome C) gave a mean air-ice dihedral angle of 132 ± 3°.

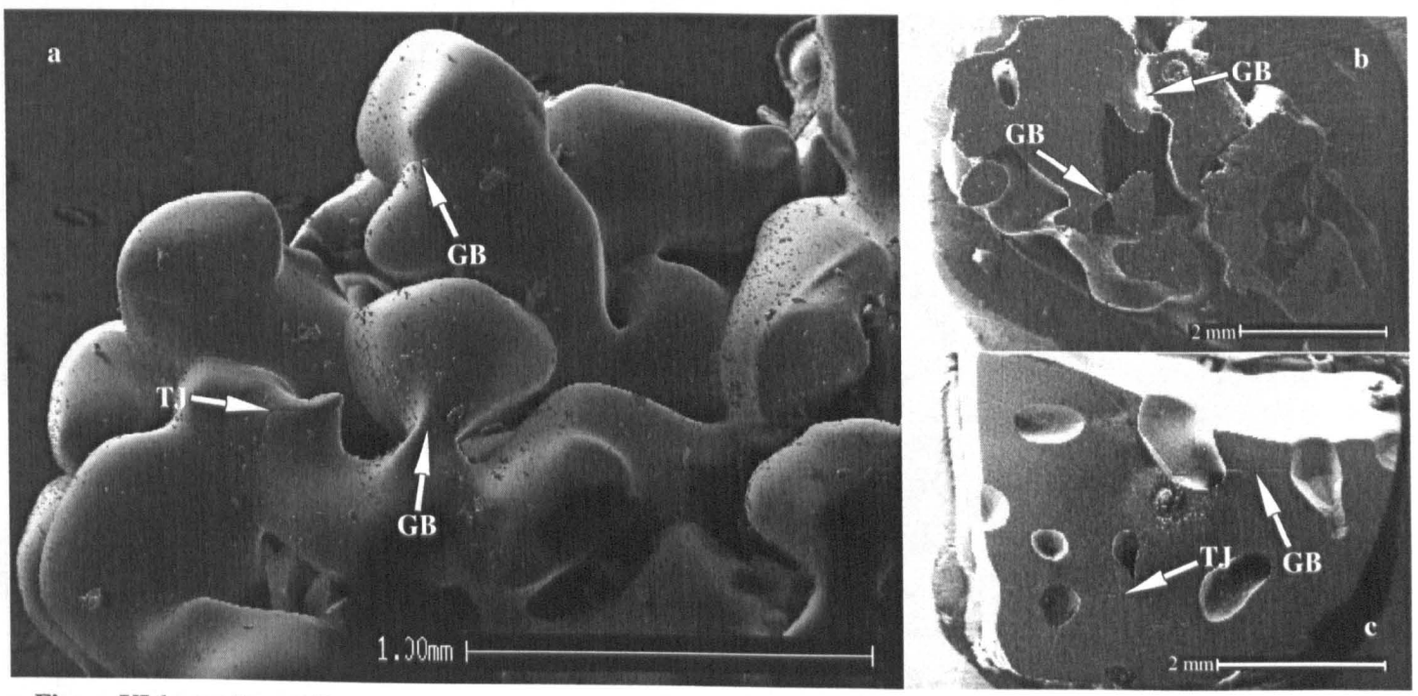

Figure VI.1. Dome C snow and firn. Examples of the location of grain boundaries (GB) and triple junctions (TJ) marked (see pp.v and appendix). **(a)** Sintering surface snow, with a density of approximately 340 kg m^{-3}. No etching has been performed on this specimen. Grain boundary grooves can be seen at the necks between grains. Small ice crystals suspended in the liquid nitrogen used to cool the ice have been deposited on the surface. **(b)** Firn from a depth 23.3 m and an approximate density 526 kg m^{-3}. The surface has been cut to reveal an un-etched section. **(c)** Firn from 95.8 m and a density of 820 kg m^{-3} around the pore close off depth. The surface has been cut, pre-etched for 1 day, and then etched in the SEM for 10 minutes at –70 °C to reveal the location of the grain boundary grooves more clearly.

VI.3.2. Pore surface impurity

Soluble impurity was detected on un-etched cavity surfaces, both on snow grains and bubble walls. Figure VI.2 shows examples of both of these features in Dome C snow and ice, it should be noted that impurity detected on an un-etched grain surface was not common. The filament of NaCl associated with the rim of the bubble in figure VI.2b has coagulated from the bubble surface during etching, and has a similar composition to other impurities noted on the sublimating surface. Coagulating spots of impurity were also seen on the rims of bubbles from other depths (table VI.1).

VI.3.3. Impurity at grain boundaries

Occasionally impurity could be located at grain boundaries without etching (Chapter III), [Barnes, *in press*]. However the examples of impurity found at grain boundaries shown here were

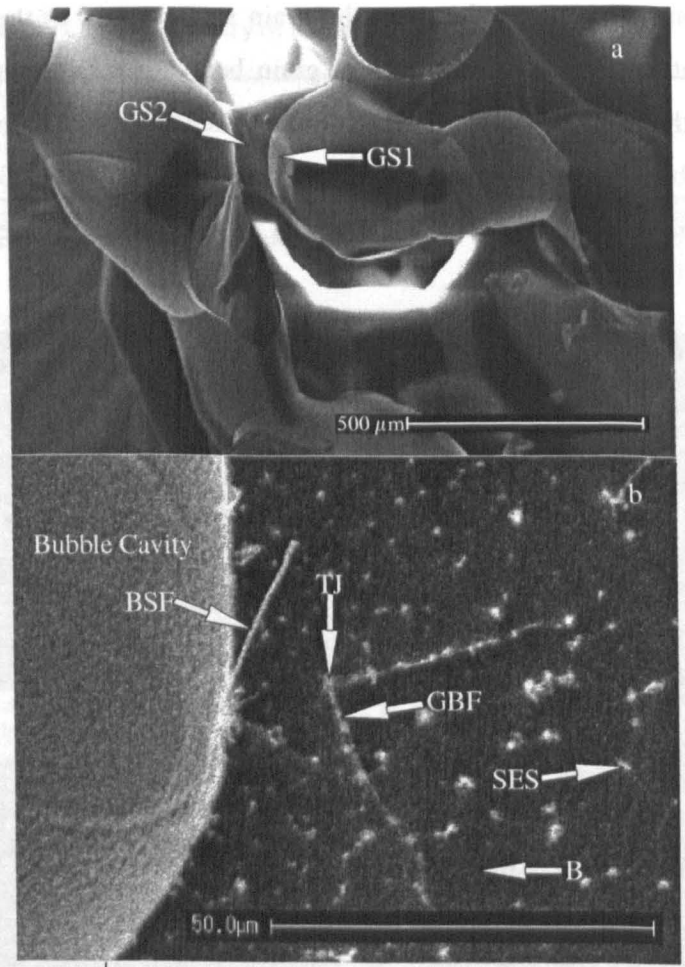

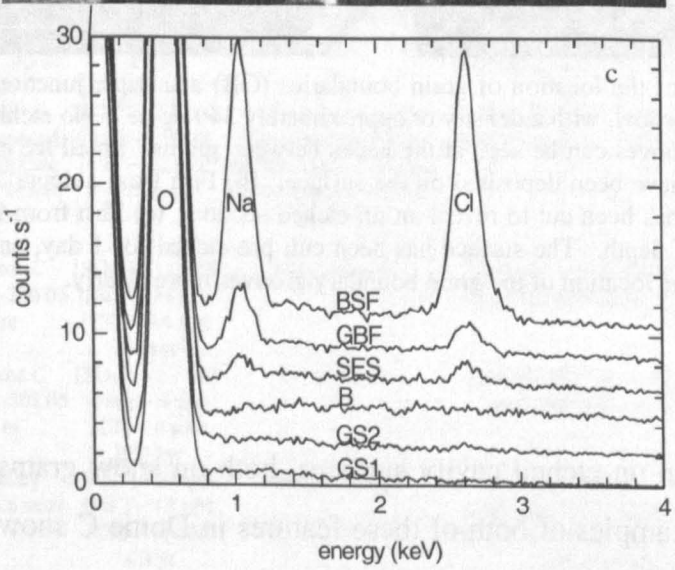

Figure VI.2. Surface impurity. **(a)** Surfaces of sintering surface snow grains from Dome C, the surfaces shown are un-etched. Traces of chlorine were detectable on some grain surfaces. Grain surface 1 (GS1) showed no detectable impurity. However the adjacent grain surface (GS2) consistently showed traces of chlorine at the detection limit; if sodium was also present, it was below the detection limit. **(b)** Section of a bubble wall, from Dome C 243.50 m. The surface has been pre-etched for one day and then etched for 8 minutes at –70 °C (~ 400 μm removed). The bubble surface filament (BSF) is a hydrated salt coagulated from the surface of the bubble at its rim during etching and has a width of ~2 μm. A grain boundary filament (GBF) has also formed at the original location of the grain boundaries on the un-etched surface, the position of filament triple junction (TJ) is marked. During etching, spots of impurity also coagulate on the surface (SES), whilst no impurity can be detected in the dark background areas (e.g. B). **(c)** X-ray spectral data for (a) and (b), offset by multiples of 2 counts s^{-1}.

all revealed by the use of surface etching, since impurity is not usually detectable on a freshly cut or pre-etched surface. Caution must be exercised when interpreting any etched surface since the process of sublimation can enhance the mobility of some coagulated impurities as well as obscuring their original location as discussed in section II.6. Figure VI.3 shows examples of filaments and impurity ridges originating from grain boundaries. Images from the etched necks of snow crystals at Halley (figure VI.3a and figure VI.3d) and Dome C are seen. The etch rate from snow surfaces is likely to be lower than for flat cut surfaces due to the porous structure. The tortuous path of the filaments at bonds between neighbouring grains suggests an impurity component with some structural strength under compression. As the radius of the bond decreases during sublimation, the initially smooth band of coagulated impurity is seen to buckle as it sticks to the surface. The presence of Mg and S (figure VI.3c) in the filament on the uncut surface but not on the cut surface of the bond shown in figure VI.3d indicates the role of pre-etching in concentrating impurities on the specimen surface.

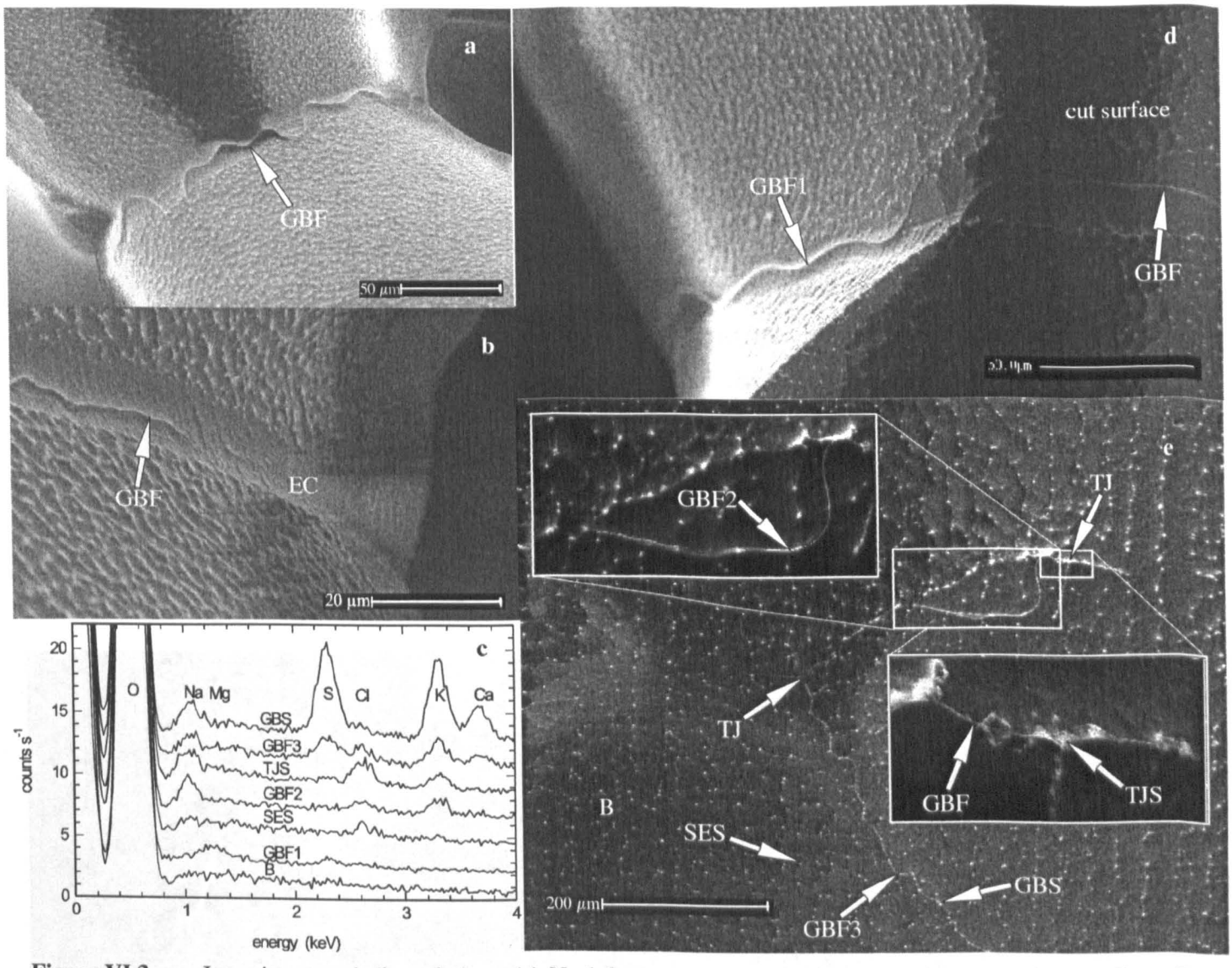

Figure VI.3. Impurity at grain boundaries. **(a)** Neck between grains of sintering surface snow from Halley. The specimen has been etched for the equivalent of 6 minutes at –70 °C. A grain boundary filament (GBF) has developed at the neck during etching. Its tortuous appearance suggests it has buckled as the neck's radius reduces with sublimation. No impurity was directly detectable in this filament. **(b)** A similar neck between grains of Dome C surface snow. The specimen has been etched for 4 minutes at –70 °C. A grain boundary filament has developed in the etching channel (EC) formed at the location of the grain boundary groove. Note that the filament, which did not contain detectable impurity, is not continuous around the boundary, suggesting the bond is only partially covered by an impurity layer. **(c)** X-ray spectra for many of the points marked with arrows on figures (d) and (e), offset by multiples of 2 counts s^{-1}. **(d)** A bond between grains of Halley surface snow that has been cut by the microtome, pre-etched for one day, and then etched in the SEM for the equivalent of 6 minutes at –70 °C. A grain boundary filament has developed at the etching channel on both the snow grain surface and the cut surface. The filament on the snow grain surface, which has split into two strands during etching, contained detectable magnesium and sulphur (GBF1) whilst no impurity was detectable in the filament on the cut surface. **(e)** Dome C ice from a depth of 243.30 m. The surface has been cut but not pre-etched and then etched in the SEM for 10 minutes at –60 °C (600 μm). A clear grain boundary filament has been produced, apparently joined at triple junctions (TJ), it can be seen in the insets, and has a diameter of approximately 400 nm. Spectra were taken from the filament (GBF2, GBF3), and also from the surface spots that have formed by the grain boundary filament (GBS) and the triple junction (TJS). Spectra were also collected from typical background surface etching spots (SES) and from the dark areas of the background (B).

The freshly cut, then etched surface shown in figure VI.3e is from Dome C at 243.30 m, a depth that corresponds to an acidic sulphate layer (probably fallout from a volcanic eruption) with a melt water concentration of about 5 μM (table VI.1). Filaments and particles have coagulated on the surface without etching channels, since there was no pre-etching. The relatively large quantity

of ice sublimed from the surface (600 μm) may have included a grain boundary plane; its contents could be added to the bulk impurity already coagulated on the surface.

VI.3.4. Impurity at triple junctions

For natural samples impurity was not noted at triple junctions without some form of pre-etching or etching. Pre-etching the surface of a specimen after cutting was found to be the most reliable method for revealing impurity at triple junctions, the greater the duration of pre-etching, the greater the likelihood of detecting impurity; the implications of this are discussed in section VI.4.2.2. Even in ice containing high bulk concentrations of acid, impurity located at triple junctions was not always apparent after pre-etching. Triple junctions can be seen in figure VI.4, prepared by a variety of methods showing examples of triple junctions with and without impurity, and their appearance after etching. Impurity concentrated at triple junctions was not normally observed in ice that did not contain relatively high bulk concentrations of acid, except where etched filaments joined (for example figure VI.3e), as can be seen from table VI.1.

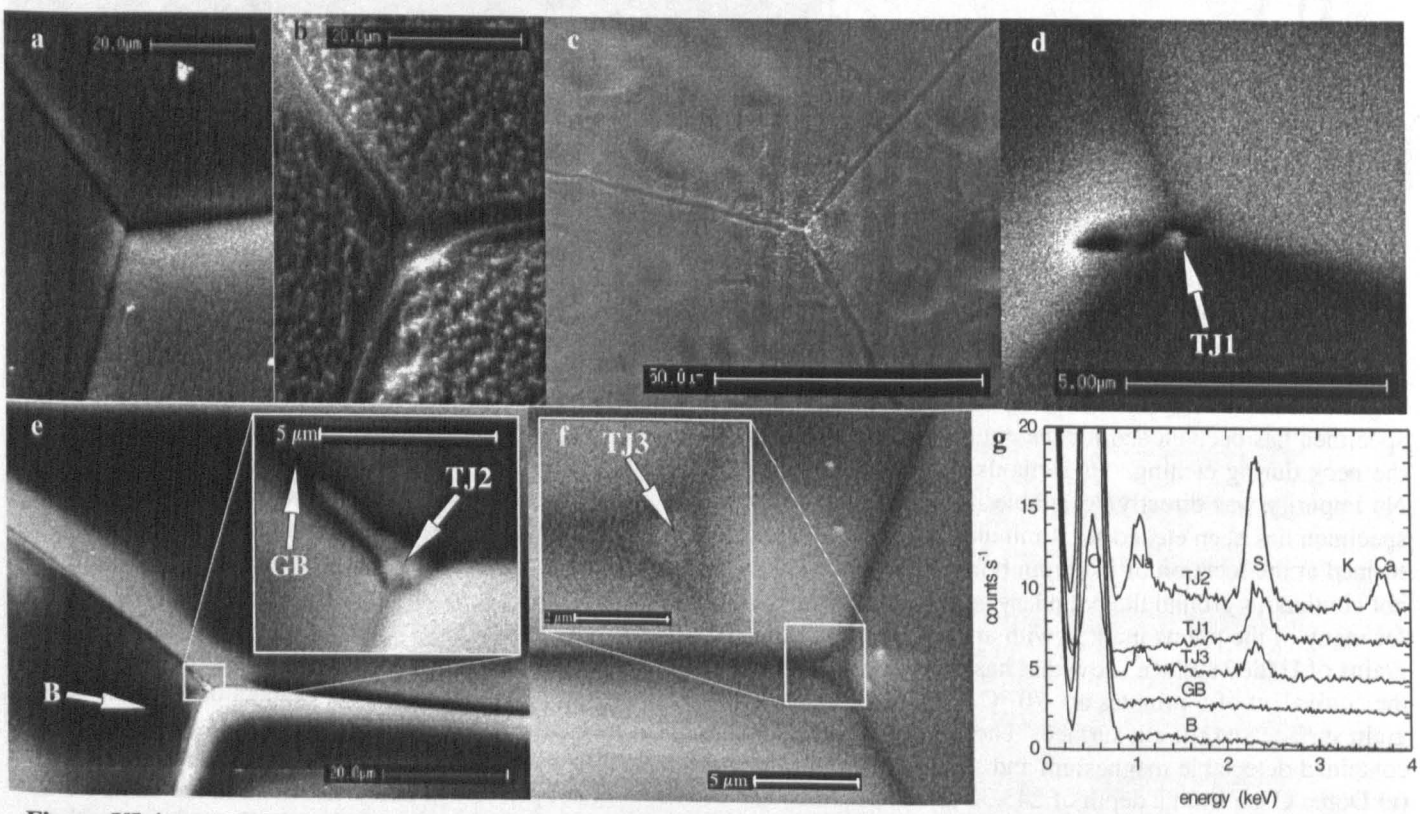

Figure VI.4. Triple Junctions. **(a)** Dome C ice from 243.30 m, surface cut and pre-etched for three days. Despite the fact that this ice contains a relatively high concentration of sulphate, no sulphur is detectable at the triple junction, although it is apparent on others on the specimen. The junction is also typical of those observed in background ice. **(b)** The triple junction seen in (a) after etching for 7 minutes at –80 °C. A grain boundary filament is visible in the etching channel, although the impurity is below the detection limit, both at the triple junction and in the filament. **(c)** Trace sodium and chlorine are revealed at this triple junction by 1 minute of etching, at –80 °C, of the surface of this Dome C ice from 501 m (the surface was not pre-etched). Note that grain boundary filaments are visible close to the triple junction; they die out after around 15 μm. **(d)** A triple junction containing only sulphur (TJ1) detected in Dome C ice from 243.30 m. The surface was pre-etched for 1 day. The dark spot to the left of the triple junction is a hole that was 'burned' by the electron beam. **(e)** A triple junction containing sulphur and other insoluble impurities (TJ2), found on the same specimen as (d). The grain boundary (GB) in the vicinity of the triple junction was not significantly different from the background spectrum (B). **(f)** Triple junction observed in Dome C ice from 218.95 m, pre-etched for 7 days. A very clear filled triple junction structure is apparent (TJ3) and the impurity appears to extend into the grain boundaries, although impurity is not detectable in these locations. **(g)** X-ray spectra for figures (d), (e) and (f), offset by multiples of 2 counts s^{-1}.

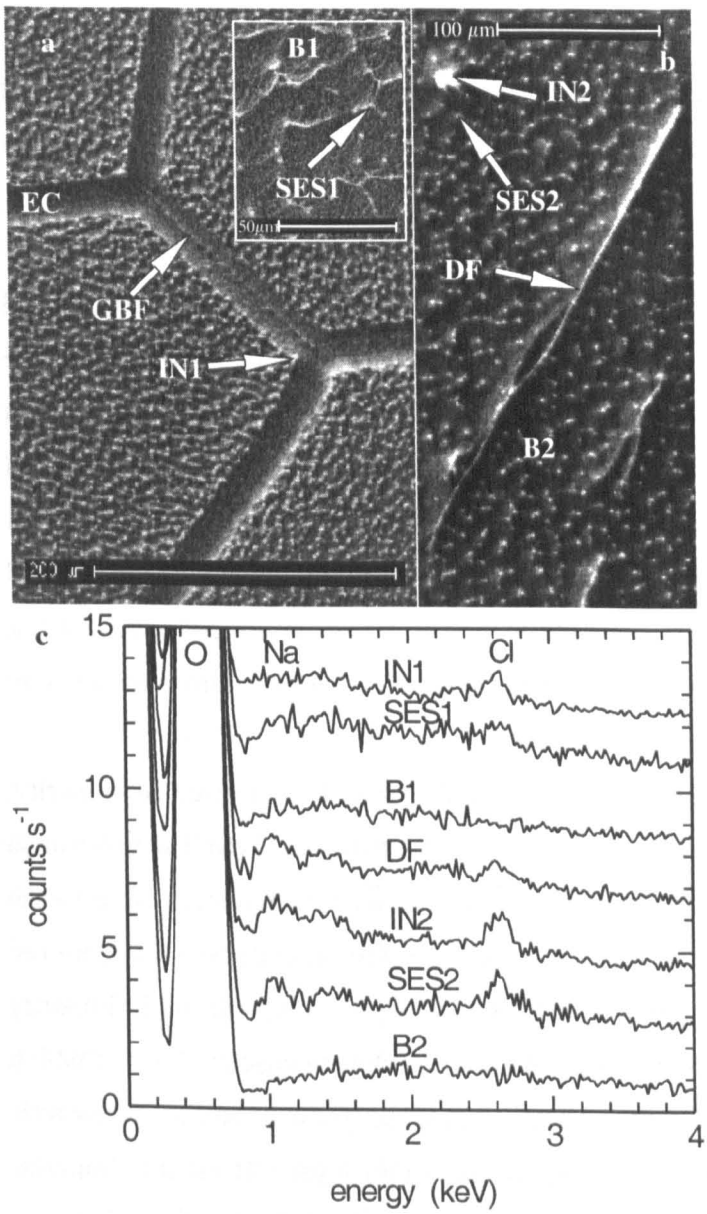

Figure VI.5. Bulk impurity and inclusions. **(a)** Dome C ice from 218.95 m, pre-etched for 7 days and then etched for 7 minutes at – 70 °C. Etch channels (EC) show original location of the grain boundaries, some contain filaments (GBF). Surface etching spots developed on surface (see inset) in which only chlorine was detectable (SES1). Either inclusions or coagulated surface etch spots (IN1) are located on the rim of the etching channels. **(b)** Dome C ice from 243.50 m, pre-etched for 10 days and etched for 5 minutes at – 70 °C. The surface imaged was located in the centre of a grain that was featureless before etching. Disconnected filaments are revealed which may be indicative of impurity located at dislocations (DF). A bulk inclusion has also been revealed (IN2) which has a similar composition to the surface etching spots (SES2). These can be compared with the dark background (B2). **(c)** X-ray spectra for figures (a) after 10 minutes at – 70 °C and (b), offset by multiples of 2 counts s^{-1}.

VI.3.5. Bulk impurity and dislocations

A significant quantity of impurity could be dissolved within the ice lattice. Furthermore impurity will be incorporated directly as inclusions. In addition to the spots of detectable impurity shown in figures 3b and 4d, figure VI.5a shows further examples of spots built up on the surface of ice from a Dome C acidic layer. They show trace of chlorine that was almost certainly dissolved in the lattice before etching. Sublimation of around 140 μm of ice has left coagulated hydrated impurity on the surface. Also shown are brighter spots or inclusions containing chlorine in greater quantities at the edge of etching channels. It is likely that these are formed by the advancing edges of the channels 'sweeping' up the smaller spots.

The surface in figure VI.5b was featureless before etching. The etching spots also contain detectable levels of sodium in contrast to the previous example, and a bulk inclusion of similar composition is also seen. However the most striking features are the long filaments seen on the surface that do not appear to be connected to any grain boundaries or triple junctions. These sodium chloride filled filaments could be residues of impurity forming dislocations within the bulk of the grain.

VI.4. Impurity arrangement

This section considers implications of information presented (section VI.3) on the factors that determine how different impurities are distributed in the ice.

VI.4.1. Grain surfaces and boundaries

Filament ridges were noted at the majority of grain boundary bonds in both Dome C and Halley snow samples after etching. This is indicative of soluble impurity, though it was below the detection limit in most cases. In sintering surface snow of 340 kg m^{-3} there is a surface area of around 26 m^2 kg^{-1} [*Dominé et al.*, 2002]. Assuming a mean grain radius of 200 μm and a bond radius of 100 μm (figure VI.1a, and other observations) we can calculate the approximate number of grains per kilogram to be $[917 \times 4/3\ \pi\ (2\times10^{-4})^3]^{-1} = 3 \times 10^7$ kg^{-1} and the mean bond area to be 3×10^{-8} m^2. The grain coordination number is approximately 3.2 neighbours per grain [*Alley*, 1986c], which gives 1.6 bond areas per grain. The grain boundary area per kilogram is then 1.6 m^2 kg^{-1}, a factor of 16 times less area than the air-ice interface.

It is illustrative to consider what proportion of this surface could be covered by impurity. For a liquid-like monolayer primarily composed of water molecules there will be of the order of $[6 \times 10^{23}$ $(mole^{-1}) \times 10^6$ $(g\ m^{-3})$ / 18 $(g\ mole^{-1})]^{2/3} \sim 1 \times 10^{19}$ molecules m^{-2} of which, close to the eutectic composition, about 10 % will be an impurity species. The monolayer will therefore require 1×10^{18} molecules of impurity m^{-2} (~ 1.7 μmoles m^{-2}). Typical bulk impurity concentrations at Dome C are around 1.5 μM for the sodium and sulphate species, both of which are highly insoluble in the lattice, however the sodium would be present below its eutectic temperature, so probably less mobile during the formation of a thin layer. If all this impurity formed a monolayer it would cover 1.5 (μmoles kg^{-1}) / 1.7 (μmoles m^{-2}) ~ 0.9 m^2 kg^{-1}. This figure is of a similar magnitude to the area of grain boundary in the snow, but considerably less than air-ice interface area, where only about 3 % would be covered, by any one species. In the case of Halley snow where sodium and chlorine concentrations are around 20 μM, there is potential for a much higher proportion of the snow surface to be coated if aerosol inclusions are available in the liquid form during the summer.

From these considerations we can surmise that, even if all impurity is on snow grain surfaces, the impurity is almost certainly distributed heterogeneously, with coatings (possibly more than a monolayer thick) on some grains and absent on others (as seen in figure VI.1a). The evidence suggesting impurity is resident at many bonds therefore implies that it is energetically preferable for at least one of the impurity species to exist at a grain boundary as opposed to a grain surface. On the few occasions where impurity was detectable in snow and upper firn at filaments, sulphate ions were common to all examples, although invariably in conjunction with other ions (table VI.1). The only location where sulphate ions were observed originating from the grain

surface was on the rim of a bubble in ice from an acidic sulphate layer in which the concentration of sulphate was high enough to coat all available grain boundaries with at least a monolayer (an acidic bulk concentration of 5.2 μM could up cover upto ~ 3 m^2 kg with a monolayer; the available grain boundary at this depth is around 2.2 m^2 kg^{-1} or ~2000 m^2 m^{-3}).

At other depths less rich in sulphate a far smaller proportion of boundaries were filled, and elements detected in filaments tended to be sodium and chlorine indicating their presence at grain boundaries (table VI.1, figure VI.3e). These impurities were also noted coating the inside of bubbles (figure VI.2b) in ice with bulk concentrations insufficient to coat all grain-boundaries, suggesting a possible affinity of sodium for grain surfaces. Whatever the case it seems clear that impurity is again heterogeneously distributed at grain boundaries. The likelihood of a boundary being occupied is probably dependent in part on its relative lattice orientations; closely aligned boundaries will exclude impurity.

The concentration of impurity situated at a grain boundary can be inferred from observation of a filament on an etched surface, for example the filament seen at GBF2 in figure VI.3e. The x-ray signal strength emitted from this filament is of a similar magnitude to that generated by the 0.5 M standard frozen into a 0.4 μm hole discussed in section II.4. If 1 μm of the filament has been stimulated to produce this signal then we expect about 1×10^{-16} moles of impurity per micrometre of filament, the radius of the filament is 200 nm, so the concentration of hydrated salt is ~ 1 M, which is of the same order as the eutectic composition. This filament was created by sublimation through up to 600 μm of grain boundary. If the whole of the boundary was perpendicular to the direction of sublimation and covered with a monolayer of impurity then we would expect the coagulation of 1×10^{-6} (m) $\times$ 600 $\times$ 10^{-6} (m) $\times$ 1.7 μmoles m^{-2} ~ 1×10^{-15} moles of impurity per micrometer of filament, which is an order of magnitude more than observed in this case. Although the whole of the grain boundary is unlikely to have been perpendicular to the surface, this calculation further supports a heterogeneous distribution of impurity at grain boundaries, where the layer thickness could be more than a monolayer.

The reasoning above relies on the assumption that impurity at a grain boundary will exist in a monolayer at concentrations close to the eutectic concentration, i.e. it is behaving in a liquid-like manner. It is quite possible that this may not be the case and that the ionic species could disperse to greater dilutions at the grain boundaries through diffusion. Grain boundary diffusivities for ions in ice are not well known. However images indicating incomplete coverage of grain boundaries such as figure VI.3b are suggestive of a liquid-like mono layer covering the maximum possible boundary area allowed by the liquidus relation for impurity spread at a boundary; further dilution by diffusion would cause an apparent phase change, hence locking the impurity in place.

VI.4.2. Triple Junctions

Impurity was generally only detected at triple junctions in specimens where a relatively high concentration of sulphate ions was present. Pre-etching served to concentrate acid at the triple-junctions probably by the slow loss of mass from the surface during pre-etching. Although it is possible that impurity located in this manner originated from the bulk surface of the crystals it is unlikely, at least for sulphate ions, since these were not generally observed as immobile surface etching spots. The dimensions of filled triple junctions seemed to be related to pre-etch time and bulk concentration, the largest triple junctions observed on pre-etched surfaces had areas of several square microns. When compared with spectra from 4.9 M sulphuric acid frozen into 2 μm holes, the triple junction in figure VI.4f produced a signal consistent with the entire electron interaction volume containing impurity at the eutectic concentration. However the x-ray spectra collected from other triple junctions gave smaller signals, which were consistent with the production of x-rays close to the surface only. For example the triple junction in figure VI.4d, which has a surface area of ~ 1.4 μm^2, produced a signal strength which could be explained by x-ray emission from impurity at the eutectic composition extending to a depth of ~ 0.4 μm. When the triple junctions were etched, no clear vein residues were revealed (often only grain boundary filaments and etching spots were detectable as exemplified by figure VI.4b). Furthermore impurity was never detectable at triple junctions on freshly cut surfaces, even in ice from the acidic layers, where pre-etched images show veins with areas of several square microns. This could, however, be an artefact of the cooling wave penetrating the specimen from the surface inwards during its immersion in liquid nitrogen; cooling specimens from the base up could test this possibility. It appears highly unlikely that veins have a diameter as large as the cross-sections observed on a pre-etched surface. It is more plausible that far narrower veins are the source for the impurity, which collects in the 'rotting' triple junctions, formed during pre-etching [*Nye*, 1991b]. Without data to constrain the rate of sublimation during pre-etching it is difficult to estimate the vein dimensions below the surface.

Despite sulphate ions being found alone in some cases (e.g. figure VI.4d), indicating the presence of sulphuric acid, it was more usual for a combination of ions to be present, particularly sulphate and sodium, suggesting the following reaction had occurred:

$$H_2SO_4 + 2NaCl \rightarrow Na_2SO_4 + 2HCl \qquad \text{(VI.1)}$$

allowing the H^+ and Cl^- ions to dissolve into the lattice and leaving a sodium sulphate residue at the veins mixed with any excess acid. This is consistent with the high lattice solubility of chloride ions compared to the other species present [*Petrenko and Whitworth*, 1999]. Chloride ions were not noted at triple junctions in any of the sulphate peaks. Similar reactions are likely with the other cations and would also release the chloride ions into the lattice.

A relatively high concentration of sulphate in the bulk ice appears necessary for impurity to be detectable at triple junctions. This is consistent with either saturation of the surrounding ice

lattice forcing any excess to concentrate at triple junctions, or a saturation of the surrounding grain boundaries perhaps with an impurity monolayer, allowing the excess to concentrate in a vein. In this study the lowest bulk concentration of sulphate ions for which filled triple junctions were detectable was 1.6 μM. This figure VI.could either represent an upper limit at which the surrounding ice (at –53 °C) is saturated, or perhaps more likely the bulk concentration at which sufficient grain boundaries are saturated to allow the collection of ice at some triple junctions.

VI.4.3. Lattice

Immobile spots of impurities that have coagulated on the surface during etching originate directly from impurity previously dissolved or included in the lattice (except in the relatively unlikely case where a grain boundary layer is deposited on the surface). The most commonly detected impurity in these spots was chlorine, particularly in the specimens from the acidic sulphate layers. It is likely that the chlorine, when detected alone, was originally deposited in a salty form, which has subsequently been liberated by the reaction given by (VI.1).

As an example we estimate the quantity of chloride dissolved in the bulk for Dome C ice at 218.95 m (figure VI.5a). Chloride in the surface etch spots after 10 minutes at – 70 °C and approximately 200 μm of ice had been sublimed from the surface, is just above the limit of detection. The number of surface spots per unit of etched volume is 1.4×10^{13} spots m^{-3}, so assuming a spot contains approximately 3×10^{-17} moles of chloride (section VI.2.1), then the bulk concentration is ~ 0.4 μM; we estimate an uncertainty of at least 50 % on this calculation. However it is consistent with the majority of the chloride in the ice, which has a bulk concentration of 0.4 μM, being dissolved in the lattice; it is considerably below the lattice solubility limit of ~ 600 μM for HCl at –53.5 °C found by Thibert and Dominé [1997].

In other cases where impurity was detectable a combination of sodium and chlorine was often noted, although generally in larger, less regularly spaced spots than those containing chlorine alone, perhaps indicative of impurity inclusions disrupting the lattice. Non-acidic chloride ions could only be substituted for H_2O molecules if an associated cation is also included interstitially within the ice molecular cage to prevent charge separation. The amount dissolved will be strongly dependent on the equilibrium partition coefficient, or solubility limit of the lattice. The possible dislocations observed in figure VI.5b could be the result of an amalgamation of inclusions formed to reduce the lattice free energy.

VI.4.4. Boundary interfaces

At a steady state interface between a grain boundary and air, the ice-vapour surface free energies are balanced by the grain boundary free energy [*Hobbs*, 1974,pp 436 - 441]. Thus the dihedral angle of the grain boundary groove (which must form to achieve equilibrium) is indicative of the surface energies of the system. The dihedral contact angle found here of 132 ± 3° is

significantly less than grain boundary contact angle of 145° quoted by Hobbs for pure ice measured at 0 °C. The value seems more consistent with the values quoted for 'unclean' ice, which contained many surface irregularities particularly at the grain boundaries, where the dihedral angles ranged from 130° to 148°.

The reduction in the dihedral angle implies a reduction in the ratio of ice-vapour to grain boundary surface free energy (γ_{iv} / γ_{ii}) [*Hobbs*, 1974,pp 436 - 441], from 1.67 to 1.23. This is hard to reconcile with the earlier observation of impurity preferentially located at grain boundaries between snow bonds (section VI.4.1) which requires γ_{ii} to be reduced by the introduction of impurities. It may be explained by a significant reduction in γ_{iv} caused by the lower observation temperature (-20 °C) and/or the addition of an impurity layer to the surface. Relevant interfacial energy information is not currently available to test this.

Figure VI.4e appears to show no sign of impurity in the grain boundaries surrounding the triple junction, although the salty composition (the following impurities were detected: Na, S, K and Ca) may indicate a solid precipitate. Etching the junction suggested the presence of trace impurity at the grain boundaries. Figure VI.4c shows sodium and chlorine extending a short distance from the grain boundary into the triple junction. Figure VI.4f however clearly shows that the dihedral angle at the triple junction is zero or very close to zero. It is not clear whether this also characterises the dihedral angle of the vein below the surface, as the vein cross-section widens like a funnel towards the surface.

At temperatures close to 0 °C liquid was not present at grain boundaries in studies of laboratory ice where dihedral angles around 32° were observed [*Mader*, 1992b], implying 1.9 γ_{il} = γ_{ii}, where γ_{il} is the ice-liquid interface energy. The concentration of solute in the veins was low enough to have a negligible impact on γ_{il}. At the temperatures typical in polar ice (-53 °C at Dome C) the higher interstitial solute concentrations could be sufficient to reduce γ_{il} such that 2 $\gamma_{il} \leq \gamma_{ii}$, allowing distribution of a layer of solute at grain boundaries to be energetically favourable. This is also born out by the wide spread observation of filaments at grain boundaries. Under this scenario once a layer of solute above the eutectic temperature is deposited at a grain boundary any excess will locate at the triple junction due to curvature effects. Different ionic species will have varying effects on γ_{il} or γ_{ii}, which might account for the apparent preference of salts for grain boundaries over veins. Note that at Dome C NaCl is present below its eutectic temperature and therefore is unlikely behave like a liquid, however it may still be able to reduce γ_{ii}, making its location at grain boundaries preferable to inclusion in the lattice. If it does not behave like a liquid, NaCl will have no significant energetic preference for triple junctions. Its significant presence at triple junctions in acidic ice (figure VI.4e and f) could be explained by diffusion from grain boundaries to the vein to fuel the reaction given by equation 1.

The SEM techniques applied in this work could be used to test the impact of impurities on boundary interface energies in laboratory grown ice prepared at different temperatures, presuming sufficient time was available for the specimens to reach equilibrium.

VI.4.5. Arrangement Summary

- Chloride is found in the lattice, probably due to its solubility. Traces of other impurities originating from the lattice were less common, except as inclusions.
- There is evidence that other impurities, particularly sodium chloride, coat bubble surfaces and grain boundaries heterogeneously.
- Where there is a high bulk concentration, acidic sulphate is often found at triple junctions, frequently in conjunction with other cations.

VI.4.6. Comparison with previous work

Some of the observed differences in the distribution previously noted are linked to small differences in the technique of the different groups. In this work we have reproduced all the features observed in the previous studies as well as new variations of them. The features of impurity filaments and inclusions observed in studies on Greenland (GISP2) and Antarctic (Byrd core) ice [*Baker and Cullen*, 2002; *Cullen and Baker*, 2000; *Cullen and Baker*, 2001], are seen in many specimens here when prepared by a similar method: pre-etching followed by etching. The inability of these studies to locate triple junctions accurately on the specimen surfaces makes conclusions drawn regarding veins doubtful except in cases where filaments are joined at triple junctions. The sulphate filled veins observed in acidic layers of H_2SO_4 seen in this work are consistent with studies of acidic Antarctic ice from Dolleman Island [*Mulvaney et al.*, 1988; *Wolff et al.*, 1988]. However the absence of detectable veins from less acidic ice casts some doubt on the concept of a fully connected vein network in the ice sheet. A more likely model includes layers of connected veins at depths where sulphate ions are already covering the majority of neighbouring grain boundaries at least in a monolayer. Triple junctions at other less acidic depths would contain little more impurity than the surrounding grain boundaries.

The study of Antarctic ice by Fukazawa *et al.* [1998], found acidic SO_4^{2-}, HSO_4^- and NO_3^- ions present in veins at –20 °C using Raman spectroscopy. They did not detect these species at grain boundaries, possibly due to the detection limit of the technique. The ice from both sites contained high concentrations of sulphuric acid (3.42 μM, Nansen and 14.35 μM, South Yamato), which is consistent with the results seen here. In the case of the South Yamato ice where only 3 % of the acid was estimated to reside at triple junctions a vein dihedral angle close to zero (as observed here) allows a significant volume of this acid to spread into the grain boundaries, in addition to a monolayer. They also observed acidic nitrate ions in veins but these cannot be

detected by the technique used here. The chloride ions apparently dissolved in the lattice are below the solubility limit found by Thibert and Dominé in laboratory grown ice [1997].

VI.4.7. Implications

The heterogeneous distribution of impurity observed in specimens of low impurity implies an absence of connected filled pathways either at grain boundaries or veins. At higher bulk concentrations the proportion of grain boundaries containing impurity will increase the connectivity at grain boundaries in the ice. If grain boundaries are saturated with at least a monolayer of impurity locally then there will be increasing connection between filled veins (probably at bulk concentrations > 1.6 μM for sulphuric acid). Hence a vertically connected network of impurity filled veins is extremely unlikely in areas of an ice sheet with low temperature and background impurity levels such as Dome C. However horizontally connected networks of impurity-filled vein remain quite feasible within sulphuric acid layers. The likelihood of connection in either veins or grain boundaries will be dependent on impurity content, grain size and temperature. Impurity coating the surfaces of bubbles should link unconnected veins within acidic layers.

The theory of conduction through sulphuric acid filled veins [*Wolff and Paren*, 1984] remains applicable in cases where bulk concentration is high enough to saturate the surrounding grain boundaries and hence fill the veins. At lower bulk concentrations another conductivity mechanism is required, perhaps by the mobilisation of protonic defects from the heterogeneous patches of impurity at grain boundaries. The ionisation defects are then free to travel either along grain boundaries or through the lattice. In regions where NaCl reacts with H_2SO_4 at triple junctions (VI.1), the release of H^+ and Cl^- ions into the lattice should allow conduction via ionisation defects in the lattice [*Petrenko and Whitworth*, 1999] to replace the liquid conduction lost from the vein.

This explanation of conduction is in good agreement with the work of Fujita [2002] who noticed a step increase in the conductivity of Dome F ice from sulphuric acid layers (10 – 20 μM) as the temperature was increased above -81 °C. They explained this by the addition of liquid conduction to the total conductivity as the frozen aqueous mixture melted in the veins at around its eutectic temperature. When the experiment was repeated on ice with background impurity levels the step change in conductivity was not seen, implying the absence of significant quantities of soluble impurity in veins.

Dust particles have been located at grain boundaries, in some cases visibly pinning them (chapter III). The widespread observation of soluble impurity species at grain boundaries in this work suggests that the post-depositional production of CO_2 suggested by [*Tschumi and Stauffer*, 2000] is feasible, although determining the rate will be complicated by factors such as the grain boundary diffusivity.

Solute above the eutectic temperature confined to a grain boundary at nanometre scale thickness will not behave as a typical liquid; water molecules will adopt a structured arrangement near the ice interface reducing solute diffusivity [*Pollack*, 2001]. If veins of diameter > ~1nm in which the solution displays properties close to the bulk liquid [*Raviv et al.*, 2001] are only present in ice containing relatively high levels of acid compared to the background then significant mobility through veins by the mechanism proposed by Rempel [2001a] would seem unlikely. Diffusion of solute under a temperature gradient would be limited by the diffusion of solute from veins into unfilled grain boundary, which would significantly reduce bulk movement of the chemical profile.

VI.5. Conclusion

Impurity has been located on grain surfaces, boundaries, triple junctions and lattice in ice from four different polar sites. The results are consistent with previous observation of impurities in polar ice by a number of different techniques. The preferred arrangement of impurities appears complex and dependent on the chemical composition and probably temperature of the ice. Layers of impurity containing NaCl and other sea salts form at grain boundaries. Sulphate ions, probably acidic, are also located at grain boundaries. When sulphuric acid is present in sufficient concentration, observed here to be around 1.6 μM for Dome C ice, the acid is able congregate in detectable quantities in veins. Consequently the proportion of acid distributed in veins is almost certainly dependent on both the total concentration of acid in the ice as well as the grain size. At this location it may react with salts from the surrounding grain boundaries, releasing acidic chloride ions into the lattice, or grain boundaries. The proposed distribution appears consistent with models of electrical conductivity. Impurity arranged in this fashion would be unlikely to allow the long distance transport of interstitial impurity through the ice under the action of a temperature gradient, unless the impurity content were consistently much greater than the levels observed in deep polar ice cores.

CHAPTER VI

CHAPTER VII

Summary and conclusion

The distribution observed using the SEM implies that a smaller proportion of acid than previously thought resides in veins, with the remainder at grain boundaries and bubble surfaces. Most other impurities are at grain boundaries or in the lattice. This is consistent with: our electrical conductivity observations, those of others, and models where acidic conduction occurs via interstitial liquid. Conductivity calibrations are dominated by ice with high acid content, while low concentration ice is relatively free of liquid. The unconnected distribution favours the model of percolation driven by grain growth as an explanation for the observed diffusion at Dome C. The connected model of diffusion through veins could only apply in ice of higher temperature where the interfacial properties of the liquid would be altered or in ice with a higher bulk concentration where a greater proportion of impurity resides in veins. Further work is required to better quantify the distribution and its implications.

VII.1. Chapter Summaries

VII.1.1. Technique for examining ice using the scanning electron microscope

Chapter II dealt with the development of a reliable method to examine ice microstructure. A scanning electron microscope (SEM) equipped with a cryo-stage allowed both high-resolution imaging and the composition of impurity to be determined within polycrystalline ice (using x-ray analysis).

Generally planed surfaces of ice were examined. However the exact features observed on the surfaces were dependent not only on specimen composition but also preparation technique. Different knife types and cutting conditions produced surfaces of varying quality. Pre-etching (sublimation under quasi-equilibrium conditions) served to smooth surfaces and enhance grain boundary grooves by the equilibration of interfacial energies at the grain boundary/cut surface intersection. In some cases pre etching could also collect impurity at grain boundaries or triple junctions, through loss of mass from the surface and grooves. The use of a brass cap to protect liquid nitrogen cooled specimens from stray condensation was essential to avoid the accumulation of frost.

Once the sample wsa in the SEM etching (sublimation under vacuum) was frequently used as a means both to remove cutting debris and to concentrate impurity on the specimen surface. It could also be used to reveal structures embedded in the ice. Caution must be exercised when

interpreting surfaces after etching because information on grain boundary location is lost during sublimation and coagulated impurity can be mobilised.

Although coating was beneficial for the purposes of imaging, the greater flexibility of leaving specimens uncoated was preferred. Gold sputter coating prevented the use of etching and reduced the sensitivity of x-ray analysis measurements. To minimise the effects of surface charging on uncoated specimens low beam power was used. Furthermore examination at temperatures around -120 to -130 °C allowed enough sublimation to mitigate some of the charging when using higher beam power for x-ray analysis.

Accurate calibration for quantitative x-ray analysis was hampered by the non-conducting nature of ice and surface charging. However an estimate of the minimum detectable quantity of impurity was obtained, and the emitted x-ray response to increasing concentration was approximately linear.

VII.1.2. Observation of polar ice morphology

Chapter III presented the physical features typically observed in polar ice using the SEM. Grain boundaries and sub-grain boundaries were clearly evident on cut surfaces, and variation in lattice orientation could be seen during etching. The majority of bubbles observed were located at the intersection of grain boundaries. Micro bubbles were noted at grain boundaries, probably forming from dissolved gas nucleating in the relaxed core. The remains of decomposed clathrate hydrates were also evident. Those that had a globular structure were generally found on grain boundaries, implying that they had originated directly from bubbles – primary hydrates. Those that had a plate-like structure were not normally associated with grain boundaries implying secondary formation.

Dust particles were also detected *in situ* by the use of etching; most were aluminium magnesium silicates in a heterogeneous distribution with particles generally grouped in small clusters. The number density of particles detected in both the Greenland and Antarctic specimens was higher than those found by other workers using different techniques. The discrepancy was accounted for by the differences in the minimum particle size detected by the different methods, and a bias towards examining dusty sections for this study.

The ratio of particles located at grain boundaries compared to those in the crystal bulk indicated that at Dome C dust particles either pin or were collected by migrating grain boundaries. In the GRIP samples this was not found for the majority of specimens except a few taken from cloudy bands where large clusters of dust and micro bubbles appeared to coat grain boundaries. The sample size and number of particles counted was inadequate for statistical certainty. Images directly showing grain boundary pinning by both dust and bubbles were also presented.

Finally examples of soluble impurities located at grain boundaries were also presented in anticipation of chapter VI.

VII.1.3. Effect of density on electrical conductivity

Chapter IV examined the variation of the high frequency electrical conductivity of Dome C ice, σ_∞, with impurity concentration and changes in density. The concentrations of both sulphuric and hydrochloric acid were calculated using chemical profiles for sulphate, chloride and sodium ions.

For solid ice multiple regression analysis was used to determine the conductivity coefficients for the main chemical species. The coefficients for sulphuric acid and hydrochloric acid were consistent with previously found values at other sites. They were also consistent with a model of two-phase conduction, by which the acid conducts through the liquid phase. Since determination of the conductivity coefficients by regression analysis is dominated by ice containing acid concentrations above the background level, the coefficients do not exclude the possibility of liquid acid only being present at relatively high concentration. The large scatter of the data meant that the possibility of a non-linear model of acidic induced conduction was not tested.

The conductivity coefficient for sodium ions was higher than the values found for more salty coastal sites. This suggests that at Dome C a higher proportion of sea salt chloride ions is incorporated into the lattice than at other warmer, higher accumulation rate sites. At these the lattice could be saturated or a higher proportion of the salty chloride excluded from the lattice.

A rolling regression method was used to examine the variation in the conductivity coefficient with depth and hence volume fraction of ice. Looyenga's dielectric mixture model applied to conduction in snow [*Glen and Paren*, 1975] under-predicted the pure component of conductivity in low density firn; this may in part be linked to a conduction mechanism not accounted for. The variation of the sulphuric acid conductivity coefficient with volume fraction showed a general increasing trend which could be explained by the application of percolation theory. The reduction in pore space was modelled as increasing the number of conductive pathways, via grain boundaries, presuming significant conduction did not occur on pore surfaces. In deeper ice conduction via filled veins could also account for the variation in conductivity coefficient. Consequently it is plausible that significant quantities of impurity only reside at triple junctions in deeper ice since by this stage the grain boundary density is greatly reduced, and boundaries may be saturated.

More scatter was seen for the conductivity coefficient at different depths in the core than could be accounted for by either experimental error or the relatively smooth variation in density. This implies factors in addition to chemistry may contribute to conductivity mechanisms. The scatter is consistent with a heterogeneous impurity distribution altering the precise conduction mechanisms at different depths in the core. Fluctuations in grain size and fabric orientation could be important in determining impurity distribution. Detailed profiles were not available for these variables, but may be published soon.

VII.1.4. Evolution of chemical peak shapes

In chapter V detailed study of the sulphate, chloride and sodium profiles used in chapter IV, indicated that the durations of chemical peaks (many of volcanic origin) were longer in deeper ice than near the surface.

Both spectral analysis and a windowed differencing operation applied to the chemical time series showed a damping (or peak broadening) of the mean signal strength, for all species. This could be attributed to either variation in the original chemical signal reaching the ice sheet at the time of deposition or to a post-depositional diffusive process.

The chemical data were rescaled to remove the impact of low frequency climatic variability on the profile characteristics. The windowed differencing operation applied to the rescaled data indicated measurable diffusion occurred in the sulphate and chloride profiles but not in the sodium profile. The rate of diffusion was insufficient to lose much resolution from the profile over a period of 10 kyr, but if continued significant signal would be lost in ice of greater age. The eutectic point of sodium chloride was higher than the temperature of this ice, whilst the eutectic points of sulphuric acid and hydrochloric acid were lower. Thus transport of chloride and sulphate could occur in the liquid phase.

Whilst it is possible and even likely that the diffusion observed for chloride ions occurred as HCl through the vapour phase in the upper section of core, this could not be the case for sulphate ions that have an extremely low vapour pressure. Mechanisms by which the acid could diffuse in the liquid phase were considered the most likely explanation.

Two models were constructed to explain the observed diffusion, each dependent on the arrangement of the sulphuric acid in the ice. One considered the case where the liquid acid resided in a network of connected veins or grain boundaries between ice crystals. If the veins are connected then fluctuation in the bulk concentration must be accounted for by variation in grain size. If not, adjacent difference in bulk concentration would quickly be lost with the equilibration of vein diameter. Under this scenario variation in the proportional rate of grain growth in regions of different grain size alter the concentration of the liquid acid in the veins. Under the influence of these concentration differences the diffusion occurs. When modelled numerically the effective diffusion by this mechanism was close to that observed.

The other model considered the case where veins or grain boundaries filled with a significant quantity of sulphuric acid were not connected. This more heterogeneous distribution allows variation in bulk concentration without variation in grain size; it is more consistent with recently published evidence from Dome C concerning grain size and chemical composition [*Weiss et al.*, 2002]. The process of grain growth increases the proportion of filled sites (grain boundaries or triple junctions), allowing percolation between neighbouring sites when a critical site occupancy is reached. This allows impurity to percolate away from acidic horizons. An estimate of the effective diffusivity of this model suggests it could also account for the observed diffusion.

VII.1.5. Distribution of soluble impurities

Chapter VI examined in detail the micro-structural arrangement of soluble impurity in polar snow firn and ice specimens (from both Greenland and Antarctica) using the SEM. With the methods described in chapter II, impurity was generally located by pre-etching or etching the specimen surfaces. The results indicated a heterogeneous distribution of impurities, particularly those located at grain boundaries and triple junctions

Chloride was frequently found in the lattice, but not usually at triple junctions. Traces of other salt ions were also found originating from the lattice, but they were more commonly noted at grain boundaries and bubble surfaces. Sulphate was frequently found at triple junctions where ice contained relatively high bulk concentrations of sulphuric acid. However even in those specimens not all triple junctions were filled. Sulphuric acid was not detected in specimens with background bulk concentrations. At most triple junctions where it was detected other cations were also present. Interpretation of these observations reconciles minor differences in the interpretation of previous direct studies on impurity distribution, the differing conclusions of which were generally due to technique.

Direct observation of the (frozen) liquid/grain boundary interface on surfaces where the triple junctions contained sulphate indicated the dihedral angle is zero or close to zero. This implies that it is energetically favourable for impurity (possibly liquid-like) to coat at least some grain boundary interfaces. This contrasts with the low concentration impurity solutions close to 0 °C which appear to be excluded from grain boundaries [*Mader*, 1992].

An approximate calculation of the quantity of impurity required to coat grain boundary surfaces with a monolayer close to the eutectic concentration indicated that at background impurity levels not all grain boundary will be coated. If it is energetically preferable for grain boundary to be coated with at least a monolayer rather then filling a vein, then a significant quantity of impurity will only reside in veins when the surrounding boundaries are close to saturated. This interpretation is consistent with the SEM observations. The presence of acidic impurity at grain boundaries and the location of dust at the boundaries in chapter III helps confirm that post-depositional reaction between acids and dust to produce CO_2 or other by-products is likely at Dome C, although it is difficult to quantify the extent of the effect.

The diffusivity of impurity in a monolayer at a grain boundary (currently not well established but likely to be significantly less than that in the bulk liquid) implies that solute transport via this route will be too slow to allow significant movement of the bulk concentration profile under a temperature gradient.

VII.2. The distribution of impurities in polar ice

The overriding feature of impurity distribution determined in this work is the heterogeneous distribution of virtually all impurity types detected. This is in part due to the very low diffusivities associated with the solid phase but also implies the absence of strong homogenising forces or concentration gradients for impurities in the liquid phase despite the long time scales available for equilibration as considered in chapter V. Figure VII.1 summarises the distribution of impurities in polar ice as found here.

The evidence presented implies that what impurity there is in the liquid phase is not fully connected in the commonly understood sense. Triple junctions will still connect impurity filled veins. However the liquid at triple junctions in low bulk concentration connecting regions will have a vein width of a few nanometres at Dome C, the presence of liquid in this case is primarily due to curvature, with a possible contribution from an impurity film in some regions. Although this liquid connects the 'filled' veins, significant transport of solute along the triple junctions will not occur. If grain boundary coated with impurity is energetically preferable to an uncoated one in most cases then solute diffusing along a vein that is not surrounded by 'saturated' grain boundaries will diffuse into the boundaries in preference to the vein hence limiting the bulk movement of solute in ice.

In regions of high acidic concentration or/and high temperature (e.g. some coastal sites), a relatively high liquid volume fraction is present and a significant proportion of the triple junctions in the ice will be impurity filled in a connected network. In these cases solute transport

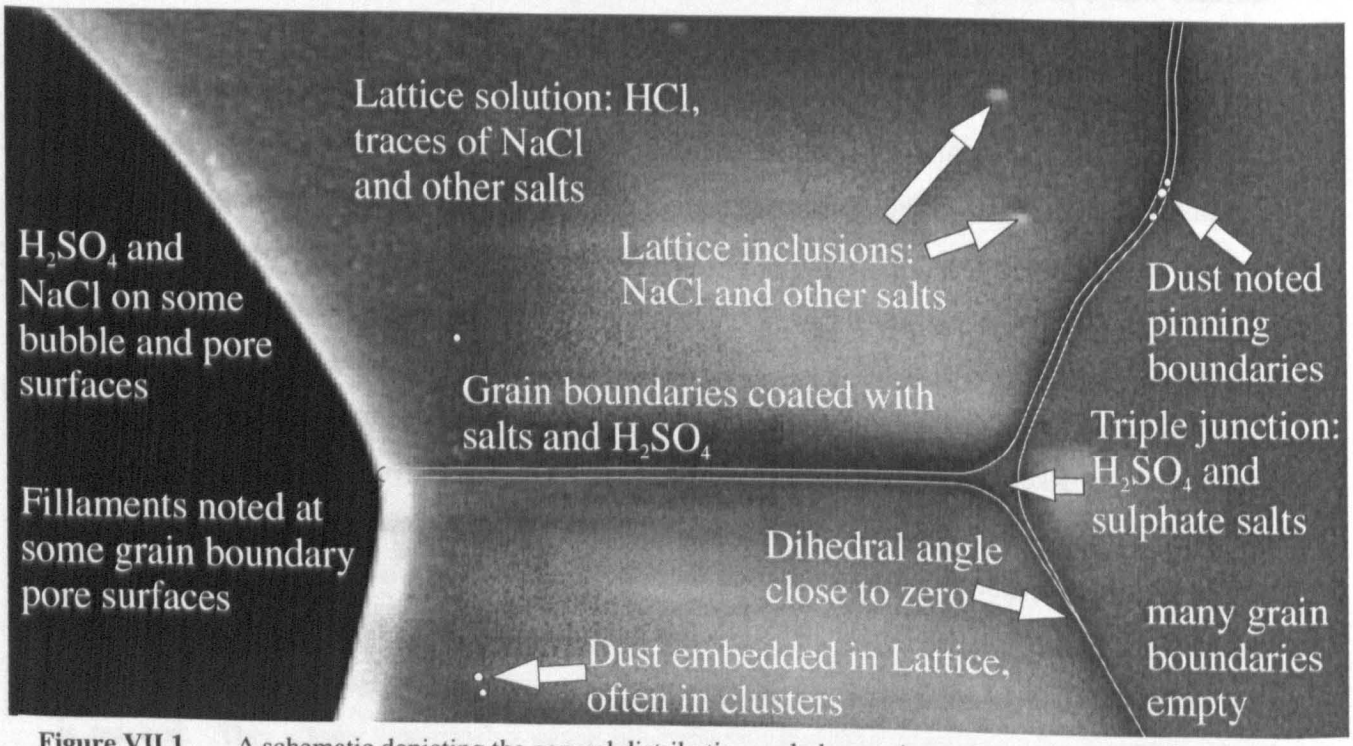

Figure VII.1. A schematic depicting the general distribution and observations of impurities in cold polar ice as seen in this work.

mechanisms causing peak diffusion by the connected mechanism driven by grain growth (section V.3.3) and by the bulk diffusion along a temperature gradient described by Rempel *et al.* [2001] are plausible.

In cold, low impurity concentration regions, typical of the bulk of the Antarctic ice sheets the unconnected distribution of soluble impurities discounts significant impurity transport by the mechanisms above. The grain growth driven percolation model for diffusion seems more likely (section V.3.4). A contribution to peak broadening via classical diffusion of impurity along grain boundaries is also likely in regions where grain boundaries are close to saturated, and this process will be enhanced by grain growth reducing the boundary density. Currently grain boundary diffusivities are not well established [*Colbeck*, 1998].

At great depth in the ice sheet other factors may further influence the impurity distribution. Continued grain growth may increase the proportion of soluble impurity resident at triple junctions. Alignment of the crystal fabric by overburden pressure will reduce the mean interfacial free energy between adjacent crystals. This process will exclude soluble impurities from grain boundaries, which would also increase the proportion of impurity located at veins.

The observed heterogeneous impurity distribution is consistent with current models for electrical conduction in polycrystalline ice, where conduction through the liquid phase is only apparent in ice containing a relatively high concentration of acid [*Fujita et al.*, 2002]. The large variability in the conductivity coefficient noted in chapter IV might be further evidence that the conductivity measured using the DEP (dielectric profiler) responds not only to chemistry, but also its distribution, which could be determined by factors such as age, grain size and fabric.

The heterogeneous distribution might also explain the non-linear ECM (dc electrical conductivity measurement) response to acid. Calibrations imply measured ECM current increases approximately (there is a great deal of scatter) with the square root of acidic concentration where the acid is thought to be in veins [*Wolff et al.*, 1997]. One explanation for the non-linearity is that calibration has been performed on ice containing a mixture of acids, some (sulphuric acid) with only one proton (of two) dissociated at high concentration. It could also be a result of the impurity distribution observed here. In the two phase electrical conduction model for polycrystalline ice [*Wolff and Paren*, 1984], the dc conductivity is determined by the liquid conductivity multiplied by the volume fraction of liquid (f) multiplied by a geometric factor. This factor has a value of 2/3 when the liquid is arranged at grain boundaries, but only 1/3 when the liquid is situated exclusively in veins. The non linearity can then be explained by a change in geometric factor as acidic concentration increases: at low concentration acid only resides at grain boundaries (2/3), however with increasing bulk concentration the grain boundaries become saturated and excess acid resides in veins and the geometric factor tends to 1/3. This assumes the monolayer can be modelled as a liquid. A similar argument could also apply for acid dissolved in the lattice; increasing the bulk concentration would mean the lattice reaches saturation and excess builds up at grain boundaries or

veins, if the interstitial acid provides a less efficient conduction mechanism then the non-linearity is also explained.

The distribution determined here will also be relevant to those considering the viability of microbial life in the ice sheet. These hypotheses are partially dependent on a significant quantity of liquid residing in veins to provide a habitat [*Price*, 2000]. If as we suggest a much smaller proportion of acid is contained in veins than previously thought then the chances of microbial viability deep in the ice are reduced.

VII.3. Future work on impurity distribution

The SEM technique developed and used in this work has provided a qualitative description of impurity distribution. Improvements in the method allowing better quantitative measurements would be of great use. The most promising route to achieving this is through the renewed use of surface coating to minimize charging effects. This has disadvantages, in particular it would increase the duration of an already relatively laborious sample preparation procedure.

Further information on impurity distribution could be gathered by examining samples with chemical compositions not covered in this work. Examining ice from hydrochloric acid peaks should give an indication of the solubility of the lattice to HCl. We have also not concentrated on the soluble impurity distribution in ice from the last glacial period in this work. The acid in this ice is neutralised by dust, and further investigation here might yield interesting results. Examination of laboratory-doped samples should also prove useful.

The relative proportions of impurity at grain boundaries (particularly NaCl) and dissolved in the lattice has not been well determined here. A calculation could be made by estimating the grain boundary density and using the equilibrium partition coefficient. However the value of the coefficient is not well established, particularly at the transition above and below the eutectic temperature for salt. Work into this area perhaps using the SEM techniques used here could help to constrain this variable and the relative distribution of salts.

Observation of high resolution chemical data from the EPICA Dronning Maud Land Core, with higher accumulation rates, may provide a profile against which to check the peak broadening observed in the Dome C core (chapter V). The analysis of high resolution chemical data from deeper in the Dome C core than examined here should also shed further light onto diffusive processes.

In this work we have not considered the impact of this distribution on the mechanical properties of the ice sheet. Quantifying this impact could be of particular relevance to the flow properties of the ice sheet at the boundaries between climatic periods (e.g. Holocene/Last Glacial) with significantly different chemical signatures.

Other techniques for examining the arrangement of impurities could further refine and quantify our knowledge of impurity distribution as well as test observations seen here. For example: further bulk electrical conductivity measurements on polycrystalline ice with varying impurity content at different temperatures and frequencies, the use of micro electrodes on ice surfaces to assess the relative contribution of grain boundaries, surfaces and impurities to conduction, and the use of nuclear magnetic resonance to assess the extent of impurity incorporation within the lattice, and liquid content.

VII.4. Concluding remarks

It is hoped that the observations made in this work will be of use to the ice core community and those interested in the general properties of ice; they should resolve some of the questions dependent on impurity location. We have broadly described the distribution of soluble impurities in cold polar ice and some of the associated implications. However many of the quantitative details of the distribution remain to be established. In addition many questions remain regarding the arrangement of impurities in other forms of naturally occurring ice. We hope that some of the principles governing distribution proposed here will prove to be a useful starting point for further investigations.

CHAPTER VII

References

Adams, E.E., D.A. Miller, and R.L. Brown, Grain boundary ridge on sintered bonds between ice crystals, *Journal of Applied Physics*, *90* (11), 5782-5785, 2001.

Alley, R.B., J.H. Perepezko, and C.R. Bentley, Grain Growth in Polar Ice: I. Theory, *Journal of Glaciology*, *32* (112), 415-424, 1986a.

Alley, R.B., J.H. Perepezko, and C.R. Bentley, Grain Growth in Polar Ice: II. Application, *Journal of Glaciology*, *32* (112), 425-433, 1986b.

Alley, R.B., Three-dimensional coordination number from two-dimensional measurements: a new method, *Journal of Glaciology*, *32* (112), 391-396, 1986c.

Alley, R.B., C.A. Shuman, D.A. Meese, A.J. Gow, K.C. Taylor, K.M. Cuffey, J.J. Fitzpatrick, P.M. Grootes, G.A. Zielinski, M. Ram, G. Spinelli, and B. Elder, Visual-stratigraphic dating of the GISP2 ice core: Basis, reproducibility, and application, *Journal of Geophysical Research-Oceans*, *102* (C12), 26367-26381, 1997.

Anderson, D.L., and C.S. Benson, The Densification and Diagenesis of Snow, in *Ice and Snow; Properties, Processes and applications*, edited by W.D. Kingerly, pp. 391-411, MIT press, Cambirdge, Mass, 1963.

Anklin, M., J.M. Barnola, J. Schwander, B. Stauffer, and D. Raynaud, Processes affecting the CO2 concentrations measured in Greenland ice, *Tellus*, *47B* (B), 461-470, 1995.

Baker, I., and D. Cullen, The structure and chemistry of 94 m GISP2 ice, *Annals of Glaciology*, *35*, 2002.

Barnes, P.R.F., Comment on "Grain boundary ridge on sintered bonds between ice crystals" [J. Appl. Phys., vol. 90, 5782-5785 (2001)]. *Journal of Applied Physics*, in press.

Barnes, P.R.F., R. Mulvaney, E.W. Wolff, and K. Robinson, A technique for the examination of polar ice using the scanning electron microscope, *Journal of Microscopy*, *205*, 118-124, 2002.

Beek, L.K.H.von., Dielectric behaviour of heterogeneous systems, *Progress in Dielectrics*, *7*, 69-114, 1967.

Benson, C.S., Stratigraphic Studies in the Snow and Firn of the Greenland Ice Sheet, *Res. Rep. 70.* U.S. Snow, Ice and Permafrost Research Establishment, 1962.

Camplin, G.C., J.W. Glen, and J.W. Paren, Theoretical Models for Interpreting the Dielectric Behaviour of HF-Doped Ice, *Journal of Glaciology*, *21*, 123-141, 1978.

Ciais, P., J. Jouzel, J.R. Petit, V. Lipenkov, and J.W.C. White, Holocene temperature variations inferred from six Antarctic ice cores, *Annals of Glaciology*, *20*, 427-435, 1994.

Colbeck, S.C., Sintering in a dry snow cover, *Journal of Applied Physics*, *84* (8), 4585-4589, 1998.

Cole-Dai, J., E. Mosley-Thompson, S.P. Wight, and L.G. Thompson, A 4100-year record of explosive volcanism from an East Antarctica ice core, *Journal of Geophysical Research*, *105* (D19), 24431-24441, 2000.

Cross, J.D., Scanning Electron Microscopy of Evaporating Ice, *Science*, *164*, 174-175, 1969.

REFERENCES

Cuffey, K.M., and E.J. Steig, Isotopic diffusion in polar firn: implications for interpretation of seasonal climate parameters in ice-core records, with emphasis on central Greenland, *Journal of Glaciology, 44* (147), 273-284, 1998.

Cullen, D., and I. Baker, The chemistry of grain boundaries in Greenland ice, *Journal of Glaciology, 46* (155), 703-706, 2000.

Cullen, D., and I. Baker, Observation of impurities in ice, *Microscopy Research and Technique, 55* (3), 198-207, 2001.

Dash, J.G., H.Y. Fu, and J.S. Wettlaufer, The Premelting of Ice and Its Environmental Consequences, *Reports on Progress in Physics, 58* (1), 115-167, 1995.

Davy, J.G., and D. Branton, Subliming Ice Surfaces: Freeze-Etch Electron Microscopy, *Science, 168*, 1216-1218, 1970.

Dominé, F., A. Cabanes, and L. Legagneux, Structure, microphysics, and surface area of the Arctic snowpack near Alert during the ALERT 2000 campaign, *Atmospheric Environment, 36* (15-16), 2753-2765, 2002.

Draper, N.R., and H. Smith, *Applied Regression Analysis*, 706 pp., Wiley, New York, 1998.

Dubochet, J., R. Lepault, J. Freeman, J.A. Berriman, and J.C. Homo, Electron microscopy of frozen water and aqueous solutions, *Journal of Microscopy, 128*, 219-237, 1982.

Duval, P., and C. Lorius, Crystal size and climatic record down to the last Ice Age from Antarctic ice, *Earth and Planetary Science Letters, 48*, 59-64, 1980.

Echlin, P., *Low-Temperature Microscopy and Analysis*, Plenum, New York, 1992.

Fujita, S., N. Azuma, H. Motoyama, T. Kameda, A. Narit, S. Matoba, M. Igarashi, M. Kohno, Y. Fujii, and O. Watanabe, Linear and nonlinear relations between the high-frequency limit conductivity, AC-ECM signal and ECM signals of Dome F Antarctic ice core from a laboratory experiment, *Annals of Glaciology, 35*, 2002.

Fukazawa, H., K. Sugiyama, S.J. Mae, H. Narita, and T. Hondoh, Acid ions at triple junction of Antarctic ice observed by Raman scattering, *Geophysical Research Letters, 25* (15), 2845-2848, 1998.

Gable, C.M., H.F. Betz, and S.H. Maron, Phase Equilibria of the System Sulphur Tioxide-Water, *Journal of the American Chemical Society, 72*, 1445-1448, 1950.

Glen, J.W., and J.G. Paren, Electrical Properties of Snow and Ice, *Journal of Glaciology, 15*, 15-38, 1975.

Gmitro, J.I., and T. Vermeulen, Vapor-Liquid Equilibria for Aqueous Sulfuric Acid, *A. I. Ch. E. Journal, 10* (5), 740-746, 1964.

Gow, A.J., On the rates of growth of grains and crystals in south polar firn, *Journal of Glaciology, 8*, 241-252, 1969.

Grousset, F.E., P.E. Biscaye, M. Revel, J.R. Petit, K. Pye, S. Joussaume, and J. Jouzel, Antarctic (Dome C) Ice-Core Dust at 18 Ky Bp - Isotopic Constraints on Origins, *Earth and Planetary Science Letters, 111* (1), 175-182, 1992.

REFERENCES

Hammer, C.U., Acidity of polar ice cores in relation to absolute dating, past volcanism, and radio echoes, *Journal of Glaciology, 25*, 359-372, 1980.

Harrison, W.D., and C.F. Raymond, Impurities and Their Distribution in Temperate Glacier Ice, *Journal of Glaciology, 16* (74), 173, 1976.

Herron, M.M., and C.C. Langway, Firn Densification: An Empirical Model, *Journal of Glaciology, 25*, 373-385, 1980.

Hobbs, P.V., *Ice Physics*, Oxford University Press, London, 1974.

Jaccard, C., Thermodynamics of irreversible processes applied to ice, *Physik der Kondensierten Materie, 3*, 99-118, 1964.

Johnsen, S.J., H.B. Clausen, W. Dansgaard, N.S. Gundestrup, C.U. Hammer, U. Andersen, K.K. Andersen, C.S. Hvidberg, D. Dahl-Jensen, J.P. Steffensen, H. Shoji, A.E. Sveinbjornsdottir, J. White, J. Jouzel, and D. Fisher, The delta O-18 record along the Greenland Ice Core Project deep ice core and the problem of possible Eemian climatic instability, *Journal of Geophysical Research-Oceans, 102* (C12), 26397-26410, 1997.

Johnsen, S.J., H.B. Clausen, K.M. Cuffey, G. Hoffmann, J. Schwander, and T. Creyts, Diffusion of stable isotopes in polar firn and ice: the isotope effect in firn diffusion, in *Physics of Ice Core Records*, edited by T. Hondoh, pp. 121-140, Hokkaido University Press, Sapporo, Japan, 2000.

Johnsen, S.J., D. Dahl-Jensen, N.S. Gundestrup, J.P. Steffensen, H.B. Clausen, H. Miller, V. Masson-Delmotte, A.E. Sveinbjornsdottir, and J. White, Oxygen isotope and paleotemperature records from six Greenland ice-core stations: Camp Century, Dye-3, GRIP, GISP2, Renland and NorthGRIP, *Journal of Quaternary Science, 16* (4), 299-307, 2001.

Jouzel, J., N.I. Barkov, J.M. Barnola, M. Bender, J. Chappellaz, C. Genthon, V.M. Kotlyakov, V. Lipenkov, C. Lorius, J.R. Petit, D. Raynaud, G. Raisbeck, C. Ritz, T. Sowers, M. Stievenard, F. Yiou, and P. Yiou, Extending the Vostok Ice-Core Record of Paleoclimate to the Penultimate Glacial Period, *Nature, 364* (6436), 407-412, 1993.

Kameda, T., K. Kawada, O. Watanabe, and H.B. Clausen, An empirical relation between overburden pressure and firn density, *Annals of Glaciology, 20*, 87-94, 1994.

Kipfstuhl, S., F. Pauer, W.F. Kuhs, and H. Shoji, Air bubbles and clathrate hydrates in the transition zone of the NGRIP deep ice core, *Geophysical Research Letters, 28* (4), 591-594, 2001.

Krauss, T.P., L. Shure, and J.N. Little, *Signal Processing Toolbox for use with MATLAB*, The MathWorks, inc., Natick (Mass.), 1994.

Kreutz, K.J., P. Mayewski, S.I. Whitlow, and M.S. Twickler, Limited migration of soluble ionic speciess in a Siple Dome, Antarctica, ice core, *Annals of Glaciology, 27*, 371-377, 1998.

Kuhs, W.F., A. Klapproth, and B. Chazallon, Chemical physics of air clathrate hydrates, in *Physics of Ice Core Records*, edited by T. Hondoh, Hokkaido University Press, Sapporo, Japan, 2000.

Kumai, M., Identification of Nuclei and Concentrations of Chemical Species in Snow Crystals Sampled at the South Pole, *Journal of Atmospheric Sciences, 33*, 833-841, 1976.

REFERENCES

Legrand, M.R., and R.J. Delmas, Soluble impurities in four Antarctic ice cores over the last 30,000 years, *Annals of Glaciology, 10*, 116-120, 1988.

Legrand, M. R., and P. Mayewski, Glaciochemistry of polar ice cores: A review, *Reviews of Geophysics, 35* (3), 219-243, 1997.

Lipenkov, V.Y., Air bubbles and air-hydrate crystals in the Vostok ice core, in *Physics of Ice Core Records*, edited by T. Hondoh, Hokkaido University Press, Sapporo, Japan, 2000.

Mader, H.M., Observations of the water vein system in polycrystaline ice, *Journal of Glaciology, 38*, 333-347, 1992a.

Mader, H.M., The thermal behaviour of the water-vein system in polycrystaline ice, *Journal of Glaciology, 38*, 359-374, 1992b.

McConnell, J.R., R.C. Bales, and D.R. Davis, Recent intra-annual snow accumulation at South Pole: Implications for ice core interpretation, *Journal of Geophysical Research, 102* (D18), 21,947-21,954, 1997.

Miners, W.D., E.W. Wolff, J.C. Moore, R. Jacobel, and L. Hempel, Modeling the radio echo reflections inside the ice sheet at Summit, Greenland, *Journal of Geophysical Research, 107* (B8), 10.1029/2001JB000535, 2002.

Miners, W.D., Electromagnetic Reflections Inside Ice Sheets, Ph.D. Thesis, Open University, 1998.

Moore, J.C., R. Mulvaney, and J.G. Paren, Dielectric stratigraphy of ice: a new technique for determining total ionic concentrations in polar ice cores, *Geophysical Research Letters, 16*, 1177-1180, 1989.

Moore, J.C., and S. Fujita, Dielectric properties of ice containing acid and salt impurity at microwave and low frequencies, *Journal of Geophysical Research, 98* (B6), 9769-9780, 1993.

Moore, J.C., E.W. Wolff, H.B. Clausen, and C.U. Hammer, The chemical basis for the electrical stratigraphy of ice, *Journal of Geophysical Research, 97* (B2), 1887-1896, 1992.

Moore, J.C., E.W. Wolff, H.B. Clausen, C.U. Hammer, M.R. Legrand, and K. Fuhrer, Electrical response of the Summit-Greenland ice core to ammonium, sulphuric acid, and hydrochloric acid, *Geophysical Research Letters, 21/7*, 565-568, 1994.

Mulvaney, R., E.W. Wolff, and K. Oates, Sulphuric acid at grain boundaries in Antarctic ice, *Nature, 331*, 247-249, 1988.

Nijsse, J., and A.C. Van Aelst, Cryo-Planning for Cryo-Scanning Electron Microscopy, *Scanning, 21*, 372-378, 1999.

Nye, J.F., and F.C. Frank, Hydrology of the Intergranular Viens in a Temperate Glacier, *Proceedings of the Syposium "Hydrology of Glaciers" IAHS - IASH, 95*, 157-161, 1973.

Nye, J.F., The Geometry of Water Veins and Nodes in Polycrystalline Ice, *Journal of Glaciology, 35* (119), 17-22, 1989.

Nye, J.F., Thermal behaviour of glacier and laboratory ice, *Journal of Glaciology, 37*, 401-413, 1991a.

Nye, J.F., The rotting of temperate ice, *Journal of Crystal Growth, 113*, 465 - 476, 1991b.

REFERENCES

Nye, J.F., Diffusion of isotopes in the annual layers of ice sheets, *Journal of Glaciology, 44*, 467-468, 1998.

Oates, K., and W.T.W. Potts, Electron-Beam Penetration and X-Ray-Excitation Depth in Ice, *Micron and Microscopica Acta, 16* (1), 1-4, 1985.

Palmer, S.A., T.D. van Ommen, M.A.J. Curran, V. Morgan, J.M. Souney, and P.A. Mayewski, High -precision dating of volcanic events (A.D. 1301-1995) using ice cores from Law Dome, Antarctica, *Journal of Geophysical Research, 106* (D22), 28089-28095, 2001.

Pasteur, E.C., and R. Mulvaney, Migration of methane sulphonate in Antarctic firn and ice, *Journal of Geophysical Research, 105* (D9), 11525-11534, 2000.

Paterson, W.B.S., *The Physics of Glaciers*, Pergamon, Oxford, 1994.

Pauer, F., S. Kipfstuhl, W.F. Kuhs, and H. Shoji, Air clathrate crystals from the GRIP deep ice core, Greenland: a number-, size- and shape-distribution study, *Journal of Glaciology, 45* (149), 22-30, 1999.

Percival, D.B., and A.T. Walden, *Spectral Analysis for Physical Applications*, Cambridge University Press, Cambridge, 1993.

Petit, J., M. Briat, and A. Ryer, Ice age aerosol content from East Antarctic ice core samples and past wind strength, *Nature, 293*, 391-394, 1981.

Petit, J.R., J. Jouzel, D. Raynaud, N.I. Barkov, J.M. Barnola, I. Basile, M. Bender, J. Chappellaz, M. Davis, G. Delaygue, M. Delmotte, V.M. Kotlyakov, M. Legrand, V.Y. Lipenkov, C. Lorius, L. Pepin, C. Ritz, E. Saltzman, and M. Stievenard, Climate and atmospheric history of the past 420,000 years from the Vostok ice core, Antarctica, *Nature, 399* (6735), 429-436, 1999.

Petrenko, V.F., Electrical Properties of Ice, CRREL,Special Report 93-20, Hanover, NH, 1993.

Petrenko, V.F., and R.W. Whitworth, *Physics of Ice*, Oxford University Press, Oxford, 1999.

Pickering, S.U., Die Hydrate der Chlorwasserstoffsäure, *Berichte der Deutschen Chemischen Gesselschaft, 26*, 277-284, 1893.

Pollack, G.H., *Cells, gels and the engines of life*, 320 pp., Ebner and Sons, Seattle, 2001.

Price, P.B., A habitat for psychrophiles in deep Antarctic ice, *PNAS, 97* (3), 1247-1251, 2000.

Ramseier, R.O., Self-diffusion of tritium in natural and synthetic ice monocrystals, *Journal of Applied Physics, 38*, 2553-2556, 1967.

Rango, A., W.P. Wergin, and E.F. Erbe, Snow crystal imaging using scanning electron microscopy: I. Precipitated snow, *Hydrological Sciences Journal-Journal Des Sciences Hydrologiques, 41* (2), 219-233, 1996.

Rango, A., W.P. Wergin, E.F. Erbe, and E.G. Josberger, Snow crystal imaging using scanning electron microscopy: III. Glacier ice, snow and biota, *Hydrological Sciences Journal-Journal Des Sciences Hydrologiques, 45* (3), 357-375, 2000.

Raviv, U., P. Laurat, and J. Klein, Fluidity of water confined to subnanometre films, *Nature, 413*, 51-54, 2001.

Reid, A.P., W.T.W. Potts, K. Oates, R. Mulvaney, and E. Wolff, Preparation of Aqueous Standards for Low Temperature X-Ray Microanalysis, *Microscopy Research and Technique*, 22, 207-211, 1992.

Reid, A.P., K. Oates, and W.T.W. Potts, The Effect of Aluminium Coating on Elemental Signals in X-Ray Microanalysis, *Microscopy Research and Technique*, *24*, 168-172, 1993.

Rempel, A.W., E.D. Waddington, J.S. Wettlaufer, and M.G. Worster, Possible displacement of the climate signal in ancient ice by premelting and anomalous diffusion, *Nature*, *411*(6837) 2001a.

Rempel, A.W., J.S. Wettlaufer, and M.G. Worster, Interfacial Premelting and the Thermomolecular Force: Thermodynamic Buoyancy, *Physical Review Letters*, *87* (8), 88501-88504, 2001b.

Reynolds, J.M., Dielectric Behaviour of Firn and Ice from the Antarctic Peninsula, Antarctica, *Journal of Glaciology*, *3* (109), 253-262, 1985.

Robin, G.d.Q., Glaciology. III. Seismic shooting and related investigations, *Norwegian-British-Swedish Antarctic Expedition, 1949-52. Scientific Results*, *5*, 1958.

Roscoe, H.K., The Risk of Large Volcanic Eruptions and the Impact of this Risk on Future Ozone Depletion, *Natural Hazards*, *23*, 231-246, 2001.

Rosen, J.M., T. Kjome, R.L. McKenzie, and J.B. Liley, Decay of Mount Pinatubo aerosol at midlatitudes in the northern and southern hemispheres, *Journal of Geophysical Research*, *99* (D12), 25733-25739, 1994.

Röthlisberger, R., M. Bigler, M. Hutterli, S. Sommer, B. Stauffer, H.G. Junghans, and D. Wagenbach, Technique for Continuous High-Resolution Analysis of Trace Substances in Firn and Ice Cores, *Environmental Science and Technology*, *34*, 338-342, 2000.

Schulson, E.M., and I. Baker, Fractography of Ice, *Journal of Materials Science Letters*, *8* (10), 1193-1194, 1989.

Schwander, J., J. Jouzel, C. Hammer, J. Petit, R. Udisti, and E. Wolff, A tentative chronology for the EPICA Dome Concordia ice core, *Geophysical Research Letters*, *28* (22), 4243-4246, 2001.

Shabtaie, S., and C.R. Bentley, Unified theory of electrical conduction in firn and ice: Site percolation and conduction in snow and firn, *Journal of Geophysical Research*, *99* (B10), 19757-19769, 1994.

Shoji, H., Microscopic observations of air hydrate inclusions in deep ice core samples, in *Physics of Ice Core Records*, edited by T. Hondoh, Hokkaido University Press, Sapporo, Japan, 2000.

Stauffer, D., and A. Aharony, *Introduction to Percolation Theory*, Taylor & Francis, London, 1992.

Steffensen, J.P., H.B. Clausen, and C. Hammer, The chemical composition of cold events within the Eemian section of the Greenland Ice Core Project ice core from Summit, Greenland, *Journal of Geophysical Research*, *102* (C12), 26,747-26,754, 1997.

Taylor, K.C., R.B. Alley, G.W. Lamorey, and P. Mayewski, Electrical measurements on the Greenland Ice Sheet Project 2 Core, *Journal of Geophysical Research*, *102* (C12), 26511-26517, 1997.

REFERENCES

Thibert, E., and F. Dominé, Thermodynamics and Kinetics of the Solid Solution of HCl in Ice, *Journal of Physical Chemistry B, 101*, 3554-3565, 1997.

Thorsteinsson, T., J. Kipfstuhl, and H. Miller, Textures and fabrics in the GRIP ice core, *Journal of Geophysical Research-Oceans, 102* (C12), 26583-26599, 1997.

Traversi, R., S. Becagli, E. Castellano, O. Largiuni, and R. Udisti, Stability of chemical species in firn layers from Antarctica, in *Conference Proceedings Italian Research on Antarctic Atmosphere*, edited by E. Colacino, and G. Giovannelli, pp. 421-443,ENEA, Bologna, Italy, 2000.

Trickett, Y.L., I. Baker, and P.M.S. Pradhan, The effects of sulfuric acid on the mechanical properties of ice single crystals, *Journal of Glaciology, 46* (153), 239-243, 2000.

Trudinger, C.M., I.G. Enting, R.J. Etheridge, V.A. Francey, V.A. Levchenko, L.P. Steele, D. Raynaud, and L. Arnaud, Modeling air movement and bubble trapping in firn, *Journal of Geophysical Research, 102* (D6), 6747-6763, 1997.

Tschumi, J., and B. Stauffer, Reconstructing past atmospheric CO_2 concentration based on ice-core analyses: open questions due to in situ production of CO_2 in the ice, *Journal of Glaciology, 46* (152), 45-53, 2000.

Uchida, T., S.J. Mae, T. Hondoh, P. Duval, and V. Lipenkov, Effects of Air-Hydrate Crystals on Ice Grain Growth, *Proc. NIPR Symp. Meteorol. Glaciol., 7*, 7-13, 1993.

Udisti, R., S. Becagli, E. Castellano, R. Mulvaney, J. Schwander, S. Toricini, and E. Wolff, Holocene electrical and chemical measurements from the EPICA-Dome C ice core, *Annals of Glaciology, 30*, 20-26, 2000.

Weast, R.C., *CRC Handbook of Chemistry and Physics*, 63rd edition, CRC Press, Florida, 1977-1978.

Weiss, J., J. Vidot, M. Gay, L. Arnaud, P. Duval, and J.R. Petit, Dome Concordia ice microstructure: impurities effect on grain growth, *Annals of Glaciology, 35*, 2002.

Wergin, W.P., A. Rango, and E.F. Erbe, Image comparisons of snow and ice crystals photographed by light (video) microscopy and low-temperature scanning electron microscopy, *Scanning, 20* (4), 285-296, 1998.

Wolff, E.W., and J.G. Paren, A Two-Phase Model of Electrical Conduction in Polar Ice Sheets, *Journal of Geophysical Research, 89* (B11), 9433-9438, 1984.

Wolff, E.W., R. Mulvaney, and K. Oates, The location of impurities in Antarctic ice, *Annals of Glaciology, 11*, 1988.

Wolff, E.W., and R. Mulvaney, Impurity distributions in ice under different environmental conditions (Abstract), *Annals of Glaciology, 14*, 362, 1990.

Wolff, E.W., W.D. Miners, J.C. Moore, and J.G. Paren, Factors controlling the electrical conductivity of ice from the polar regions - a summary, *Physical Chemistry B, 101* (32), 6090-6094, 1997.

Wolff, E.W., I. Basile, J.R. Petit, and J. Schwander, Comparison of Holocene electrical records from Dome C and Vostok, Antarctica, *Annals of Glaciology, 29*, 1999.

REFERENCES

Wolff, E.W., History of the Atmosphere from Ice Cores, in *From Weather Forecasting to Exploring the Solar System*, edited by C. Bourtron, pp. 147-177, EDP Sciences, Les Ulis, France, 2001.

Woodruff, D.P., *The Solid -Liquid Interface*, Cambridge University Press, Cambridge, UK., 1973.

Zielinski, G.A., P. Mayewski, L.A. Meeker, K. Grönvold, M.S. Germani, S.I. Whitlow, M.S. Twickler, and K.C. Taylor, Volcanic aerosol records and tephrochronology of the Summit, Greenland, ice cores, *Journal of Geophysical Research*, *102* (C12), 26625-26640, 1997.

APPENDIX

Enlarged micrographs

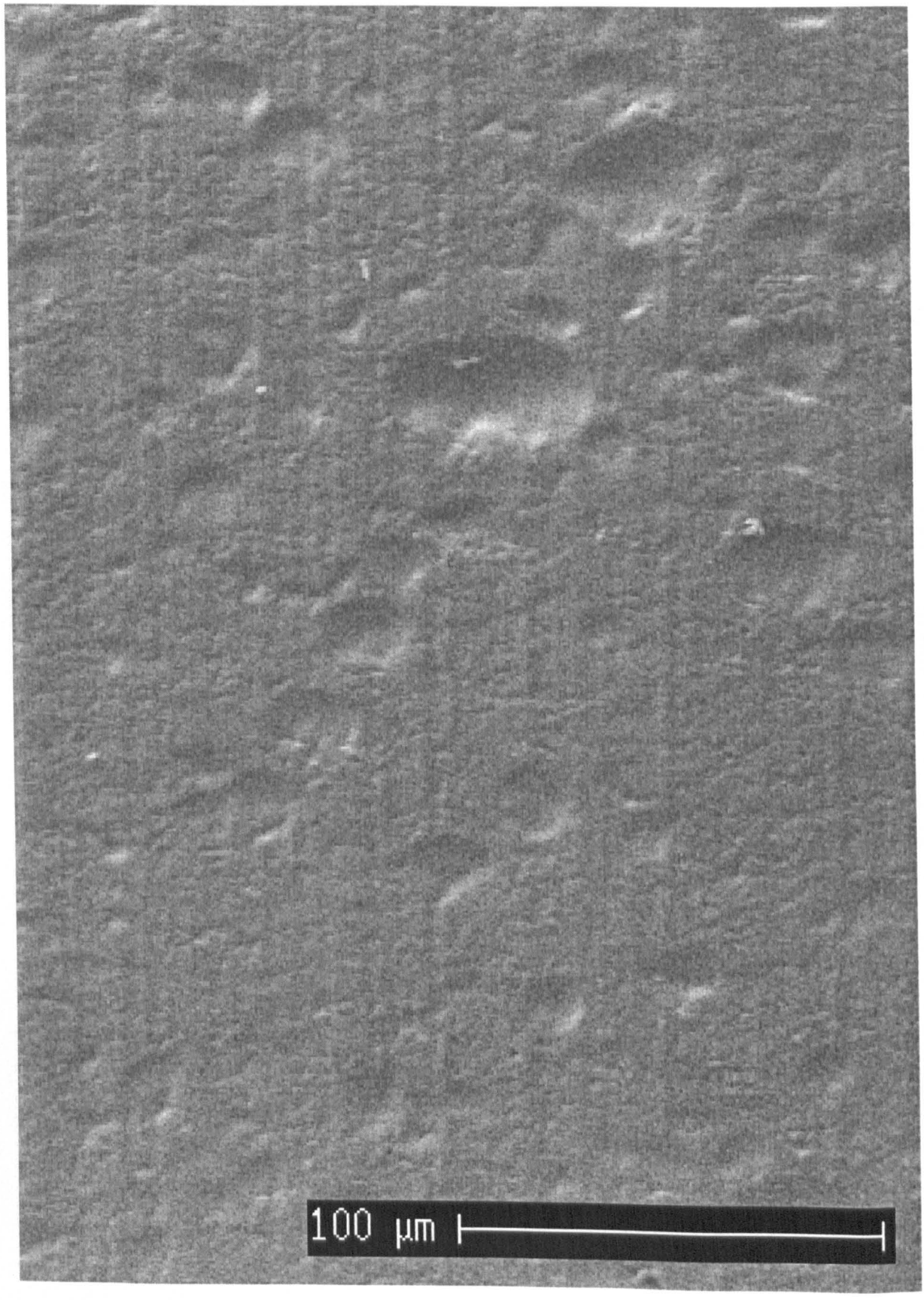

Figure A.II.3a. Surface cut with tungsten carbide blade.

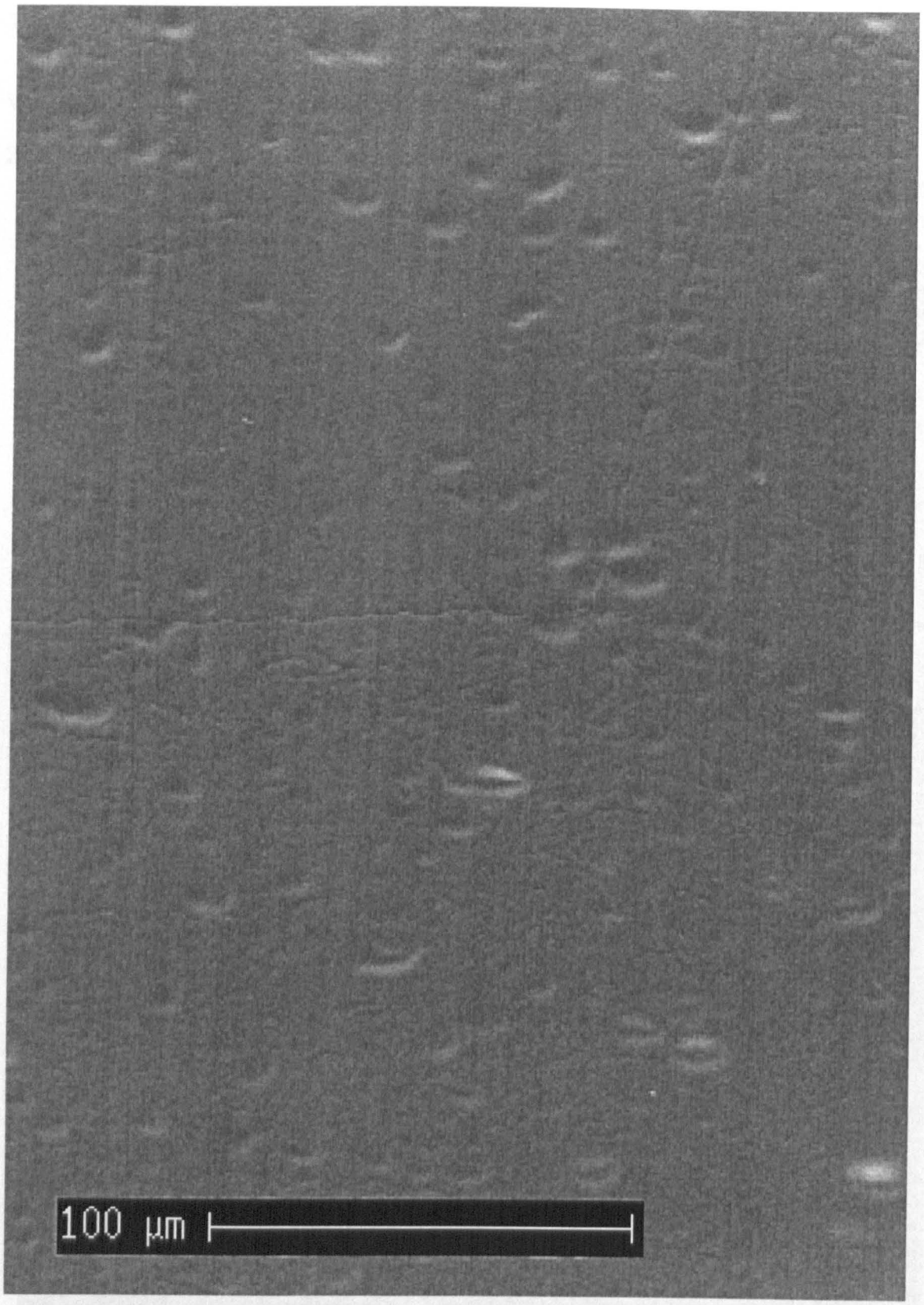

Figure A.II.3b. Surface cut with tungsten hardened steel blade immediate transfer.

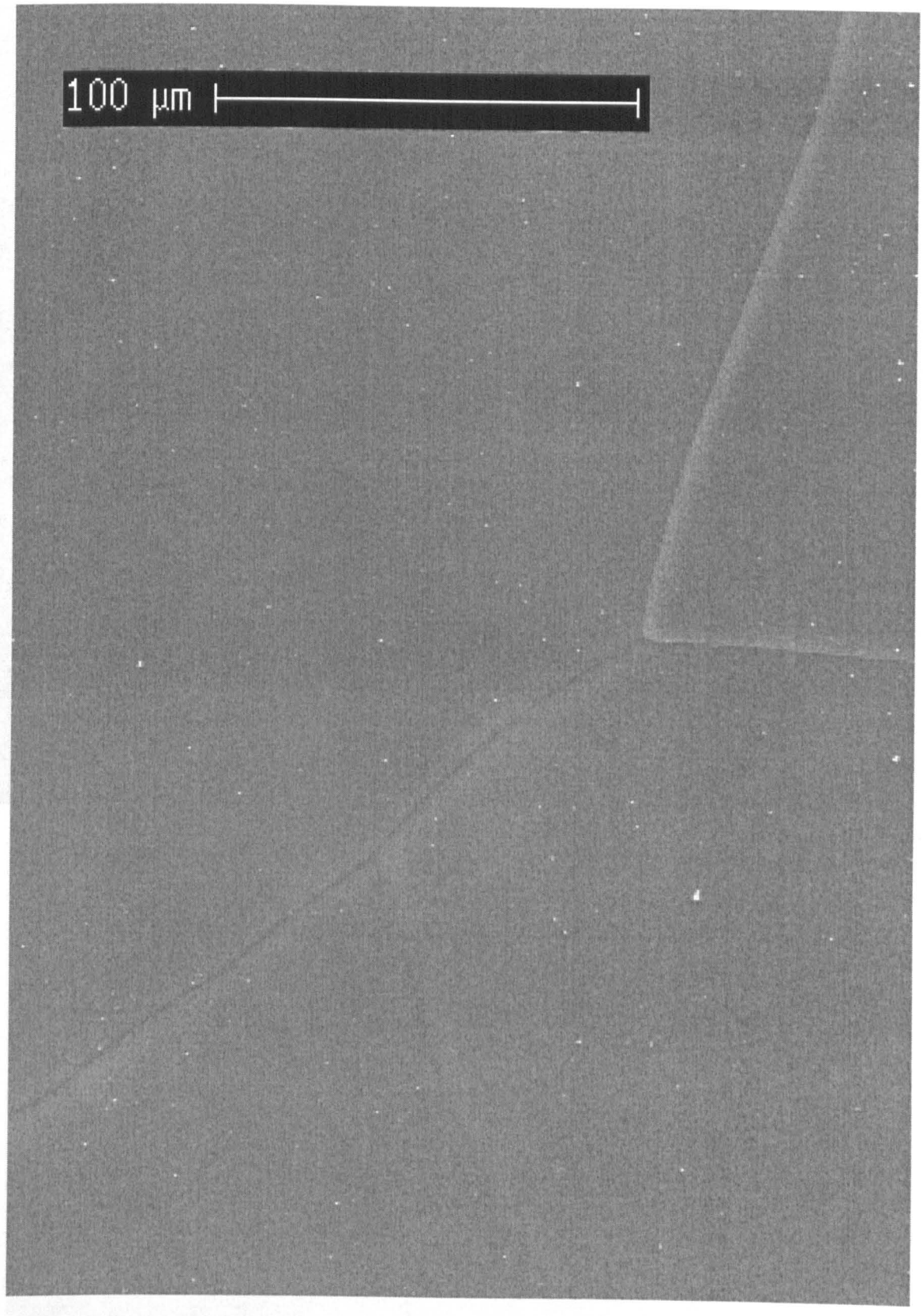

Figure A.II.3c. Similar prepare similarly to figure A.III.3b, but pre-etched for 4 hours, grain boundary grooves and subgrain boundaries now clearly visible.

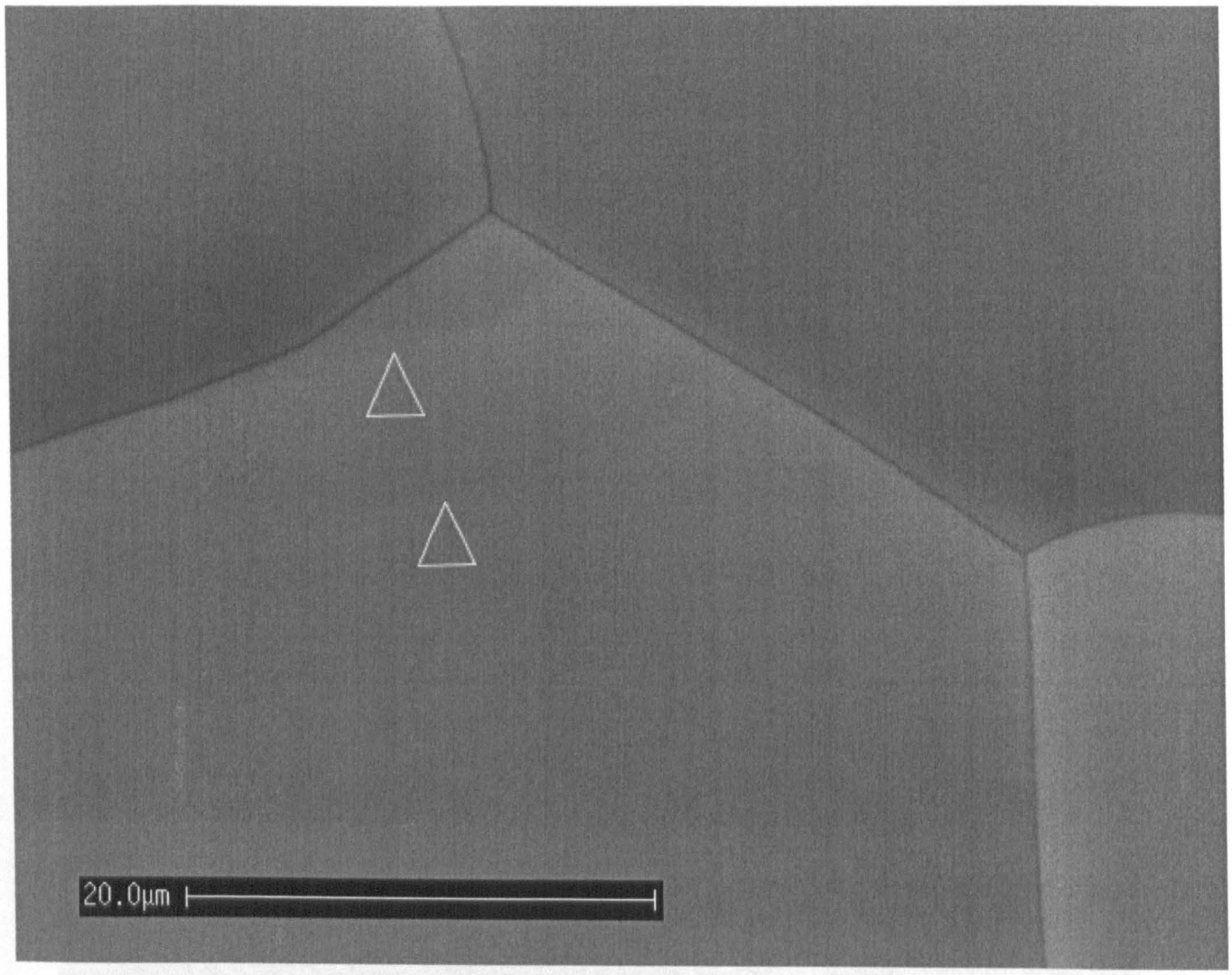

Figure A.III.1a. Grain boundary grooves on surface of pre-etched ice from Dronning Maud Land, sub-grain boundaries are also apparent (arrows)

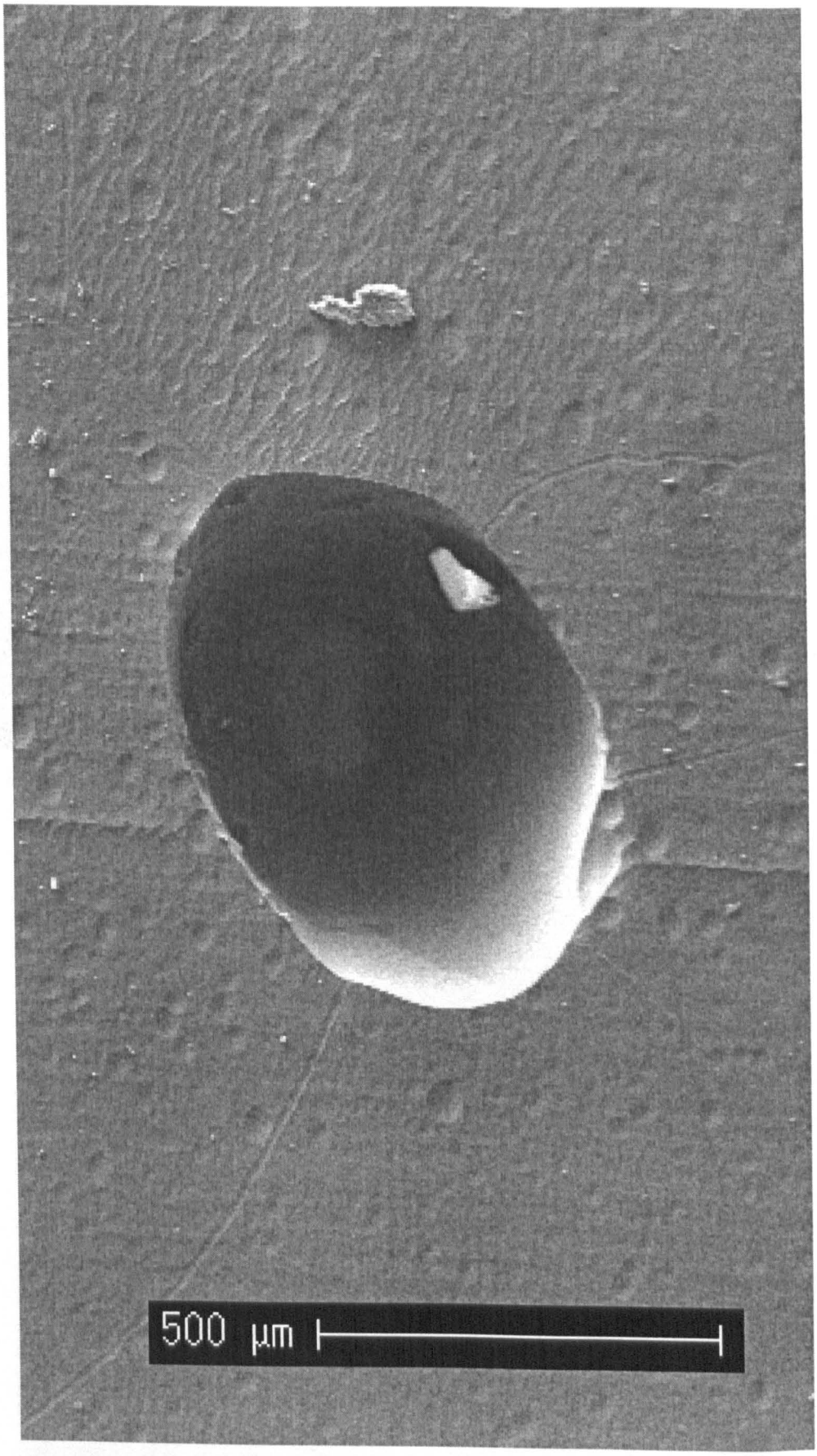

Figure A.III.2a. An air bubble in Dronning Maud Land ice (115 m) at the intersection between several grain boundaries. Etching channels are apparent because the specimen was inserted into the SEM at -20 °C.

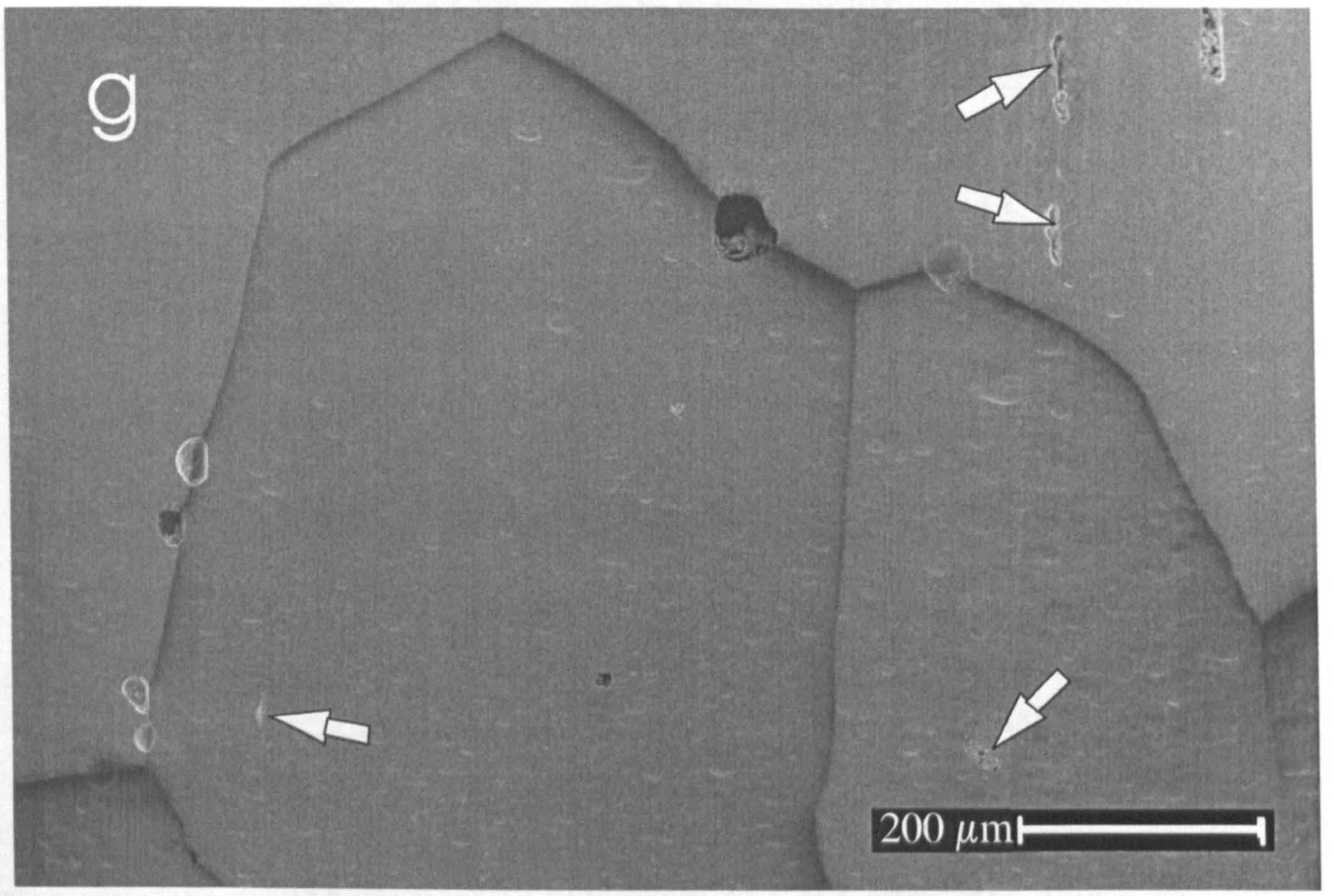

Figure A.III.3g. Globular hydrate structures at grain boundaries and plate like structures in grain interiors in GRIP glacial ice.

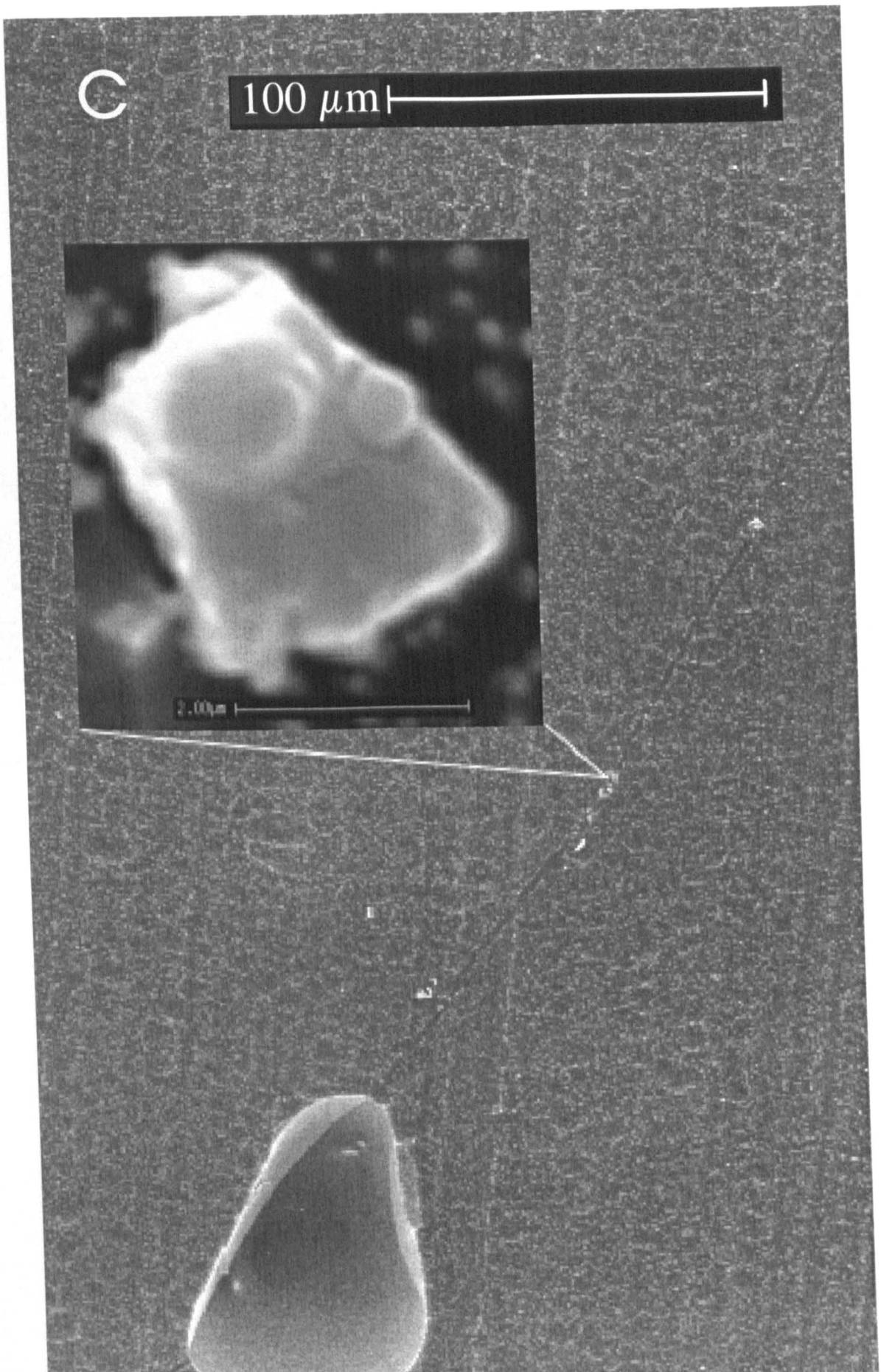

Figure A.III.4c. Particles at grain boundary in GRIP glacial ice, note the slight bend in the boundary coincident with the dust particles.

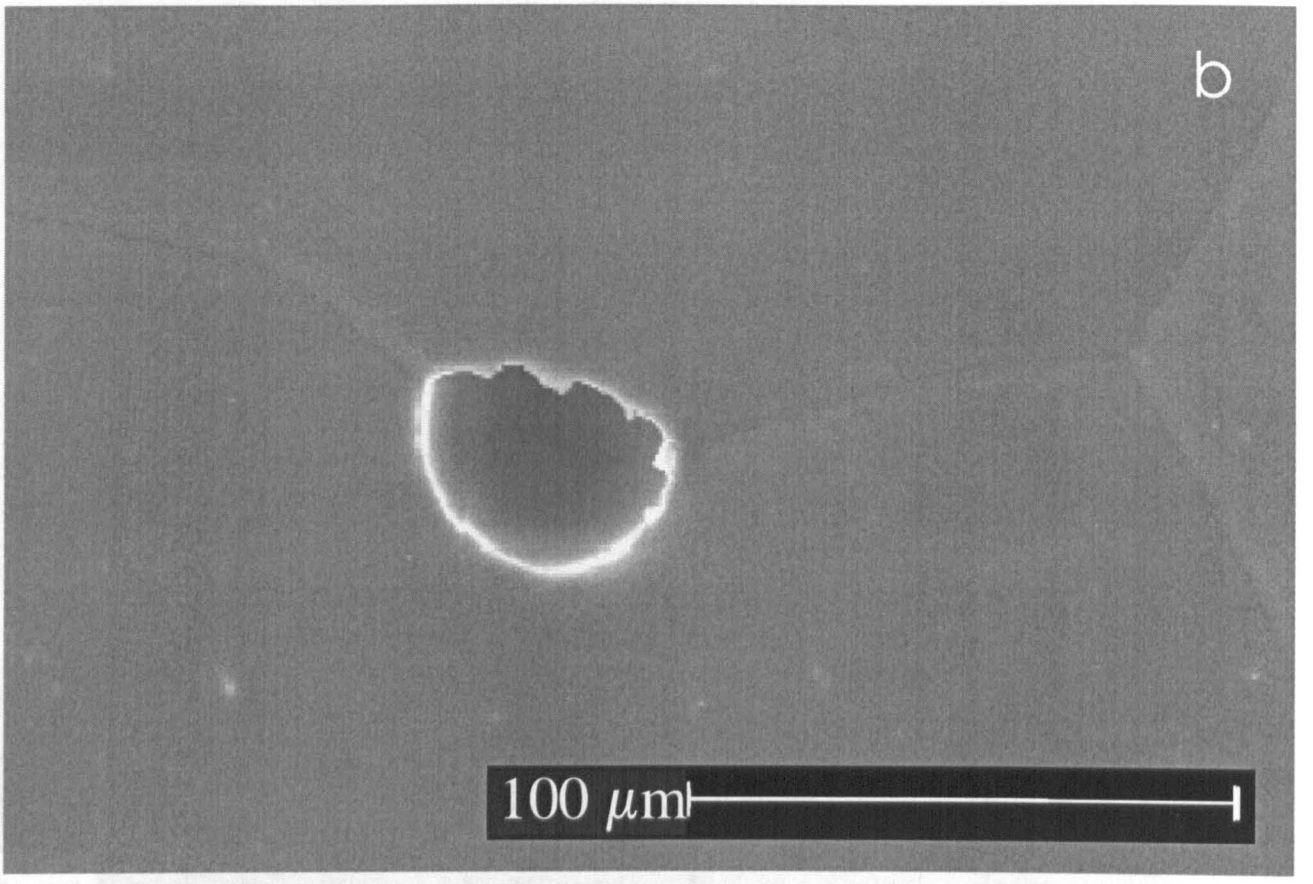

Figure A.III.5b. Bubble impeding grain boundary migration in Dronning Maud Land ice (115 m).

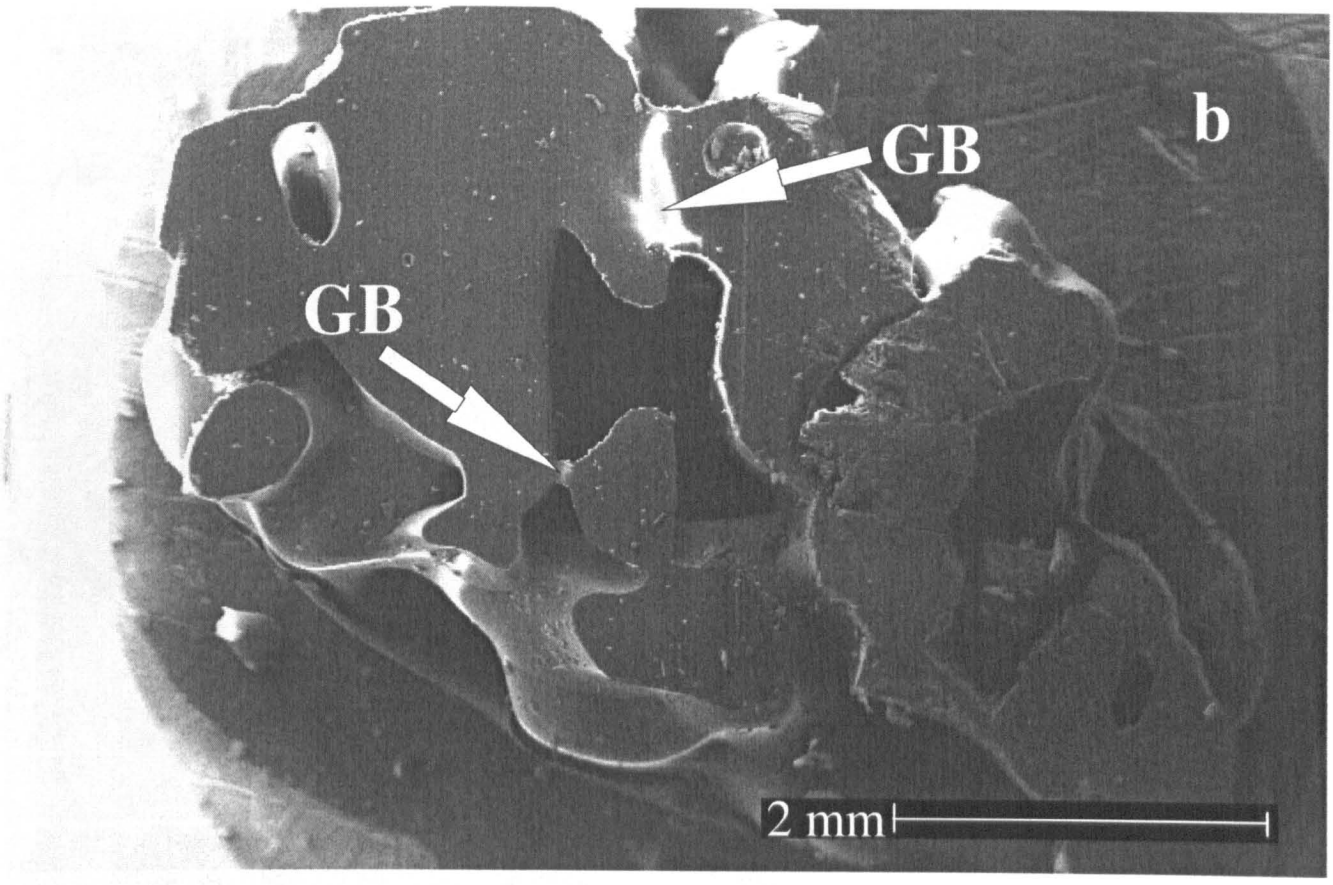

Figure A.VI.1b. Dome C firn from 23.3 m, density 526 kg m^{-3}.

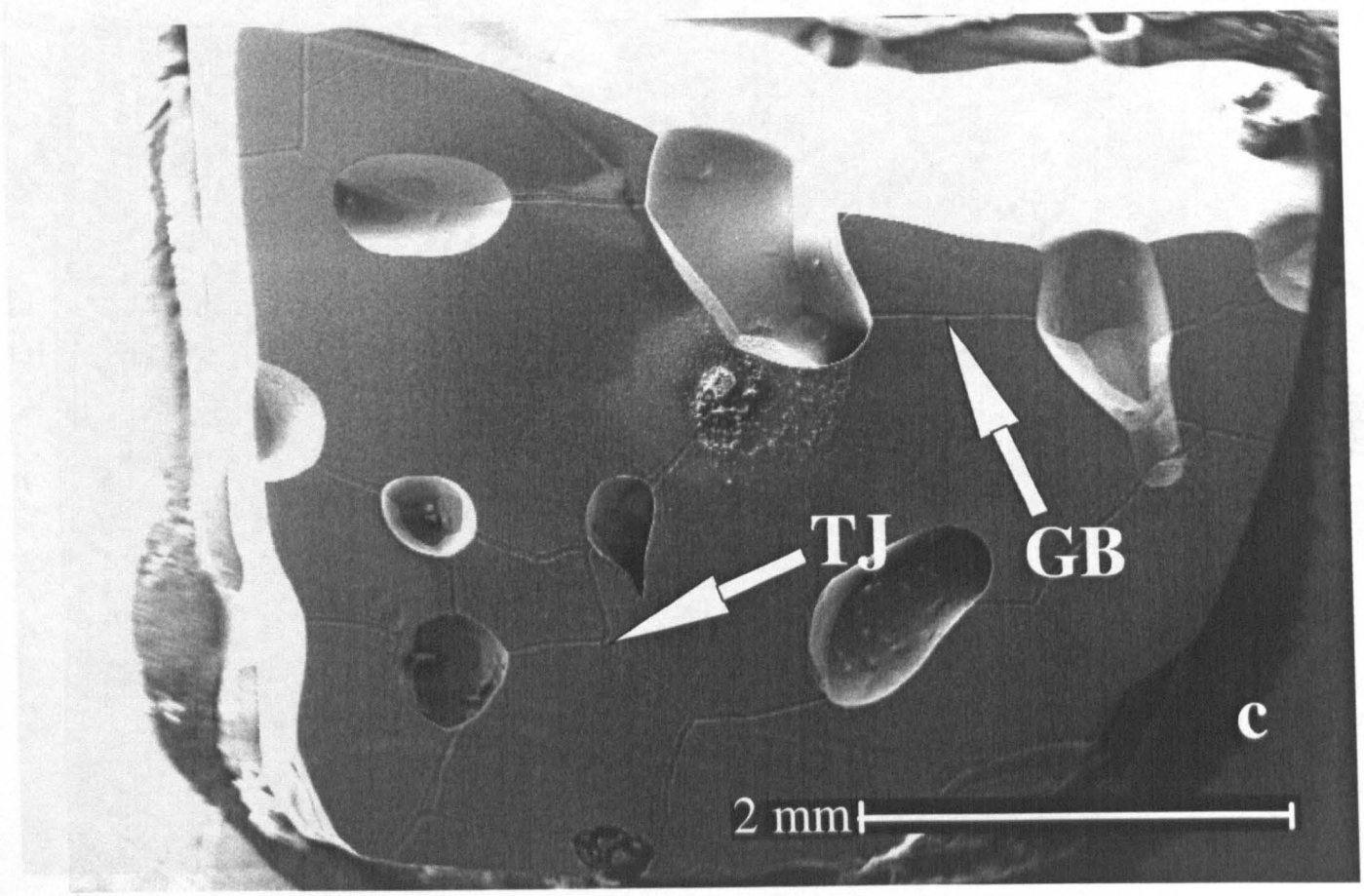

Figure A.VI.1b. Dome C firn from 95.8 m, density 820 kg m^{-3}.

Any pages, tables, figures or photographs, missing from this digital copy, have been excluded at the request of the university.